Université d'Ottawa · University of Ottawa

Université d'Ottawa · University of Ottawa

FACULTÉ DE ÉTUDES SUPÉRIEURES ET POSTDOCTORALES

FACULTY OF GRADUATE AND POSTDOCTORAL STUDIES

Ziyad Ahmed TAHA

AUTEUR DE LA THÈSE - AUTHOR OF THESIS

Ph.D. (Chemistry)

GRADE - DEGREE

Department of Chemistry

FACULTÉ, ÉCOLE, DÉPARTEMENT - FACULTY, SCHOOL, DEPARTMENT

TITRE DE LA THÈSE - TITLE OF THE THESIS

Silica-supported Vanadium Complexes : Structure, Characterization and Reactivity, Especially towards Olefins

H. Alper

DIRECTEUR DE LA THÈSE - THESIS SUPERVISOR

CO-DIRECTEUR DE LA THÈSE - THESIS CO-SUPERVISOR

EXAMINATEURS DE LA THÈSE - THESIS EXAMINERS

C. Crudden

S. Gambarotta

A. Sayari

M. Ternan

J.-M. De Koninck, Ph.D.

LE DOYEN DE LA FACULTÉ DES ÉTUDES SUPÉRIEURES ET POSTDOCTORALES

DEAN OF THE FACULTY OF GRADUATE AND POSTDOCTORAL STUDIES

Silica-supported Vanadium Complexes: Structure, Characterization and Reactivity, Especially towards Olefins

By

Ziyad Ahmed Taha

Thesis submitted to the
Faculty of Graduate and Postgraduate Studies
In partial fulfillment of the requirements for the degree of

Doctor of Philosophy
in
Chemistry

Department of Chemistry
University of Ottawa
Ottawa, Ontario
Canada

Professor Howard Alper
Research Supervisor

Ziyad A. Taha
Ph. D. Candidate

THE UNIVERSITY OF OTTAWA
January 2004-05-11

Your file Votre référence
ISBN: 0-494-01771-6
Our file Notre référence
ISBN: 0-494-01771-6

To

My Late Father, My Mother, My Brothers and My Sisters

Abstract

This thesis is divided into four major parts. The first part describes a simple method to measure the content of reactive hydroxyls of various amorphous silicas before and after thermal treatment. The reaction of excess $VOCl_3$ vapor with surface OH groups of partially dehydroxylated silica is rapid and quantitative. Regardless of the degree of dehydroxylation, the stoichiometry of the reaction is invariable, as demonstrated by ^{51}V magic angle spinning NMR spectroscopy and X-ray absorption spectroscopy (XAS). Using this method, we have quantified the reacive hydroxyls of fumed and precipitated silicas as a function of temperature. Non-porous Aerosil silicas have hydroxyl contents that decrease linearly with increasing temperature of thermal treatment. Porous Sylopol silicas have higher hydroxyl contents per unit surface area than Aerosil silicas treated at the same temperature.

The second part deals with characterization of silica-supported vanadium complexes using XAS. A combination of X-ray absorption fine structure (EXAFS) and X-ray-absorption near edge structure (XANES) has been used to characterize the local structure around the vanadium metal center for a series of silica-supported vanadium complexes prepared at various temperatures and on different supports (Aerosil and Sylopol silicas). XAS spectra of all the materials were very similar. The local structure around vanadium was not affected by the thermal treatment and the kind of support. Vanadium has a formal oxidation state of +5 and pseudotetrahedral coordination geometry.

The third part deals with the preparation and characterization of new vanadium-based Ziegler-Natta catalysts. The catalysts were prepared by sequential reaction of volatile $VOCl_3$ and trimethylaluminum (TMA) with silica. They were characterized by infrared spectroscopy (IR), electron spin resonance spectroscopy (ESR) and stoichiometric analysis. The interaction of TMA with silica/$VOCl_3$ and silica/TMA/$VOCl_3$ results in the grafting of two Al per original hydroxyl group with concomitant formation of two equiv. CH_4. In contrast, the reaction of $VOCl_3$ with silica/TMA results in the grafting of two V per original OH group with concomitant formation of two equiv. CH_3Cl.

The last part of this thesis describes the reaction of the new vanadium-based Ziegler-Natta catalysts with ethylene, propylene and ethylene-propylene mixture. Kinetics at the gas-solid interface were monitored by *in situ* IR spectroscopy. The reaction is first order in olefin and first-order in vanadium. Based on kinetics and isotope effects, a mechanism of migratory insertion of the olefin into a vanadium-carbon-α-bond (Cossee mechanism) is proposed for the propagation step.

Acknowledgments

The completion of this work would not have been possible without a number of people to whom I am very grateful. First I would like to thank my supervisors, Prof. Susannah Scott and Prof. Howard Alper for their support, encouragement, patience, guidance and for being very understanding persons. I would like to thank Dr. Scott for giving me the opportunity to work in her lab and willingness to share her expertise through the course of my graduate work. I would like to thank Dr. Alper for taking care me after Dr. Scott leaving.

I would like to thank Dr. George Meitzner and Eric Deguns for the XAS analysis, Dr. Glen Facey for his help with running the solid state NMR spectra, Ron Hartree for XRF, Dr. Victor Terskikh (NRC) for recording EPR spectra, Dr. Wenxing Kuang for measuring silica surface area, Tamer El Bokl and Mohammed Moniruzzaman for running the DSC, Andrew Zlotorzinski for some of the GC-MS analysis, John Hopkins, Don Hopkins and Lee Sorensen.

I would like to thank Lise Maisonneuve, Lorraine Houle and the entire chemistry Department supporting staff. Your work does not go unnoticed or unappreciated.

I would like to thank my colleagues and friends whom I had the pleasure of working with over the years. There are fare many of you to mention but I would like to thank particularly Fuad A., Tamara C., Dao, Salo, Azfar H., Ghazar A. and Rashed T. who have been with me for the most of my time here at Ottawa University.

Finally, I would like to thank deeply my family whom I love very much, My late father, my mother, my brothers, my sisters and their families for their unselfish and unwavering support which made this work possible. You have always been there for me whenever I needed you.

Table of Contents

Page

Chapter 2. Experimental Techniques

Page

Chapter 5. Reactions of Vanadyl Chloride and Trimethylaluminum at Silica Surface

List of Figures

Chapter 4 Page

Chapter 6

List of Schemes

List of Tables

Chapter One

Introduction

1.1 Ziegler-Natta catalysts for olefin polymerization

Prior to 1953, polyethylene was known only as a low melting and highly branched material, with a broad molecular weight distribution. It was made by radical polymerization at very high pressures (1000-3000 atm) and moderate temperatures (150-230°C).[1] In the 1950's, Karl Ziegler discovered that certain combinations of transition metal compounds and main group organometallic compounds catalyze the polymerization of ethylene to high molecular weight linear polyethylene at low pressures and even at room temperature.[2] Soon after, Giulio Natta showed that one of the Ziegler catalysts polymerizes propylene to isotactic polypropylene under the same mild conditions.[3] When their discoverers shared the 1963 Nobel Prize in chemistry, these catalysts became known as Ziegler-Natta catalysts.

Ziegler-Natta polymerization catalysts are formed by a combination of a group I-III organometallic compound with inorganic compounds of group IV-VIII transition metals. By convention, the transition metal component is referred to as the catalyst and the main group component as the cocatalyst. Catalysts include halides or oxyhalides of titanium, vanadium, chromium, molybdenum and zirconium. The most common Ziegler-Natta catalysts are combinations of $TiCl_4$

or $TiCl_3$ with $Al(C_2H_5)_2Cl$ or with $Al(C_2H_5)_3$.[4] The functions of the cocatalyst in the Ziegler-Natta olefin polymerization process include:[5]

- scavenging oxygen, water and other impurities that would otherwise deactivate the catalyst through poisoning;
- reducing the transition metal catalyst to its active oxidation state;
- initiating polymerization by alkylation of the transition metal;
- generating and stabilizing cationic charge at the active site by abstraction of a ligand from the transition metal complex.

Silica, alumina, zirconia, titania and magnesium chloride have all been used as supports for Ziegler-Natta catalysts. Using a support for the polymerization catalyst results in several advantages, such as lowering the required ratio of alkylaluminum cocatalyst to transition metal catalyst, reducing catalyst manufacturing costs and producing less hazardous waste in catalyst synthesis.

Silica-supported Ziegler-Natta catalysts have been employed for the synthesis of high-density polyethylene (HDPE), linear low-density polyethylene (LLDPE), polypropylene, ethylene-propylene copolymers and polybutadiene, as well as many other products. The catalyst's activity changes with time, and it is not uncommon for maximum activity to be reached after an induction period of for one or two hours. Catalyst activity decreases with increasing steric hindrance about the double bond. The observed order of reactivity for 1-alkenes is:[4]

$CH_2=CH_2$ >> $CH_2=CHCH_3$ > $CH_2=CHCH_2CH_3$ > $CH_2=CHCH_2CH(CH_3)_2$ > $CH_2=CHCH(CH_3)_2$ > $CH_2=CHCH(CH_2CH_3)_2$ > $CH_2=CHC(CH_3)_3$

Ziegler-Natta catalysts are inactive towards other kinds of monomers. For example, vinyl chloride and acrylates are not polymerizable by Ziegler-Natta catalysts.

1.1.2 Mechanism of olefin polymerization

The mechanism for transition-metal-catalyzed olefin polymerization involves initiation, propagation and termination. The generation of the active catalyst from an inactive catalyst precursor, for example by alkylation, is known as initiation. Propagation involves polymer chain growth. The commonly accepted mechanism is that proposed by Cossee,[6] involving migratory insertion of an alkene into a metal-carbon σ-bond. Monomer precoordination, if required, presupposes a vacant site on the metal center in a position adjacent to the growing alkyl chain.

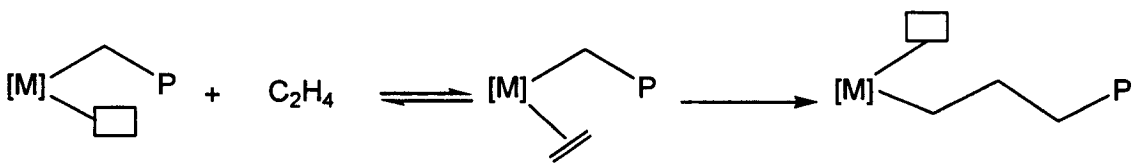

Green and Rooney proposed an alternative mechanism based on α-elimination to give a carbene intermediate.[7,8] This mechanism requires two vacant sites on the metal center and a metal oxidation state which can increase by two.

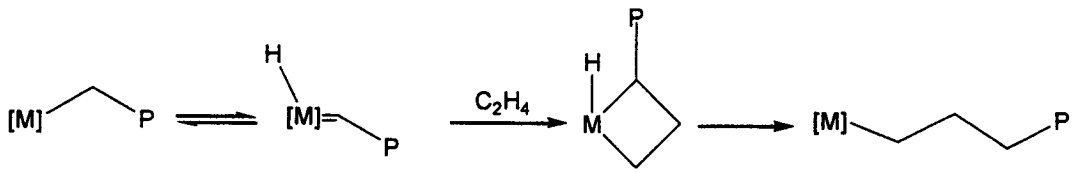

Finally, it is possible that the α-H is not completely transferred to the metal but instead engages in an agostic interaction which facilitates ethylene insertion.[9]

The polymerization mechanisms are readily distinguished by their kinetic isotope effects. Polymerization of a mixture of ethylene and perdeuteroethylene by $Cp_2TiCl(C_2H_5)$ showed no evidence for H/D scrambling and gave $k_H/k_D = 1.04$, causing Grubbs to conclude that polymerization occurred by Cossee mechanism.[10] In contrast, Brintzinger reported that dimerization of trans-1-D-hexene with Cp_2ZrCl_2/MAO in the presence of H_2 gave a 1.3:1 ratio of syn- and anti-products, suggesting that α-agostic interactions are important.[11]

Termination (chain transfer) is a reaction that interrupts polymer chain growth. A variety of termination mechanisms have been reported, including β-H elimination, hydrogenation, β-R elimination, chain transfer to monomer and chain transfer to aluminum.[6,12,13]

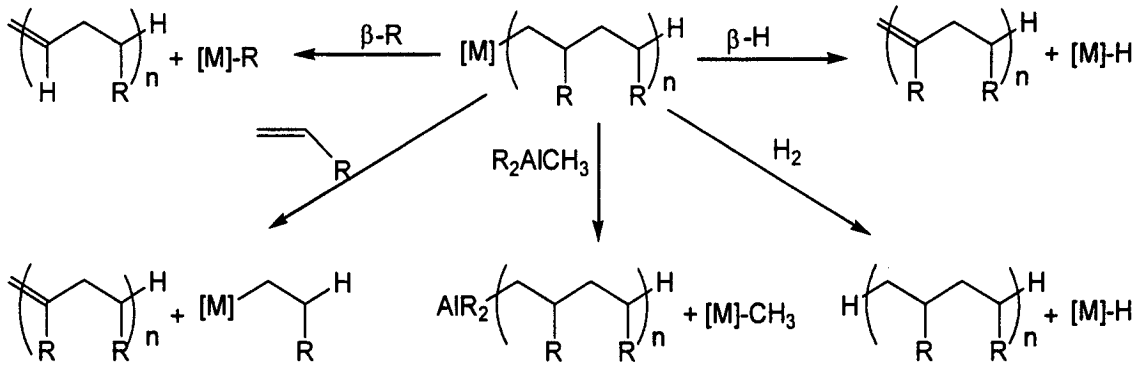

1.2 Vanadium-based Ziegler-Natta catalysts

There are important differences between vanadium- and titanium-based Ziegler-Natta catalysts. For example, vanadium-based catalysts are unique in their ability to randomly incorporate comonomers. This leads to an amorphous, elastomeric product.[14] In industry, vanadium-based catalysts are generally used in the production of ethylene-propylene copolymers and ethylene-propylene-diene terpolymers.[14]

In the 1970s, both Monsanto and Cities Service Company investigated and developed silica-supported vanadium catalysts for olefin polymerization. Their catalysts were prepared by treatment of silica first with an alkylaluminum compound followed by addition of a vanadium complex. These catalysts produced high-density polyethylene.[15-18]

In 1981, Chemplex Company described a new method for the preparation of silica-supported vanadium catalysts by first treatment of porous silica with an alkylmagnesium compound followed by addition of aluminum alkyls.[19,20] In either case, Chemplex or Cities Service, certain halocarbons ($CHCl_3$, $CFCl_3$, CH_2Cl_2, $CF_2ClCFCl_2$, $C_3H_2Cl_6$ and C_3Cl_8) are used as promoters to maximize activity.

Agglomeration of polyethylene which occurs in fluidized-bed polymerization when silica supported vanadium catalyst prepared by Cities Service is used, Union Carbide used a different preparation method for preparing silica-supported vanadium catalysts. This method involved impregnation of silica with vanadium trihalide in THF followed by solvent removal and addition of a boron trihalide or alkylaluminum halide modifier.[21] The loading of the Union Carbide catalyst is typically 0.05-0.5 mmol V / g silica. A catalyst with 0.27 mmol V / g has a productivity in gas-phase ethylene polymerization in the range 2000-2800 g / g catalyst. This catalyst produces polyethylene with a broad molecular weight distribution (M_w/M_n = 10) and very low C=C. Similar M_w/M_n values are observed for silica-supported chromium catalysts, but with a higher degree of unsaturation.

Exxon has also carried out much research on silica-supported vanadium catalysts for olefin polymerization. The catalyst requires a group III metal halide (boron trichloride or ethylaluminum dichloride) in addition to silica, an alkylmagnesium, and a vanadium compound.[22,23] It produces polymer with a narrow molecular weight distribution as well as low molecular weight oligomers.

An important question in the chemistry of vanadium-based Ziegler catalysts is the oxidation state of the active species. Early studies indicated that V(0) and V(I) species were inactive, but it was unclear whether V(II), V(III), V(IV) and V(V) were active.[24] Nowadays, it is commonly accepted that the active sites contain V(III), however, the alkylaluminum cocatalyst has sufficient reducing strength to reduce the vanadium further. Some V(II) salts have been reported to be active ethylene polymerization catalysts, although ESR experiments have indicated that the oxidation state (II) might be inert toward polymerization.[25,26] Recently, Gambarotta reported that V(IV) is the most stable and active oxidation state for olefin polymerization.[27] Two methods used to overcome the problem of reduction of vanadium to lower, inactive oxidation states include using mild oxidizing agents (chlorinated esters or halocarbons) to reoxidize the metal center to a higher oxidation state (III or IV)[28] and ancillary ligands, such as bidentate aminophenolate,[29] to stabilize the higher oxidation states of vanadium.

1.2.1 Silica-supported vanadium catalysts

Silica-supported vanadium catalysts have been studied because of their activity and selectivity in the oxidation of hydrocarbons,[30] sulfur dioxide[31] and carbon monoxide, as well as in the selective catalytic reduction of NO_x by NH_3.[32] Silica-supported vanadium catalysts are also widely used for olefin polymerization.[33,34]

Several methods have been used to prepare silica-supported vanadium oxide catalysts, including chemical vapor deposition of vanadium alkoxides[35-37] and $VOCl_3$,[38-41] gas phase impregnation of vanadium alkoxides,[42] vanadium acetate[43] and aqueous impregnation of vanadium oxalate.[44] Although surface reactions between the metal complex and the surface hydroxyls determine the structure of supported vanadium oxides, there have been few reports about the elementary reactions involved in their preparation. Hanke et al.[45] reported that gas phase impregnation of $VOCl_3$ on silica at 375 K under nitrogen, followed by purging in N_2 to remove physisorbed $VOCl_3$, produce $\equiv SiOVOCl_2$. Hydrolysis at 375 K and calcination in dry oxygen at 675 K gives mononuclear tetrahedral V(V) oxides. Anpo et al.[41] observed that chemical vapor deposition of $VOCl_3$ at 273 K on porous Vycour glass forms $\equiv SiOVOCl_2$ species via reaction with hydroxyl groups and HCl elimination. Hydrolysis and calcination gives a tetrahedral V(V) mononuclear species. In contrast, Inumaru et al.[35] reported that $[VO(OC_2H_5)_3]$ reacts at 423 K with OH groups of a high surface area silica to produce a mixture of two surface species, eq. 1.1 and 1.2. Further treatment at 623 or 723 K under vacuum produced highly dispersed V_2O_5 overlayers.

$$VO(OC_2H_5)_3 + \equiv SiOH \rightarrow \equiv SiOVO(OC_2H_5)_2 + C_2H_5OH \quad (1.1)$$

$$VO(OC_2H_5)_3 + 2\equiv SiOH \rightarrow (\equiv SiO)_2VO(OC_2H_5) + C_2H_5OH \quad (1.2)$$

Kijenski et al.[37] studied the reaction between $VO(OC_4H_9)_3$ and the surface hydroxyl groups and observed that the number of V atoms deposited were nearly equal to those of surface OH group of silica.

Rice et al.[39] reported that the reaction of the molecular precursors VOX_3 (X = Cl or O^iPr) with the surface hydroxyl groups of Aerosil-200 silica, dehydroxylated at 25, 200, or 500°C, at room temperature gives a single chemisorbed product, $\equiv SiOVOX_2$, regardless of the density of surface hydroxyl groups with a concurrent liberation of protonated HX ligand, eq. 1.3:

$$\equiv SiOH + VOX_3 \rightarrow \equiv SiOVOX_2 + HX \qquad (1.3)$$

The reaction products have been characterized by ^{51}V MAS NMR, IR, ^{13}C NMR, GC-MS and elemental analysis. These spectroscopic characterization techniques give only indirect information about the local structure around the vanadium center.

In order to confirm the preliminary results obtained, a detailed study of the above reaction was carried out. This work involved the use of various kinds of silicas never studied before, and the catalyst characterization by various spectroscopic techniques. To obtain structural information, both Extended X-ray Absorption Fine Structure (EXAFS) and X-ray Absorption Near Edge Structure (XANES) region of the vanadium X-ray absorption spectrum were used for the first time. Since the maximum amount of chemisorbed vanadium was found to be equal to the initial quantity of surface hydroxyl groups, eq. 1.3, this reaction was proposed studied as a new possible chemical method for the analysis of reactive hydroxyl groups. Various kinds of silica: non-porous fumed Aerosil (A300 and A380) and porous, Sylopol (S952, S952X and S948) shall be used for reaction

with VOX_3 complexes. Since hydroxyl content has a dramatic effect on catalyst activity, its accurate determination is of high significance. Therefore the effect of the dehydroxylation temperature on the OH density was also studied for "as-received" and rehydrated silicas. Also a comparison of surface area and OH content shall be made.

Various techniques have been used to characterize the structure of vanadium species present on the silica surface in an attempt to understand their catalytic properties. On the basis of FTIR, Raman spectroscopy, XPS, solid-state ^{51}V NMR, V K-edge XAS, UV-Vis DRS and luminescence spectroscopy, a variety of active site architectures have been proposed, ranging from isolated pseudotetrahedral and octahedral to oxo-bridged oligomers and V_2O_5 crystallites.[39]

1.3 Silica-supported cocatalysts

The reactions of $AlMe_3$ with oxide supports have been studied by many different groups, dating back to 1967. [46] In 1969, Yates *et al.*[47] reported the first detailed spectroscopic studies, and reports have continued to appear periodically to the present day.[48-60] The scrutiny resulted originally from the use of $AlMe_3$ as a hydrogen-sequestering agent,[50] as a probe of the surface hydroxyl content and structure of the silica and as a synthetic route to silica-alumina cracking catalysts.[58] More recently, silicas modified with $AlMe_3$ and MAO

(methylaluminoxane, a form of partially hydrolyzed $AlMe_3$) have attracted attention as cocatalysts for olefin polymerization.[61]

Several possible reactions of $AlMe_3$ with silica have been proposed, leading to the structures shown in Figure 1.1. The formation of methane as the only volatile product and the disappearance of the IR band assigned to the υ(OH) during the grafting of the TMA on the silica surface allowed Sato, et al.[46] and Peglar et al.[48] to propose that TMA reacts directly with isolated silanol groups of the silica to form siloxy-dimethylaluminum $\equiv SiOAlMe_2$ groups, eq. 1.4, which can react further with neighboring surface silanol sites, eq. 1.5:

$$\equiv SiOH + AlMe_3 \rightarrow \equiv SiOAlMe_2 + MeH \qquad (1.4)$$

$$\equiv SiOAlMe_2 + \equiv SiOH \rightarrow \equiv SiOAlMeOSi\equiv + MeH \qquad (1.5)$$

Thermogravimetric analysis of the product shows that the weight gain of silica exceeds the predicted by eq. 1.4 by 100%. The Al uptake of silica is greater than its hydroxyl content by a factor of two and uptake of TMA was observed to continue even after the surface hydroxyls have been completely consumed. The extra weight gain was explained by reaction of $\equiv SiOAlMe_2$ further with siloxane bridge, eq. 1.6, or by reaction between TMA and siloxane bridge to result in cleavage of $\equiv SiOSi\equiv$ bond with methyl transfer to silicon forming $\equiv SiMe$ and $\equiv SiOAlMe_2$, eq 1.7:[47]

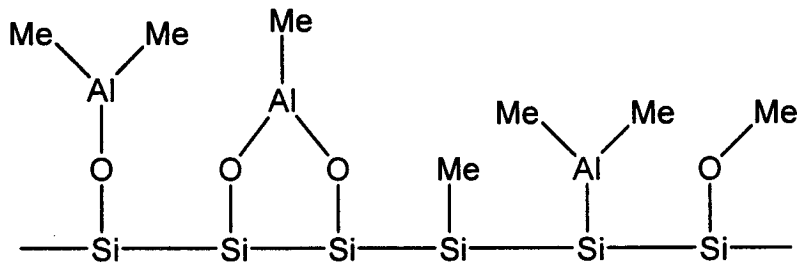

a

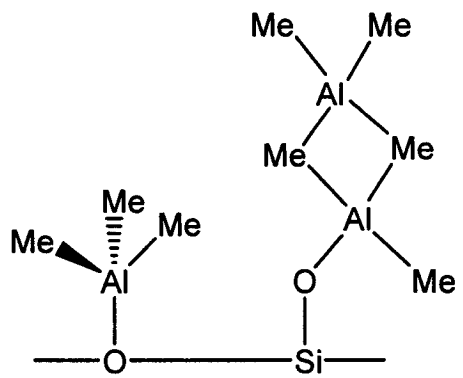

b

Figure 1.1. Previously proposed surface structures resulting from the grafting of $AlMe_3$ on silica: (a) chemisorbed, (b) physisorbed.

$$\equiv SiOSi\equiv + \equiv SiOAlMe_2 \rightarrow (\equiv SiO)_2AlMe + \equiv SiMe \quad (1.6)$$

$$\equiv SiOSi\equiv + AlMe_3 \rightarrow \equiv SiOAlMe_2 + \equiv SiMe \quad (1.7)$$

IR analysis allowed Low et al.[51] to suggest that the reaction of TMA with isolated silanol and siloxane bridge may also give $\equiv SiAlMe_2$ surface species along with methanol or surface methoxy groups, eq. 1.8 and 1.9:

$$\equiv SiOH + AlMe_3 \rightarrow \equiv SiAlMe_2 + MeOH \quad (1.8)$$

$$\equiv SiOSi\equiv + AlMe_3 \rightarrow \equiv SiAlMe_2 + \equiv SiOMe \quad (1.9)$$

Recently solid state NMR study showed that TMA does not cause any methylation of the silica surface.[57] The proposed mononuclear, three- coordinate methylaluminum or dimethylaluminum fragments are unusual in the known aluminum organometallic chemistry, which strongly favours oligomeric complex except in the presence of sterically demanding ligand. The idea of methoxy groups could arise by cleavage of siloxane bridge accompanied by formation of silicon-bonded $AlMe_2$ fragment is chemically implausible.

On the basis of quantitative analysis combined with IR, ^{13}C and ^{29}Si CP/MAS NMR, church et al.[62] reported that the grafting of $AlMe_3$ on silica releases two equiv. methane per surface hydroxyl, resulting in the formation of dialuminum surface species as shown in eq. 1.6:

$$\equiv SiOH + Al_2Me_6 \rightarrow Al_2Me_3(\mu\text{-}OSi\equiv)(\mu\text{-}CH_2) + 2\ MeH \quad (1.10)$$

They proposed that the Al_2Me_6 reacts with surface hydroxyl groups initially forming organometallic fragment bridged by the siloxy ligand (**1a**), since this interaction is much stronger than that of bridging methyl, with releasing one equiv. of methane. The next step is C-H activation leading to methylene bridged (**1b**) species with formation of a second equiv. of methane. Since **1b** is asymmetric, with one Al atom bearing two Me ligand while the other bears only one, they suggest that the second Al atom, which bears a single methyl ligand, may coordinate to a neighboring siloxane oxygen forming (**1**), Scheme 1.1.

The vanadyl chloride modified silica $\equiv SiOVOCl_2$ and organoaluminum-modified silica are by themselves ineffective as polymerization catalysts. While the impregnation the support with $VOCl_3$ followed by treatment with alkylaluminum cocatalyst results in activity for olefin polymerization.[63]

In this work chemical vapor deposition (CVD) method was used to prepare new Ziegler-Natta catalysts. The effect of the order of addition of $VOCl_3$ and the co-catalyst (TMA) on olefin polymerization was studied in detail. The following order of CVD was used: (i) Silica/TMA/$VOCl_3$, (ii) Silica/TMA/$VOCl_3$ and (iii) Silica/$VOCl_3$/TMA. To our knowledge, this catalyst preparation procedure for silica/$VOCl_3$ system has not been reported in the literature to date.

1.4 Surface chemistry of the silica

Silicas in their various crystalline and amorphous forms are used in many technologies such as mineral processing, production of silicon, glasses, ceramics

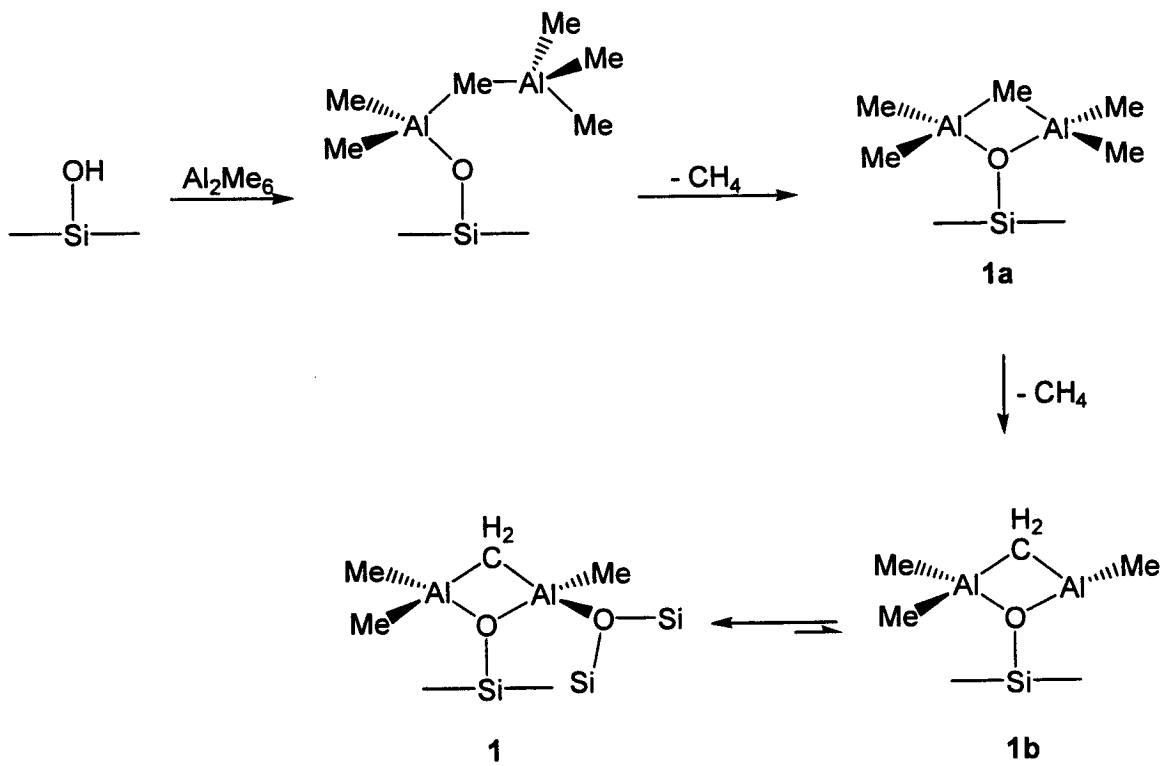

Scheme 1.1. Proposed mechanism for the reaction of TMA with silica.[62]

and adsorbents.[64] As discussed above, silica is also widely used as a support in heterogeneous catalysis. Its surface is composed of relatively unreactive siloxane bridges, Si-O-Si, and reactive hydroxyl groups.[65] The physical and chemical properties of the hydroxyl groups on the surface are largely responsible for the surface chemistry of silica.[66] Lewis acid/base sites are absent in silica unless it is activated at very high temperatures.[67,68]

High surface area silicas are amorphous and can be manufactured in one of several ways.[65,69] The amorphous silicas used in this work are pyrogenic or fumed silicas from Degussa with the trade-name Aerosil™, and precipitated silicas from Grace-Davison, with the trade-name Sylopol. Pyrogenic silicas are produced by the flame hydrolysis of tetrachlorosilane, eq. 1.7 and 1.8.[70] The resulting material consists of small, non-porous particles of very high purity (99.8%) with 0.2% impurity including: 0.05% Al_2O_3, 0.01% Fe_2O_3, 0.03% TiO_2 and 0.025% HCl.

$$SiCl_4 + O_2 \rightarrow SiO_2 + 2\,Cl_2 \qquad (1.7)$$

$$2\,H_2O + 2\,Cl_2 \rightarrow 4\,HCl + O_2 \qquad (1.8)$$

Precipitated silicas are synthesized in solution via the reaction of an alkali metasilicate, $Si(OR)_4$ (R= Me, Et) with acid.[65,69] The result is porous particles of larger size and lower purity (99.6%) than the pyrogenic silicas. They contain Al_2O_3, Na_2O, SO_4, Fe_2O_3, Ca and Mg impurites.

The structures of the crystalline forms of silica, i.e., quartz, cristobalite (related to diamond or zinc blende with Si in all C, or Zn and S, positions) and tridymite (which is related similarly to wurtzite, or hexagonal ZnS) have been proposed as models for amorphous silica. All consist of three-dimensional framework structures with corner-sharing SiO_4 tetrahedra.[71,75-78] The total concentration of silanol groups on a fully hydroxylated silica surface at ambient temperature is ca. 4-5 OH nm^{-2} regardless of the origin or crystallinity of the silica.[71-75] However, if the silica is dehydroxylated at 450°C under dynamic vacuum, the silanol density drops to 1.2-1.5 nm^{-2}.[72,74,75]

In 1958, DeBoer and Vleeskins[71] suggested a model for the silica surface based on the (111) face of β-cristobalite or a similar face of β-tridymite, Figure 1.2. Each isolated silanol on this surface is surrounded by six equidistant isolated silanols in a hexagonal arrangement at a distance of 5 Å. This corresponds to a surface density of 4.55 OH nm^{-2}, consistent with the experimental value of 4.6 OH found in dehydration/rehydration studies of various silica gels reported by the same authors.

Hockey attributed excess hydroxyl groups on untreated silicas to surface defects in the lattice structure.[76] Because of their close proximity, hydroxyls on such defect surfaces may condense at about 450°C, resulting in the β-cristobalite structure.

A number of difficulties are raised by the DeBoer-Vleeskins model in conjunction with the lattice-defect mechanism of Hockey. One is the observation that some surface hydroxyls are present as pairs even after the silica has been

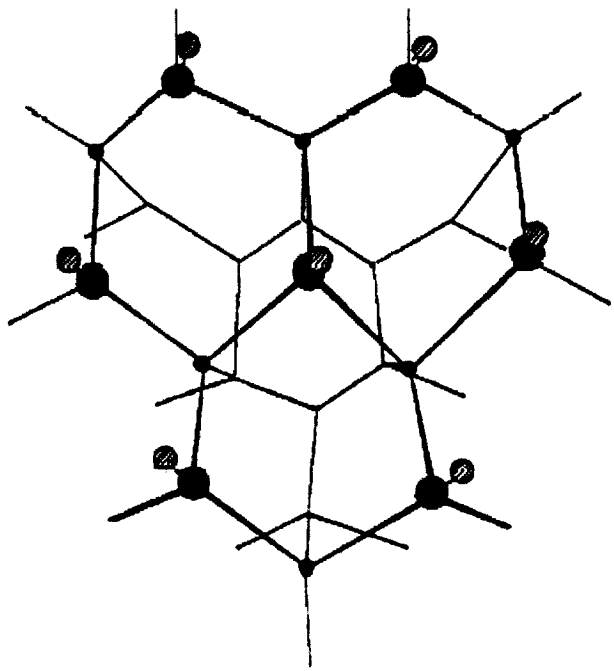

Figure 1.2. Model of the (111) face of β-cristobalite showing the arrangement of surface hydroxyls. Large black circles indicate surface silicon atoms; small hatched circles indicate hydroxyl groups.[78]

heated above 450°C. This is inconsistent with the geometry of the (111) face of β-cristobalite. According to this model, reducing the silanol density below 4.55 nm^{-2} is impossible due to the constraint imposed by the underlying lattice. Nevertheless, thermally treated silica surfaces are capable of supporting hydroxyl group densities of less than 1.0 nm^{-2}, with little decrease in overall surface area.

To overcome these difficulties, Peri and Hensley proposed another model for the silica surface based on the (100) face of β-cristobalite, Figure 1.3.[77] Each silicon atom on the fully hydroxylated silica bears two silanol groups for a total surface concentration of 7.9 OH nm^{-2}, Figure 1.3a. According to this model, the process of dehydration involves condensation of hydroxyl groups along surface rows, Figure 1.3b. Assuming random condensation, the concentration of the silanols on the partially dehydrated surface is 4.56 OH nm^{-2} after treatment at 100°C. Further condensation would have to involve vicinal pairs of hydroxyl groups forming strained siloxane linkages. The minimum silanol density according to this model is 1.2 OH nm^{-2}. Unlike the DeBoer and Vleekins model, there is no clear mechanism for the formation of isolated hydroxyl groups.

Maciel suggested that the amorphous silica surface is a hybrid of intersecting (111)-type β-cristobalite bearing isolated silanols and (100)-type β-cristobalite where geminal silanols are located.[80] This model can accommodate a silanol density between 4.55 and 7.88 nm^{-2} on a fully hydroxylated silica surface.

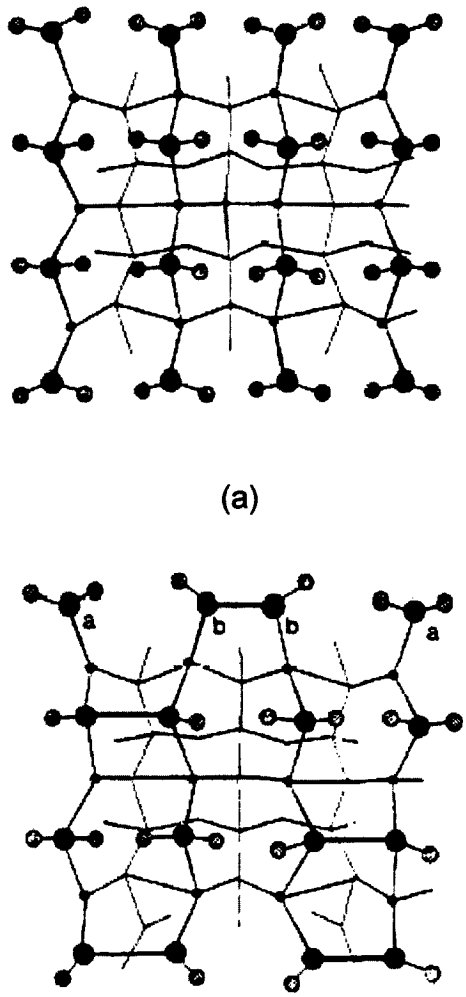

(a)

(b)

Figure 1.3. Surface geometry of the (100) face of β-cristobalite: (a) fully hydrated; (b) following partial dehydration. Large circles indicate surface silicon atoms, small circles indicate hydroxyl groups.[78]

1.5 Goal and survey of this thesis

The goal of this research was to extend the chemistry of silica-supported vanadium catalysts, with special emphasis on understanding catalysts for olefin polymerization. In Chapter Two, experimental procedures are described. Chapter Three describes a new method for determining the accessible hydroxyl content of pyrogenic or fumed silicas and precipitated silicas at different temperatures based on chemisorption of vanadium complexes. In Chapter Four, we elucidate the structure of a silica-supported vanadium complexes using X-ray absorption near-edge structure (XANES) and extended X-ray absorption fine structure (EXAFS). Chapter Five describes the synthesis and characterization of Ziegler-Natta catalysts by sequential gas phase reactions of volatile $VOCl_3$ and $AlMe_3$ with the surface of silica. Chapter Six is a study of kinetics of homopolymerization of ethylene, propylene, as well as copolymerization of ethylene-propylene mixtures, catalyzed by the silica-supported vanadium catalysts described in Chapter 5.

1.6 References

1) Gavens, P. D.; Bottril, M.; Kelland, J. W.; McMeeking, J. *In Comprehensive Organometallic Chemistry*; Wilkinson, G.: Stone, F. G. A.; Abel, E. W., Eds.; Pergamon Press: Oxford, **1982**; Vol. 3, ch. 22.

2) Ziegler, K.; Holzkamp, E.; Breil, H.; Martin, H. *Angew. Chem.* **1955**, *67*, 541-547.

3) Natta, G.; *Pno, P.;* Corradini, P.; Danusso, F.; Mantica, E.; Mazzanti, G.; Moraglio, G. *J. Am. Chem. Soc.* **1955**, *77*, 1708-1710.

4) Stevens, P. M. *Polymer Chemistry: An Introduction*; Oxford University Press: New York, **1990**.

5) Tullo, A. H. *Chemical and Engineering News* **2001**, *79*, 38-39.

6) Cossee, P. J. Catal. **1964**, *3*, 80-88.

7) Ivin, K. J.; Rooney, J. J.; Stewart, C. D.; Green, M. L. H.; Mahtab, R. *J. Chem. Soc., Chem. Commun.* **1978**, 604-606.

8) Dawoodi, Z.; Green, M. L. H.; Mtetwa, V. S. B. *J. Chem. Soc., Chem. Commun.* **1982**, 1410-1411.

9) Brookhart, M.; Green, M. L. H. *J. Organomet. Chem.* **1983**, *250*, 395-408.

10) Soto, J.; Steigerwald, M. L.; Grubbs, R. H. *J. Am. Chem. Soc.* **1982**, *104*, 4479-4480.

11) Krauledat, H.; Brintzinger, H. H *Angew. Chem. Int. Ed. Engl.* **1990**, *42*, 1412-1413.

12) Kissin, Y. V.; Nowlin, T. E.; Mink, R. I. *Macromol.* **1993**, *26*, 2151-2158.

13) McDaniel, M. P. *Adv. Catal.* **1985**, *29*, 85-93.

14) Parshall, G. W.; Ittel, S. D. *Homogeneous Catalysis, the Application and Chemistry of Catalysis by Soluble Transition Metal Complexes*, 2nd Ed., Wiley: New York, **1992**, Ch. 4.

15) Ort, M. R., U. S. Patent 3,784,539, **1974**.

16) Ort, M. R., U. S. Patent 3,956,255, **1976**.

17) Pennington, B. T.; Rolling, P. V.; Aylward, D. E., U. S. Patent 4,435,518, **1984**.

18) Arylward, D. E., U. S. Patent 4,435,520, **1984**.

19) Shida, M.; Pullukat, T. J.; Hoff, R. E., U. S. Patent 4,263,171, **1981**.

20) Pullukat, T. J.; Hoff, R. E., U. S. Patent 4,530.913, **1985**.

21) Beran, D. L.; Cann, K. J.; Jorgensen, R. J.; Karol, F. J.; Maraschin, N. J.; Marcinkowsky, A. E., U. S. Patent 4,508,842, **1985**.

22) Best, S. A., U. S. Patent 4,579,834, **1986**.

23) Best, S. A., U. S. Patent 4,954,471, **1990**.

24) Henrici-Olivé, G.; Olivé, S. *Angew. Chem. Int. Ed. Engl.* **1971**, *10*, 776-786.

25) Smith, P. D.; Martin, J. L.; Huffman, J. C.; Bansemer, R. L.; Caulton, K. G. *Inorg. Chem.* **1985**, *24*, 2997-3002.

26) Chan, M. C. W.; Cole, J. M.; Gibson, V. C.; Howard, J. A. K. *J. Chem. Soc., Chem. Commun.* **1997**, *24*, 2345-2347.

27) Gambarotta, S. *Coord. Chem. Rev.* **2003**, 237, 229-243.

28) Ma, Y.; Reardon, D.; Gambarotta, S.; Yap. G. *Organometallics* **1999**, *18*, 2773-2781.

29) Hagen, H.; Boersma, J.; Lutz, M.; Spek, A. L.; Van Koten, G. *Eur. J. Inorg. Chem.* **2001**, 117-123.

30) Oyama, S. T. *Res. Chem. Intermed.* **1991**, *15*, 165-182.

31) Dobkina, E. I.; Petrovskaya, G. I.; Kuznestova, S. M. *Russ. J. Appl. Chem.* **1996**, *69*, 835-838.

32) Miyamoto, A.; Yamazaki, Y.; Inomata, M.; Murakaml, Y. *J. Phys. Chem.* **1981**, *85*, 2366-2372.

33) Smith, W. E.; Zelmer, R. G. *J. Polym. Sci. A* **1963**, *1*, 2587-2600.

34) Damyanov, D.; Velikova, M. *Eur. Polym. J.* **1979**, *15*, 1075-1078.

35) Inumaru, K.; Okuhara, T.; Misono, M. *J. Phys. Chem.* **1991**, *95*, 4826-4832.

36) Nickl, J.; Dutoit, D.; Bailker, A. *Appl. Catal.* **1993**, *98*, 173-193.

37) Kijenski, J.; Baiker, A.; Glinski, M.; Dollenmeir, P.; Wokaun, A. *J. Catal.* **1986**, *101*, 1.

38) Haber, J.; Kozlowska, R.; Kozlowski, *J. Catal.* **1986**, *102*, 52-63.

39) Rice, G. I.; Scott, L. S. *Langmuir* **1997**, *13*, 1545-1551.

40) Bond, G. C.; Konig, P. *J. Catal.* **1982**, *77*, 309-315.

41) Anpo, M.; Sunamoto, M.; Che, M. *J. Phys. Chem.* **1989**, *93*, 1187-1189.

42) Deo, G.; Wachs, I. E. *J. Catal.* **1994**, *146*, 323-334.

43) van Hengstrum, A. J.; van Ommen, J. G.; Bosch, H.; Gellings, P. *J. App. Catal.* **1983**, *8*, 369-373.

44) Wachs,I. E.; Saleh, R. Y.; Chen, S. S.; Chersich, C. C. *Appl. Catal.* **1985**, *15*, 339-352.

45) Hanke, W.; Blenert, R.; Jerschkewitz, H. G. Z. *Anog. All. Chem.* **1975**, *414*, 109-114.

46) Sato, M.; Kanbayashi, T.; Kobayashi, N.; Shima, Y. *J. Catal.* **1967**, *7*, 342-351.

47) Yates, D. J. C.; Debinski, G. W.; Kroll, W. R.; Elliott, J. J. *J. Phys. Chem.* **1969**, *73*, 911-921.

48) Peglar, R. J.; Hambleton, F. H.; Hockey, J. A. *J. Catal.* **1971**, *20*, 309-320.

49) Kunawicz, J.; Jones, P.; Hockey, J. A. *Trans. Farad. Soc.* **1971**, *67*, 848-853.

50) Morrow, B. A.; Hardin, A. H. *J. Phys. Chem.* **1979**, *83*, 3135-3141.

51) Low, M. J. D.; Severdia, A. G.; Chan, J. *J. Catal.* **1981**, *69*, 384-391.

52) Kinney, J. B.; Staley, R. H. *J. Phys. Chem.* **1983**, *87*, 3735-3740.

53) Morrow, B. A.; McFarlan, A. J. *Langmuir* **1991**, *7*, 1695-1699.

54) Bartram, M. E.; Michalske, T. A.; Rogers Jr. J. W. *J. Phys. Chem.* **1991**, *95*, 4453-4463.

55) Kratochvila, J.; Kadlc, Z.; Kazda, A.; Salajka, Z. *J. Non-Cryst. Solids* **1992**, *143*, 14-20.

56) Anwander, R.; Palm, C.; Groeger, O.; Engelardet, G. *Organometallics* **1998**, *17*, 2027-2036.

57) Tao, T.; Maciel, G. E. *J. Am. Chem. Soc.* **2000**, *122*, 3118-3126.

58) Peglar, R. J.; Murray, J.; Hambleton, F. H.; Sharp, M. J.; Parker, A. J.; Hockey, J. A. *J. Chem. Soc. (A)* **1970**, 2170-2172.

59) Puurunen, R. L.; Root, A.; Haukka, S.; Iiskola, E. I.; Lindblad, M.; Krause, A. O. I. *J. Phys. Chem. B* **2000**, *104*, 6599-6609.

60) Lakomaa, E.-L.; Root, A.; Suntola, T. *Appl. Surf. Sci.* **1996**, *107*, 107-115.

61) Abbenhuis, H. L. *Angew. Chem. Int. Ed.* **1999**, *38*, 1058-1060.

62) Church, T. L.; Li, F.; Facey, G. A.; Mader, E. A.; Scott. S. L. submitted for publication.

63) Ghiotti, G.; Garrone, E.; Zecchina, A. *J. Mol. Catal.* **1988**, *46*, 61-77.

64) Leonardelli, S.; Facchini, L.; Fretigny, C.; Tougne, P.; Legrand, A. P. *J. Am. Chem. Soc.* **1992**, *114*, 6412-6418.

65) Morrow B. A. *Stud. Surf. Sci. Catal.* ***1990***, *57A*, 161-224.

66) Iler, R. K. *The Chemistry of Silica*; Wiley: New York, **1979**.

67) Morrow, B. A.; Cody, I. A. *J. Phys. Chem.* **1976**, *80*, 1995-1998.

68) Child, M. J.; Heywood, M. J.; Yong, G. H.; Rochester, C. H. *J. Chem. Soc. Faraday Trans. 1* **1982**, *78*, 2005-2008.

69) Augustine R. L. *Heterogeneous Catalysis for the Synthetic Chemist*, Dekker: New York, **1996**.

70) Heaney, P. J.; Prewitt, C. T.; Gibbs, G. V. *Silica: Physical Behavior, Geochemistry and Materials Applications*; Mineralogical Society of America: Washington, D. C., **1994**.

71) DeBoer, J. H.; Vleeskins, J. M.; Proc. K. *Ned. Akad. Wet.* **1958**, *B61*, 85-93.

72) Armistead, G. G.; Tyler, A. J.; Hambleton, F. H.; Mitchell, S. A.; Hockey, J. A. *J. Phys. Chem.* **1969**, *73*, 3947-3953.

73) Zhuravlev, L. T. *Langmuir* **1987**, *3*, 316-318.

74) Peussa, M.; Härkönen, S.; Puputti, J.; Niinisto, L. *J. Chemometrics* **2000**, *14*, 501-512.

75) Morrow, B. A.; McFarlan, A. J. *Langmuir* **1991**, *7*, 1695-1701.

76) Hockey, J. A. *Chem. Ind. (London)* **1965**, 57-63.

77) Peri, J. B.; Hensley, Jr. A. L.. *J. Phys. Cem.* **1968**, *72*, 2926-2933.

78) Boehm, H. P. *Adv. Catal.* **1966**, *16*, 179-274.

79) Sindorf, D. W.; Maciel, G. E. *J. Am. Chem. Soc.* **1983**, *105*, 1487-1493.

80) Chuang, I-S.; Maciel, G. E. *J. Phys. Chem. B.* **1997**, *101*, 3052-3064.

Chapter Two

Experimental Techniques

2.1. Reagents

2.1.1 Silicas

Nonporous pyrogenic Aerosil silicas (A200, A300 and A380, where the number indicates the approximate surface area) were obtained from Degussa Corp. Porous silicas (S952, S952X1836 and S948, where the number is a trade designation) were donated by Grace-Davison. The thermal pretreatment temperature of each silica sample is indicated by an appended number. For example, A200-100 denotes a sample of Aerosil-200 treated at 100°C, while S952-300 denotes as a sample of Sylopol 952 treated at 300°C.

Exact surface areas of the silica samples were determined by nitrogen adsorption using the BET method, Table 2.1. Prior to determination of their surface areas, the samples were pretreated by heating to 150°C in order to remove adsorbed water.

2.1.2 Commercial liquids

$VOCl_3$ (yellow liquid) and $VO(O^iPr)_3$ (colorless liquid) were purchased from Aldrich and transferred under N_2 into glass reactors equipped with either high vacuum Teflon stopcocks (Young valves) or high vacuum stopcocks greased

Table 2.1. Properties of various silica samples

Silica	Surface area (m^2/g)	Particle size[a] (μm)
Aerosil 200	183 ± 1	$12*10^{-3}$
Aerosil 300	318 ± 2	$7*10^{-3}$
Aerosil 380	340 ± 2	$7*10^{-3}$
Sylopol 948	265 ± 2	55
Sylopol 952	258 ± 1	112
Sylopol 952X1836	249 ± 2	33

[a] Grace Davison analysis.

with the perfluorinated grease Krytox (Aldrich). Neat trimethylaluminum $Al_2(CH_3)_6$, also referred to as TMA (colorless liquid), was purchased from Aldrich. Caution! Neat TMA is extremely pyrophoric. Handle only very small quantities of the neat material and dispose of unreacted material by controlled alcoholysis in a fumehood. A small quantity (ca. 1 mL) was transferred to a high vacuum glass reactor equipped with two Teflon Young Valves connected in series. The transfer was effected in a glove box. Water was double distilled and then transferred into a high vacuum glass reactor equipped with a glass stopcock greased with Apiezon-H.

Before use, each liquid reagent was subjected to several freeze-pump-thaw cycles to remove dissolved gases, and then introduced into the reactor via vapor phase transfer through a high vacuum manifold.

All solvents used, including diethyl ether, THF and toluene, were obtained free of moisture and air from solvent purification columns, and were stored under N_2 in glass reactors equipped with high vacuum Teflon stopcocks.

2.1.3 Gases

CH_2CH_2, CH_3Cl, CH_4, CH_3CHCH_2 and HCl (Matheson Gas Products), and CD_2CD_2 (98% D) (Cambridge Isotopes) were purchased in a gas cylinder. A known pressure of the desired gas was transferred into the reactors through a high vacuum line equipped with a Baratron capacitance manometer. Gases such as CD_2CD_2, CH_3CHCH_2 and CH_2CH_2 were first passed through a trap containing a mixture of BTS Deoxo Catalyst (Caledon Laboratories Ltd.) and 3 Å molecular sieves (Aldrich) to remove any oxygen and water present. The trap was previously activated under a flow of H_2 at 200°C for four hours in order to remove water. Oxygen was passed through a trap containing only 3 Å molecular sieves to remove traces of water, and then stored in a glass high vacuum bulb equipped with molecular sieves. HCl, CH_3Cl and CH_4 were used as received.

2.2 Preparation of supported vanadium complexes

2.2.1 Pretreatment of silica

A standard pretreatment procedure was followed in order to ensure reproducibility of the experiments. For all reactions, silica-500 was prepared by first calcining, to remove adsorbed hydrocarbons, in the presence of 300 Torr O_2 at 500°C for at least three hours. The silica was then partially dehydroxylated at 500°C for at least four hours under dynamic vacuum ($<10^{-4}$ Torr). To prepare silica at lower dehydroxylation temperatures, the calcination step was omitted. The silica was simply heated to the appropriate temperature for four hours under dynamic vacuum. These thermal treatments do not change the surface area of the silica, but they do standardize the number of surface hydroxyl groups.

2.2.2 Breakseal techniques

Whereas TMA and $VOCl_3$ are sufficiently volatile to be transferred into reactors via the vapor phase, $VO(O^iPr)_3$ had to be introduced using breakseal techniques. A breakseal reactor, Figure 2.1, was assembled and leak-tested under high vacuum line. $VO(O^iPr)_3$ was syringed into the breakseal reactor under flowing nitrogen, then frozen in liquid N_2 while the reactor was evacuated. Metal reagents were subjected to three freeze-pump-thaw cycles on a high vacuum line, to remove dissolved gases. While the complex was still frozen in liquid N_2, the

breakseal was sealed off from the rest of the reactor at the restriction with a torch, leaving the reagent sealed inside the breakseal under static vacuum.

A hammer, usually made from a piece of iron sealed inside a glass tube, was placed in the open end of the breakseal, and held in place with a magnet, as shown in Figures 2.2 and 2.3. A restriction was created in the glass to facilitate sealing off of the breakseal after the reaction. The open end of the breakseal was then attached to the desired reactor, as in Figures 2.2 and 2.3.

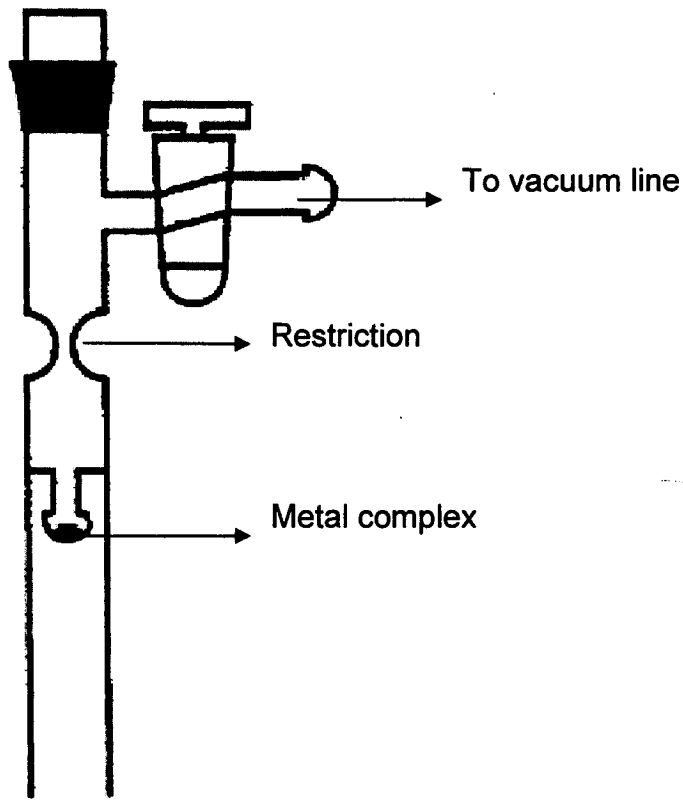

Figure 2.1. Schematic of a breakseal reactor.

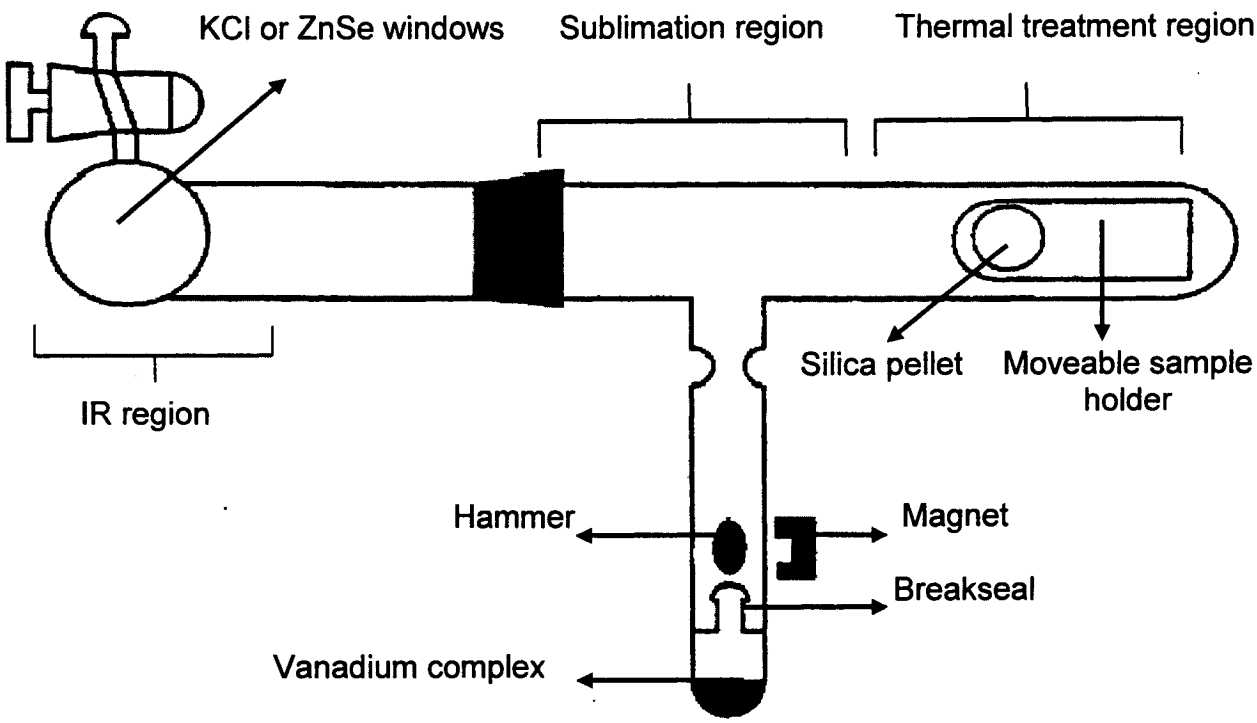

Figure 2.2. Schematic of an *in situ* infrared cell (side view).

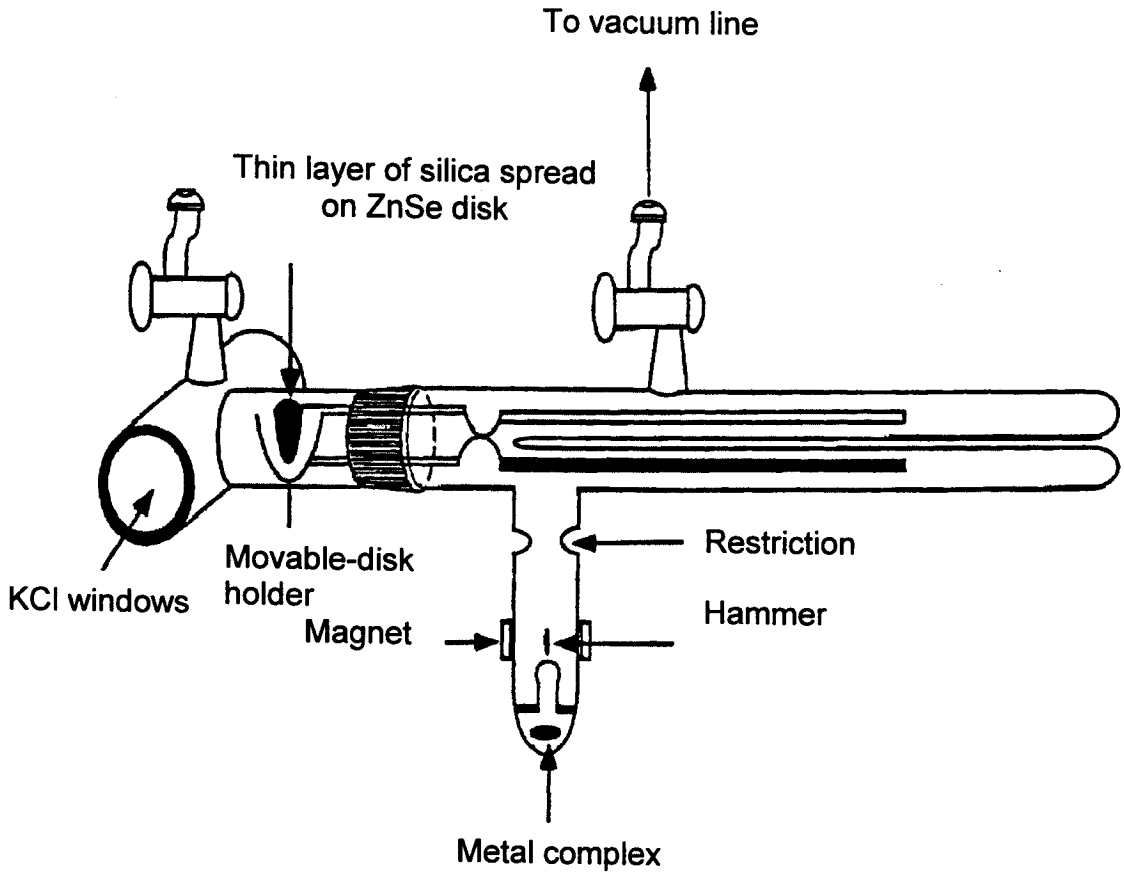

Figure 2.3. Schematic of an *in situ* thin film infrared cell.

2.2.3 Grafting of organometallic complexes

2.2.3.1 Grafting of $VOCl_3$

After thermal pretreatment and cooling of the silica to room temperature, the thermal treatment region of the reactor, containing the silica, was placed in liquid nitrogen and an excess of the volatile metal complex was introduced by vapor phase transfer via a high vacuum line. The reactor was allowed to stand for 30 minutes at room temperature until the reaction was deemed complete. The reactor was then evacuated for at least 2 hours to remove the excess metal reagent as well as volatile products formed by reaction with silica, leaving only chemisorbed species in the reactor.

2.2.3.2 Grafting of TMA

After pretreatment and cooling of the silica, a small amount of TMA was sublimed with the aid of a liquid N_2 trap into the reactor through a glass T-shaped joint. The reactor was allowed to warm up to room temperature, upon which the reaction of silica with TMA was allowed to proceed for at least one hour. Excess TMA was removed by desorption, under dynamic vacuum, to a liquid N_2-cooled trap equipped with two grease-free high vacuum Young Valves. After desorption was complete, both stopcocks were closed to isolate the desorbed TMA, which was usually so little as to be visually undetectable. The trap was then allowed to warm

to room temperature. The trap was opened in the fumehood, and air was allowed to slowly diffuse in and destroy the residual TMA. Water was then added drop-wise to the trap to ensure its complete destruction. This procedure was found to be effective in destroying extremely small amounts of TMA without any visible sign of highly exothermic reactions. The trap was cleaned using a concentrated KOH solution, rinsed thoroughly with water, and oven-dried before the next use.

2.2.3.3 Grafting of $VO(O^iPr)_3$

This complex was introduced into reactors containing pretreated silica using a breakseal. The breakseal containing the metal complex was broken under vacuum using a hammer, Figures 2.2 and 2.5. The thermal treatment region of the reactor was placed into liquid N_2 and the metal complex was sublimed from the breakseal to the cold trap for at least 1 hour. At this time, the reactor was removed from the liquid N_2 and allowed to stand at room temperature for at least 1 hour, when the reaction was deemed complete. Unreacted material was then desorbed from the silica by immersing the breakseal sidearm for several hours in a liquid nitrogen trap. The breakseal was flame-sealed at the restriction. Vanadium-modified silica was thus isolated inside the reactor vessel for further manipulations, which were performed in situ without exposing the samples to solvents or inert gas atmosphere at any time during the experiment.

2.3 Characterization of silica-supported metal complexes

2.3.1 Infrared spectroscopy

All IR experiments were performed in a high vacuum in situ IR cell, Figures 2.2 and 2.3, equipped with either KCl or ZnSe windows. KCl is hygroscopic and is not appropriate for experiments where H_2O is used. ZnSe is not sensitive to water and is transparent to 400 cm^{-1}, but is fragile. Transmission infrared spectra were recorded on a Mattson Research Series FT-IR spectrometer equipped with a DTGS detector and purged with CO_2-free dry air. Background and sample spectra were recorded by co-adding 32 scans at a resolution of 2 cm^{-1}.

2.3.1.1 Infrared spectroscopy of self-supporting disks

In self-supporting disk experiments, silica was pressed (125 kg/cm^2 for Aerosil silicas and 600 kg/cm^2 for Sylopol silicas) into pellets 1.6 cm in diameter containing ~15 mg of silica. The pellets were placed in a sample holder inside the *in situ* infrared cell, Figure 2.2.

The silica was prepared by moving the sample holder to the thermal treatment area of the cell, where calcination and dehydroxylation take place. After cooling to room temperature and recording the spectra of both the silica pellet, Figure 2.4, and windows, a metal complex was introduced into the cell as described above.

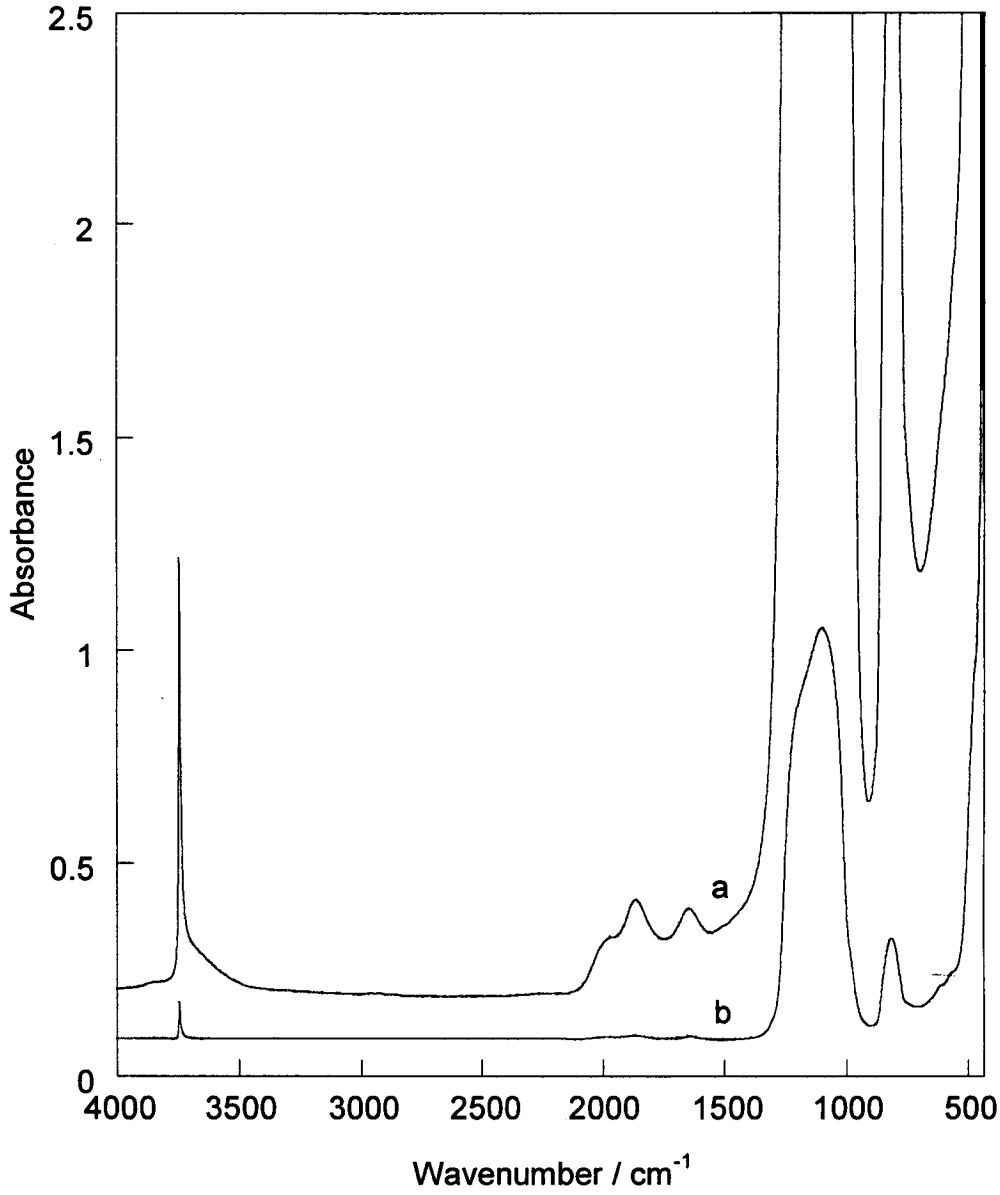

Figure 2.4. FTIR spectra of (a) A380-500 self-supporting disk; (b) A380-450 thin film supported on ZnSe disk.

Sample scans, taken at each stage of reaction, were obtained by sliding the sample holder into the IR region of the cell and aligning the pellet perpendicular to the IR beam of the spectrometer. Spectra of gas phase products were obtained by sliding the sample holder out of the IR region of the cell leaving only the KCl windows in the beam.

2.3.1.2 Thin film experiments

Thin film experiments were performed in a specially designed IR cell, Figure 2.3. The cell was modified to contain a sample holder that holds a 25 mm ZnSe disk and which slides to end without being able to rotate, so that the ZnSe disk is always parallel to the IR windows of the cell. A thin film was prepared by evenly spreading a small quantity of silica (0.1-0.5 mg/cm^2) on a transparent support window (ZnSe), then using a spatula to lightly wipe the surface. The thin film was then placed inside the modified IR cell. Thermal treatment was carried out in the usual manner but with an upper limit of 450°C rather than 500°C because of the thermal limitation of the ZnSe disk.

After cooling, the IR cell was placed inside the spectrometer and the silica film was aligned in the IR beam. Once aligned, neither the silica film nor the IR cell was moved for the remainder of the experiment to ensure accurate spectral subtraction, Figure 2.4b. Otherwise the same experimental conditions were used as for a self-supporting disk (e.g., resolution, number of scans).

2.3.2 Solid state NMR spectroscopy

^{51}V MAS NMR spectra were recorded on either a Bruker ASX-200 or Bruker Advance 500 spectrometer. NMR experiments used compacted silica rather than pellets. The silica was prepared by first pressing into thick pellets of 50-100 mg, followed by grinding in a mortar. Samples were prepared in a reactor equipped with a high vacuum stopcock modified with one or more 5 mm pyrex NMR glass tubes welded onto the main tube at right angles, Figure 2.5. After reaction, approximately 50 mg aliquots of silica were transferred under vacuum into the NMR tubes, then sealed off under vacuum at a 30 mm length with a torch. Each glass tube was then inserted into a 5 mm zirconia rotor. ^{51}V MAS NMR spectra were recorded on a Bruker ASX-200 spectrometer at 52.6 MHz. The spectra were collected using a 4.8 μs 90° pulse with a relaxation delay of 0.20 s. Samples were spun at 3000-5000 Hz and the spin rate was varied in order to identify spinning side bands.

To obtain higher field spectra, samples were packed directly into a 4 mm zirconia rotor in a glove box. ^{51}V MAS NMR spectra were recorded on a Bruker Advance 500 spectrometer at 131.4 MHz. The spectra were collected using a 2 μs 45° pulse (90° pulse = 4 μs), with a relaxation delay of 0.20 s. Samples were spun at 11000-14000 Hz.

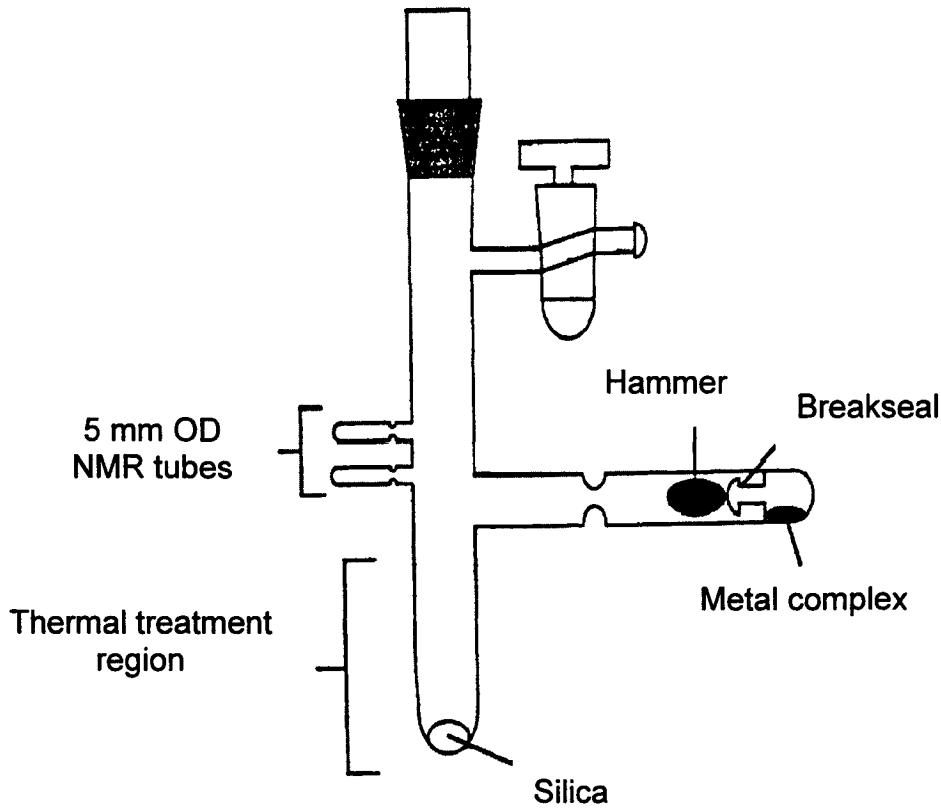

Figure 2.5. Schematic of an NMR reactor.

2.3.3 ESR spectroscopy

Samples for ESR spectroscopy were prepared in the same manner as NMR samples, with the exception that the reactors were equipped with 8 mm o.d. quartz tubes attached to cylindrical quartz-pyrex graded seals welded at right angles to the main body of the reactor. Samples were transferred in vacuo then sealed off, under vacuum, using a torch to give tubes 15 cm in length containing

approximately 50 mg of sample. ESR spectra were recorded on a Bruker ESP 300 spectrometer at X-band frequencies (~9 GHz).

2.3.4 X-ray absorption spectroscopy (XAS)

XAS is a powerful method of analyzing local structure in a wide variety of amorphous materials. The main advantage of XAS is that it can reveal detailed information about powdered samples, unlike single-crystal X-ray diffraction. Since the XAS technique is somewhat specialized, its use will be described in some detail.

2.3.4.1 Background

X-ray absorption generally occurs between 200 and 35000 eV. In this range, a photon is completely absorbed by the atom of interest, ejecting a core photoelectron and leaving behind a core hole. Generally, the proportion of X-rays absorbed (the absorption coefficient) decreases as their energy increases, but at certain values of energy, specific to each element, a sudden increase in the amount of energy absorbed is observed. This energy is known as the edge and corresponds to ejection of the electron from the atom.

The ejected photoelectron has an energy equal to that of the incoming photon, less its binding energy in the core. The ejected photoelectron can be considered as a wave traveling outward from the central absorbing atom, which scatters off neighboring atoms, producing backscattered wave. The outgoing and backscattered waves interfere, Figure 2.6. Interference due to the presence of other atoms (in a molecule or condensed phase) around the absorber causes oscillation in the absorption coefficient near the edge.

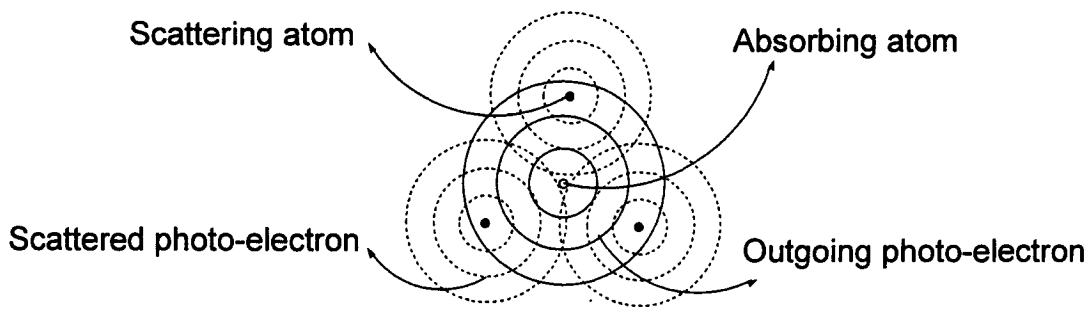

Figure 2.6. Schematic diagram of the radial portion of the photoelectron wave (solid line) being backscattered by neighboring atoms (dotted line)

An X-ray absorption spectrum is usually divided into two energy regions: (i) X-ray Near Edge Structure (XANES), and (ii) Extended X-ray Absorption Structure (EXAFS), Figure 2.7.

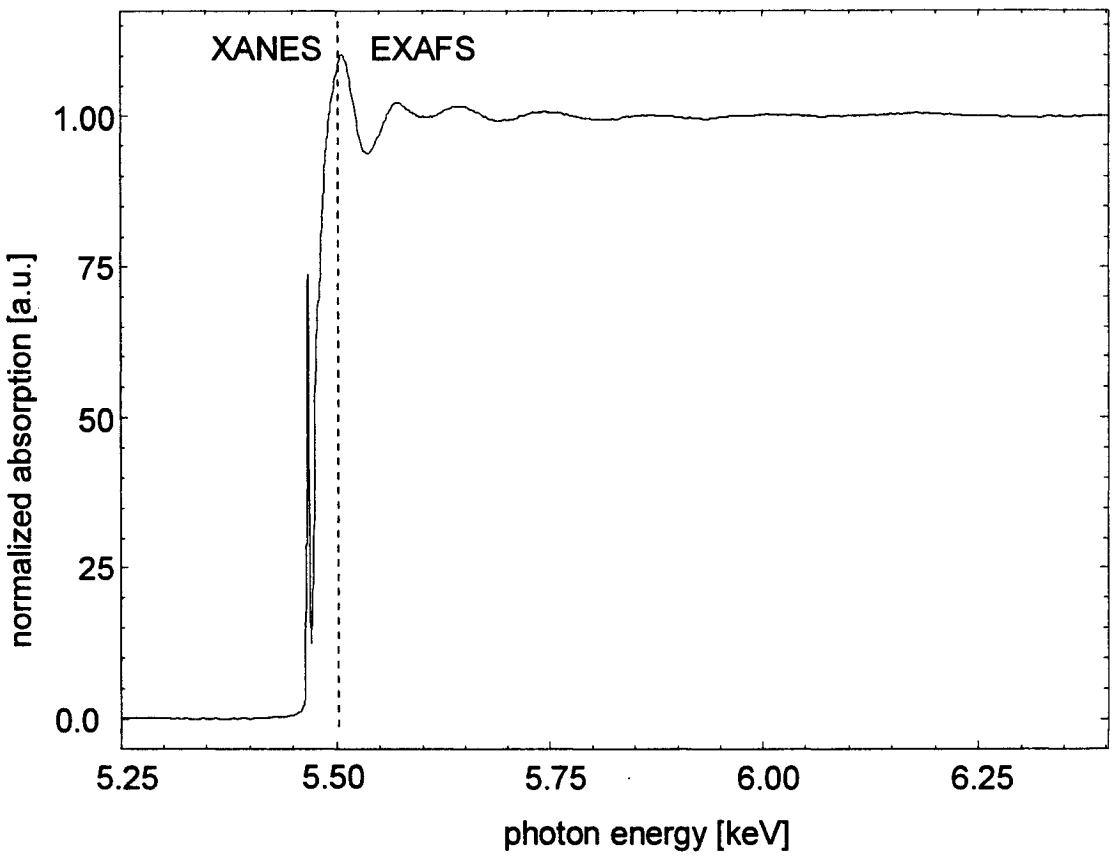

Figure 2.7. Typical XAS spectrum of a silica-supported vanadium catalyst. The vertical line divides the spectrum into XANES and EXAFS regions.

2.3.4.2.1 XANES region

X-ray Absorption Near Edge Structure refers to the region ca. 50 eV before and 30 eV after the absorption edge. This includes electronic transitions which occur prior to ejection of a photoelectron. Analysis of the XANES region gives information about metal oxidation state, as well as qualitative information on ligand environment, coordination geometry and coordination number.

2.3.4.2 EXAFS region

Extended X-ray absorption fine structure refers to the oscillatory structure beyond the position 30 eV after the absorption edge. Since the oscillation amplitude depends on the type of neighboring atoms and their distance from the central atom, the EXAFS contains qualitative and quantitative information on the coordination environment.

After several approximations, the fine-structure function XAFS can be written as eq. 2.1:

$$\chi(k) = \sum_j \frac{N_j f_j(k) e^{-2R_j/\lambda(k)} e^{-2k^2\sigma_j^2}}{kR_j^2} \sin\left[2kR_j + \delta_j(k)\right] \qquad (2.1)$$

where Nj, R_j, and σ_j^2 are the number of neighbors, the absorber-neighbor distances and mean-square relative displacements (Debye-Waller factors) of the jth-shell atoms relative to the absorber atom and k is the photoelectron wave

vector ($Å^{-1}$), $f_j(k)$ and $\delta_j(k)$ are amplitude- and phase-dependent functions which, to a first approximation, depend on the type of atom in the jth shell. Stern et *al.*[1] showed that the phase shift $\delta_j(k)$ is approximately linear in k over the energy of the EXAFS range with a negative slope, so the Fourier transform of x with respect to 2k yields peaks located at $R_j + \alpha$, where α is an average of $2(d\delta/dk)$ over the spectrum.

2.3.4.3 Experimental considerations

The intense X-ray radiation required for XAS must be produced at a synchrotron X-ray source by accelerating electrons to a speed approaching that of light. The XAS experiment involves placing a sample of the compound in the path of X-ray beam and varying the energy of incident X-rays using a monochromator, Figure 2.8. The incident and transmitted X-ray intensities are measured by ionization counters.

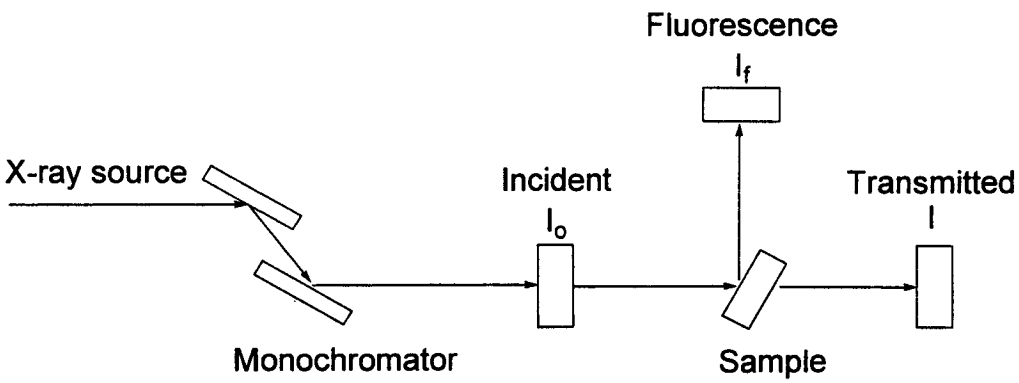

Figure 2.8 Block diagram of an XAS experiment.

Samples were prepared in the same manner as NMR samples with the exception that the reactors were equipped with glass ampules welded at right angles to the main body of the reactor. Experiments were performed at the Stanford Synchrotron Research Laboratory (SSRL) on beamline BL2-3 (Bend) which operates at 3.0 GeV with a current of 2-3 mA. Samples were packed under N_2 in a glove box into square, 2 mm thick, polished Al plates with 35 X 5 mm sample slots. The samples were held in the slots with 6.0 μm gauge polypropylene windows (Chemplex) affixed with double-sided tape to each side of plate. Samples were transported to the hutch under N_2 inside a container sealed in the glove box.

Synchrotron X-rays were monochromatized via reflection from a pair of Si(111) crystals through a 1 mm entrance slit. The subsequent beam was detuned by ca. 50% to reduce harmonics. The fundamental reflection intensity was measured by an initial ion chamber detector (I_o) and then passed through the sample, mounted at a 45° angle to the beam. The beam path was purged with helium gas to minimize scattering from the air. Transmitted X-rays were detected by a second ion chamber (I_1) and subsequently passed through a vanadium calibration foil into a third ion chamber (I_2). Fluorescence was recorded in a argon-purged Lytle detector, optimized for sensitivity by removing its Soller slits. Data at SSRL was acquired on a Sun workstation using the program XASCollect and subsequently exported as ASCII files.

Experiments were performed at room temperature unless otherwise noted. Spectra acquired at cryogenic temperatures were recorded in a liquid helium-cooled cryostat mounted in the beam path.

2.3.4.4 Data analysis

XANES and EXAFS data were generated from at least three separate ASCII files averaged and analyzed using WinXAS (version 2.3).[2] Sample spectra were calibrated with respect to a V calibration foil (K-edge 5465.0 eV), whose spectrum was recorded simultaneously for each sample. Background corrected spectra were obtained by fitting a seventh order polynomial to the post-edge region and extrapolating a linear function from the pre-edge region to the remainder of the spectrum, through the EXAFS energy range.

The border of the XANES spectrum was set at the first inflection point of the K-edge. Pre-peak heights and positions were computed via a least squares fit of the normalized XANES region with a Lorentzian function for the K-edge (normalized to 1) and ArcTAN functions for the pre-peaks. The threshold position is defined as the first peak in the derivative spectrum. The positions of the threshold and the K-edge were identified in first derivative plots of the XANES region.

EXAFS spectra were k^3-weighted and fit with seven cubic-splines from 0.75 to 16.1 $Å^{-1}$. A 20% Hanning window was applied to the data before Fourier-transformation to R-space.

Models of the surface species were constructed using FEFF 8.2 and ATOMS, based on crystal structure data for $VOCl_3$ for the first coordination sphere.[3,4] Cambridge Soft's ChemDraw and Chem3D 2002 were used to create X/Y coordinates for export to FEFF for electronic approximations. The models were then fit to R-space data by least squares analysis using the WinXAS EXAFS Fit feature. Coordination numbers (CN) were fixed as integers in order to reduce the number of independent variables during refinement. This approximation is reasonable for samples of uniform composition. For each shell, the following free variables were sequentially refined: path length (R), Debye-Waller factor (σ^2), and inner potential energy (E_0). The amplitude reduction factor (S_0^2) was calculated as a global variable in the fit refinement.

In the absence of systematic fitting errors, errors for first shell scatting fits calculated against EXAFS data are generally to be accepted as follows:[5] CN: ±10%, R: ±0.02 Á, σ^2: ±20%, E_0: ±20%. Typical systematic errors during fit refinement include forcing additional shells at distances not supported by the FT magnitude data or incorporating an incorrect backscatter (*i.e.*, N instead of O).[6] Discrimination between early elements in the periodic table is often more reliable than between "heavier" elements, barium and larger.[7] Systematic errors manifest themselves in "many body effects" and are detectable as deviations of the amplitude reduction factor (S_0^2) from 1 and large Debye-Waller factors (σ^2).[8] For model refinements with small S_0^2 and σ^2 values, it is appropriate to consider the generally accepted errors (listed above) as reliable, except in cases where other information precludes these assumptions.[5]

2.4 Elemental analysis

At the end of each experiment, the amount of chemisorbed metal was determined by extraction. V analysis was performed in air. The sample was weighed and stirred in 1.0 M H_2SO_4 to which 3.5% aqueous H_2O_2 (0.03 mL/mL sample solution) was added to extract the vanadium as its orange mono-peroxo complex, followed by filtration. (The color of the solution depends on the amount of peroxide present. If the concentration is too high, the pale yellow diperoxo complex is formed). The orange complex has a clear peak in the visible at λ_{max} 453 nm, with extinction coefficient 0.0054 L/(cm mg). A calibration curve was prepared under the same conditions using ammonium vanadate, Figure 2.9.[9] The spectra were recorded in quartz cuvettes of 1 cm pathlength and referenced to a H_2SO_4/H_2O solution containing approximately the same amount of H_2O_2 per mL sample solution.

2.4.1 Simultaneous analysis of vanadium and aluminum

2.4.1.1 Atomic Absorption Spectroscopy

At the end of each experiment, 10-20 mg of the modified silica was stirred overnight in 1.0 M H_2SO_4 treated with 3.5% aqueous H_2O_2 (0.03 mL/mL sample solution) in order to extract aluminum and vanadium.

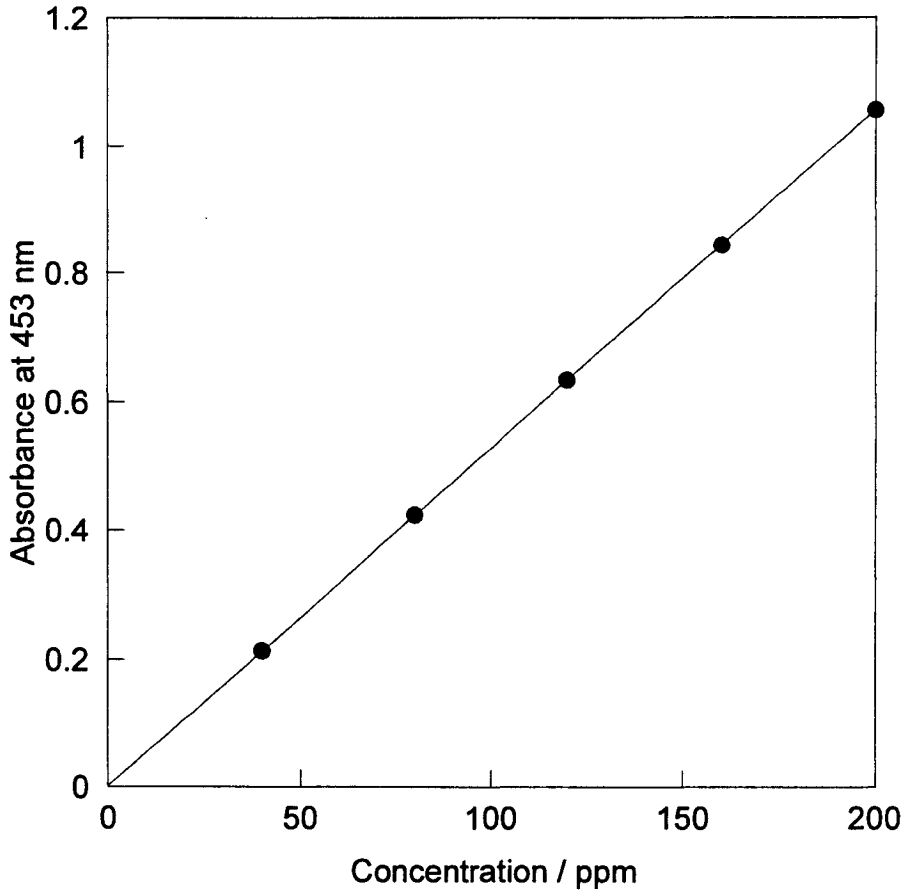

Abs=ε ℓ [V]		
	Value	Error
ε ℓ	0.005279	0.000005
R^2	1	NA

Figure 2.9. Calibration curve for vanadium analysis.

The aluminum content of each sample was analyzed by Flame Ionization Atomic Emission on a Perkin-Elmer 303 Atomic Absorption spectrometer. An Instrumentation Laboratory Inc. Visimax Hollow Cathode lamp specific to aluminum was used in conjunction with a reducing acetylene-N_2O flame. The emission of the sample at 307 nm was compared to a calibration curve constructed from a standard solution prepared by diluting a VWR brand 998 ppm Al standard solution. A new calibration curve was constructed on each day samples were run. The vanadium content of the samples was analyzed as described above.

2.4.1.2 X-Ray Fluorescence Spectroscopy

To test the accuracy of our analysis, samples were also analyzed by XRF. Spectra were recorded on a Philips PW2400 X-Ray fluorescence spectrometer. The calibration curve for Si covered the range 37.39 to 46.74%, for Al 0.00 to 10.58% and for V 0.00 to 11.20%. The standards were made using oxides of Si, Al and V. The analysis software is Philips SuperQuant.

A comparison of the results of simultaneous analysis of vanadium and aluminum by different methods is shown in Table 2.2. The results are comparable, generally within 5%, which is considered to be the experimental error.

Table 2.2. Comparison of different methods for simultaneous analysis of vanadium and aluminum contents of modified silicas

Sample	UV-Vis	AAS	XRF	
	%V	%Al	%V	%Al
1	3.16	4.56	2.93	4.47
2	7.00		7.32	
3	7.80	3.97	7.69	3.71
4	3.30	3.89	3.20	3.71
5		4.37		4.47

2.5 Qualitative analysis of volatile products

The gases liberated by reactions of $VO(O^iPr)_3$ or TMA with silica and in subsequent reactions were analyzed by GC and GC/MS. Gases were identified by GC on a Hewlett-Packard 5710A gas chromatograph with variable temperature oven control, equipped with a 2 m ¼" stainless steel Porasil packed column and an FID detector. Retention times were confirmed with standards injected under the same experimental conditions.

2.6 Quantitative analysis of volatile products

The gases liberated by reaction of $VOCl_3$, $VO(O^iPr)_3$ and TMA with silica and in subsequent reactions were quantified by gas-phase IR spectroscopy using pressure versus absorbance calibration curves, Figures 2.10-2.12. For each experiment, 100-200 mg of compacted silica powder was used.

The methane produced in the reaction of TMA with silica and vanadium-modified silica was quantified in situ in a grease-free IR cell (path length 8.0 cm) by measuring the intensity of the ν(C-H) peak at 3015 cm^{-1} and comparing it to a calibration curve, Figure 2.10a, constructed from spectra recorded using known pressures of methane. The volume of the cell was measured after each experiment. CH_3Cl, HCl, CO_2 and ^iPrOH were quantified in the same way by measuring the intensity of their peaks at 731, 2943, 667 and 2965 cm^{-1}, respectively.

In order to quantify the gases liberated from the hydrolysis of vanadium modified silica, water vapor was transferred under vacuum into the reactor through a T-joint using a liquid nitrogen path. After warming to room temperature, the gas formed was quantified in the same manner as described previously.

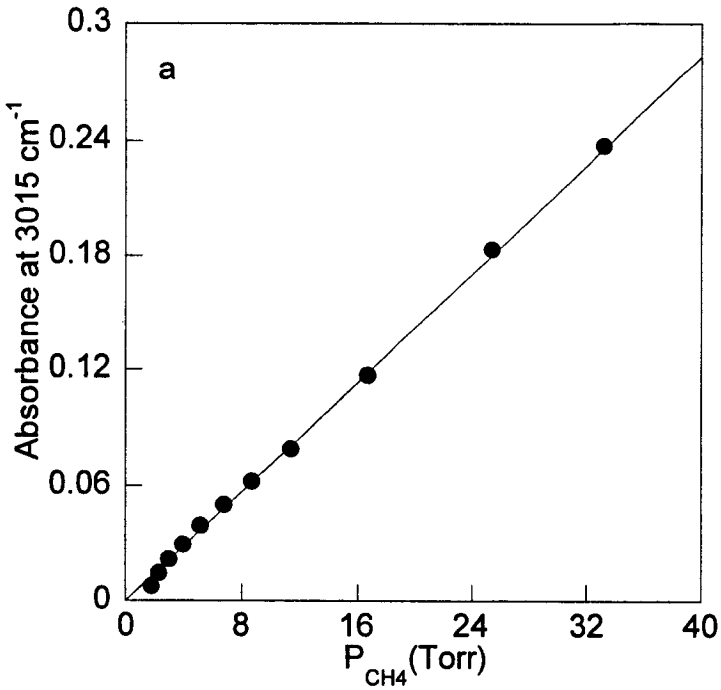

Abs=ε ℓ P		
	Value	Error
ε ℓ	0.00709	0.00005
R^2	0.999	NA

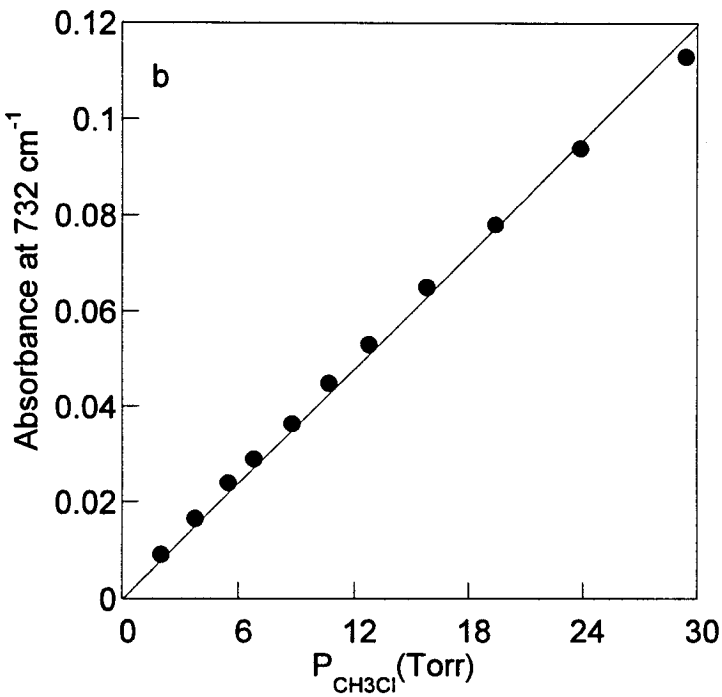

Abs=ε ℓ P		
	Value	Error
ε ℓ	0.00397	0.00004
R^2	0.999	NA

Figure 2.10. Calibration curves for (a) CH_4; (b) CH_3Cl.

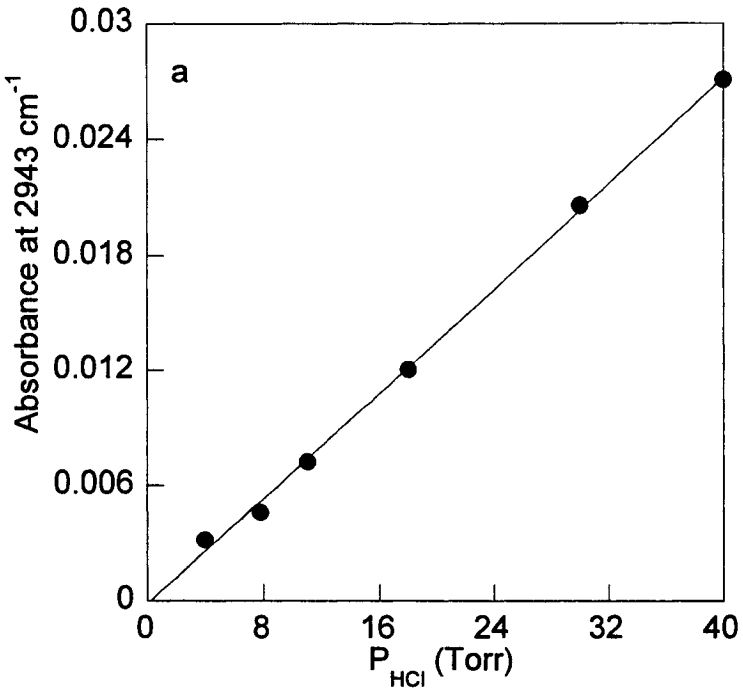

Abs=ε ℓ P		
	Value	Error
ε ℓ	0.000677	0.000001
R^2	0.9984	NA

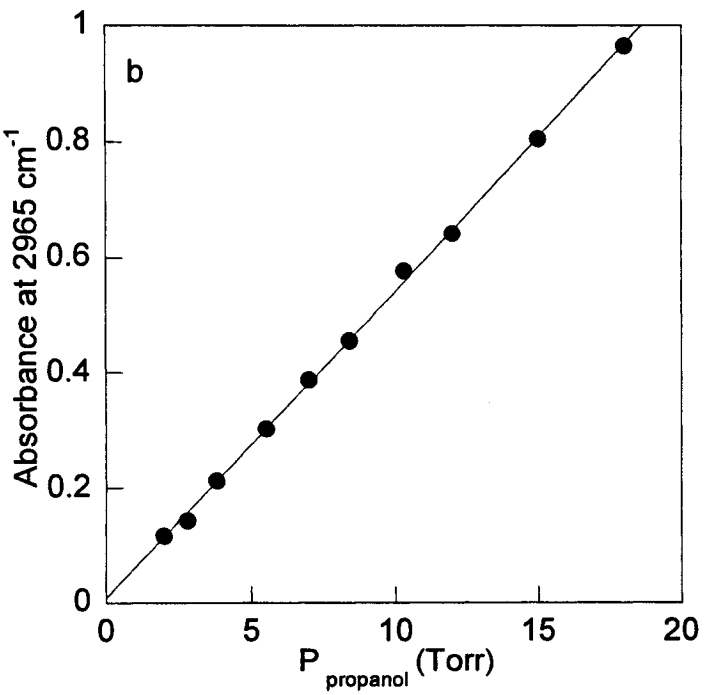

Abs=ε ℓ P		
	Value	Error
ε ℓ	0.0532	0.0001
R^2	0.9995	NA

Figure 2.11. Calibration curves for (a) HCl; (b) 2-propanol.

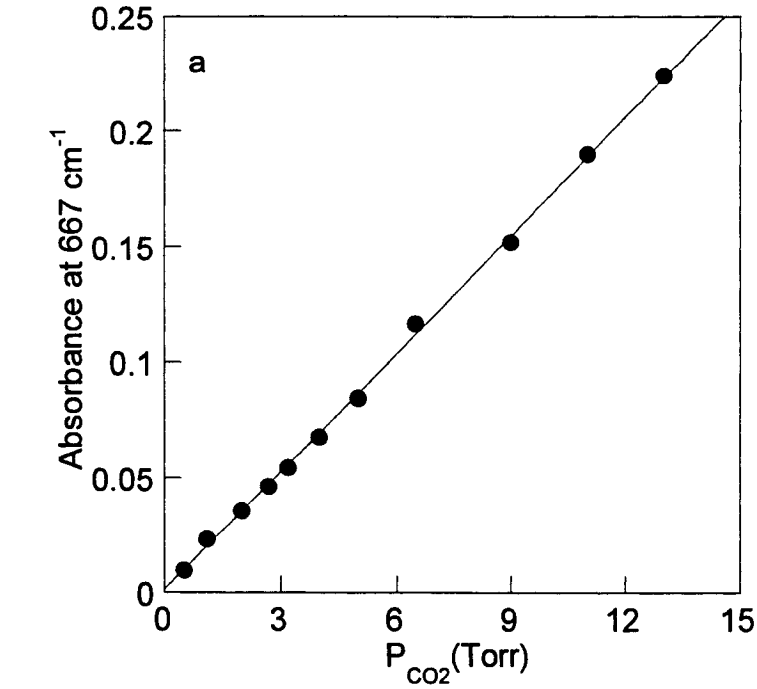

Abs=ε ℓ P		
	Value	Error
ε ℓ	0.0170	0.0001
R^2	0.9994	NA

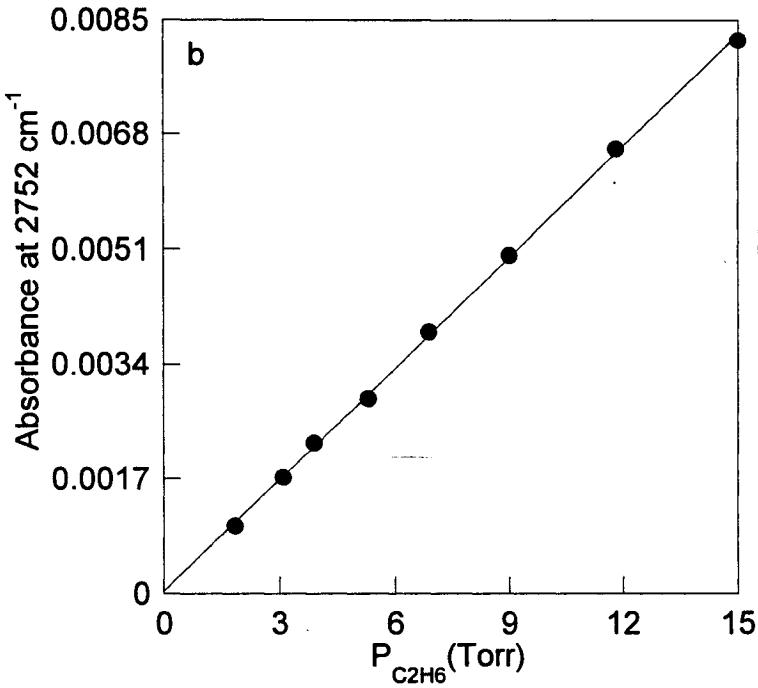

Abs=ε ℓ P		
	Value	Error
ε ℓ	0.000553	0.000004
R^2	0.9996	NA

Figure 2.12. Calibration curves for (a) CO_2; (b) C_2H_6.

2.7 Kinetics experiments

For kinetic studies, 100 mg of modified silica was transferred in the glove box into a breakseal reactor, then removed and sealed off with flame. A hammer was placed in the open end of the breakseal containing the modified silica, which was then attached to an IR cell, Figure 2.2. In all experiments, 100 Torr olefin was introduced into the IR cell which was placed inside the IR spectrophotometer, so that the IR beam sampled the gas phase. Once aligned, the IR cell was not moved for the duration of the experiment. In order to maintain constant temperature during the reaction, the breakseal was placed either in a water bath (21°C) or a preheated tube furnace equipped with a thermocouple (±1 K). The breakseal was broken with the hammer to initiate the reaction. The gas phase IR spectrum was recorded at regular time intervals, without moving the IR cell, until the reaction was complete.

The relative amount of product in the gas phase was evaluated by performing an integration of the ν(C-H) spectral region to give values of absorbance A_t. Nonlinear least-squares fits were performed with three variable parameters A_∞, A_0 and k, using the first-order integrated rate equation, eq 2.2, and the program Kaleidagraph (Abelbeck Software).

$$A_t = A_\infty - (A_\infty - A_0)e^{(-kt)} \qquad (2.2)$$

Activation parameters were derived by linear curve-fitting of the plot of $\ln(k/T)$ versus T^{-1}. Errors in the parameters were calculated according to the error propagation formula.[10]

2.8 Polymer Characterization

2.8.1 Molecular weight and polydispersity

Molecular weights and molecular weight distributions of polyethylene and polypropylene were determined using a high-temperature gel permeation chromatograph (GPC) instrument equipped with a light scattering detector at The Advanced THermal AnalysiS (ATHAS) and Polymer Characterization Laboratory (PCL), University of Tennessee, USA. Polymer samples were dissolved by stirring in 1,2,4-trichlorobenzene (TCB) at 160 °C for 3-4 hours, and then purified following the procedure for PL-GPC 220. Analyses were performed at 140 °C. Columns were calibrated with standard narrow molar mass distribution polystyrene, and with standard polyethylene and polypropylene.

2.8.2 NMR spectroscopy

NMR can be a useful tool for polymer characterization, but paramagnetic vanadium must be extracted with aqueous acid prior to the NMR analysis. Sample solutions 0.25 wt.% in polymer were prepared in 1,2,4-trichlorobenzene

at 125 °C.[11] ^{13}C and ^{1}H NMR spectra were recorded on a Bruker AMX-500 spectrometer at frequencies of 125 MHz and 500 MHz, respectively. ^{1}H NMR spectra were collected using a 3.0 μs 45° pulse and an interpulse decay of 4.7 s. C_6D_6 was added to provide the internal signal lock. ^{13}C NMR spectra were collected using a 5 μs 45° pulse with relaxation delay of 1.5 s. Polypropylene pentad distributions were determined by integration of peaks in the methyl region (19-22 ppm) of the ^{13}C NMR spectrum.[12] ^{13}C CP-MAS NMR spectra were recorded on a Bruker ASX-200 spectrometer operating at 50.32 MHz and a spinning rate of 5.0 kHz.

2.8.3 Differential scanning calorimetry

Thermal measurements were carried out on a SDT 2960 Simultaneous DSC-TGA instrument under flowing nitrogen. A 3 to 5 mg polymer sample was weighed and placed in an aluminum DSC pan. Cyclic heat-cool-heat experiments were performed on each sample. An empty aluminum DSC pan was used as the reference. The polymer sample and reference were heated at a rate of 10 °C/min from –50 to 200 °C.

2.9 References

1) Gosink, H.–J.; Roesky, H. W.; Noltemeyer, M.; Schmidt, H.–G.; Freier-Erdmgger, C.; Sheldriek, G. M. *Chem. Ber.* **1993**, *126*, 279.

2) WinXAS is an XAS data analysis program for PCs running Windows, written by Thorton Ressler. (E-mail: t-ressler@winax.de; http://www.winxas.de). For recent references concerning WinXAS, see: Ressler, T. *J. Synch. Rad.* **1998**, *5*, 118-122.

3) Polmer, K. *J. Am. Chem. Soc.* **1938**, *60*, 2360-2369.

4) Hawthorne, F. C.; Calvo, C. *J. Solid State Chem.* **1977**, *22*, 157-170.

5) Vaarkamp, M. *Catal. Today* **1998**, *39*, 271-279.

6) Li, G. G.; Bridges, F.; Booth, C. H.; *Phys. Rev. B* **1995**, *52*, 6332-6348.

7) Teo, B. K.; Lee, P. A. *J. Am. Chem. Soc.* **1979**, *101*, 2815-2832.

8) Vaarkamp, M.; Dring, I.; Oldman, R. J.; Stern, E. A.; Koningsberger, D. C. *Phys. Rev. B* **1994**, *50*, 7872-7883

9) Vogel, A. J. *Textbook of Quantitative Inorganic Analysis*; Longman: London, **1961**.

10) Morse, P. M.; Spencer, M.D; Wilson, S. R.; Girolami, G. S. *Organomet.* **1994**, *13*, 1646-1655.

11) Smith, P. D.; McDaniel, M. P. *J. polym. Sci.: A: Polym. Chem.* **1990**, *28*, 3587-3601.

12) Busico, V.; Cipullo, R. *Prog. Polym. Sci.* **2001**, *26*, 443-533.

Chapter Three

A Chemical Method for Measuring the Reactive Hydroxyl Content of Partially Dehydroxylated Fumed and Precipitated Silicas

---

3.1 Introduction

The silica surface consists of hydroxyl groups (silanols) and siloxane bridges. The latter are generally unreactive towards all but highly aggressive reagents (e.g., MeLi).[1] In contrast, the hydroxyl sites are reactive towards a wide variety of organic and organometallic reagents, which can be used to functionalize the surface of the silica for applications in chromatography,[2,3] catalysis[2-7] and composite fillers incorporated into polymer matrices.[2-10] The hydroxyl groups on the surface may be classified into free silanols, geminal silanols, vicinal silanols and hydrogen-bonded silanols, Figure 3.1.

Upon heating, pairs of surface hydroxyl groups on the silica condense to give siloxane bridges and liberate water, rendering the surface of silica more hydrophobic. It follows that the temperature of dehydroxylation of the silica controls the density of the hydroxyl groups on the surface. When the silica is used to support a catalyst, the hydroxyl density is an important parameter for catalyst activity. In order to establish the stoichiometry of grafting in catalyst preparation, it is necessary to accurately know the accessible hydroxyl content of the silica support after subjecting it to the thermal treatment which precedes grafting.

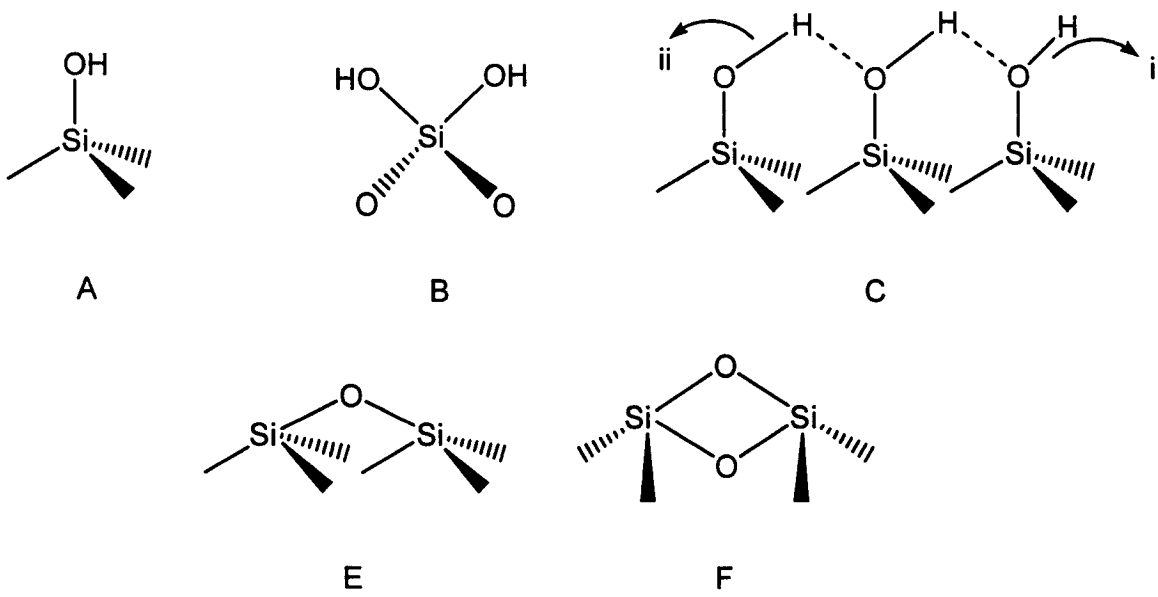

Figure 3.1. Possible silanol and siloxane configurations for silica surfaces: (A) non-nearest-neighbour (or non-interacting, isolated) silanol; (B) geminal silanols; (C) hydrogen-bonded silanols: (i) terminal free hydroxyl of an H-bonded pair or chain silanol, (ii) H-bonded pairs or chains of silanols; (D) unstrained siloxane bridge; and (E) strained four-membered siloxane ring.

The number of silanols has been determined quantitatively by a variety of physical and chemical methods. The former include thermal gravimetric analysis (TGA), FTIR and NMR spectroscopy.[11-26] These techniques require access to special equipment such as a vacuum microbalance or solid state NMR spectrometer and yield measurements of total hydroxyl content, including those which are not reactive in subsequent grafting reactions.

In contrast, active hydroxyl group measurements have been made using chemical titrating agents[18, 27-44] such as trichlorosilane,[34, 36] alkylmagnesium bromide,[16] trimethylaluminum (TMA),[27-33] and titanium tetrachloride.[34-37] These methods invariably involve quantitation of volatile products, such as HCl generated from the reaction of $TiCl_4$ with silica or CH_4 from the reaction of TMA with silica. Such reactions can be difficult to implement and are limited in their accuracy by the presence of hydrolysis products (e.g., HCl, CH_4) as impurities in the reagents, which can be tedious to remove. Some chemical methods employ reagents which are difficult to handle, such as pyrophoric organolithiums and organoaluminums, and they may react with sites other than surface hydroxyls (e.g., organoaluminum reagents react with siloxanes).[33, 36]

Thus, the quantitation of reactive OH groups is a subject of ongoing research. The ideal titrating agent will react with all reactive OH groups, give a simple and invariant reaction stoichiometry, will not react with other sites (e.g., siloxanes), undergoes ready desorption of physisorbed material, be easily quantified and easy to handle.

In this chapter, we describe a chemical method for the analysis of reactive hydroxyl group content on two families of silicas: non-porous, fumed Aerosils, and porous, Sylopol silica gels. We demonstrate that the reaction stoichiometry for the grafting of $VOCl_3$ vapour on these supports is invariant and there is no reaction with siloxanes up to thermal treatment temperatures of 600°C. The method involves simple extraction of vanadium and analysis by colorimetry, involving no special instrumentation or equipment other than that required to create a vacuum.

3.2 Infrared characterization of the supported vanadium complex

3.2.1 Spectra of untreated silicas

The surface silanol groups on silica show their characteristic OH stretching vibration in the spectral region from 3800-3200 cm^{-1}. The infrared spectrum of a self-supporting disk of fully hydroxylated Aerosil 380 after vacuum activation at 25°C for 2 hours shown in Figure 3.2a has a sharp absorption band at 3747 cm^{-1} due to non-nearest-neighbour (non-interacting, isolated) and geminal silanols on the silica surface. It is not possible to distinguish between isolated and geminal silanols in the infrared, since their stretching frequencies are so similar.[43] The maxima near 3720 and 3520 cm^{-1} have been attributed to the stretching modes of terminal and internal silanol groups, respectively, located in H-bonded pairs or chains, Figure 3.1. A third broad band centered at approximately 3665 cm^{-1}

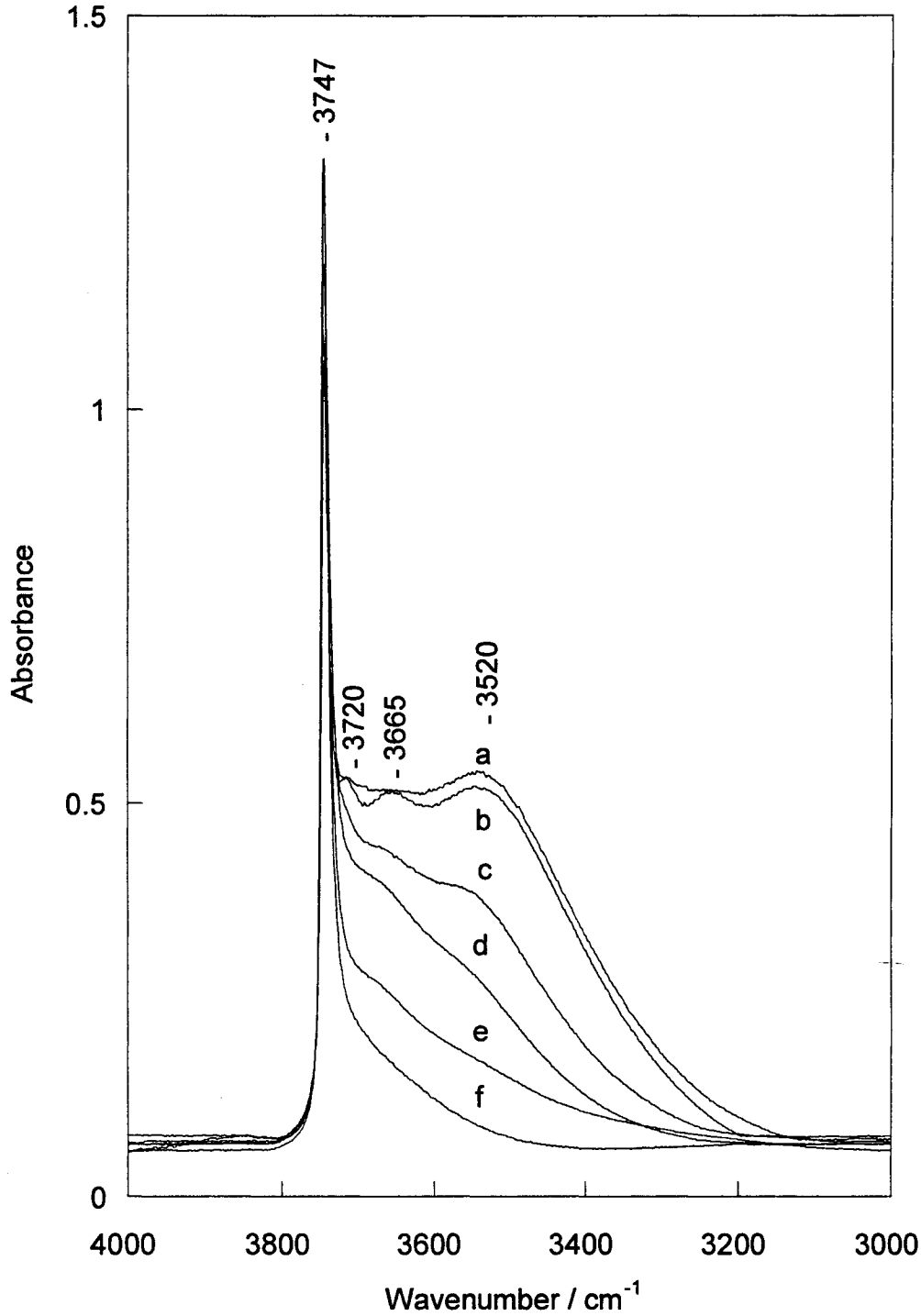

Figure 3.2. Infrared spectra of a 12.5 mg self-supporting 16 mm disk of Aerosil-380 progressively dehydroxylated at: (a) 25, (b) 100, (c) 200, (d) 300, (e) 400, and (f) 500 °C.

represents the same mode for unreactive hydroxyl groups perturbed by hydrogen-bonding, which have been called internal silanols.[43]

Similar bands are seen in the OH stretching region for Sylopol 952 activated at 25°C, Figure 3.3a. The S952-25 spectrum is more intense in the region 3200-3750 cm^{-1} than was observed for the higher surface area A380-25, even after normalization for the amount of silica present by matching the intensities of the silica at 2069 cm^{-1}, and the broad bands are better resolved. Also, the relative intensities of the sharp and broad peaks are lower for S952-25 than for A380-25.

3.2.2 After thermal treatment

As silica is subjected to progressively higher temperatures, its broad O-H stretching bands decrease in intensity, while the sharp band initially increases in intensity. On A380, after treatment at 500°C, the broad band has almost completely disappeared, leaving the sharp band at 3747 cm^{-1} with a pronounced shoulder at lower wavenumbers, Figure 3.2. A similar series of experiments were undertaken on S952 silica, Figure 3.3.

Visual comparison of the spectra of A380 and S952 dehydroxylated at the same temperature shows that the Sylopol bands are more intense than those of the Aerosil. This suggests that there are more hydrogen-bonded silanols on the silica gel and they persist to higher temperatures. This observation is consistent with our findings on $VOCl_3$ uptake, as will be discussed in more detail below.

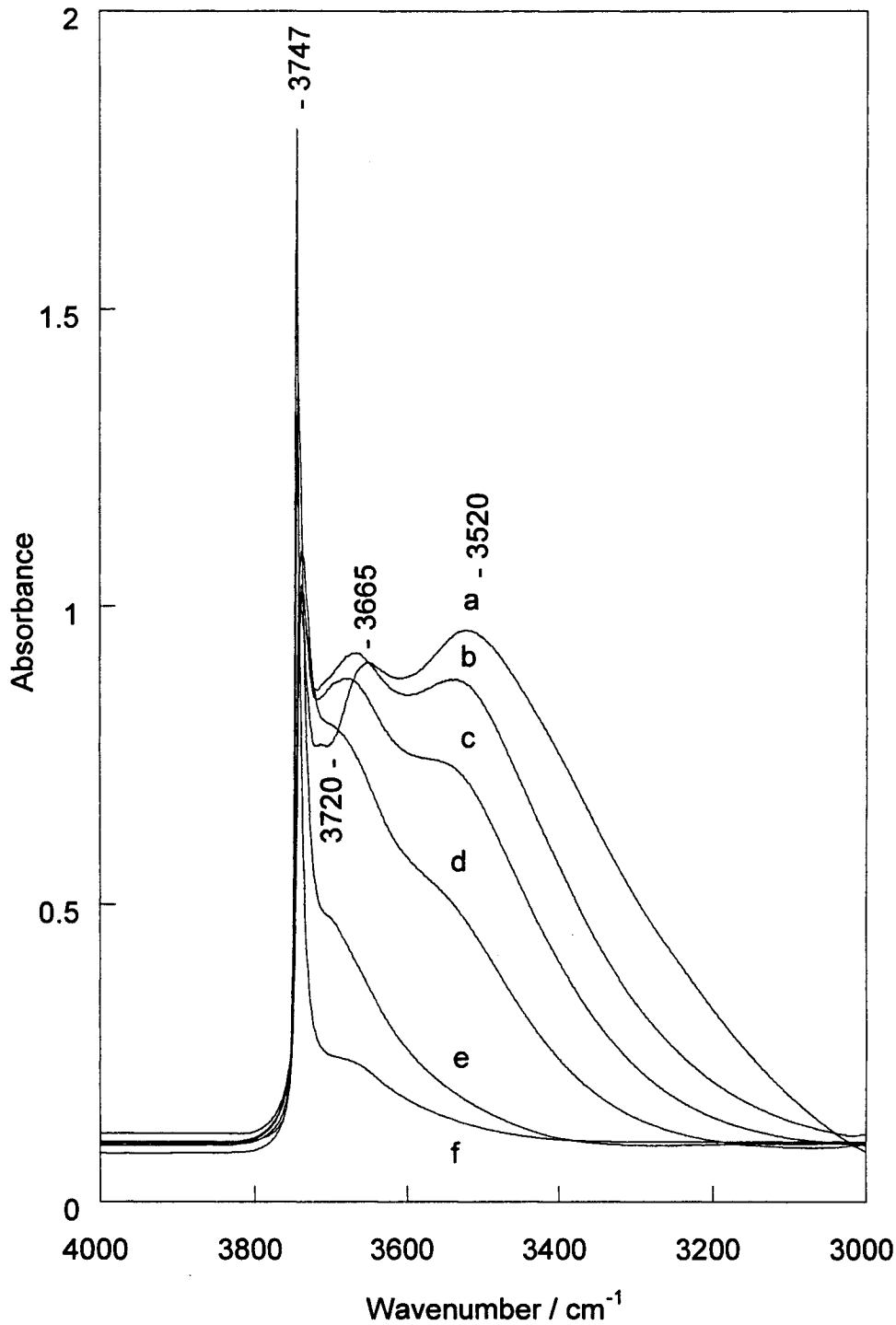

Figure 3.3. Infrared spectra of a 13.7 mg self-supporting 16 mm disk of S952 progressively dehydroxylated at: (a) 25, (b) 100, (c) 200, (d) 300, (e) 400, and (f) 500°C.

In both cases, activation at higher temperatures caused a loss in intensity associated with hydrogen-bonded silanol groups, which can be attributed to condensation resulting in concomitant increases in the isolated silanol population due to elimination of silanols in chains containing odd numbers of silanols, eq 3.1.[29]

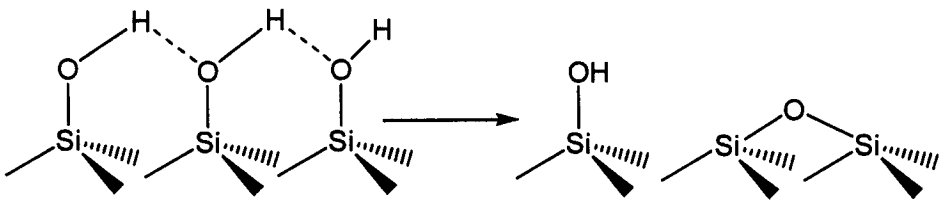

(3.1)

3.2.3 After chemical modification

Upon reaction of the Aerosil silica with excess $VOCl_3$ at room temperature, HCl was detected by its IR spectrum in the gas phase above the silica pellet. The sharp absorption band of the silica pellet at 3747 cm^{-1} due to isolated surface silanols almost completely disappears, Figure 3.4. Only a weak broad absorption band remains in the ν(O-H) region. This band, at approximately 3665 cm^{-1} and previously assigned to internal silanols, represents hydroxyl groups which are unreacted towards all hydrogen-sequestering agents tested to date. They do not exchange even with D_2O.[29,45] They are therefore accurately described as unreacted silanols. It appears that the reactive hydroxyl groups of silica are completely consumed by reaction with $VOCl_3$.

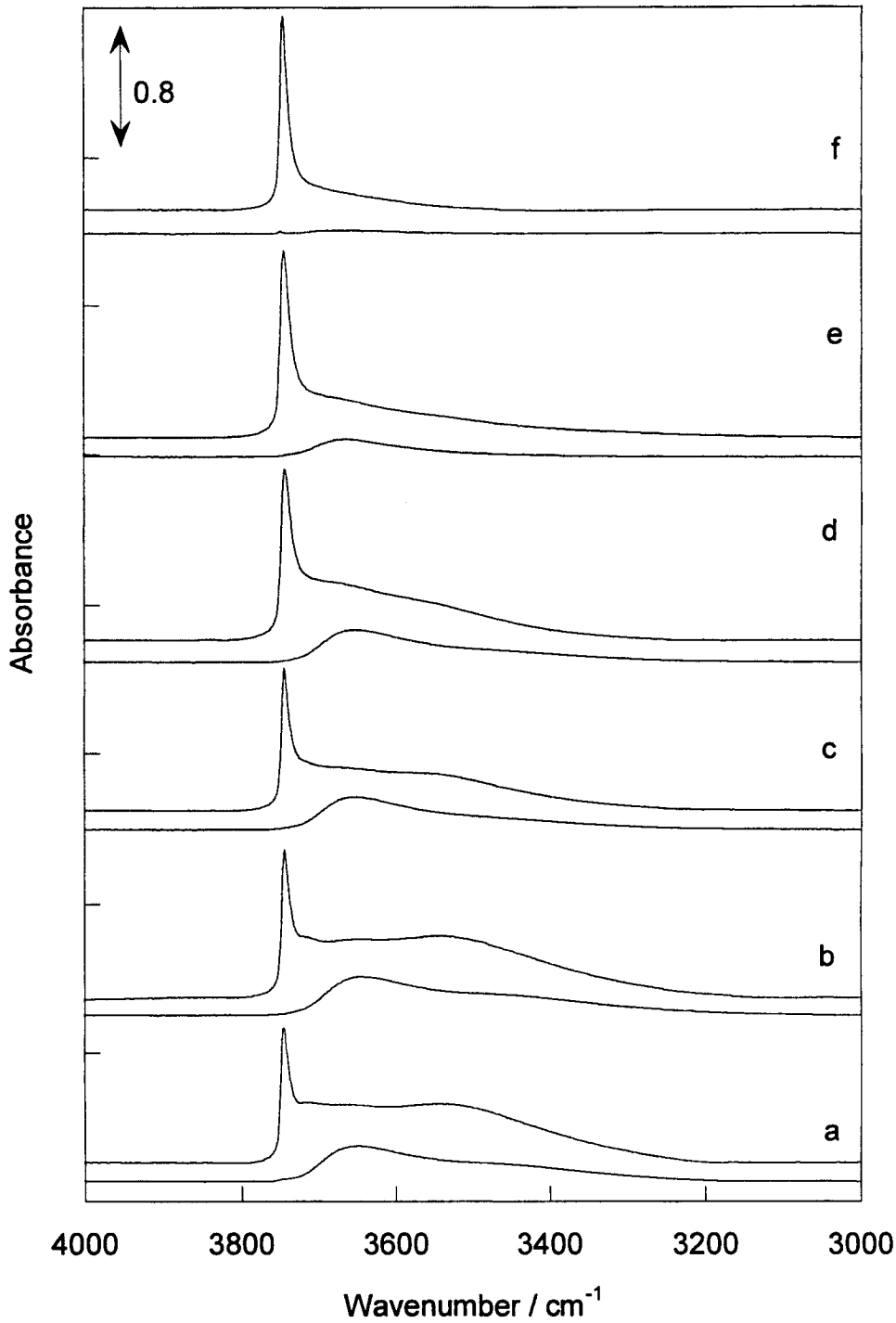

Figure 3.4. Infrared spectra of self-supporting disks of Aerosil-380 partially dehydroxylated at: (a) 25, (b) 100, (c) 200, (d) 300, (e) 400, and (f) 500°C, before (upper trace) and after (lower trace) reaction with excess $VOCl_3$.

The only new feature in the mid-IR spectrum is a weak band at 2069 cm^{-1} assigned to the $2\nu(V=O)$ overtone, Figure 3.5. The presence of only one such band in all spectra indicates the formation of a single grafted complex, $\equiv SiOVOCl_2$, since successive replacement of each chloride ligand in the coordination sphere of vanadium results in a substantial shift of the $\nu(V=O)$ frequency and its overtone.[46]

Spectral changes observed after grafting $VOCl_3$ on the S952, Figure 3.6, are similar to those on A380, but the fraction of unreacted hydroxyl groups appears to be larger on S952. Hockey reported that the number of unreacted silanols on Aerosil silicas increases with the pressure used to prepare self-supporting disks.[47-49] The pressure used to prepare Sylopol disks is at least four times higher than that used for Aerosil disks. As for A380, $VOCl_3$-modified S952 shows a single $2\nu(V=O)$ overtone in all spectra, Figure 3.5 c, d.

Similar experiments were performed on two other Aerosil silicas (A200 and A300) of different surface areas, and two other Sylopol silicas (S952X1836 and S948) with different particle sizes. The same IR spectral changes were observed upon increasing the dehydroxylation temperature and after grafting $VOCl_3$.

3.3 Solid-state NMR characterization

The ^{51}V MAS NMR spectra of the products of reaction of $O=VCl_3$ with S952 are shown in Figure 3.7. The peak at -293 ppm was identified as the only

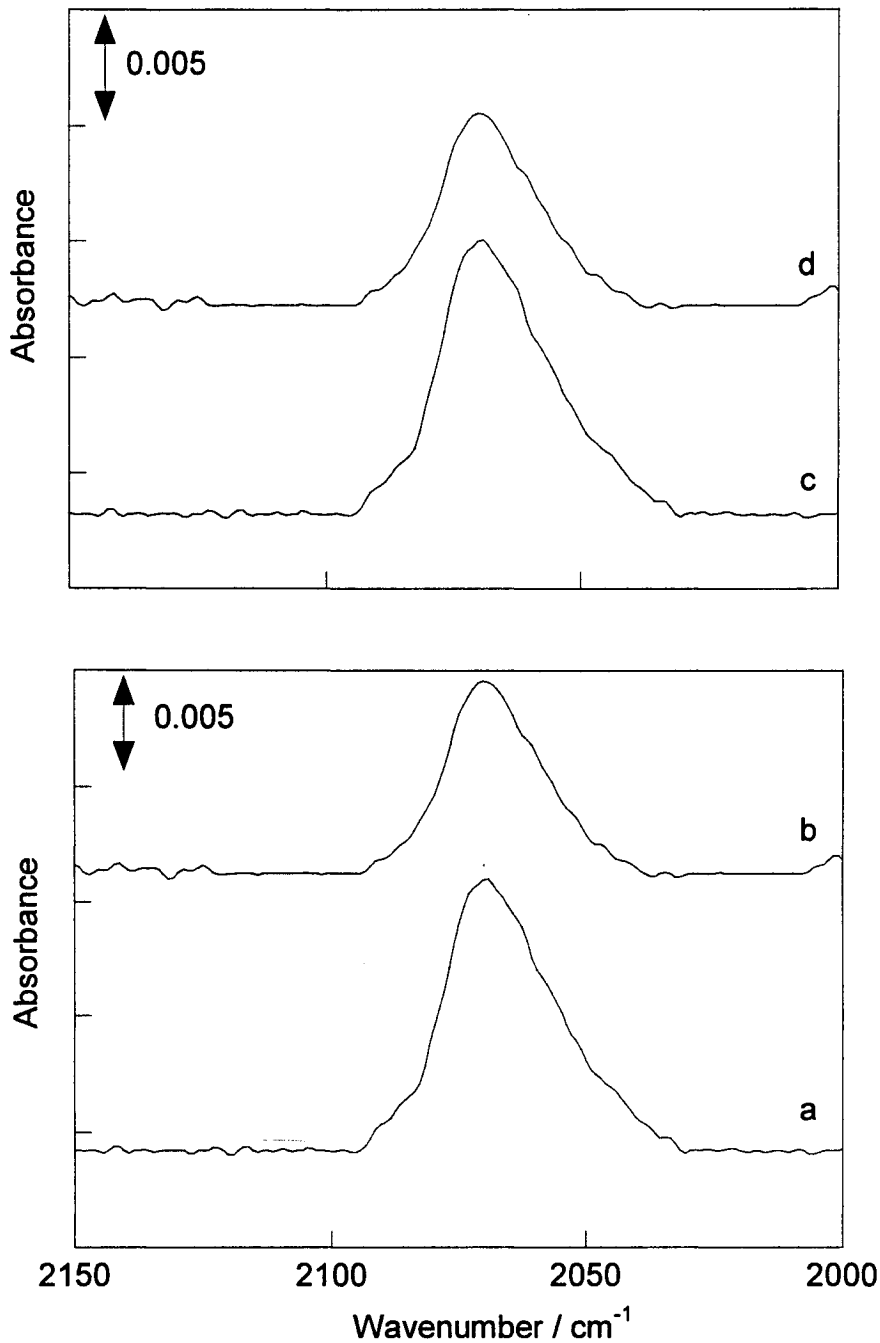

Figure 3.5. Difference infrared spectra of the ν(V=O) overtone region of $VOCl_3$-modified self-supporting disks of (a) A380-25, (b) A380-500, (c) S952-25, and (d) S952-500. The silica background was subtracted from each spectrum.

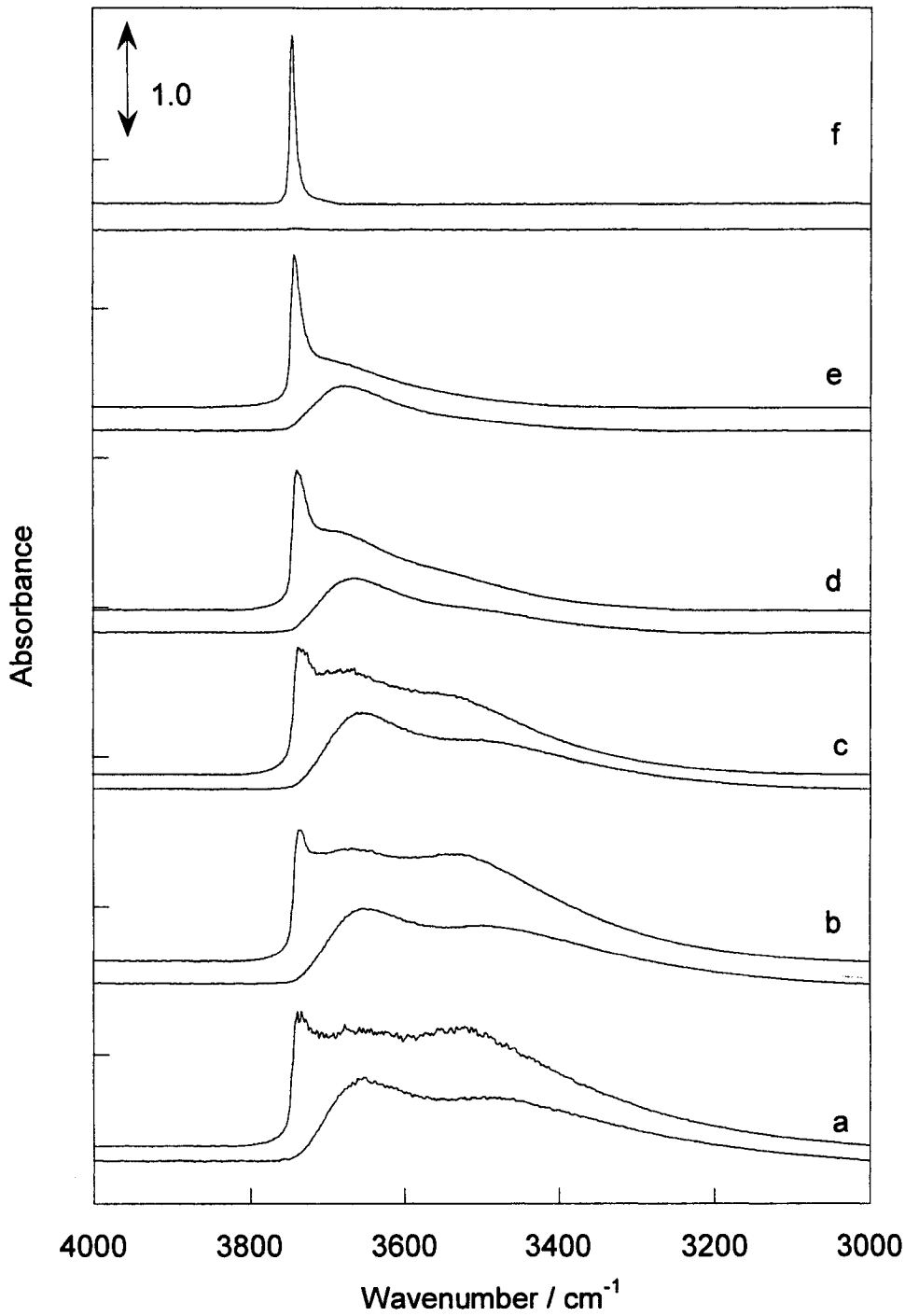

Figure 3.6. Infrared spectra of self-supporting disks of Sylopol-952 partially dehydroxylated at: (a) 25, (b) 100, (c) 200, (d) 300, (e) 400, and (f) 500°C, before (upper trace) and after (lower trace) reaction with excess $VOCl_3$.

isotropic signal; all other bands are spinning side bands whose position shifted when the spin rate was changed. Physisorbed $VOCl_3$ was observed as a signal at 0 ppm only in samples from which unreacted $VOCl_3$ was not desorbed.

Similar spectra were obtained for $\equiv SiOVOCl_2$ supported on Aerosil silicas dehydroxylated at various temperatures. The presence of only one signal in the ^{51}V MAS NMR spectrum on all silicas at all temperatures, and its isotropic chemical shift, is consistent with the formation of a single grafted complex, $\equiv SiOVOCl_2$.[46]

The ^{51}V MAS NMR spectrum of S952X1836-100 after grafting less than the maximum loading of $O{=}VCl_3$ (0.67 mmol V/g silica; full loading 1.23 mmol V/g silica) also shows only one signal at -293 ppm, Figure 3.8a. The ^{1}H NMR spectrum of the same sample shows a signal at 1.89 ppm due to unreacted silanols on the surface of the silica, Figure 3.8b. This finding rules out the formation of di- and trisubstituted vanadium centres on silica, Figure 3.9, even in the presence of unreacted silanols.

3.4 Stoichiometry of the reaction of VOX_3 with silica

The reaction between excess $VOCl_3$ and A380 results in the evolution of HCl, as confirmed by gas phase IR. The amount of HCl was quantified by gas phase IR spectroscopy by measuring the intensity of the vibrational mode in the HCl spectrum at 2943 cm^{-1}.

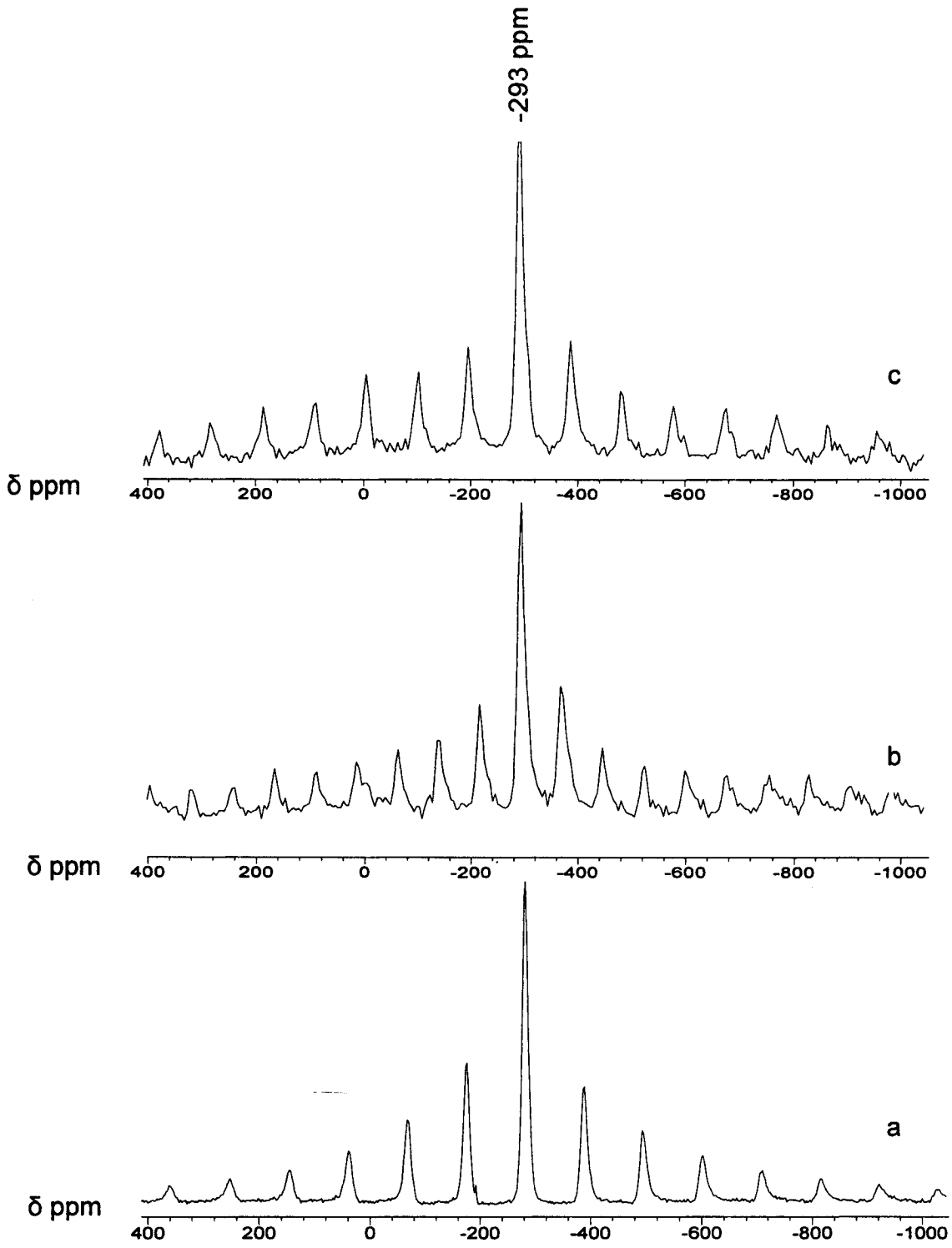

Figure 3.7. ^{51}V MAS NMR spectra of ≡SiOVOCl$_2$ (maximum coverage) on a) S952-25 (spin rate 14 kHz, 131.5 MHz); b) S952-200 (spin rate 3 kHz, 52.6 MHz); c) S952-500 (spin rate 5 kHz, 52.6 MHz).

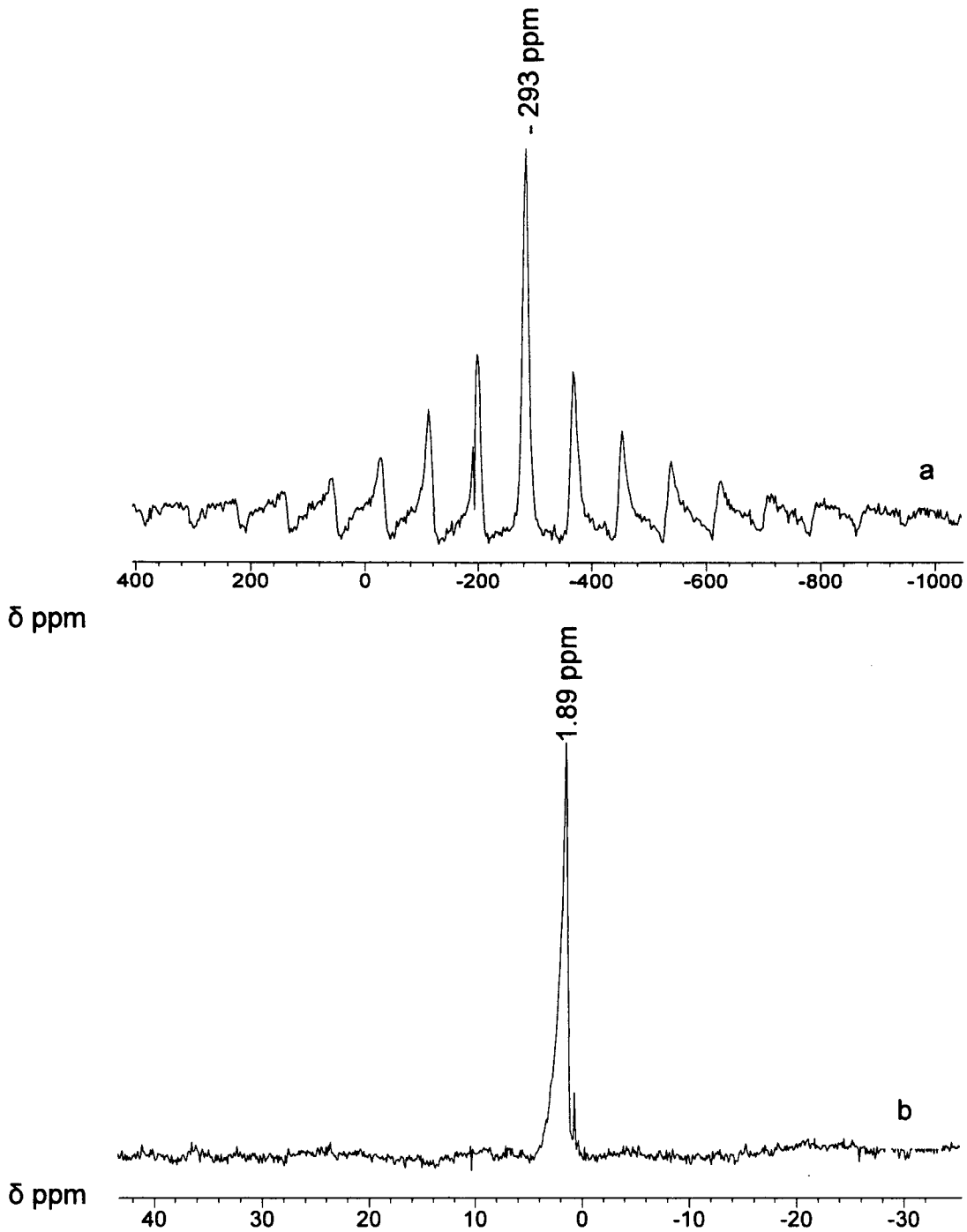

Figure 3.8. a) ^{51}V MAS NMR (131.5 MHz), and b) ^{1}H MAS NMR (500 MHz) spectra of S952X-100 modified with 0.67 mmol V/g, spinning at 11 and 11 kHz, respectively.

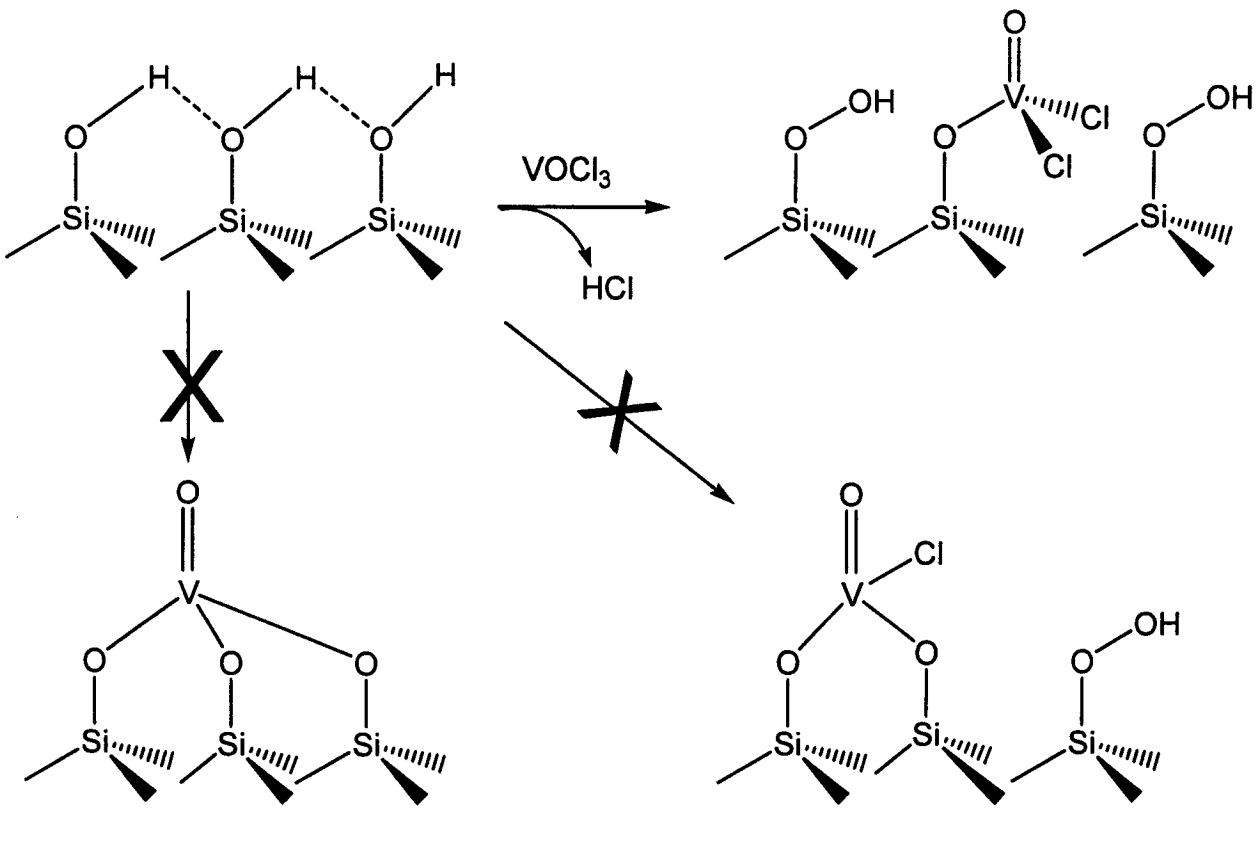

Figure 3.9. Schematic representation of the possible reactions of $VOCl_3$ with silica surfaces.

For example, when a 16.8 mg self-supporting disk of A380-25 was exposed to excess $VOCl_3$ vapor, 1.09 mmol HCl/g silica was formed. After desorption of unreacted $VOCl_3$, chemisorbed vanadium was extracted from the silica. The sample contained 5.65% V by mass or 1.11 mmol V/g silica. This experiment was repeated twice more: on average, (1.03 ± 0.04) mmol HCl was liberated per mmol of grafted V. Based on this and the average of fourteen experiments for A380 at various temperatures, (1.01 ± 0.03) mmol HCl was liberated per mmol of grafted V. This result suggests that the following stoichiometric reaction occurs, eq. 3.2, on all Aerosil silicas regardless of their thermal activation.

$$\equiv SiOH + VOCl_3 \rightarrow \equiv SiOVOCl_2 + HCl \qquad (3.2)$$

where ≡SiOH represents an accessible hydroxyl group on the silica surface. The same reaction stoichiometry was established for the grafting of $VO(O^iPr)_3$ on silica.

The stoichiometry was confirmed by quantitation of HCl or 2-propanol liberated from the surface upon addition of excess water vapour to the supported vanadium complexes. For example, prolonged hydrolysis results in the liberation of 2.15 mmol HCl per g silica, corresponding to 1.94 HCl per original silanol. Thus the total HCl recovered from the grafting and subsequent hydrolysis of the chemisorbed vanadium complex is 2.94 HCl per silanol (the average OH content based on 14 experiments is (3.01 ± 0.06)). In addition to quantitative release of

HX (X is Cl, O^iPr), the addition of water leads to color change from colorless to red and eventually to yellow-green. Our finding for A200-500 is consistent with those reported by Rice *et al.*[9] The results are summarized in Tables 3.1, 3.2 and 3.3 for Aerosil silicas activated at various temperatures.

A similar series of experiments were performed on Sylopol silicas. The same stoichiometry was obtained on all silicas at all activation temperatures. The results are summarized in Tables 3.4, 3.5 and 3.6. Thus on both kinds of silica, the amount of chemisorbed vanadium is equivalent to the initial concentration of accessible OH groups on the surface.

The density of silanol groups on Sylopol silicas that react with $VOCl_3$ is thus approximately 50% greater than that on the Aerosil silicas at the same dehydroxylation temperature (for example, the average OH density for Aerosil silicas treated at 200°C is 1.90 OH/nm^2, while for Sylopol silicas it is 2.80 OH/nm^2). However, the difference between the hydroxyl populations decreases as the activation temperature increases.

3.5 Temperature effect

Vanadium uptake by Aerosil and Sylopol silicas, which can be equated to the chemically reaqctive OH content according to eq. 3.2, is plotted as a function of dehydroxylation temperature in Figures 3.10 and 3.11, respectively. After the onset of dehydroxylation, there is a roughly linear decrease in the number of the reactive OH groups as the temperature is raised.

Table 3.1. VOX_3 (X = Cl, O^iPr) uptake by Aerosil 380 silica

Temperature	vanadium loading			HX	HX
°C[a]	wt%	mmol/g	V/nm^2	mmol/g[b]	mmol/g[c]
25	5.65	1.11	1.97	1.09	2.15
	6.07	1.19	2.10	1.25	2.45
	5.78	1.14	2.02		
	5.87	1.15	2.04		
	5.67	1.11	1.97	1.17[d]	2.22[d]
Average	5.80±0.18	1.14±0.03	2.02±0.05	1.17±0.08	2.27±0.16
100	5.83	1.14	2.02		
	5.94	1.16	2.05	1.14	2.25
	5.89	1.15	2.04		
Average	5.89±0.08	1.15±0.01	2.04±0.02	1.14	2.25
200	5.48	1.07	1.90	1.10	2.15
	5.27	1.04	1.84		
	5.64	1.10	1.95	1.08	2.22
	5.54	1.09	1.93		
Average	5.48±0.16	1.08±0.03	1.91±0.04	1.09±0.01	2.19±0.05
300	4.99	0.98	1.74	1.01	2.04
	5.04	0.99	1.75	0.98	2.00
	5.21	1.02	1.81		
	5.16	1.01	1.79		
Average	5.10±0.10	1.00±0.02	1.77±0.03	1.00±0.02	2.02±0.03
400	4.79	0.94	1.66	0.90	1.85
	4.41	0.87	1.54		
	4.67	0.92	1.63		
	4.56	0.89	1.58	0.87	1.80
Average	4.61±0.16	0.91±0.03	1.61±0.05	0.89±0.02	1.83±0.03

Table 3.1, continued

Temperature	vanadium loading			HX	HX
°C[a]	wt%	mmol/g	V/nm^2	mmol/g[b]	mmol/g[c]
500	4.38	0.86	1.52	0.84[d]	1.65[d]
	4.00	0.78	1.38		
	4.22	0.83	1.47		
	4.15	0.82	1.45		
	4.30	0.82	1.45	0.85	1.63
	4.05	0.80	1.42	0.82[d]	1.65[d]
	3.95	0.78	1.38	0.80[d]	1.65[d]
Average	4.15±0.16	0.81±0.03	1.43±0.05	0.83±0.02	1.65±0.01

[a] Temperature of thermal pretreatment of silica *in vacuo*. All reactions of silicas with VOX_3 were performed at room temperature.

[b] HX liberated during grafting $O{=}VX_3$ on silica. X = Cl, except where noted.

[c] HX liberated by hydrolysis of surface complexes. X = Cl, except where noted.

[d] HX is HO^{i}Pr.

Table 3.2. VOX_3 (X = Cl, O^iPr) uptake by Aerosil 300 silica

Temperature	vanadium loading			HX	HX
°C[a]	wt%	mmol/g	V/nm^2	mmol/g[b]	mmol/g[c]
25	5.55	1.08	2.05	1.05	2.13
	5.52	1.08	2.05	1.10	2.23
	5.56	1.09	2.06		
	5.44	1.07	2.03		
	5.59	1.10	2.08		
	5.58	1.09	2.06	1.06[d]	2.10[d]
Average	5.54±0.05	1.09±0.01	2.06±0.02	1.07±0.03	2.18±0.07
100	5.60	1.10	2.08	1.08	2.15
	5.53	1.09	2.06		
	5.48	1.08	2.04		
Average	5.54±0.06	1.09±0.01	2.06±0.02	1.08	2.15
200	5.06	0.99	1.87	0.98	2.00
	4.99	0.98	1.86		
Average	5.03±0.05	0.99±0.01	1.87±0.01	0.98	2.00
500	3.77	0.74	1.40		
	3.82	0.75	1.42		
	3.92	0.77	1.45		
Average	3.83±0.14	0.75±0.03	1.42±0.05		

[a] Temperature of thermal pretreatment of silica *in vacuo*. All reactions of silicas with VOX_3 were performed at room temperature.

[b] HX liberated during grafting $O{=}VX_3$ on silica. X = Cl, except where noted.

[c] HX liberated by hydrolysis of surface complexes. X = Cl, except where noted.

[d] HX is HO^iPr.

Table 3.3. $VOCl_3$ (X = Cl, O^{i}Pr) uptake by Aerosil 200 silica

Temperature	vanadium loading			HX	HX
°C[a]	wt%	mmol/g	V /nm^2	mmol/g[b]	mmol/g[c]
25	3.03	0.60	1.97	0.62	1.23
	2.84	0.56	1.84		
	3.10	0.60	1.97		
	2.93	0.57	1.87	0.60	1.20
Average	2.98±0.11	0.58±0.02	1.91±0.06	0.620.02	1.220.02
100	3.04	0.60	1.96	0.57	1.20
	2.89	0.57	1.87		
	2.93	0.58	1.89		
Average	2.95	0.58	1.91±0.14	0.57	1.20
200	3.27	0.64	2.11		
	3.06	0.60	1.97	0.60	1.18
	2.68	0.53	1.74		
	2.67	0.53	1.74	0.55	1.10
	2.87	0.57	1.88	0.56	1.12
	3.11	0.61	2.01	0.57[d]	1.20[d]
Average	2.88±0.21	0.57±0.04	1.91±0.11	0.57±0.02	1.15±0.05
500	2.35	0.46	1.51	0.45	0.94
	2.00	0.39	1.28	0.42	0.83
	2.20	0.43	1.42		
	2.29	0.45	1.48	0.43	0.86
	2.24	0.44	1.45		
	2.32	0.45	1.48	0.42[d]	0.80[d]
Average	2.23±0.13	0.44±0.03	1.44±0.08	0.43±0.01	0.86±0.06

[a] Temperature of thermal pretreatment of silica *in vacuo*. All reactions of silicas with VOX_3 were performed at room temperature.

[b] HX liberated during grafting $O{=}VX_3$ on silica. X = Cl, except where noted.

[c] HX liberated by hydrolysis of surface complexes. X = Cl, except where noted.

[d] HX is HO^{i}Pr.

Table 3.4. $VOCl_3$ uptake by Sylopol 952 silica

Temperature °C[a]	vanadium loading			HCl mmol/g[b]	HCl mmol/g[c]
	wt%	mmol/g	V/nm^2		
25	6.22	1.23	2.97	1.20	2.45
	6.28	1.24	3.10		
	6.55	1.29	3.12		
	6.38	1.26	3.05	1.23	2.50
Average	6.36±0.14	1.26±0.03	3.06±0.06	1.22±0.02	2.48±0.04
100	6.76	1.32	3.19	1.26	2.48
	6.45	1.27	3.07		
	6.22	1.22	2.95	1.27	2.50
	6.37	1.25	3.02		
Average	6.45±0.23	1.27±0.04	3.06±0.10	1.27±0.01	2.49±0.01
200	6.39	1.26	3.05	1.25	2.53
	6.19	1.22	2.95		
	6.50	1.28	3.10		
Average	6.36±0.16	1.25±0.03	3.03±0.07	1.25	2.53
300	5.30	1.04	2.52	1.05	2.12
	5.73	1.12	2.71		
	5.56	1.10	2.66		
Average	5.53±0.22	1.09±0.04	2.63±0.10	1.05	2.12
400	4.62	0.91	2.20	0.92	1.85
	4.44	0.87	2.10		
	4.77	0.93	2.25		
Average	4.61±0.13	0.90±0.02	2.18±0.07	0.92	1.85
500	3.60	0.71	1.72	0.73	1.45
	3.88	0.76	1.84		
	3.73	0.73	1.77		
	3.21	0.63	1.52		
Average	3.61±0.29	0.71±0.06	1.71±0.13	0.73	1.45

[a] Temperature of thermal pretreatment of silica *in·vacuo*. All reactions of silicas with $VOCl_3$ were performed at room temperature.

[b] HCl liberated during grafting.

[c] HCl liberated by hydrolysis of surface complexes.

Table 3.5. VOX_3 (X = Cl, O^iPr) uptake by Sylopol 952X1836 silica

Temperature	vanadium loading			HX	HX
°C[a]	wt%	mmol/g	V/nm^2	mmol/g[b]	mmol/g[c]
25	5.68	1.12	2.61	1.15	2.28
	5.88	1.16	2.71		
	5.90	1.16	2.71		
Average	5.82	1.15±0.02	2.68±0.05	1.15	2.28
	5.86	1.15	2.68	1.14	2.43
	5.65	1.11	2.59		
	6.01	1.18	2.765		
Average	5.84	1.15±0.04	2.68±0.08	1.14	2.43
200	6.17	1.21	2.82	1.20	2.43
	6.17	1.21	2.82	1.08	2.15
	5.40	1.06	2.47	1.10[d]	2.30[d]
	5.69	1.12	2.61		
	5.74	1.13	2.64		
Average	5.83±0.33	1.15±0.06	2.67±0.15	1.13±0.06	2.29±0.14
500	4.20	0.82	1.91	0.81	1.58
	4.16	0.82	1.91		
	4.10	0.81	1.89	0.82	1.64
	4.11	0.81	1.89		
Average	4.14±0.05	0.82±0.01	1.90±0.01	0.82±0.01	1.61±0.04

[a] Temperature of thermal pretreatment of silica *in vacuo*. All reactions of silicas with VOX_3 were performed at room temperature.

[b] HX liberated during grafting $O{=}VX_3$ on silica. X = Cl, except where noted.

[c] HX liberated by hydrolysis of surface complexes. X = Cl, except where noted.

[d] HX is HO^iPr.

Table 3.6. $VOCl_3$ uptake by Sylopol 948 silica

Temperature	vanadium loading		
°C[a]	wt%	mmol/g	V/nm^2
25	6.32	1.24	2.81
100	6.19	1.22	2.76
	6.23	1.22	2.78
Average	6.21±0.03	1.21±0.01	2.77±0.01
200	6.37	1.25	2.84
	6.02	1.18	2.67
Average	6.20±0.25	1.22±0.05	2.76±0.11
300	5.52	1.08	2.46
400	4.98	0.98	2.22
	4.90	0.96	2.19
Average	4.94±0.06	0.97±0.01	2.20±0.03
500	3.62	0.71	1.62
	3.65	0.72	1.63
	3.82	0.75	1.71
	3.73	0.73	1.67
	4.33	0.85	1.93
	4.05	0.80	1.81
	4.16	0.82	1.86
	4.44	0.87	1.98
Average	3.98±0.31	0.78±0.06	1.78±0.14

[a] Temperature of thermal pretreatment of silica *in vacuo*. All reactions of silicas with $VOCl_3$ were performed at room temperature.

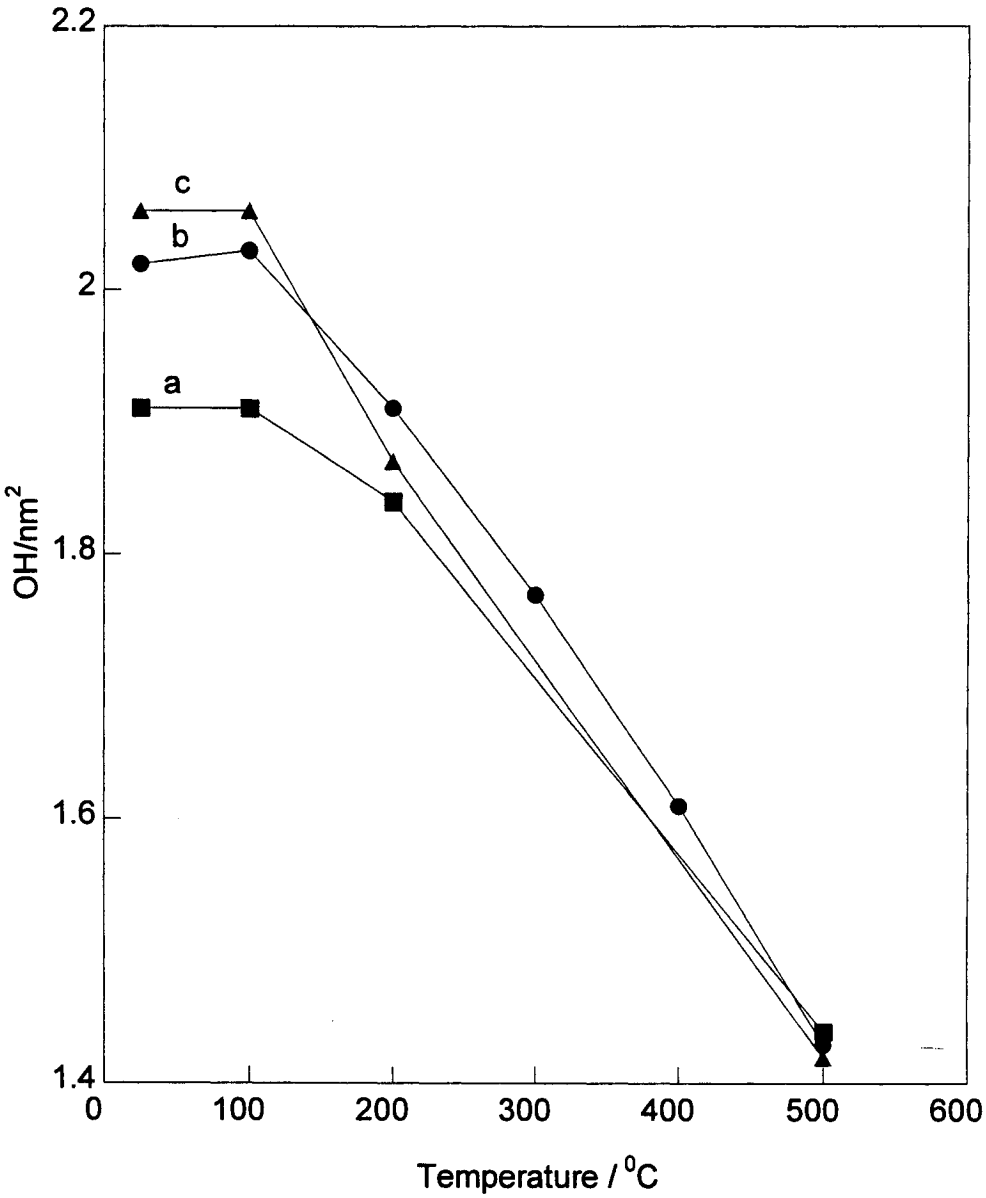

Figure 3.10. OH content of Aerosil silicas as a function of dehydroxylation temperature; (a) A200, (b) A380, and (c) A300.

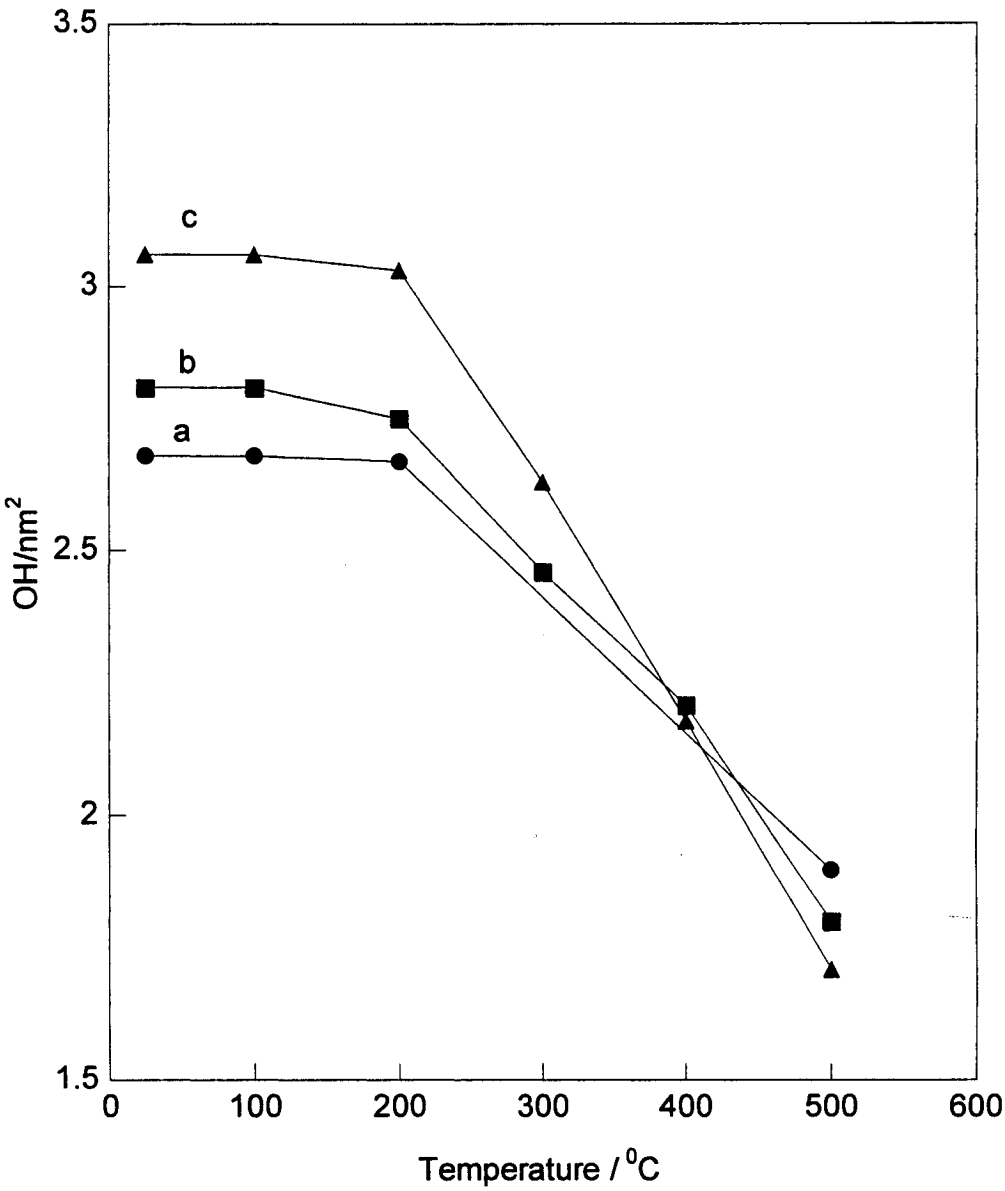

Figure 3.11. OH content of Sylopol silicas as a function of dehydroxylation temperature; (a) S952X1836, (b) S948, and (c) S952.

Dehydroxylation starts at 100°C for Aerosil silicas and at 200°C for Sylopol silicas. This difference may result from the different silanol group populations of the two types of silicas. From Figures 3.1 and 3.2, it is apparent that Sylopol silicas have a higher proportion of hydrogen-bonded hydroxyl groups. Since the energy required to break up the hydrogen-bonded network is greater than that required to cause condensation of neighbouring but not hydrogen-bonded silanols, the onset of Sylopol dehydroxylation is expected to be at a higher temperature.[50]

3.6 Surface area effect

The hydroxyl density on Aerosil silicas is plotted as a function of surface area in Figure 3.12. The OH density on fumed silicas is roughly independent of surface area, consistent with previous studies.[40]

3.7 Comparison of "as-received" and rehydrated silicas

Rehydrated silicas were prepared by placing 2-3 grams silica in a glass vial. The vial was filled with distilled deionized water, and the resulting silica suspension was allowed to stand at ambient temperature for few days. The excess water was removed to a liquid N_2 trap under vacuum at room temperature.

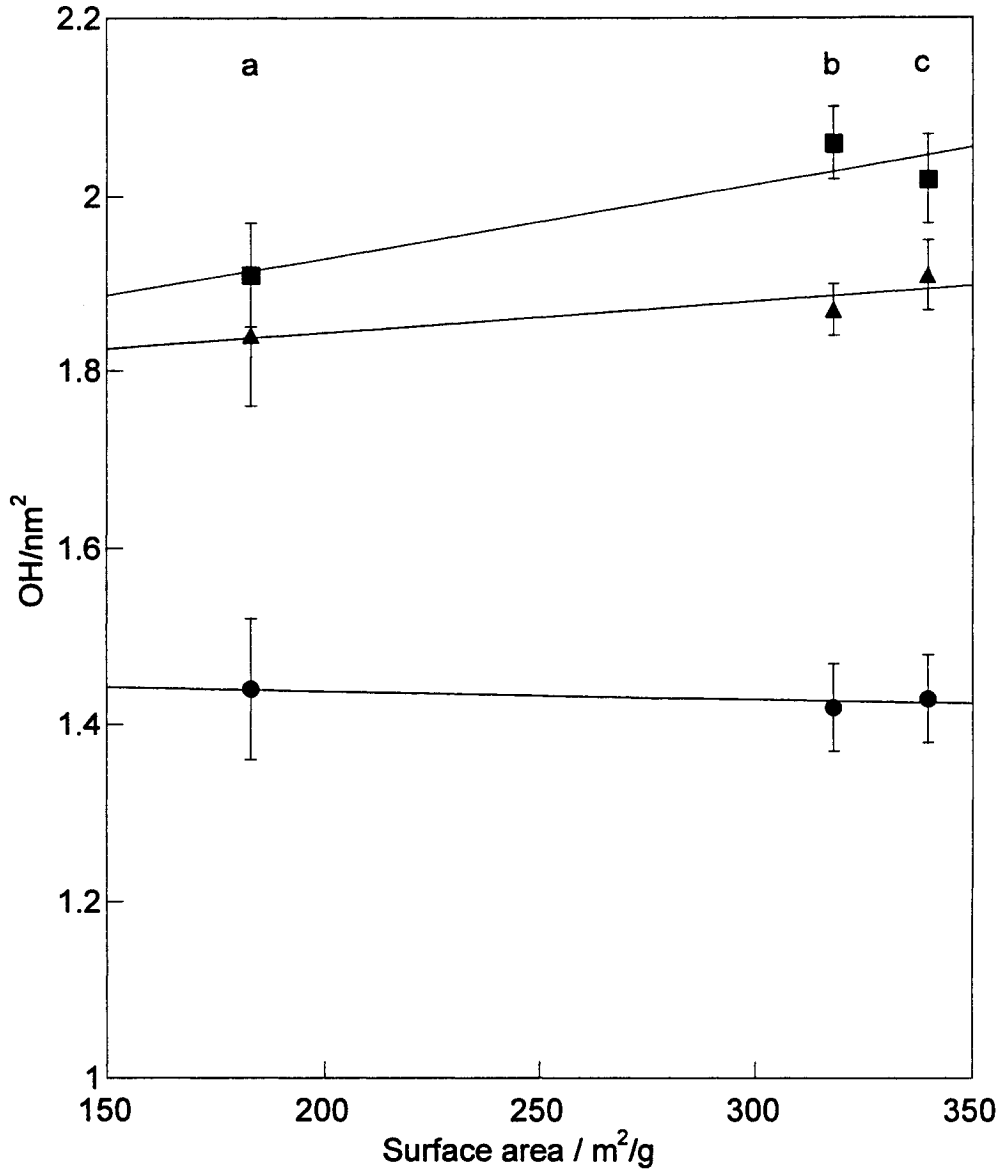

Figure 3.12 OH content of Aerosil silicas partially dehydroxylated at 500°C (●), 200°C (▲), and 25°C (■), as a function of the surface areas of (a) A200, (b) A300, and (c) A380.

Infrared spectra of a self-supporting disk of rehydrated A200, Figure 3.13, and rehydrated Sylopol 952 (not shown), have the same features as the "as-received" silicas in the OH region. However, the intensity of the sharp band due to isolated silanols is less intense while the broad band due to hydrogen-bonded hydroxyl groups is more prominent than in the "as-received" silicas at the lower dehydroxylation temperatures. Consistent with that, vanadium analyses for rehydrated A200 and S952, tabulated in Table 3.7 and depicted in Figures 3.14 and 3.15, reflect their higher OH contents compared to the "as-received" silicas.

These results clearly indicate that there is an increase in the total number of surface silanols upon exposure of silica to water. This is attributed to a cleavage of siloxane bonds, eq. 3.3.[41]

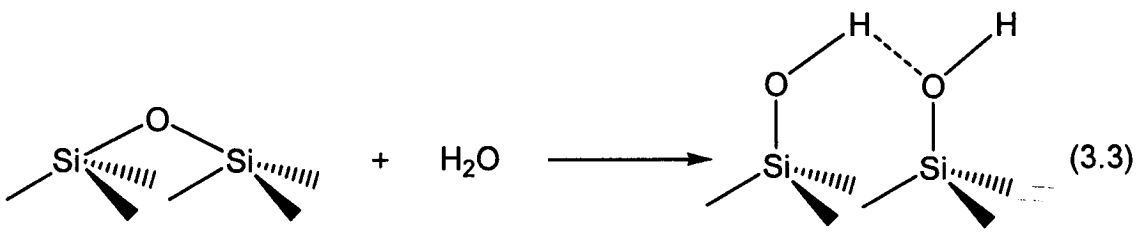

(3.3)

The increased surface silanol density results in greater numbers of silanols that are close enough for hydrogen bond formation. For "as-received" A200 silica, the total silanol density of 1.91 OH/nm^2 is too low for formation of many intramolecular hydrogen bonds, and the hydrogen-bonds are primarily intermolecular, *i.e.*, between primary particles. In the case of rehydrated A200, the greater silanol density of 3.22 OH/nm^2 increases the possibility of intramolecular hydrogen bond formation.

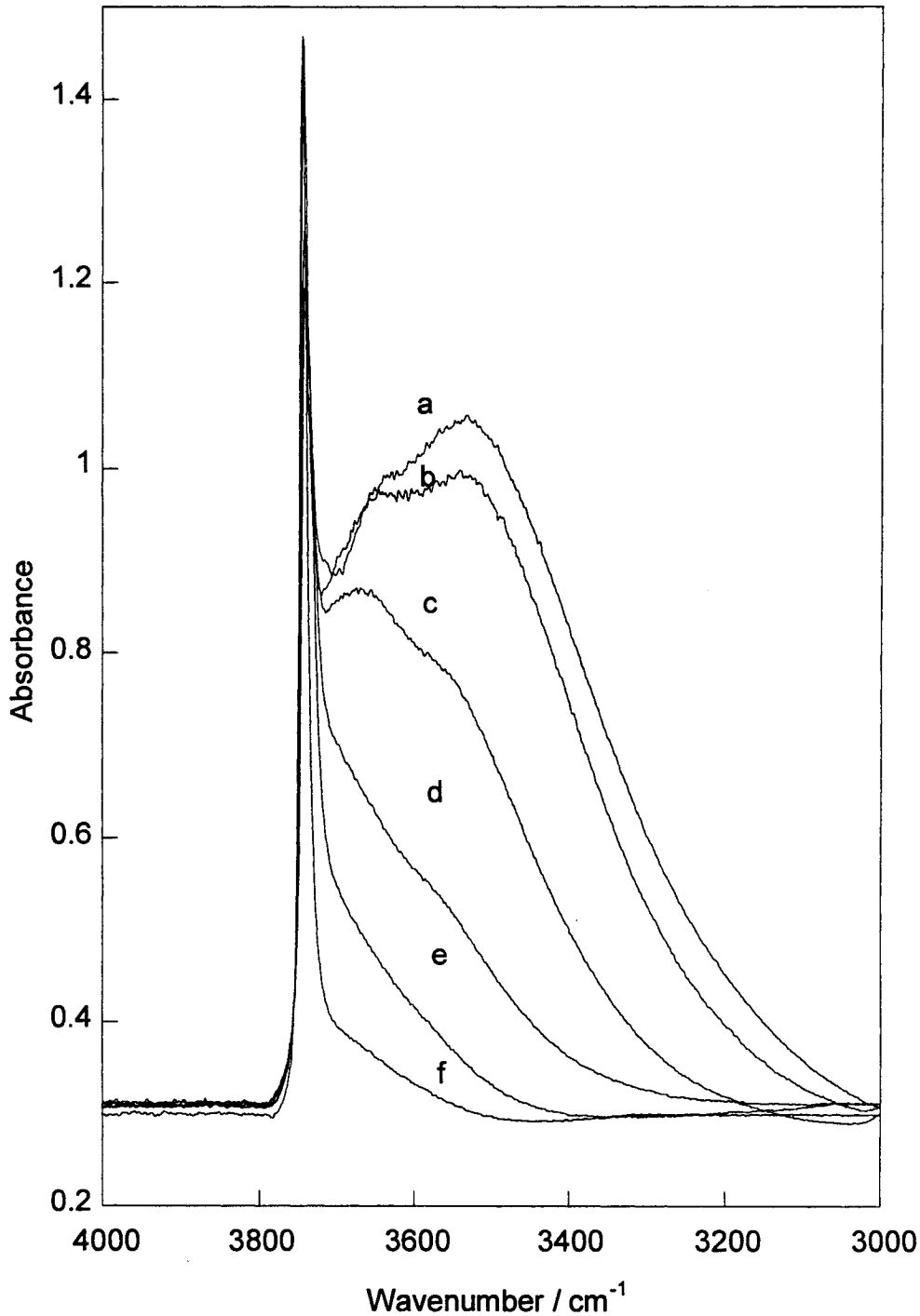

Figure 3.13. Infrared spectra of a self-supporting disk of rehydrated Aerosil-200 progressively dehydroxylated at: (a) 25, (b) 100, (c) 200, (d) 300, (e) 400, and (f) 500°C.

Table 3.7. Vanadium uptake of rehydrated silicas

Silica	Temperature	vanadium loading		
	°C[a]	wt%	mmol/g	V/nm^2
S952	25	7.65	1.53	3.70
		7.84	1.54	3.72
		7.69	1.51	3.65
	Average	6.61±0.07	1.31±0.02	3.69±0.04
	200	6.53	1.31	3.18
		6.72	1.33	3.20
		6.57	1.29	3.13
	Average	6.61±0.07	1.31±0.02	3.17±0.04
	500	3.70	0.73	1.76
		3.30	0.65	1.57
		3.46	0.68	1.64
	Average	3.49±0.20	0.68±0.04	1.66±0.10
A200	25	4.99	0.98	3.23
		4.94	0.97	3.19
	Average	4.97±0.04	0.97±0.01	3.22±0.02
	200	3.99	0.78	2.57
		4.30	0.84	2.76
		4.21	0.83	2.73
		4.17	0.82	2.70
	Average	4.17±0.13	0.82±0.02	2.70±0.09
	500	2.20	0.43	1.42
		2.25	0.44	1.45
		2.14	0.42	1.38
	Average	2.20±0.06	0.43±0.01	1.4±20.05

[a] Temperature of thermal pretreatment of silica *in vacuo*. All reactions of silicas with $VOCl_3$ were performed at room temperature.

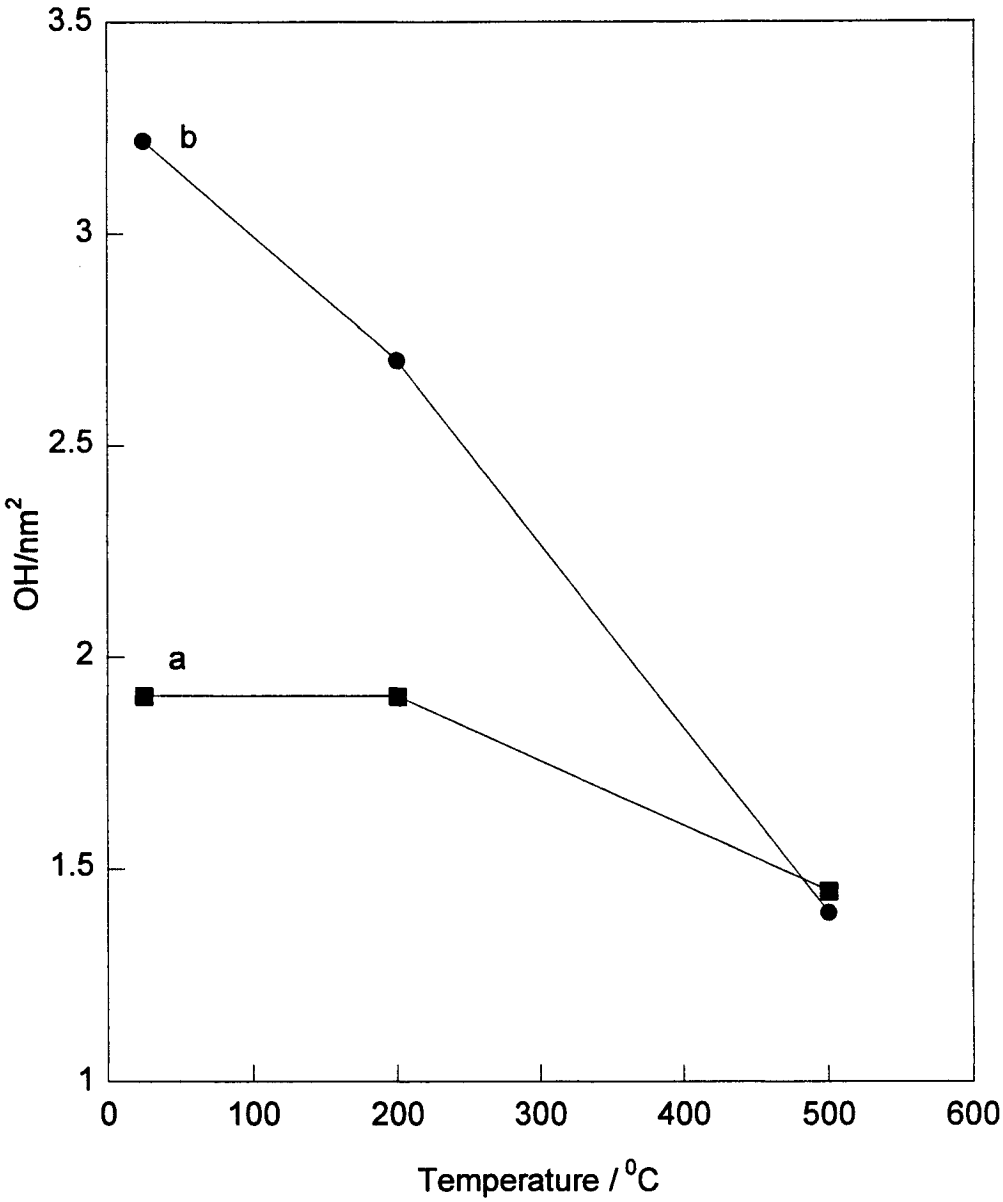

Figure 3.14. OH content as a function of dehydroxylation temperature, for (a) as-received, and (b) rehydrated A200.

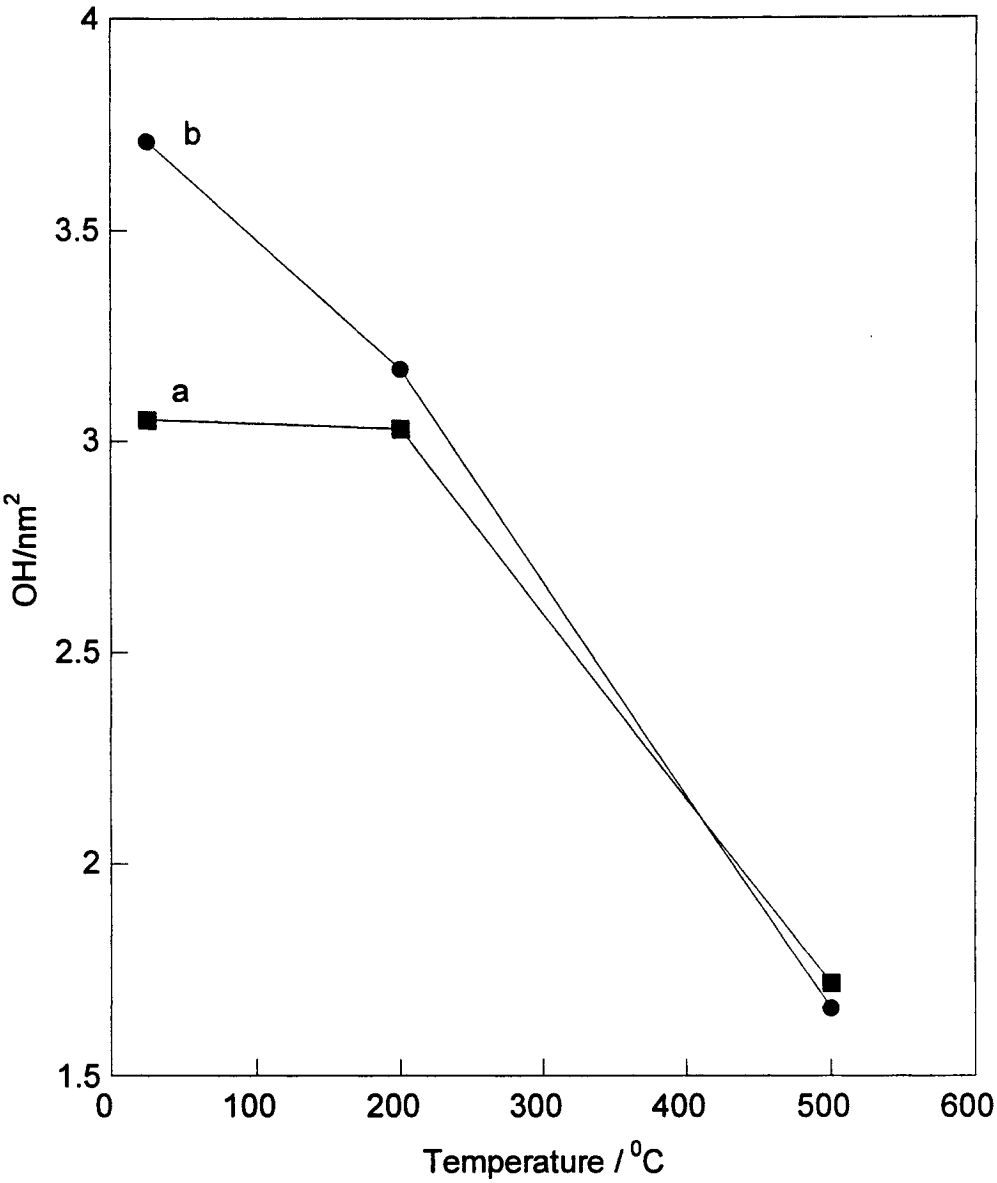

Figure 3.15. OH content as a function of dehydroxylation temperature, for (a) as-received, and (b) rehydrated S952.

At higher temperatures, the infrared spectra and OH contents of both rehydrated and "as-received" silicas are similar, due to complete removal of hydrogen-bonded hydroxyl groups by condensation and the presence of only isolated silanol groups.

3.8 Grafting of vanadium complexes from solution

When VOX_3 is grafted by vapour deposition, A380-200 silica takes up 1.08 mmol V/g silica. When the same silica was stirred with a solution of VOX_3, elemental analysis of the material after prolonged desorption of the solvent and other volatiles to a liquid N_2 trap revealed the presence of only ca. 0.20 mmol V/g silica. The results are tabulated in Table 3.8 for solution grafting from toluene, diethyl ether and THF. They indicate that the reactive hydroxyl groups react completely with VOX_3 only in the absence of the solvent.

Solvents with donor heteroatoms, such as ethers, interact directly with $VOCl_3$, either via simple coordination or by displacement of one or more chloride ligands.[53] Such modified vanadium complexes may be inactive towards silanols. However, this explanation does not account for our observation of the same phenomenon in toluene. Instead, we propose that the reaction is effectively an equilibrium process, eq 3.4:

$$\equiv SiOH + VOCl_3 \leftrightarrows \equiv SiOVOCl_2 + HCl \qquad (3.4)$$

Table 3.8 Vanadium uptake of A380 dehydroxylated at 200°C

Reagent	Solvent	vanadium uptake		
		wt%	mmol/g	V/nm^2
$VOCl_3$	toluene[a]	1.08	0.22	0.66
		0.88	0.18	0.54
	diethylether[a]	1.29	0.26	0.78
		1.20	0.24	0.72
	None[b]	5.46	1.08	1.91
$VO(O^iPr)_3$	THF[a]	1.19	0.24	0.72
		1.29	0.25	0.75
	toluene[a]	0.97	0.19	0.57
		1.03	0.20	0.60
	None[b]	5.40	1.06	1.88

[a] Solution grafting.

[b] Chemical vapour deposition.

In toluene, which solvates polar molecules like HCl poorly, the equilibrium lies to the left. However, in the reaction of adsorbed $VOCl_3$ in the absence of solvent, liberation of HCl into the gas phase provides an entropic driving force which shifts the equilibrium to the right.

3.9 Discussion

Using thermogravimetric analysis, de Boer and Vleeskens found that the maximum number of hydroxyl groups on fully hydrated silica surfaces is 4.6 OH/nm^2.[34, 51] They concluded that the fully annealed and rehydrated surface of amorphous silicas closely resemble the rhombohedral face of β-tridymite, in which hydroxyl groups exist in hexagonal arrays separated by 5 Å. These hydroxyls, which cannot hydrogen-bond to each other, have a density of 4.55 OH/nm^2.

Peri and Hensley described the surface of untreated silica as a combination of two models.[16] The (001) face of β-tridymite contains approximately 1.50 isolated hydroxyl groups per nm^2 and 3-3.5 hydrogen-bonded hydroxyl groups per nm^2. The second model is the (100) face of β-cristobalite, on which each silicon atom is connected to two (geminal) hydroxyl groups, with a total concentration of 7.9 OH/nm^2.

Using chemical reactions of $SiMe_2Cl_2$, $TiCl_4$ and BCl_3 with surface hydroxyl groups followed by Cl analysis of the solid, Armistead[34] showed that the fully hydroxylated Aerosil surface at room temperature has (1.4±0.1) isolated hydroxyl

groups per nm^2 and (3.2±0.1) paired hydroxyl groups per nm^2. By heating *in vacuo* at 500°C, all the paired hydroxyl groups are eliminated leaving only isolated hydroxyl on the surface. Our measured hydroxyl density of 1.45 OH/nm^2 for Aerosil silicas at 500°C is very close to previous results, but at ambient temperatures, it is very different. This inconsistency may be due to differences in the pre-treatment of the silica.

Zhuravlev[11] found, by deuterium-exchange experiments on more than one hundred samples of amorphous silicas, with specific surface areas from 9.5-950 m^2/g, a mean hydroxyl concentration between 4.6 and 5.0 OH/nm^2. This value is independent of the origin of the silica, structural characteristics such as surface area, and the type and size distribution of pores. It is only for fully hydroxylated silicas. However, we have shown that silicas of different origin undergo very different dehydroxylation processes. Decreasing hydroxyl group concentration was observed upon increasing the temperature of dehydroxylation, in agreement with our results.

Using multivariate calibration of diffuse reflectance infrared fourier transform spectroscopy (DRIFTS) with thermogravimetry, Peussa et *al.* reported that total hydroxyl concentrations for A200-550 and A200-105 are 1.20 and 4.40 OH/nm^2, respectively.[52] The latter number is for the fully hydroxylated silica and represents the total hydroxyl content, including those which are inaccessible in grafting reactions.

Our reported hydroxyl contents of 2.04, 2.06 and 1.91 OH/nm^2 for A380-100, A300-100 and A200-100, respectively, are close to those reported by Mathias *et al.*[41] They cited hydroxyl group densities of "as-received" A380, A300 and A200 are 2.5, 2.08 and 2.4 OH/nm^2 using the $LiAlH_4$ method and H-D exchange. Wang *et al.* reported that the hydroxyl density for "as received" A380 is 2.70 OH/nm^2 by gravimetric analysis.[50]

The surface coverage of 2.06 OH/nm^2 obtained on Aerosil silicas at 200°C is in good agreement with that obtained by Morrow and McFarlan.[29] They determined that 95% of surface hydroxyls exchange with D_2O and (64-76)% react with hydrogen sequestering agents (64% $TiCl_4$, 74% $AlMe_3$, 69% BCl_3 and 47% $ZnMe_2$). The size of $VOCl_3$ is similar to these reagents, and 70% of the total SiOH content is approximately 2.1 OH/nm^2, which is close to our measured value.

Morrow *et al.* also reported that the total OH group density of precipitated silica is 6.8 OH/nm^2, using a thermogravimetric method.[29] They determined that 95% of the ≡SiOH exchange with D_2O at 150°C, while ca. 35% react with each of $TiCl_4$, $AlMe_3$, BCl_3 and $ZnMe_2$, *i.e.*, 2.3 OH/nm^2 silica are accessible to chemical titrating agents. Our average value for Sylopol silicas at 200°C, 2.8 OH/nm^2, is in a good agreement with those results.

Haukka and Rott[44] reported 2.0-2.1 OH/nm^2 while Morrow and McFarlan[29] determined 1.63 OH/nm^2 for 450°C-treated precipitated silica. Our results for precipitated silicas treated at 500°C indicate the presence of 1.72 and 1.68 OH/nm^2 for S952 and S948, respectively, consistent with the value reported by

Morrow, while for S952X1836, 1.92 OH/nm^2 is in a good agreement with that reported by Haukka. Differences in published numbers of accessible OH groups could be due to the different silicas used.

3.10 Conclusion

$VOCl_3$ chemisorption has been used to measure the number of reactive hydroxyls on various fumed and precipitated silicas before and after thermal treatment. Our findings can be summarized as follows:

- vanadyl chloride reacts completely with free hydroxyl groups and partially with H-bonded hydroxyl groups;
- the amount of chemisorbed vanadium (number of reactive hydroxyl groups on the silica surface) decreases as the dehydroxylation temperature increases;
- there is no significant effect of surface area on the accessible hydroxyl group density.
- porous Sylopol silicas have higher hydroxyl densities than non-porous Aerosil silicas at the same temperature;
- the number of silanol groups which are unreacted to $VOCl_3$ is greater on porous Sylopol silicas than on fumed silica;
- grafting of VOX_3 (X = Cl, O^iPr) from solution results in incomplete reaction of the hydroxyls.

3.11 References

1) Fripiat, J. J.; Uytterhoeven, J. *J. Phys. Chem.* **1962**, *66*, 800-805.

2) Iler, R.,"The Chemistry of Silica", Wiley: New York, **1978**, p. 258.

3) Unger, K. K.,"Porous Silica", Elsevier: Amsterdam, **1979**, p. 76.

4) Grote, R. *Catal. Lett.* **1999**, *62*, 1-13.

5) De Ganw, F. J. M.; Van Santen, R. A. *Stud. Surf. Sci. Catal.* **2000**, *130A,* 127-135.

6) Fink, G.; Steenmetz, B.; Zechlin, J.; Przybyla, C.; Tesche, B. *Chem. Rev.* **2000**, *100*, 1377-1390.

7) Hlatky, G. G. *Chem. Rev.* **2000**, *100*, 1347-1376.

8) McCarthy, D. W.; Mark, I. E.; Schaefer, D. W. *J. Polym. Sci., B: Polym. Phys.* **1998**, *36*, 1167-1189.

9) Choi, S. S. *J. Appl. Polym. Sci.* **2001**, *79*, 1127-1123.

10) Yoshinaga, K.; Yoshida, H.; Yamamoto, Y.; Takakura, K.; Komatsu, M. *J. Coll. Interf. Sci.* **1992**, *153*, 207-211.

11) Zhuravlev, L. T. *Langmuir* **1987**, *3*, 316-318.

12) Ishikawa, T.; Matsuda, M.; Yasukawa, A.; Kandori, K.; Inagaki, S.; Fukushima, T.; Kondo, S. *J. Chem. Soc., Faraday Trans.*, **1996, *92*, 1985-1989.

13) Davydov, V. Ya.; Kiselev, V. A.; Zhuravlev, V. A. *Trans. Faraday Soc.***1964, *60*, 2254-2264.

14) Sindorf, W. D.; Maciel, E. G. *J. Am. Chem. Soc.* **1983**, *105*, 1487-1493.

15) Curthoys, G.; Davydov, V. Ya.; Kiselev, V. A.; Kiselev, S. A.; Kuznetsov, B. V. *J. Coll. Interf. Sci.* **1974**, *48*, 58-72.

16) Peri, B. J.; Hensley, L. A. *J. Phys. Chem.* **1968,** *72*, 2926-2933.

17) Gillis-D'Hamers, I.; Cornelissens, I.; Van der Voort, P.; Vrancken, C. K.; Vansant, F. E.; Dealemans, *J. Chem. Soc., Faraday Trans.* **1992**, *88,* 723-727.

18) Sindorf, W. D.; Maciel, E. G. *J. Phys. Chem.* **1983**, *87*, 5516-5521.

19) Van Der Voort, P.; Gillis-D'Hamers, I.; Vansant, F. E. *J. Chem. Soc., Faraday Trans.* **1990**, *86*, 3751-3755.

20) Lochmuller, H. C.; Hersey, T. M. *Langmuir*, **1988,** *4*, 572-578.

21) Van Der Voort, P.; Gillis-D'Hamers, I.; Vrancken, K. C.; Vansant, F. E. *J. Chem. Soc. Faraday Trans.* **1991**, *87*, 3899-3905.

22) Davydov, V. Y.; Kiselev, A. V.; Lokutsievskii, V. A.; Lygin, V. I. *Russ. J. Phys. Chem.* **1974**, *48*, 1342.

23) Panasyuk, G. P., Budova, G. P., Lazarev, V. B. *J. Thermal Anal.* **1979**, *16*, 441-448.

24) Franklin, K. R.; Lowe, B. M. *Thermochim. Acta*, **1988**, *127*, 319-327.

25) Huhn, H. J. *J. Thermal Anal.* **1988**, *33*, 851-856.

26) De Farias, R. F.; Airoldi, C. *J. Thermal Anal.* **1998**, *53*, 751-756.

27) Kunawicz, J.; Jones, P.; Hockey, J. A. *Trans. Faraday Soc.* **1971**, *67*, 848-853.

28) Morrow, B. A.; Hardin, A. H. *J. Phys. Chem.* **1979**, *83*, 3135-3141.

29) Morrow, B. A.; McFarlan, A. J.; *Langmuir* **1991**, *7*, 1695-1701.

30) Sato, M.; Kanbayashi, T.; Shima, Y. *J. Catal.* **1967**, *7*, 342-351.

31) Peglar, R. J.; Murray, J.; Hambleton, F. H.; Sharp, M. J.; Parker, A. J.; Hockey, J. A. *J. Chem. Soc. A.* **1970**, 2170-2172.

32) Low, M. J. D.; Severdia, A. G.; Chan, J. *J. Catal.* **1981**, *69*, 384-391.

33) Yates, D. J. C.; Dembinski, G. W.; Kroll, W. R.; Elliott, J. J. *J. Phys. Chem.* **1969**, *73*, 911-921.

34) Armistead, C. G.; Tyler, A. J.; Hambleton, F. H.; Mitchell, S. A.; Hockey, J. A. *J. Phys. Chem.* **1969**, *73*, 3947-3953.

35) Morrow, B. A.; McFarlan, A. J. *J. Non-Cryst. Solids* **1990**, *120*, 61-71.

36) Kinney, J. B.; Staley, R. H. *J. Phys. Chem.* **1983**, *87*, 3735-3740.

37) Morrow, B. A. *Stud. Surf. Sci. Catal.* **1990**, *57A*, 161-224.

38) Bunker, B. C.; Haaland, D. M.; Ward, K. J.; Michalske, T. A.; Smith, W. L.; Binkley, J. S.; Melius, C. F.; Balfe, C. A. *Surf. Sci.* **1989,** *210*, 406-428.

39) Bunker, B. C.; Haaland, D. M.; Michalske, T. A.; Smith, W. L. *Surf. Sci.* **1989,** *222*, 95-118.

40) Fripiate, J. J.; Gastuche, M. C.; Brichard, R. *J. Phys. Chem.* **1962**, *66*, 805-812.

41) Mathias, J.; Wannemacher, G. *J. Coll. Interf. Sci.* **1988**, *125*, 61-68.

42) Haukka, S.; Lakomaa, E. L.; Root, A. *J. Phys. Chem.*, **1993**, *97*, 5085-5094.

43) Burneau, A.; Barres, O.; Gallas, J. P.; Lavalley, J. C. *Langmuir* **1990**, *6,* 1364-1372.

44) Haukka, S.; Root, A. *J. Phys. Chem.*, **1994**, *98*, 1695-1703.

45) Fierro, J. L. G. *Stud. Surf. Sci. Catal.* Elsevier: Amsterdam, **1990**; *57B*, 1-66.

46) Rice, G. L.; Scott, S. L. *Langmuir* **1997,** *13*, 1545-1551.

47) Hambleton, F. H.; Hockey, J. A.; Taylor, I. A. G. *Trans. Faraday. Soc.* **1966,** *62*, 801-807.

48) Hambleton, F. H.; Hockey, J. A.; Taylor, I. A. G. *Nature* **1965**, *208*, 138-139.

49) Tyler, A. J.; Hambleton, F. H.; Hockey, J. A. *J. Catal.* **1969**, *13*, 35-42.

50) Wang, R.; Wunder, S. L. *Langmuir*, **2000**, *16*, 5008-5016.

51) de Boer, J. H.; Hermans, M. E. A.; Vleeskens, J. M.; *Koninkl. Ned, Akad. Westenschap., Proc. Ser.* **1957**, *60B*, 45-53.

52) Peussa, M.; Härkönen, S.; Puputti, J.; Niinisto, L.; *J. Chemometrics,* **2000,** *14,* 501-512.

53) Carola, W.; Dieter, R. *Inorganica Chimica Acta,* **1986**, *120,* 15-20.

Chapter Four

X-ray Absorption Spectroscopy of Silica-supported Vanadyl Chloride

4.1 Introduction

The importance of vanadium-containing silicates as catalysts for the selective oxidation of hydrocarbons[1] and for the selective reduction of NO_x by NH_3[2,3] has stimulated widespread investigation of their synthesis and characterization. Preparation of these materials either by chemical vapor deposition or wetness impregnation is effective in producing a specific concentration of vanadium centers in both micro- and mesoporous materials. Several groups have reported that a mono-oxo pseudotetrahedral site, $(\equiv SiO)_3V{=}O$, is the predominant species in silica-supported materials.[4-8] Results from IR, ^{51}V MAS NMR and elemental analysis allowed Rice *et al.*[9] and Kijenski *et al.*[10] to propose that compounds of the form VOX_3 (X; Cl, O^{i}Pr, OC_4H_9) react directly with the OH groups of the silica to form $\equiv SiOVOX_2$. In contrast, Inumaru *et al.*[11] proposed that chemical vapor deposition of $VO(OC_2H_5)_3$ on silica gives a mixture of two sites: $\equiv SiOVO(OC_2H_5)_2$ and $(\equiv SiO)_2VO(OC_2H_5)$. The models proposed for silica-supported vanadium catalysts are depicted in Figure 4.1.

Most spectroscopic characterization techniques give only indirect information about the local structure around the vanadium center. In order to obtain structural information, we undertook a study of one such system by X-ray absorption spectroscopy (XAS). This technique has been used successfully by

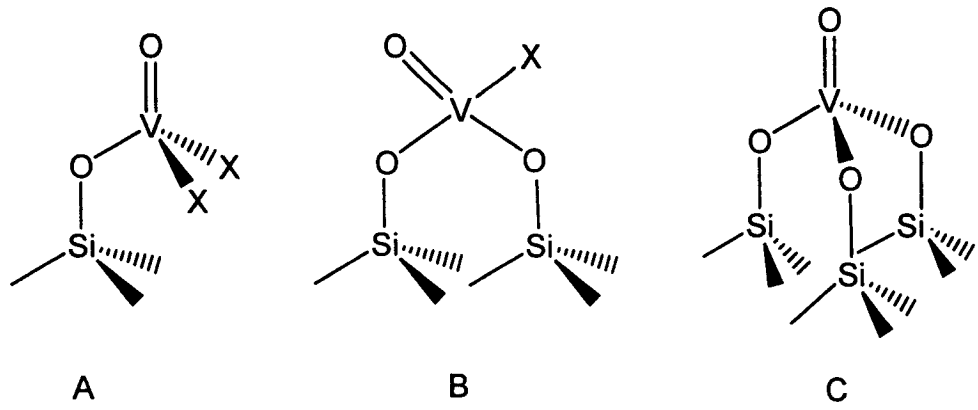

Figure 4.1. Proposed structures of isolated vanadium(V) sites on silica.

several groups to determine the local structure of the active metal center in heterogeneous catalysts,[12-20] since XAS is atom-specific.

In this chapter, both Extended X-ray Absorption Fine Structure (EXAFS) and X-ray Absorption Near-edge Structure (XANES) regions of the vanadium X-ray absorption spectrum are reported and analyzed for a silica-supported vanadium complex prepared, as described in the previous chapter, by chemical vapor deposition of $VOCl_3$ on porous and nonporous silicas pretreated at various temperatures.

4.2 X-ray absorption near-edge structure

Normalized V K-edge XANES spectra of vanadium-modified A200-200, A200-500, S952X-200 and S952X-500 are shown in Figure 4.2. The XANES regions for all four samples are virtually superimposable. The appearance of three pre-edge features in each spectrum

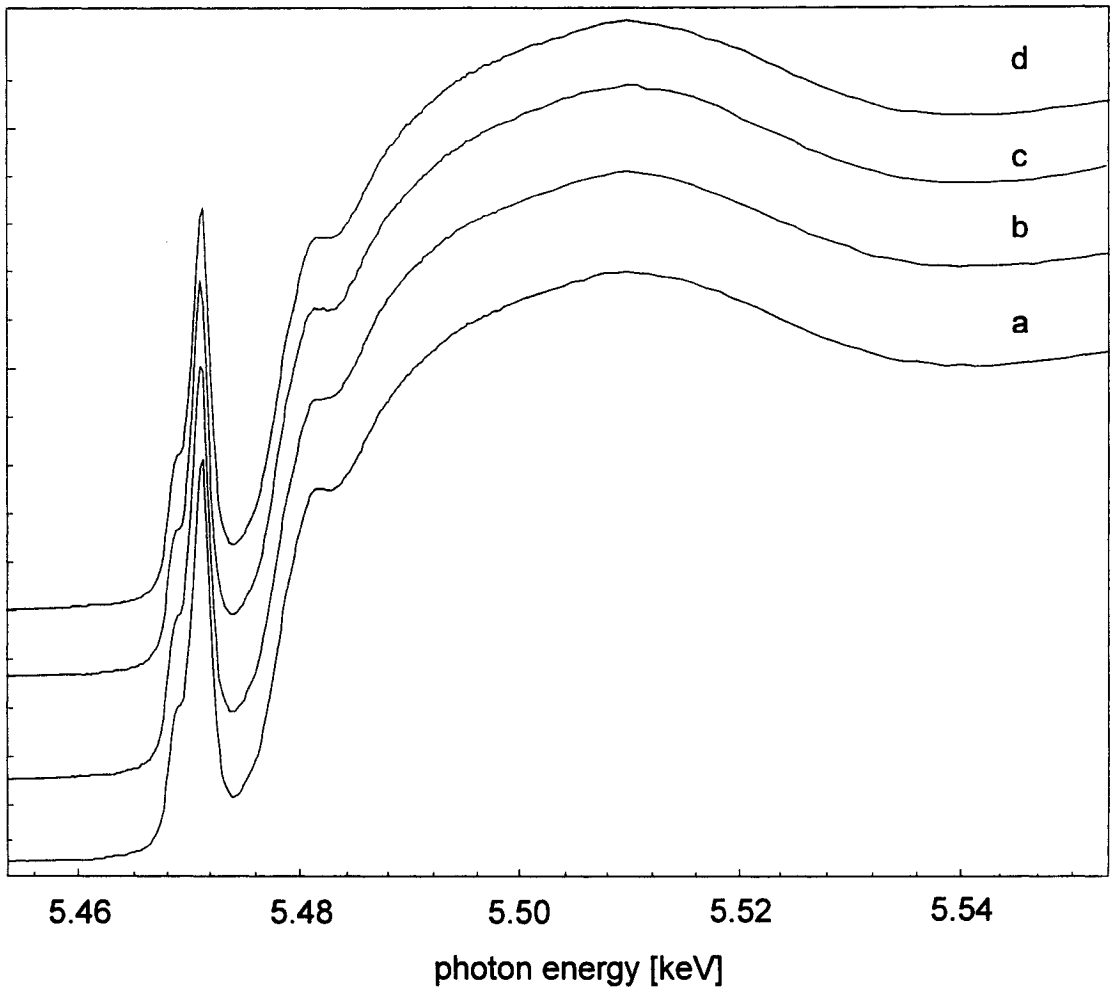

Figure 4.2. V K-edge XANES spectra of $VOCl_3$ grafted onto (a) A200-500; (b) A200-200; (c) S952X-200, (d) S952X-500. Y axis should read "norm. absorption".

suggests that the electronic structure of the photoabsorber is very similar in each case. The intensities of the pre-edge features suggest strongly dipole-allowed electronic transitions in a non-centrosymmetric envrironment.[21] In the case of vanadium, the intensity is increased by distortion to lower symmetry and 3d-4p mixing with overlap of a 3d orbital with ligand 2p orbitals (especially in compounds having V=O bonds).[17]

Pre-edge intensity is related to photoabsorber concentration, which is slightly different for each sample due to variations in metal loadings on the different supports. For comparison purposes, each XAS spectrum was normalized to the midpoint of its EXAFS oscillations. The samples exhibited pre-edge intensities of 0.66-0.69. Values of 0.76 and 0.62 were reported for NH_4VO_3 (tetrahedral structure) and V_2O_5 (distorted square pyramidal), respectively, Table 4.1. Therefore it seems likely that grafted vanadyl chloride is pseudo-tetrahedral, as expected for $\equiv SiOVOCl_2$.

Figure 4.3 shows the XANES region expanded and its first derivative for vanadium-modified S952-500. The pre-edge features at 2.4 eV (a) and 4.8 eV (b) are assigned to the $1s \rightarrow E$ and $1s \rightarrow T_2$ transitions, respectively. The weak pre-edge shoulder (a) has also been observed by Wong et *al.*[14] and Gao[18] et *al.* for several V_xO_y species lacking inversion centers. In tetrahedral symmetry, the d orbitals split into E and T_2 levels and both transitions $1s \rightarrow E$ and $1s \rightarrow T_2$ are allowed. By measuring the energy difference between the two transitions, the crystal field splitting of the excited state is estimated to be 2.3 eV.

Table 4.1. Relative energies and intensities of features in V K-edge XANES spectra

Sample	Threshold (a) (eV)	Pre-edge (b) (eV)	Pre-edge intensity	K edge (c) (eV)	Reference
V foil	n/a	n/a	n/a	0[a]	
V/A200-200	2.4	4.8	0.66	13.2	this work
V/A200-500	2.5	4.9	0.67	13.1	this work
V/S952X-200	2.5	4.9	0.67	12.8	this work
V/S952X-500	2.5	4.9	0.69	12.9	this work
V/S952X-200 (decomposed)	0.01	1.9	0.53	15.9	this work
V_2O_5	4.8	5.6	n/a	15.1	14
	n/a	6.1	0.62	16.6	18
	n/a	5.6	n/a	16.4	16
	n/a	4.3	0.64	6.9	23
NH_4VO_3	4.1	4.8	n/a	17.2	14
	n/a	5.6	0.89	18.0	18
	n/a	4.8	n/a	18.0	16
	n/a	4.1	0.85	6.9	22
V_2O_5/SiO_2	n/a	6.0	0.56	16.7	18
(hydrated)	n/a	5.6	n/a	n/a	16
V_2O_5/SiO_2 (dehydrated)	n/a	6.0	0.76	18.9	18

[a] By definition.

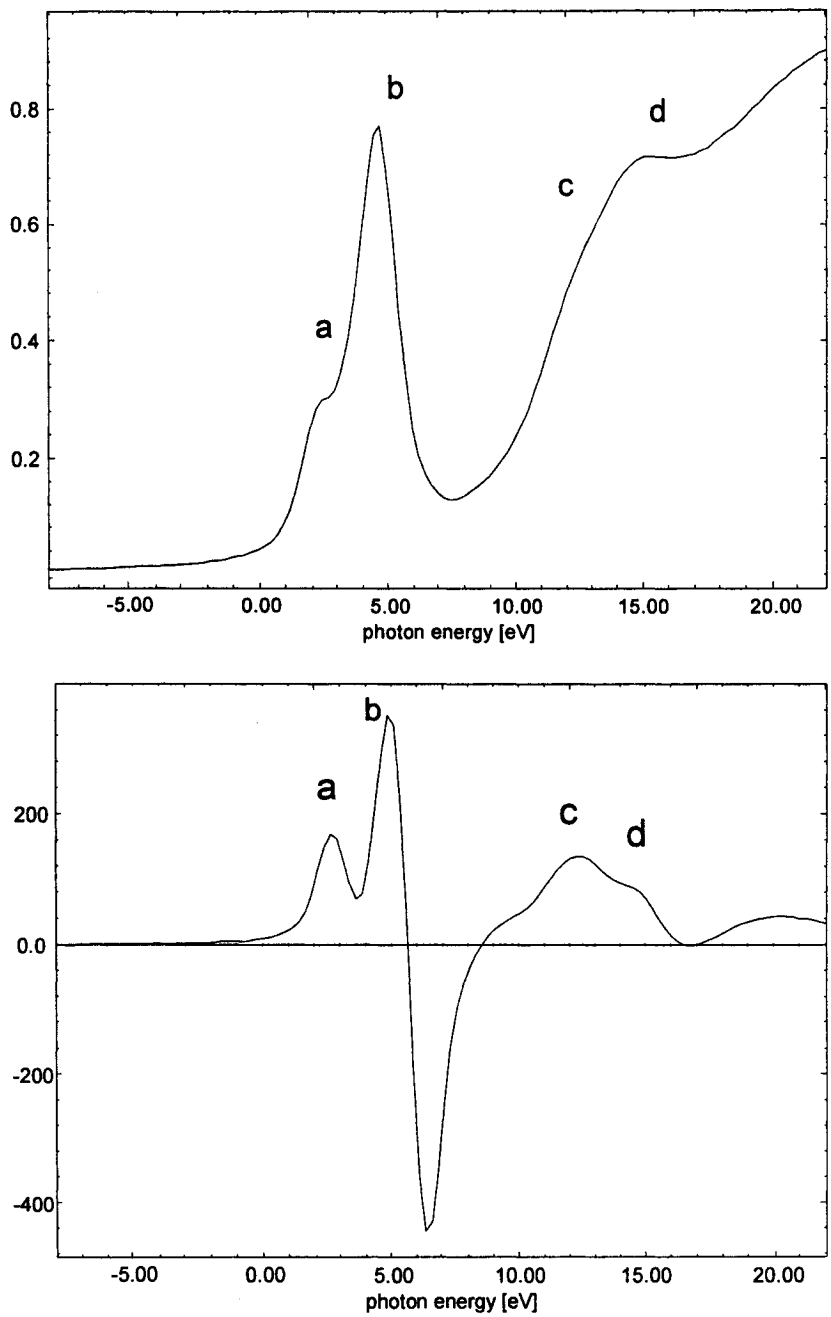

Figure 4.3. XANES and first derivative for $VOCl_3$-modified S952X-500, referenced to a V calibration foil (0 on this axis corresponds to 5465.0 eV). Y axis labels – top box: Normalized absorption; bottom box: Absorption derivative.

A third, weak shoulder (c) immediately after the K-edge is tentatively assigned to 1s → 4p transitions. The transitions manifest themselves in broad absorptions spanning the region immediately before and after the K-edge making assignments difficult.

The energies of the XANES features relative to V foil are summarized in Table 4.1 and compared to literature values for V_2O_5 and NH_4VO_3. The pre-edge positions, calculated as the difference in energy between the first inflection point in the vanadium foil spectrum at 5465.0 eV (i.e., the K edge) and the first inflection point in the sample spectra (b), are ca. 4.9 eV. The sample K edge positions (d) are ca. 13 eV from the foil K edge. The relative energies of pre-edge peaks and the K edge depend on the vanadium oxidation state.[14] V(V) is characterized by a pre-edge energy of ca. 5 eV and an edge energy of ca. 15 eV relative to the K edge of V foil.[14] Examples of V(III) K edge position include V_2O_3, 10.7eV, and V_2S_3 10.5.[14] Stable oxides of pure V(IV) are rare and have precluded detailed XANES studies. The displacements of the most intense pre-edge peak (b) and the K edge (c) in all of our vanadium-modified silicas are consistent with the presence of V(V).

The extent of hydrolysis of vanadium-modified silicas upon exposure to moisture was evident in their XANES spectra. Figure 4.4 shows the XANES of an intact sample of $VOCl_3$-modified S952X-200 (white), a slightly hydrolyzed sample exposed to air for 20 min (light yellow) and a completely hydrolyzed sample exposed to air for two days (green). The relative pre-edge intensity decreased from 0.67 in the intact sample to 0.56 in the hydrolyzed sample. The

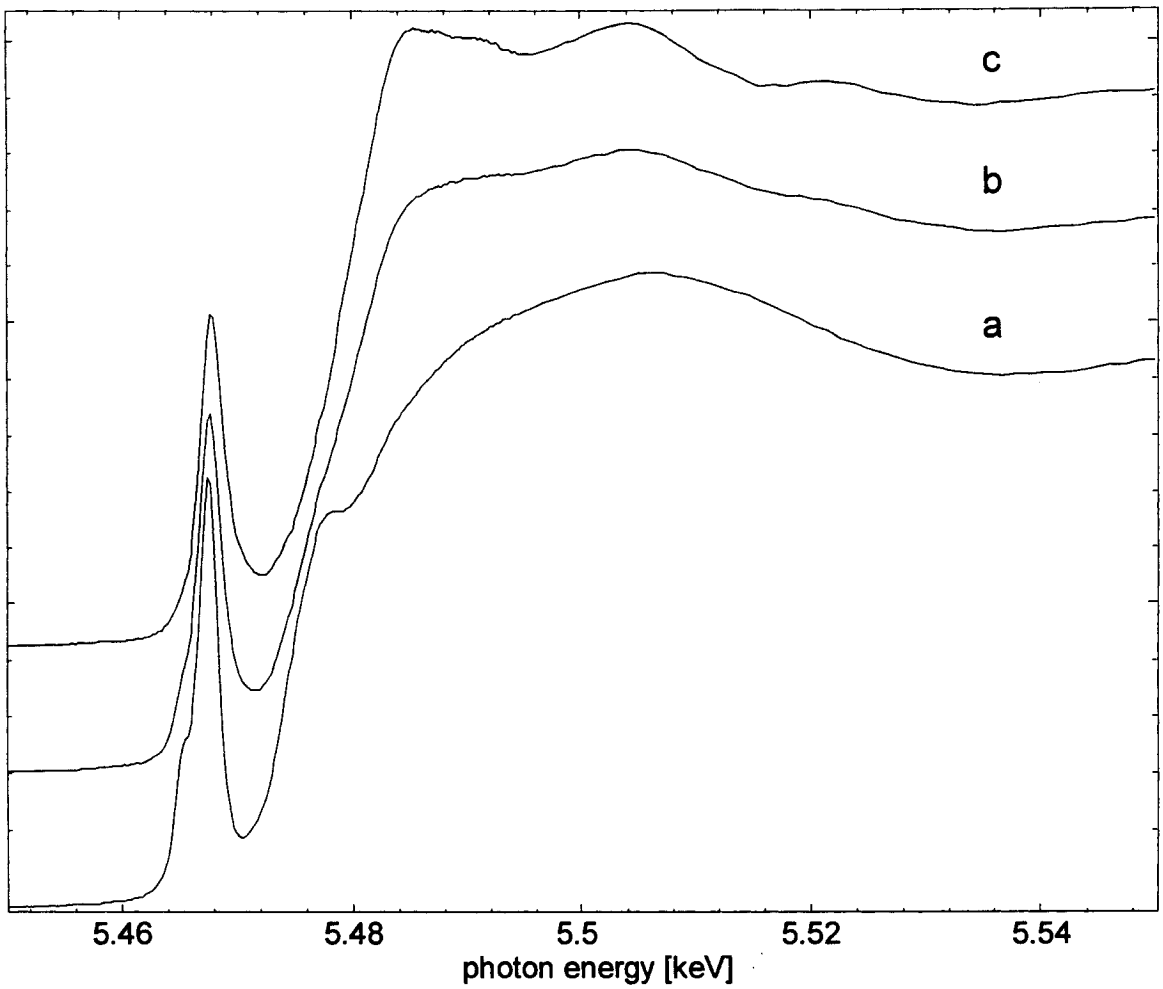

Figure 4.4. Evolution of V K-edge XANES spectra for vanadium-modified S952X-500 during hydrolysis: (a) intact sample; (b) slightly hydrolyzed sample (exposed to air for 20 min), (c) completely hydrolyzed sample (exposed to air for 2 days). y axis: normalized absorption.

latter value is comparable to that of hydrated V_2O_5/SiO_2, Table 4.1. Upon decomposition, the pre-edge peaks (a) and (d) disappeared (and are likewise absent from the spectrum of V_2O_5/SiO_2).[14] The region immediately following the absorption edge also changes in appearance, becoming similar to the XAS of $(^iC_3H_7O)_3V{=}O$ (i.e., no chloride ligands).[24]

Principal component analysis was used to estimate the degree of hydrolysis of samples considered "intact". Assuming the spectrum in Figure 4.4c is that of the fully hydrated state, we calculate that the "slightly" decomposed sample (Figure 4.4b) contains 41% of the characteristic features of the hydrolyzed sample, while the "intact" sample (Figure 4.4a) is less than 2% hydrolyzed. The % hydrolysis in the spectra of "intact" samples of $VOCl_3$-modified S952X-500, A200-500 and A200-200 are 1, 5 and 2.5%, respectively, and assumed to be statistically irrelevant in our analyses.

4.3 Extended X-ray absorption fine structure

The k-space EXAFS for vanadium-modified S952X-500 is shown in Figure 4.5. The k^3-weighted Fourier transforms of this data as well as for vanadium-modified A200-200, A200-500 and S952X-200 are shown in Figure 4.6. They show a strong resemblance to radial distribution data obtained from the gas phase electron diffraction of $VOCl_3$.[25] Furthermore, the spectra are nearly identical between 1.0 and 2.5 Å. This suggests that all samples have identical first coordination spheres. Peaks below 1.0 Å are not associated with real

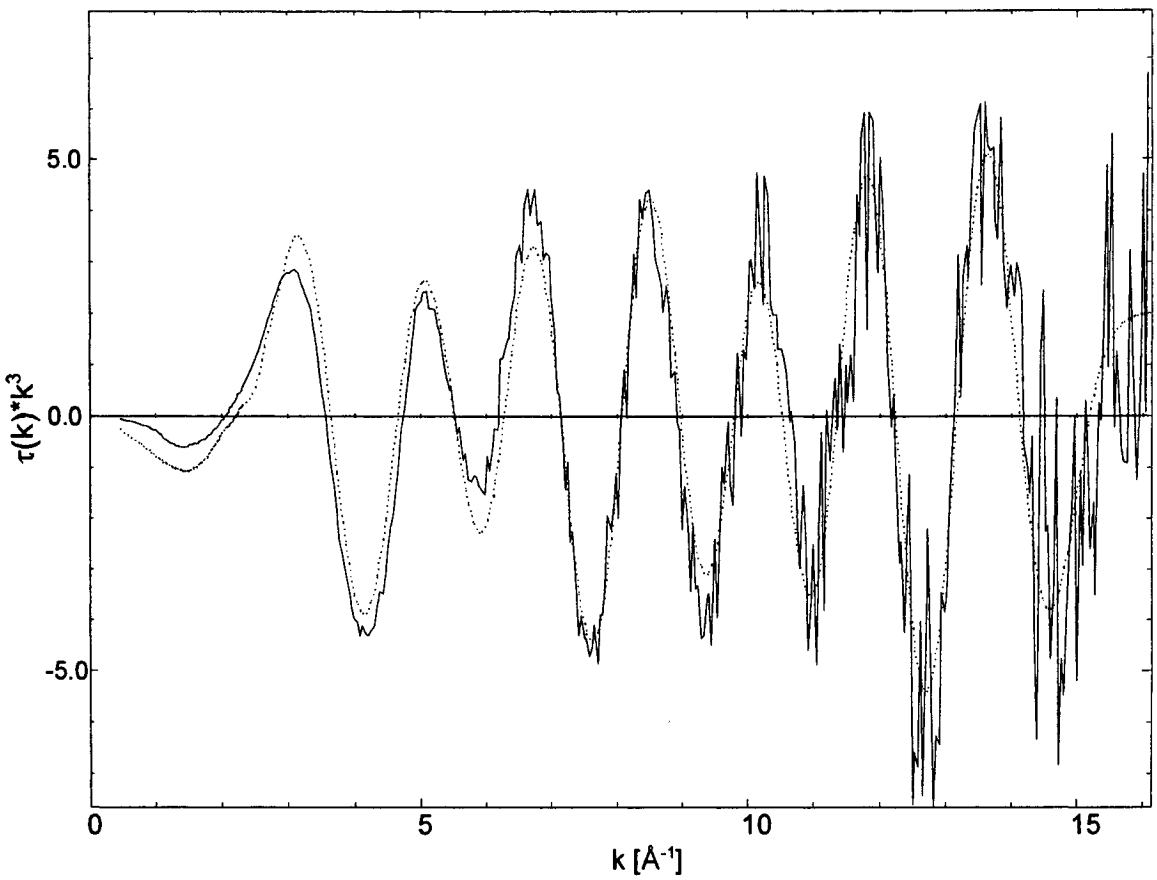

Figure 4.5. EXAFS k-space amplitude oscillation for vanadium-modified S952X-500 (solid line) and calculated (dotted line) from the simulated first shell of $\equiv SiOVOCl_2$ (asymmetric chlorides) using parameters given in Table 4.3.

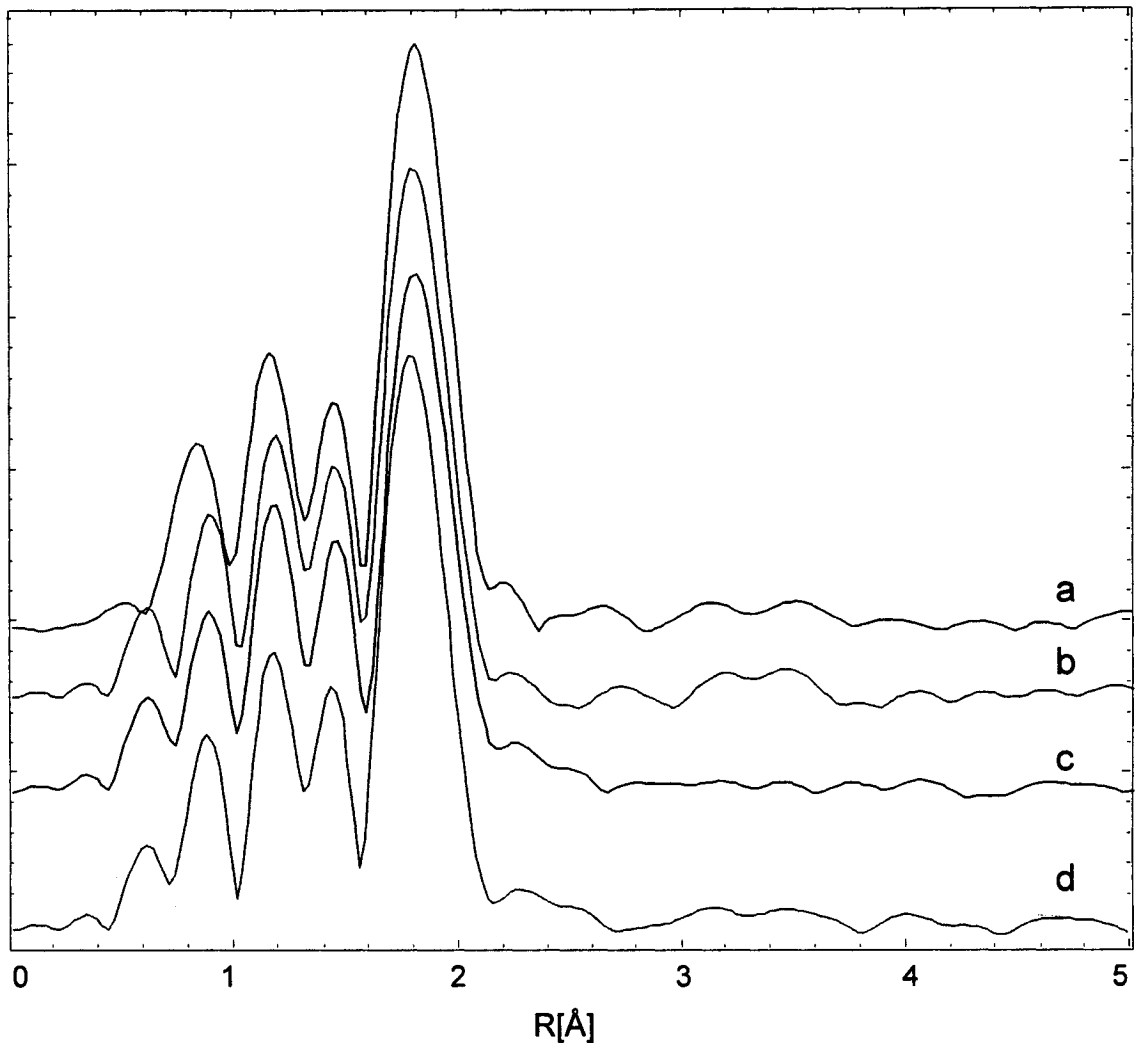

Figure 4.6. Fourier transformed V K-edge EXAFS for vanadium-modified silicas: (a) S952X-500; (b) S952X-200; (c) A200-500; (d) A200-200.

scattering pathways. Analysis of EXAFS spectra is facilitated by subtraction of the atomic absorption background of the photoabsorber via spline fitting prior to Fourier transformation. However, spline fitting does not correct the dataset optimally since the atomic background is not measured experimentally. Therefore k^3-weighting of the Fourier transform magnitude causes small discrepancies in the polynomial fit during correction to appear as peaks early in the spectra.[26,27] They can be corrected and minimized by the extensive study of related compounds,[28] however, this is beyond the scope of our study.

The EXAFS data was fitted to a model consisting of two oxygen and two chlorine neighbors. The calculated spectrum is shown superimposed on the experimental data in k-space, Figure 4.5, and in R-space, Figure 4.7

The fitted V=O and V-O distances are 1.58 and 1.75 Å, respectively. These are in a good agreement with known radial distribution data for $VOCl_3$ as well as crystal structures of pseudotetrahedral vanadyl silanolates, Table 4.2. Typical V=O distances are 1.562 Å for $VOCl_3$[29] and 1.596 Å for $VO[OSi(O^tBu)_3]_3$.[13] The V-O distance is 1.770Å in $VO[OSi(O^tBu)_3]_3$ and 1.779 for $(^tBuO)_2V[OSi(O^tBu)_3]_2$.[13]

For comparison, the V-Cl bond distance in $VOCl_3$ is 2.13 Å.[29,30] Longer V-Cl distances are found in mixed chloride alkoxide complexes of vanadium, such as $VOCl_2(OR)$, with V-Cl at 2.157(0) and 2.1715(5) Å.[32] Mixed chloride silanolate complexes are expected to have similar properties, although monomeric $V(O)X_2(OSiR_3)$ complexes are rare, and those that have been reported were not structurally characterized due to their reactivity.[32]

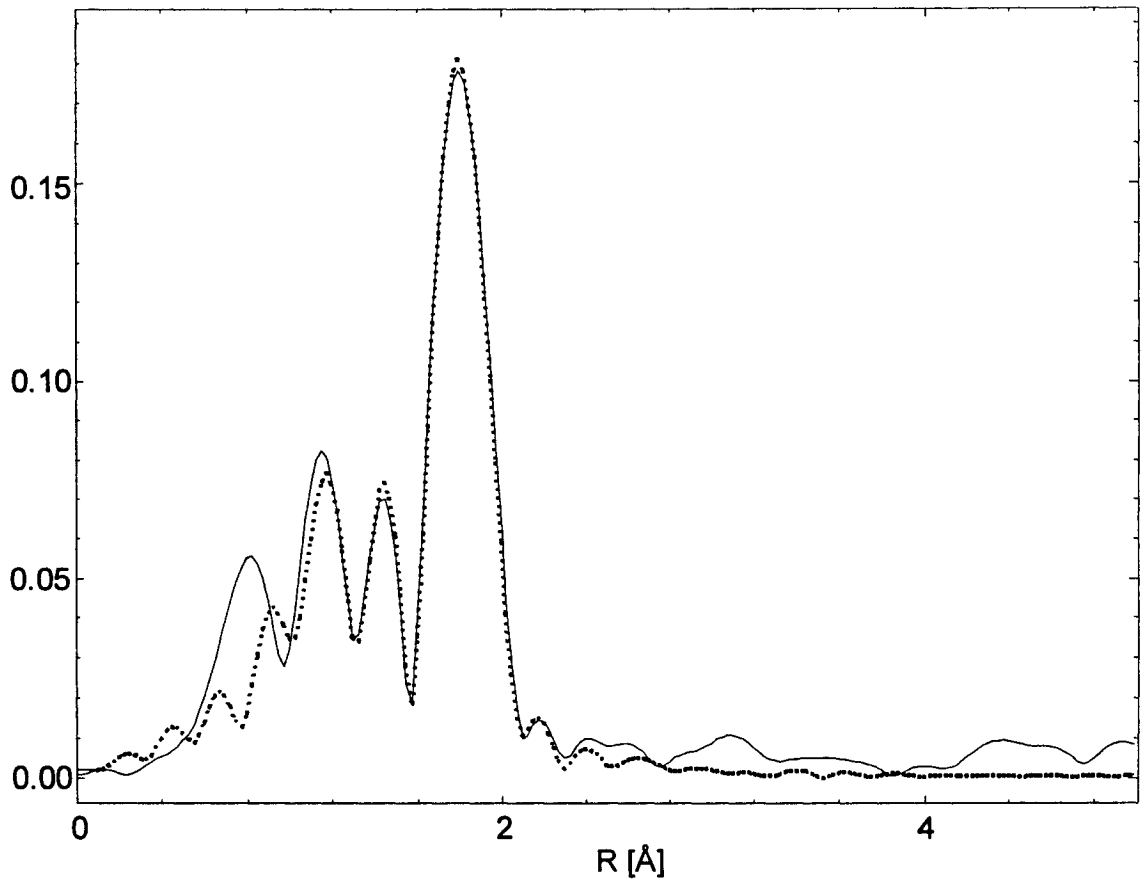

Figure 4.7. Fourier transform magnitude of the k^3-weighted EXAFS for vanadium-modified S952X-500 (solid line) and the calculated spectrum (dotted line) based on the simulated first shell of ≡SiOVOCl$_2$. Fitted parameters are given in Table 4.2.

Table 4.2. Bond distances for structurally characterized pseudotetrahedral vanadyl complexes

Compound	V=O Å	V-Cl Å	V-O Å	V-Si Å	Ref.
$VOCl_3$ (solid)	1.562	2.125			29, 30[a]
		2.124			
		2.124			
$VOCl_3$ (gas)	1.57	2.142			25[b]
		2.142			
		2.142			
$VO(OSiPh_3)_3$	1.564		1.743	3.3(4)	7[b]
			1.745		
			1.739		
$[(c\text{-}C_6H_{11})_7(Si_8O_{12})VO]_2$	1.564		1.772		7[b]
			1.737		
			1.746		
$[VOCl(OSi^tBu)_2]_3$	1.589	2.1	1.727		31[b]
$VO[OSi(O^tBu)_3]_3$	1.596		1.770	n/a	13[c]

[a] X-ray crystallography.

[b] Electron diffraction.

[c] EXAFS.

When the V-Cl distances were allowed to vary independently, the fit improved substantially (σ^2 values of 0.0005 and 0.0003, and an amplitude reduction factor S_0^2 of 0.97, where 1 is ideal). However, the fitted V-Cl distances, at 2.09 and 2.21 Å, differ by over 0.12 Å, Table 4.3. This difference is well beyond the ±0.02Å accepted error for path length (see section 2.3.5.4). The model is depicted in Figure 4.8. The reason for inequivalence of the chloride ligands is not obvious.

Siloxane coordination to the ≡SiOV(O)Cl_2 site is inconsistent with the symmetry supported by the XANES spectra. However, a model with one or two siloxane ligands was tested against the EXAFS. Refinement of the additional V-O path(s) was not possible to complete since the bond distances were correlated to each other and increased the error of the fit.

The fitted V-Si distance, (3.12 ± 0.23) Å, has a large associated value of σ^2, 0.0434. The error was calculated over five subsequent iterations of the ≡SiOV(O)Cl_2 model (with asymmetric chloride ligands) to the S952X-500 EXAFS, in which the other path lengths did not vary beyond their significant figures. Although the V-Si distance should not be regarded as reliable, the fitted value of 3.12 Å is reasonable, since $VO(OSiPh_3)_3$[7] and $[VOCl(OSi\text{-}^tBu)_2]_3$[31] have V-Si distances of ~3.22 Å[7] and ~3.13 Å, respectively.

Table 4.3. Fitted parameters for the single scattering pathways of the ≡SiOV(O)Cl_2 model

Path	Model with inequivalent chlorides[a]		Model with constrained equidistant chloride paths[b]	
	Bond length (Å)[c]	σ^2	Bond length (Å)[c]	σ^2
V=O	1.58	0.0014	1.58	0.0034
V-O	1.76	0.0013	1.76	0.0078
V-Cl	2.09	0.0006	2.16	0.0135
V-Cl	2.21	0.0003	2.16	0.0135
V-Si	3.13[d]	0.0434	3.13[d]	0.2954

[a] $S_0^2 = 0.97$ for this model optimization.

[b] $S_0^2 = 0.89$ for this model optimization.

[c] Error estimated as ± 0.02 Å (see section 2.3.5.4)

[d] The large associated Debye-Waller factor suggests that the error is much larger than ± 0.02Å and should not be taken as a reliable interatomic distance.

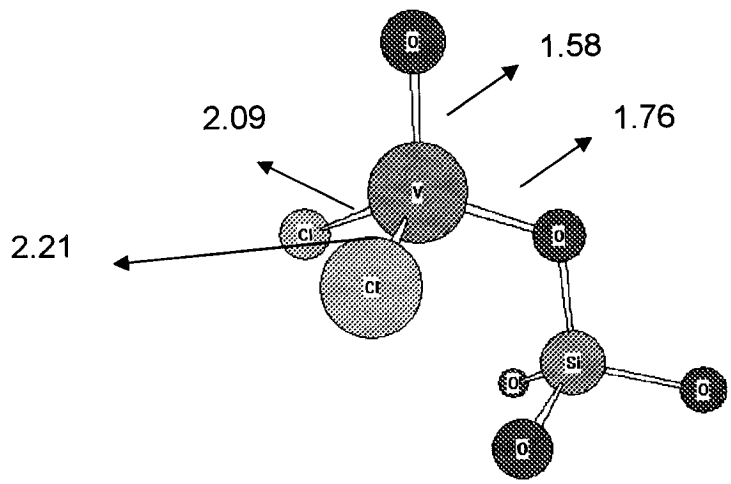

Figure 4.8 Proposed model for silica-supported vanadyl chloride.

A model for $(\equiv SiO)_3VO$, proposed as the major surface species in many vanadium-containing silicate materials, was constructed using structural data from Tilly's vanadyl silanolates and fitted to the experimental EXAFS spectrum. Fitting of a model for $(\equiv SiO)_2V(O)Cl$ was also attempted.[13] Figure 4.9 shows the experimental spectrum for S952X-500 superimposed on modeled spectra of $(\equiv SiO)_3VO$ (S_0^2 = 0.71) and $(\equiv SiO)_2VOCl$ (S_0^2 = 0.57). Both amplitude reduction factors are unrealistically low and, as Figure 4.9 shows, the correspondence between the experimental and calculated spectra is poor. Thus we conclude that the $\equiv SiOVOCl_2$ model best describes the first coordination sphere of vanadium in $VOCl_3$-modified silicas.

Multiple scattering paths were added to the $\equiv SiOVOCl_2$ model in an attempt to gain more structural information about the supported complex (i.e., bond angles). Addition of chlorine-chlorine and the vanadyl oxygen-chlorine scattering paths did not enhance the fit. The spectra show an absence of intensity at ~3.0 Å and ~3.5 Å, where O-Cl and Cl-Cl multiple scattering was observed by Karakida for $VOCl_3$.[25] It is possible that multiple scattering contributions cancel and are therefore not apparent in the EXAFS spectra, as has been shown elsewhere.[33] However this result, and the silica-dependent variations in the spectra at radial distributions greater than 2.5 Å (Figure 4.6), may also be ascribed to inhomogeneity of the environment beyond the first coordination sphere.

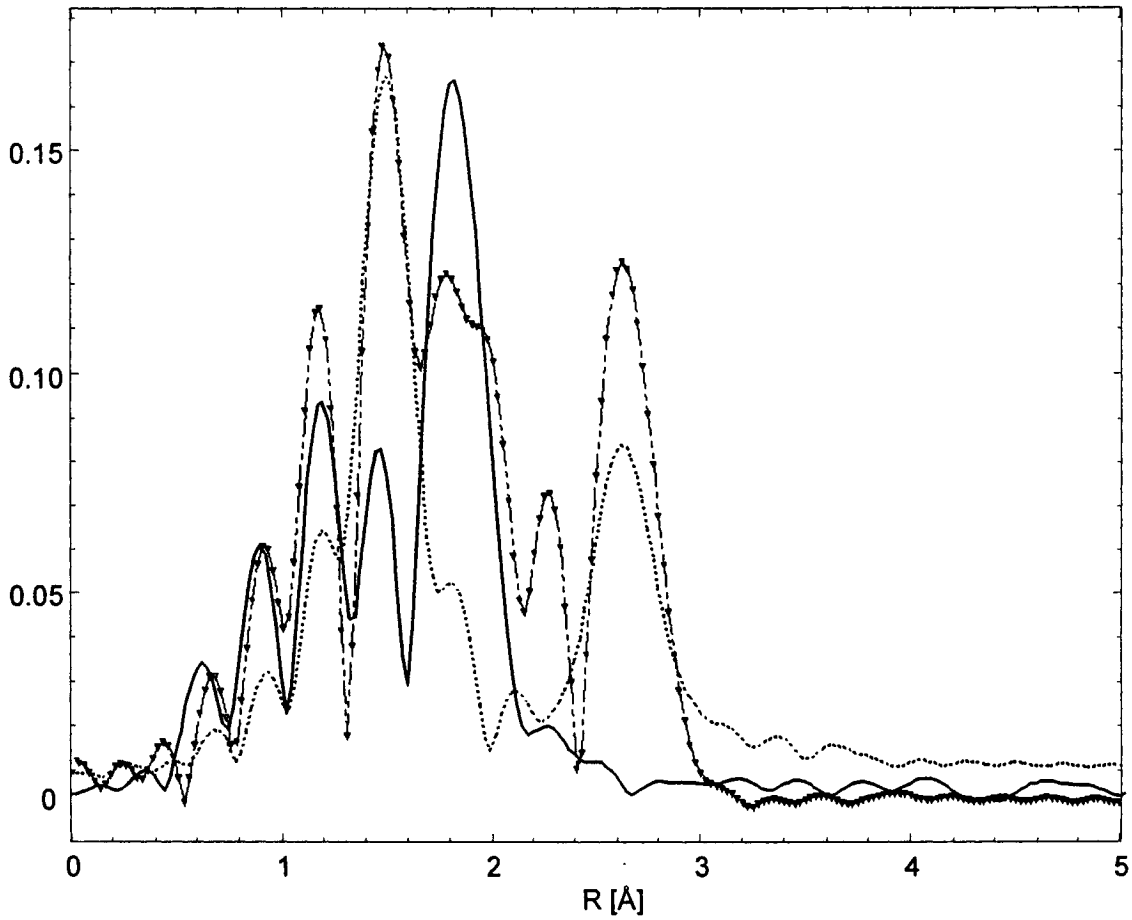

Figure 4.9 Fourier transform magnitude of the EXAFS (k^3-weighted) for vanadium-modified S952X-500 data (solid line) and calculated spectra for models $(\equiv SiO)_3VO$ (dotted line) and $(\equiv SiO)_2VOCl$ (dotted-dashed line).

Finally, we attempted to resolve the multiple scattering paths by minimizing thermal motion around vanadium. Others have used cryogenic cooling to prevent X-ray radiation damage to XAS samples[34] and to minimize thermal disorder in the EXAFS.[35] Reduced thermal motion results in more resolved features in the radial distribution spectrum, with lower associated Debye-Waller factors. However, most reports of XAS cryogenic cooling have involved highly ordered metal samples[36-40] rather than amorphous powders.

The EXAFS of vanadium-modified S952X-500 recorded at 295 and 20 K are compared in Figure 4.10. No new signals (*i.e.*, multiple scattering paths) are observed at the lower temperature. Single scattering paths of a larger model $(\equiv SiO)_3SiOV(O)Cl_2$ were refined to the cryogenic data set, giving $S_0^2 = 0.92$, Table 4.4. Debye-Waller factors were constrained between 0 and 0.1 in order to minimize the correlation of free variables. While the first-shell, single scattering fit agrees well with the fit to the spectrum recorded at 295 K (Table 4.3), improvement in the region past 2.5 Å is not significant. The associated Debye-Waller factors for paths longer than 2.5 Å expanded to their maximum limit in the model refinement and are indicative of unreliable fitting.

This result, as well as variations in spectra at radial distributions >2.5 Å, are apparently not a result of thermal motions but a lack of structural uniformity beyond the first coordination sphere in $\equiv SiOVOCl_2$.

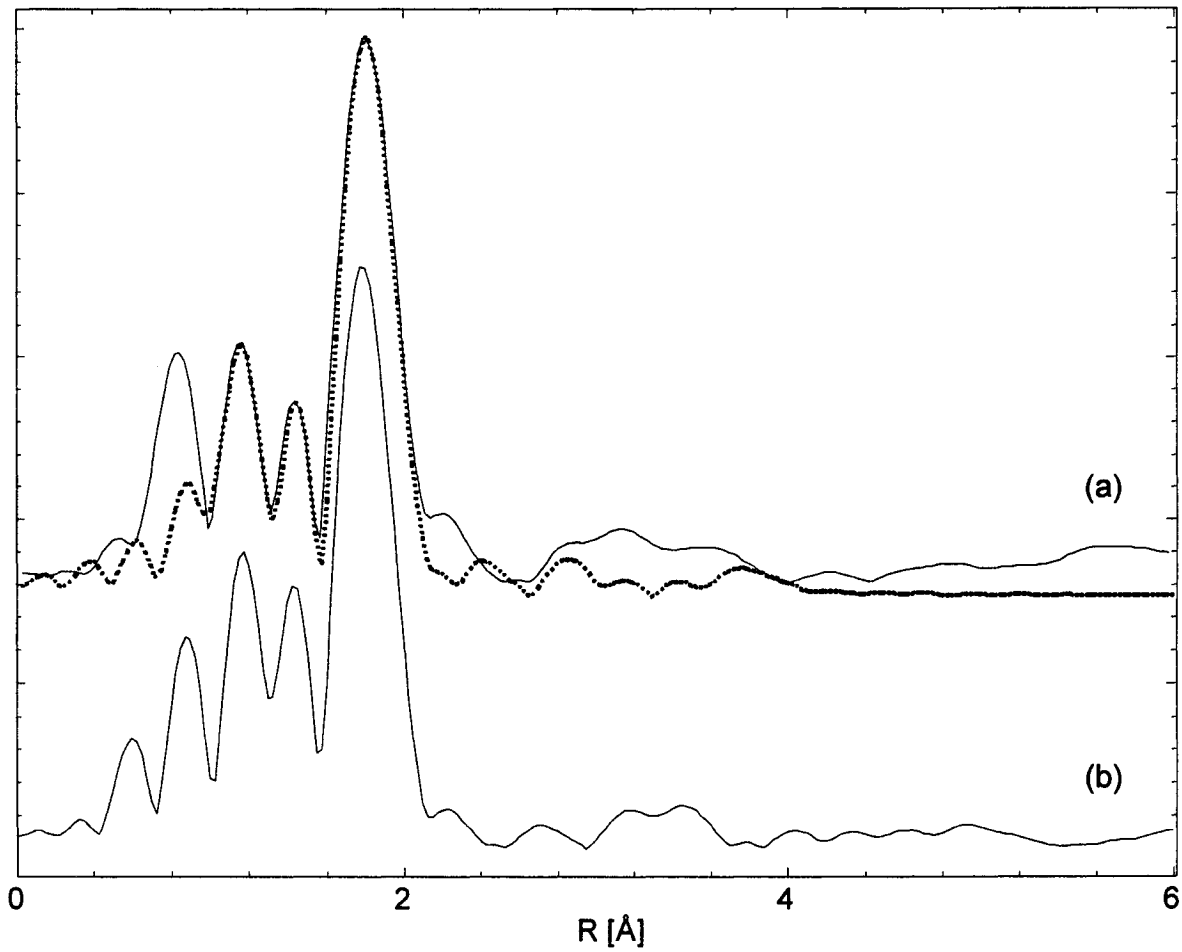

Figure 4.10 Comparison of k^3-weighted EXAFS for vanadium-modified S952X-500 recorded at (a) 20 K; and (b) 295 K (solid lines). Spectra were normalized and vertically offset. The model refinement (dotted line) for $(\equiv SiO)_3SiOV(O)Cl_2$ is superimposed on the spectrum acquired at 20K.

Table 4.4 Fitted parameters for the single scattering pathways of $(SiO)_3SiOV{=}OCl_2$ model.

Path	Bond length (Å)	Debye-Waller[a] σ^2
V=O	1.59	0.0003
V-O	1.75	0.0003
V-Cl	2.11	0
V-Cl	2.22	0.0001
V-Si	3.22	0.1
V-O	3.77	0.1
V-O	4.10	0.1
V-O	4.44	0.1
V-Si	4.83	0.1
V-Si	5.29	0.1
V-Si	5.58	0.1

[a] Debye-Waller factors were constrained to have a maximum value of 0.1 in order to complete the fit. The errors for shells with reported Debye-Waller factors of 0.1 are likely to be much higher, and their paths are not indicative of actual interatomic distances. Error estimated as ± 0.02 Å (see section 2.3.5.4)

Although neither single nor multiple scattering analysis allowed us to directly determine the V-O-Si angle, we can confidently assume that this fragment is not linear. Assuming an Si-O distance of 1.61 Å,[41] the fitted Si-V and V-O distances require an Si-O-V angle of (140 ± 30)°. This value compares well to those for molecular vanadium silanolates: for example, $[(c\text{-}C_6H_{11})_7(Si_8O_{12})VO]_2$ has Si-O-V angles of 136.0, 145.6 and 146.4°,[7] while a cyclic V(IV) silanolate has Si-O-V angles of 134.0 and 135.6°.[41] There are no molecular examples in the literature of a pseudo-linear arrangement of Si-O-V allowing delocalization of an oxygen lone pair onto the metal.[42] Furthermore, significant amplification of the multiple scattering paths between Si-O-V are expected for angles approaching 180°, due to the focusing effect described by Teo.[43] This amplification was not apparent during our fitting attempts, supporting the more plausible bent structure.

4.4 Conclusion

XAS has considerably expanded the information we possess regarding the vanadium site in silicas modified with vanadyl chloride. Both XANES and EXAFS are consistent with coordination to two oxygen and two chlorine atoms, giving pseudotetrahedral geometry at vanadium. A model based on $(\equiv SiO)VOCl_2$ and shown in Figure 4.8 is proposed for the local structure of the vanadium site, confirming our earlier hypothesis. This result is independent of the nature of the silica (pyrogenic or precipitated) or its pretreatment temperature. However, longer range order does depend on the nature of the silica and may ultimately influence catalytic behavior.

Finally, EXAFS indicates that the chloride ligands of $(\equiv SiO)VOCl_2$ are inequivalent. Since the model shows no obvious reason why this should be so, we presume that an interaction between one chloride and the silica surface is the origin of the effect. However, this hypothesis awaits further confirmation.

4.5 References

1) Oyama, S. T. *Res. Chem. Intermed.* **1991**, *15*, 165-182.

2) Miyamoto, A.; Yamazaki, Y.; Inomata, M.; Murakaml, Y. *J. Phys. Chem.* **1981**, *85*, 2366-2372.

3) Inomata, M.; Miyamoto, A.; Murakami, Y. *J. Catal.*, **1980**, *62*, 140-148.

4) Jonson, B.; Rebenstorf, R.; Larsson, R.; Andersson, S. L. T. J. *Chem. Soc., Faraday Trans 1* **1988**, *84*, 1897-1910.

5) Chien, J. C. W. *J. Am. Chem. Soc.* **1971**, *93*, 4675-4684.

6) Gritscov, A. M.; Shrets, V. A.; Kazansky, V. B. *Chem. Phys. Lett.* **1975**, *35*, 511-512.

7) Feher, F. J.; Walzer, J. F. *Inorg. Chem.* **1991**, *30*, 1689-1694.

8) Das, N.; Eckert. H.; Hu, H.; Wachs, I. E.; Walzer, J. F.; Feher, . F. J. *J. Phys. Chem.* **1993**, *97*, 8240-8243.

9) Rice, G. L.; Scott, S. L. *Langmuir* **1997**, *13*, 1545-1551.

10) Kijenski, J.; Hombek, R.; Malinowski, S. *J. Catal.* **1977**, *50*, 186-189.

11) Inumaru, K.; Okuhara, T.; Misono, M. *J. Phys. Chem.* **1991**, *95*, 4826-4832.

12) Higashimoto, S.; Matsuoka, M.; Zhang, S. G.; Yamashita, H.; Kitao, O.; Hidaka, H.; Anpo, M.; *Micropor. Mesopor. Mater.* **2001**, *48*, 329-335.

13) Ruklens, R.; Male, J. L.; Terry, K. W.; Olthof, B.; Khodakov, A.; Bell, A. T.; Iglesia, E.; Tilley, D. *Chem. Mater.* **1999**, *11*, 2966-2973.

14) Wong, J.; Lytle, F. W.; Messmer, R. P.; Maylotte, D. H. *Phys. Rev. B* **1984**, *30*, 5596-5610.

15) Gao, X.; Bare, S. R.; Fierro, J. L. G.; Banares, M. A.; Wachs, I. E. J. *Phys. Chem. B* **1998**, *102*, 5653-5666.

16) Yoshida, S.; Tanaka, T.; Hanada, T.; Hiraiwa, T.; Kanai, H.; Funabiki, T. *Catal. Lett.* **1992**, *12*, 277.

17) Zhang, H. H.; Filipponi, A.; Di Cicco, A.; Loee, S. C.; Scott, M. J.; Holm, R. H.; Hedman, B.; Hodgson, K. O. *Inorg. Chem.* **1996**, *35*, 4819-4828.

18) Gao, X.; Bare, S. R.; Weckhuysen, B. M.; Wachs, I. E. *J. Phys. Chem. B* **1998**, *102*, 10842-10852.

19) Yamamoto, T.; Tanaka, T.; Matsuyama, T.; Funabiki, T.; Yoshida, S. *Solid State Comm.* **1999**, *111*, 137-142.

20) Inumaru, K.; Misono, M.; Okuhara, T. *Appl. Catal. A: Gen.* **1997**, *149*, 133-149.

21) Westre, T. E.; Kennepohl, P.; DeWitt, J. G.; Hedman, B.; Hodgson, K. O.; Solomon, E. I. *J. Am. Chem. Soc.* **1997**, *119*, 6297-6314.

22) Arber, J. M.; de Boer, E.; Garner, C. D.; Hasnain, S. S.; Weaver, K. *Biochemistry,* **1989**, *28*, 7968-7973.

23) Hawthorne, F. C.; Calvo, C. *J. Solid State Chem.* **1977**, *22*, 157-170.

24) Zhang, S. G.; Higashimoto, S.; Yamashita, H.; Anpo, M.; *J. Phys. Chem. B* **1998**, *102*, 5590-5594.

25) Karakida, K.; Kuchitsu, K. *Inorganic Chimica. Acta.* ***1975***, *13*, 113-121.

26) Wang, W.-C.; Chen, Y. *Physica Status Solidi A* **1998**, *168*, 351-7.

27) Antonioli, G.; Lottici, P.; Manzini, I.; Ganappi, G.; Montenro, A.; Paloschi, F.; Parent, P. *J. Non-Cryst. Solids* **1994**, *77*, 179-186.

28) Mustre de Leon, J.; Conradson, S. D.; Batistić, I.; Bishop, A. R. *Phys. Rev. B* **1991**, *44*, 2422-2425.

29) Palmer, K. *J. Am. Chem. Soc.* **1938**, *60*, 2360-2369.

30) Galy, J.; Enjalbert, R.; Jngie, G.; Strahle, J. *J. Solid State Chem.*, **1983**, *47*, 143-150.

31) Gosink, H. –J.; Roesky, H. W.; Noltemeyer, M.; Schmidt, H. –G.; Freier-Erdmgger, C.; Sheldriek, G. M. *Chem. Ber.* **1993**, *126*, 279-283.

32) Priebsch, W.; Rehder, D. *Inorg. Chem.* **1990**, *29*, 3013-3019.

33) Martens, G.; Rabe, P.; Wenck. P. *Physica Status Solidi A* **1985**, *88*, 103-111.

34) Nave, C. *Radiat. Phys. Chem.* **1995**, *45*, 483-490.

35) Hanawalt, J. D.; *Z. Physik* **1931**, *70*, 293-305.

36) Lytle, F. W. "*Developments in Applied Spectroscopy*" Vol. 2, eds. Ferraso, J. R.: Ziomek, J. S. **1963**, Plenum: New York., p 285.

37) Eisenberger, P.; Brown G. S. *Solid State, Commun.* **1979**, *29*, 481-484.

38) Böhmer, W.; Rabe, P. *J. Phys. C: Solid State Phys.* **1979**, *12*, 2465-2474.

39) Sevillano, E.; Meuth, H.; Rehr, J. J. *Phys. Rev. B* **1979**, *20*, 4908-4911.

40) Sandstrom, R.; Marques, E. C.; Biebesheimer, V. A.; Lytle, F. W.; Greegor, R. B. *Phys. Rev. B.* **1985**, *32*, 3541-3548.

41) Motevalli, M.; Shah, D.; Syed, A. A.; Sullivan, A. C. *Organometallics*, **1994**, *13*, 4109-4112.

42) Babaian, E. A.; Hrncir, D. C.; Bott, S. C.; Atwood, J. L. *Inorg. Chem.* **1986**, *25*, 4818-4821.

43) Teo, B.-K.; *EXAFS: Basic Principles and Data Analysis.* Springer-Verlag, New York, USA, 1986.

Chapter Five

Reactions of Vanadyl Chloride and Trimethylaluminum on Silica

---

5.1 Introduction

Reactions of vanadyl chloride with trimethylaluminum are of particular interest as model Ziegler-Natta catalysts system for olefin polymerization. Previous work in the Scott group confirmed that vanadyl chloride-modified silica and organoaluminum-modified silica are by themselves ineffective as polymerization catalysts.[1,2] However, impregnating the support with $VOCl_3$,[3] VCl_4,[4] or even VCl_3[5] followed by treatment with an alkylaluminum cocatalyst results in activity for olefin polymerization.[6] There is as yet little understanding of the nature of the vanadium active sites.

Feher and coworkers observed that interaction between the alkylaluminum co-catalyst and inorganic or organometallic oxovanadium(V) complexes, $O{=}VX_3$ where X = CH_2SiMe_3, O^iPr, Cl, $OSiPh_3$, as well as oxovanadium(V) silsesquioxanes, consists of coordination of aluminum to the vanadyl oxygen with alkyl transfer from aluminum to vanadium.[7-9] These materials are active catalysts for olefin polymerization and co-polymerization.

In this chapter, we report three methods for creating Ziegler-Natta catalysts by reacting volatile $VOCl_3$ and TMA sequentially with silica. Infrared spectroscopy, electron spin resonance (ESR) spectroscopy and stoichiometric analysis have been used to investigate the reactions that occur and the

composition of the active centers present in the resulting catalytically active material.

5.2 Reaction of $AlMe_3$ with the silica surface

5.2.1 Stoichiometry of the reaction

When $AlMe_3$ (TMA) is sublimed onto A380-500 and allowed to react at room temperature with its surface hydroxyl groups, a chemical reaction takes place resulting in the formation of chemisorbed aluminum species and liberation of methane. A380-500 contains (0.81 ± 0.03) mmol accessible OH/g silica, as measured by $VOCl_3$ chemisorption in Chapter 3. Elemental analysis of the TMA-modified silica after prolonged desorption of volatiles under dynamic vacuum reveals the presence of (1.51 ± 0.08) mmol Al/g silica. The ratio of chemisorbed aluminum to surface hydroxyl groups is therefore (1.88 ± 0.10) and the chemisorbed organometallic fragment is judged to be dinuclear in aluminum. The quantity of methane liberated was determined by gas phase IR spectroscopy to be (1.41 ± 0.10) mmol/g silica, which corresponds to (0.93 ± 0.05) equivalents per aluminum, Table 5.1. These results support the stoichiometry of TMA grafting shown in eq 5.1:

Table 5.1 Quantitative analysis of grafting of trimethylaluminum on A380-500 [a]

mmol Al[b]	Al/OH	Product of grafting	
		mmol CH_4[b]	CH_4/Al
1.53	1.90	1.41	0.92
1.66	2.05	1.44	0.87
1.51	1.86	1.30	0.86
1.44	1.78	1.36	0.94
1.51	1.86	1.44	0.95
1.54	1.90	1.52	0.99
1.38	1.70	1.25	0.91
1.53	1.89	1.57	1.03
1.51 ± 0.08	1.88 ± 0.10	1.41 ± 0.10	0.93 ± 0.05

[a] Hydroxyl content is (0.81±0.03) mmol OH/g silica after 500°C treatment.

[b] All values are normalized per gram of silica.

$$\equiv SiOH + Al_2Me_6 \longrightarrow \equiv SiOAl_2Me_3(CH_2) + 2\,MeH \quad (5.1)$$

and are consistent with the report of Church et al.[1]

5.2.2 Infrared characterization

The infrared spectrum of a self-supporting disk of unmodified A380-500 is shown in Figure 5.1a. Addition of TMA vapor at room temperature to the in situ IR cell containing the self-supporting disk led to immediate spectral changes. CH_4 was detected by its gas phase IR spectrum, GC and GC-MS. The band at 3747 cm^{-1}, assigned to non-hydrogen-bonded silanol groups, almost completely disappeared. The broad, weak absorption band centered at approximately 3670 cm^{-1}, assigned in Chapter 3 to inaccessible silanol groups,[10] does not change.

New bands in the ν(C-H) region, were observed at 2962, 2941, 2898 and 2831 cm^{-1}, Figure 5.2b. Two $\delta(CH_3)$ bands are present in the spectrum at 1435 and 1412 cm^{-1}, Figure 5.3a. In the low frequency region, the reaction of the TMA with a thin film of silica shows the loss of the shoulder at 980 cm^{-1} and growth of two new peaks at 715 and 687 cm^{-1}, Figure 5.4i. The negative band at 980 cm^{-1} is due to disappearance of the ν(Si-O) mode of ≡SiOH. By spectral subtraction, additional bands at 917, 869, 820 and 606 cm^{-1} were observed, Figure 5.4ii.

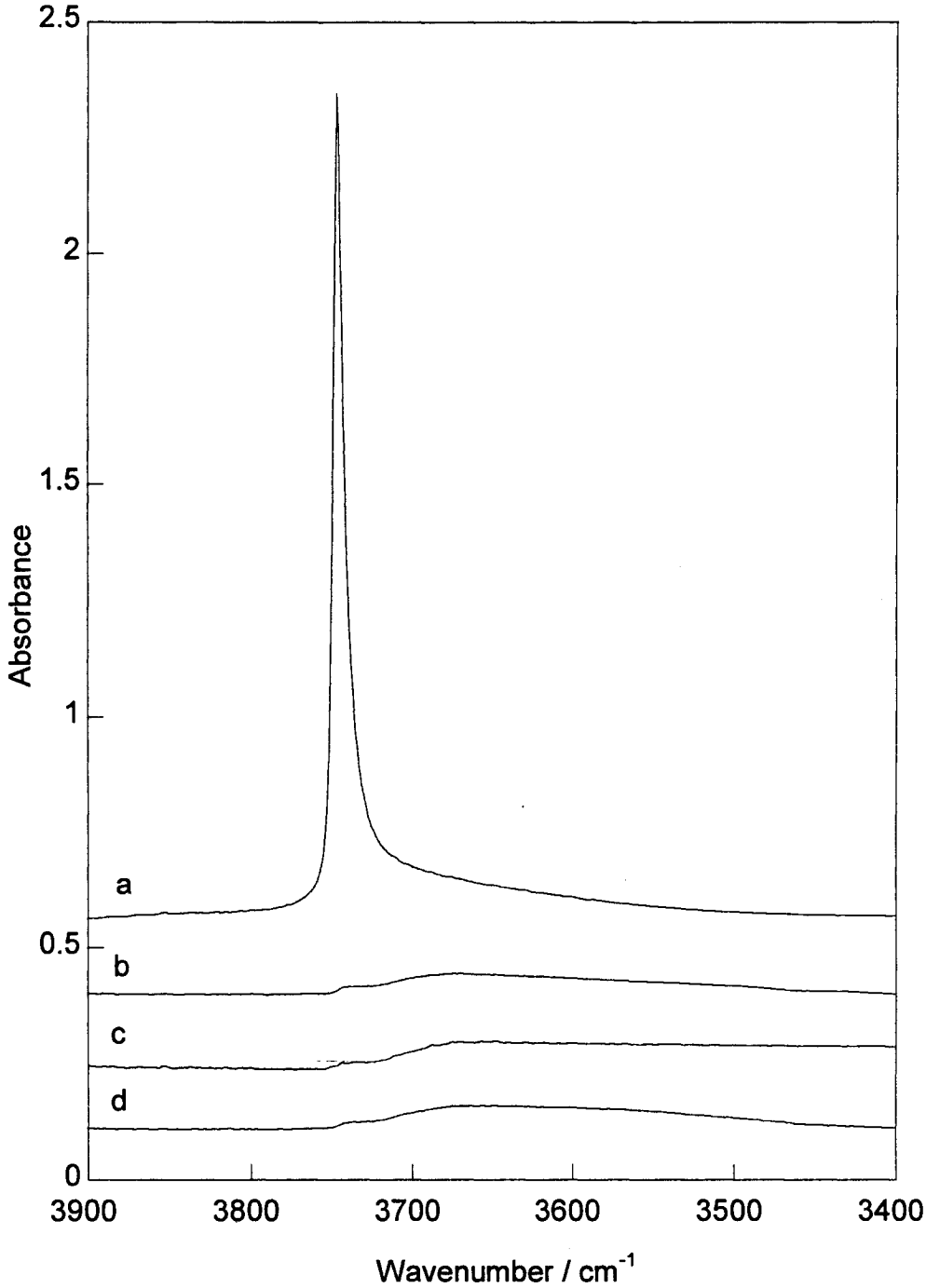

Figure 5.1 Infrared spectra of a self-supporting disk in the ν(OH) region, of (a) A380-500, (b) A380/TMA, (c) A380/TMA/$VOCl_3$, (d) A380/TMA/$VOCl_3$/TMA.

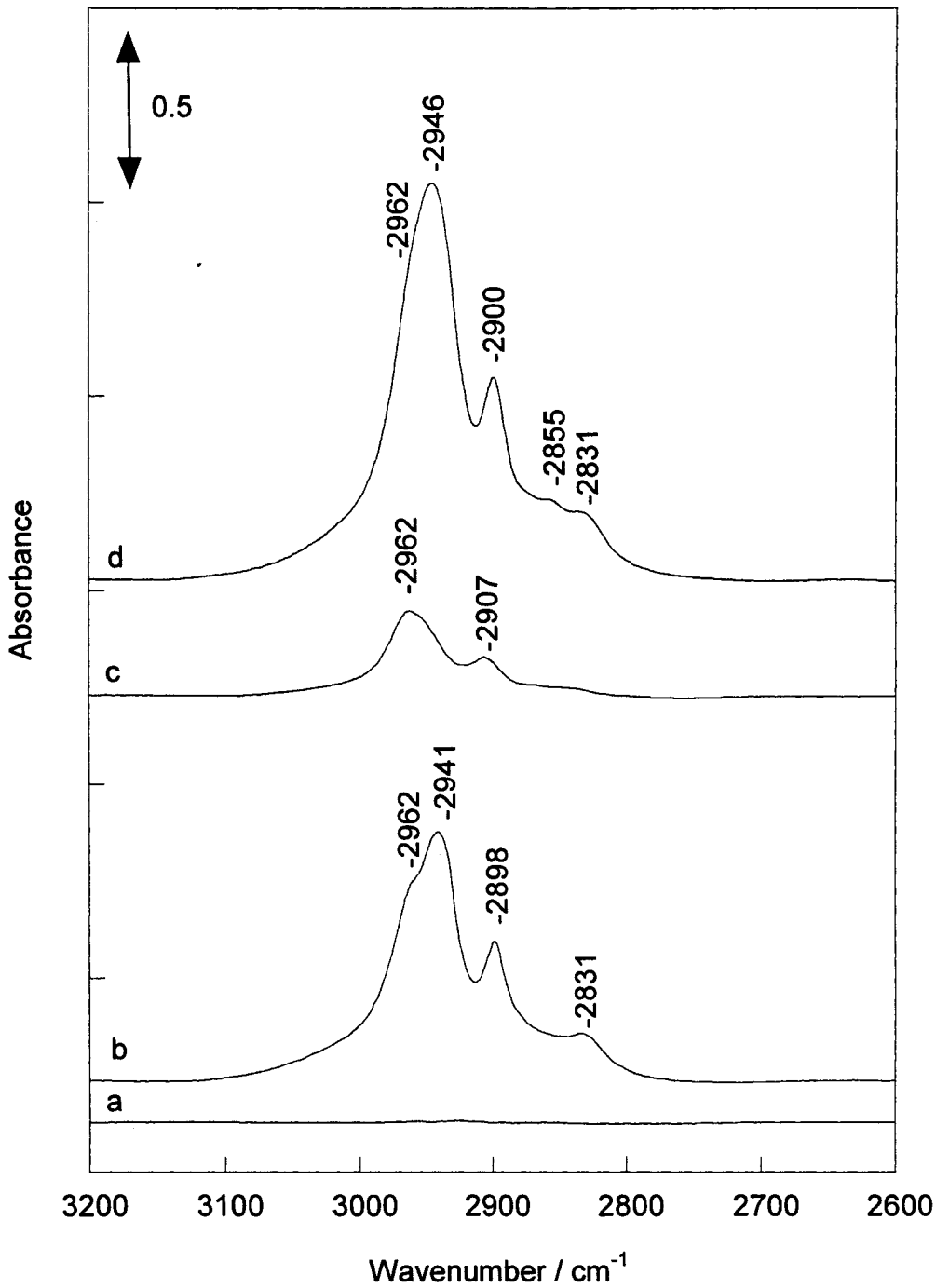

Figure 5.2 Infrared spectra in the ν(C-H) region of a self-supporting disk of (a) A380-500, (b) A380/TMA, (c) A380/TMA/$VOCl_3$, (d) A380/TMA/$VOCl_3$/TMA.

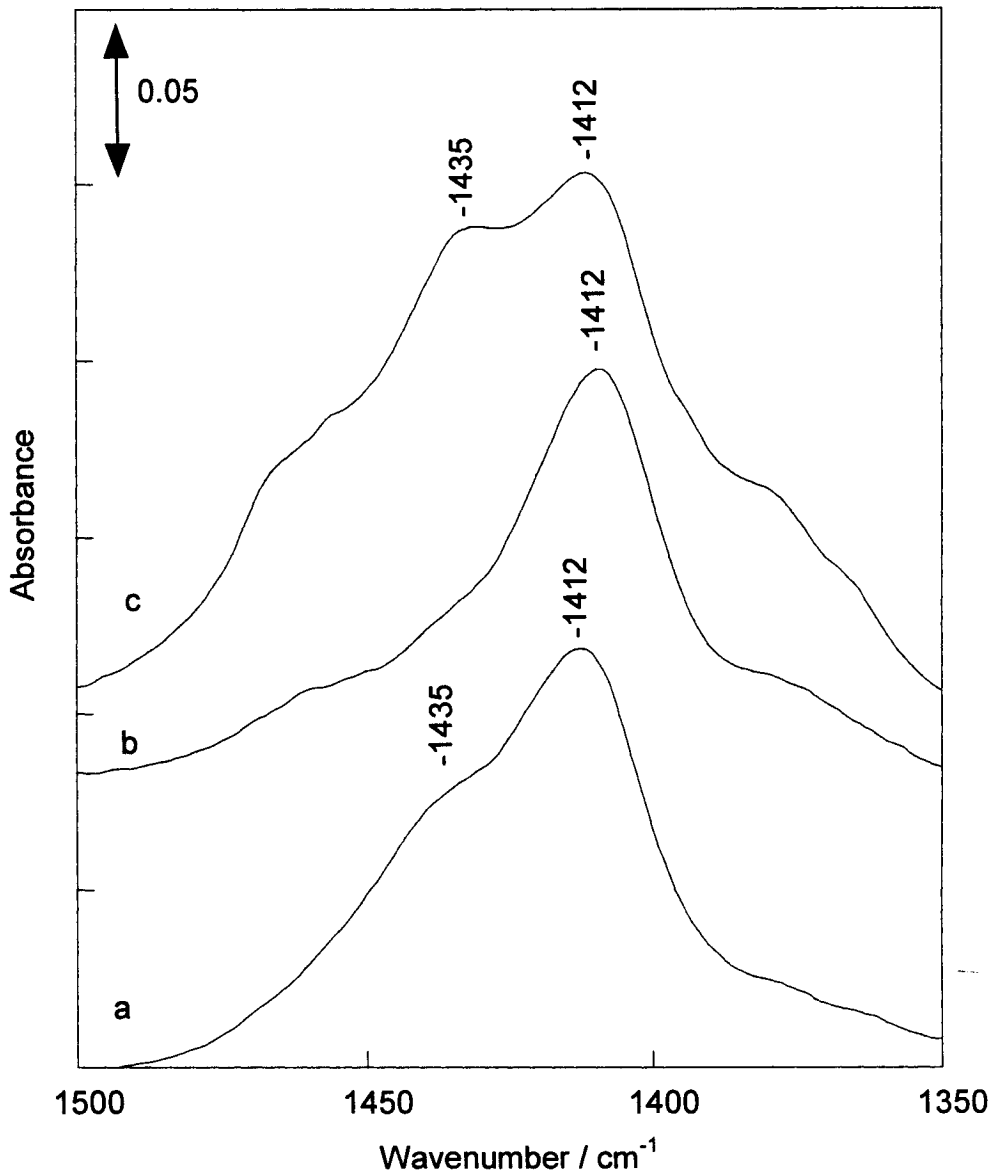

Figure 5.3 Difference infrared spectra of a self-supporting disk showing the $\delta(CH_3)$ region for (a) A380/TMA, (b) A380/TMA/$VOCl_3$, (c) A380/TMA/$VOCl_3$/TMA. The difference spectra were generated by subtracting the spectrum of A380.

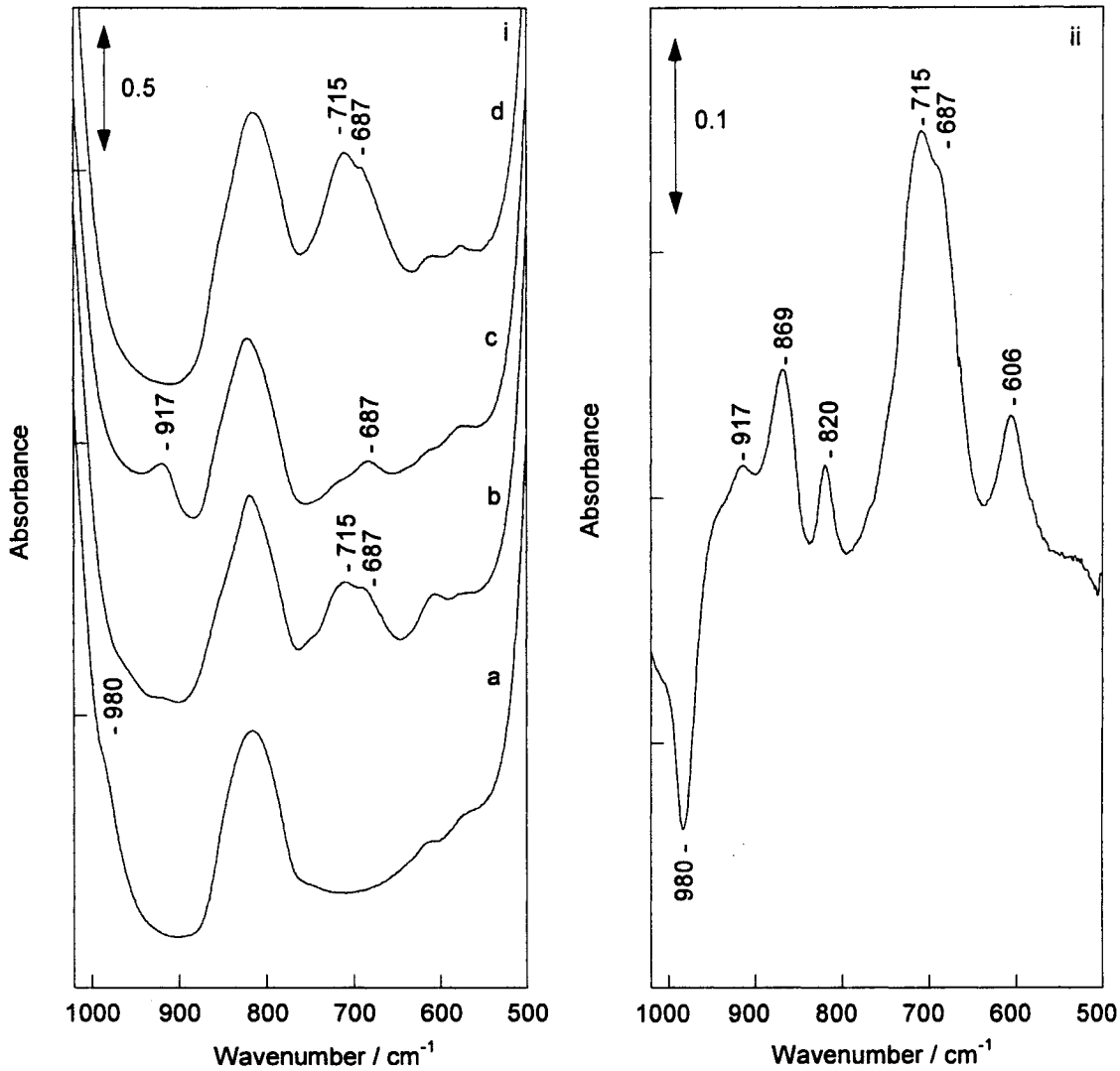

Figure 5.4 Infrared spectra in the low frequency region of a ZnSe-supported silica thin film (i): a) A380-450, b) A380/TMA, c) A380/TMA/$VOCl_3$, d) A380/TMA/$VOCl_3$/TMA, (ii) difference spectrum of A380/TMA. The difference spectrum was generated by subtracting the spectrum of A380.

These results support the structure for TMA on silica proposed by Church et al.[1]

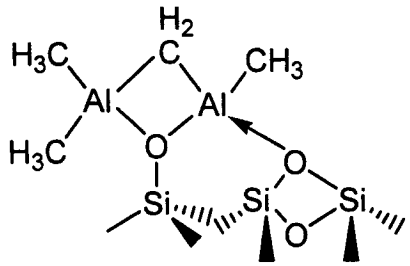

(**1**)

5.3 Reaction of $VOCl_3$ with TMA-modified silica

When TMA-modified silica is exposed to $VOCl_3$ vapor at room temperature, no hydroxyl groups reappear, Figure 5.1c. However, CH_3Cl was observed in the gas phase. CH_3Cl is readily identified by its characteristic gas phase IR spectrum, with ν(C-Cl) at 732 cm^{-1}, and its identity was confirmed by GC and GC-MS. The color of the silica changed from white to dark green, suggesting a change in the oxidation state of vanadium.

5.3.1 Stoichiometry of the reaction

The nature of the reaction of $VOCl_3$ with TMA-modified silica was further investigated by quantitation of the Al and V contents of the silica, the amount of CH_3Cl released in the grafting reaction, and the number of hydrolysable methyl groups remaining in the supported organometallic fragments. The goal is to obtain a complete mass balance for the reaction.

The CH_3Cl released upon contact of $VOCl_3$ with **1** was quantified by gas phase IR spectroscopy. When excess $VOCl_3$ vapor was added to **1**, (1.47 ± 0.07) mmol CH_3Cl/g silica was evolved, Table 5.2. The ratio of CH_3Cl to the original surface hydroxyl groups is therefore (1.80 ± 0.09). No HCl was detected during $VOCl_3$ chemisorption.

The number of hydrolysable methyl groups present on the surface was determined by addition of excess water vapor with quantitation of the methane released. Prolonged hydrolysis at room temperature resulted in liberation of (1.67 ± 0.03) mmol CH_4/g silica, corresponding to (2.06 ± 0.08) CH_4 per original OH. Thus the total carbon equivalents recovered during grafting of TMA (1.74 CH_4/OH), grafting $VOCl_3$ (1.80 CH_3Cl/OH) and subsequent hydrolysis (2.06 CH_4/OH) is (5.60 ± 0.24) per original OH site.

Calcination of the sample at 500°C in 400 Torr oxygen caused complete loss of surface hydrocarbon groups with formation of water and (1.72 ± 0.12) mmol CO_2/g silica, equivalent to 2.12 carbons per original silanol. Thus the total carbon recovered from grafting of TMA (1.74 CH_4/OH), $VOCl_3$ (1.80 CH_3Cl/OH) and subsequent calcination (2.12 CO_2/OH), is 5.66 per original OH site.

The metal content of the material after $VOCl_3$ chemisorption was determined to be (1.47 ± 0.09) mmol V/g silica and (1.48 ± 0.06) mmol Al/g silica, respectively, Table 5.2. The ratios of chemisorbed V and Al to surface hydroxyl groups are therefore (1.82 ± 0.10) and (1.83 ± 0.07), respectively, and the ratio of Al:V:OH is 2:2:1.

Table 5.2 Quantitative analysis of grafting of $VOCl_3$ on TMA-modified A380-500 [a]

Al mmol/g	Al/OH	V mmol/g	V/OH	CH_3Cl mmol/g	CH_3Cl/OH	Al:V:CH_3Cl
1.50	1.85	1.53	1.89	1.60	1.98	1.00:1.02:1.07
1.60	1.98	1.66	2.05	-	-	1.00:1.04: -
1.44	1.78	1.38	1.75	1.41	1.74	1.00:0.96:0.98
1.53	1.89	1.51	1.86	-	-	1.00:0.99: -
1.40	1.73	1.42	1.75	1.45	1.79	1.00:1.01:1.04
1.44	1.78	1.43	1.77	1.52	1.88	1.00:0.99:1.06
1.49	1.84	1.51	1.86	1.43	1.76	1.00:1.01:1.04
1.45	1.79	1.41	1.74	1.43	1.77	1.00:0.97:0.97
1.42	1.75	1.38	1.75	1.38	1.70	1.00:0.97:0.97
1.48 ± 0.06	1.83 ± 0.07	1.47 ± 0.09	1.82 ± 0.10	1.46 ± 0.07	1.80 ± 0.09	1.00:0.99:0.99

[a] Hydroxyl content is (0.81±0.03) mmol OH/g silica after 500°C treatment.

Hydrolysis also resulted in the liberation of (3.20 ± 0.06) mmol HCl/g silica corresponding to 3.95 HCl per original silanol. Thus the total chloride recovered during grafting (1.80 equiv. per OH as CH_3Cl) and hydrolysis (3.95 equiv. per OH as HCl) is (5.75 ± 0.32) equiv. per OH. Our finding that a total of 6 equiv. of Cl are involved in the reaction with **1** suggest that 2 equiv.$VOCl_3$ react. Thus, the reaction stoichiometry can be formulated as in eq. 5.2:

$$\equiv SiOAl_2(CH_2)(CH_3)_3 \quad (\mathbf{1}) \quad + \quad 2\ VOCl_3 \longrightarrow \equiv SiOAl_2(CH_2)(CH_3)(VOCl_2)_2 \quad (\mathbf{2}) \quad + \quad 2\ CH_3Cl \qquad (5.2)$$

The oxidation state of the vanadium was determined to be (III) by measuring the quantity of oxygen consumed during the reoxidation of V(III) to V(V), according to eq. 5.3:

$$V^{+3} \quad + \quad 1/2\ O_2 \longrightarrow \quad V^{+5} \quad + \quad O^{-2} \qquad (5.3)$$

where (0.67 ± 0.09) mmol oxygen were used to reoxidize (1.42 ± 0.05) mmol vanadium.

5.3.2 Infrared characterization

The reaction of aluminum-modified silica with $VOCl_3$ results in several changes in the IR spectrum. The peaks found in the ν(C-H) region, Figure 5.2c, decrease in intensity. Two small peaks remain at 2960 and 2907 cm^{-1}, with roughly 30% of the original peak area. These changes are similar to those observed upon reaction of TMA-modified silica with either water[1,11] or $TiCl_4$.[12]

In the deformation region, the weak band at 1435 cm^{-1} completely disappears, Figure 5.3b, while the band at 1412 cm^{-1} did not change. In the low frequency region, the spectrum of the silica thin film shows a new, strong peak at 917 cm^{-1}, Figure 5.4i. We assign this band to a vibration (Al-O-V). By spectral subtraction of the thin film spectra, Figure 5.5i, the bands at 820 and 862 cm^{-1} are seen to decrease in intensity. The peak at 715 cm^{-1} has almost completely disappeared, while the peak at 689 cm^{-1} remains unchanged.

5.3.3 ESR spectroscopy

The ESR spectrum recorded after A380/TMA is exposed to $VOCl_3$ is shown in Figure 5.6i. The appearance of a signal with hyperfine splitting to the ^{51}V nucleus (I = 7/2) is evidence of reduction of vanadium. A broad background and some weak satellite lines are observed.

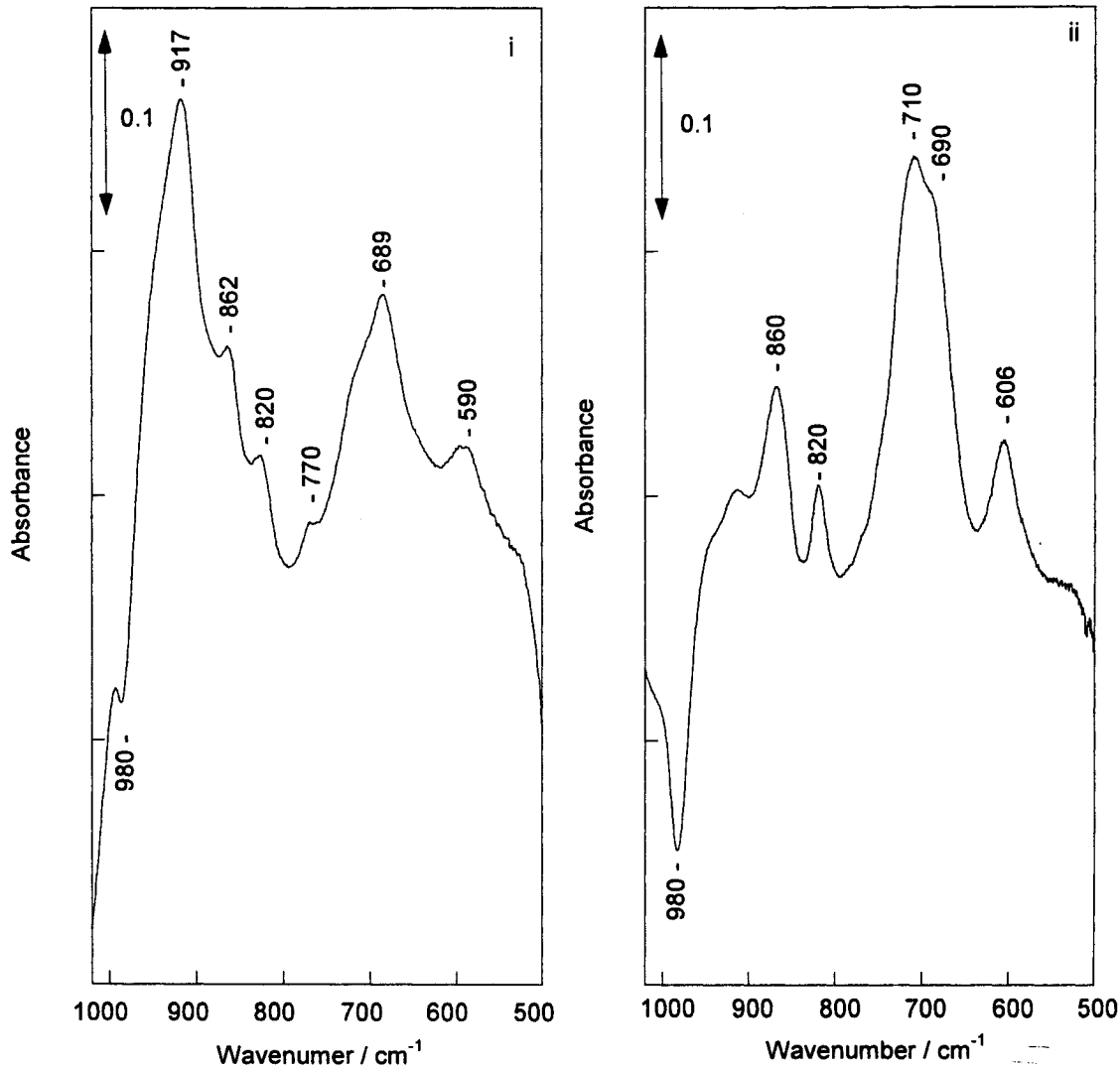

Figure 5.5 Difference Infrared spectra in the low frequency region of a ZnSe-supported silica thin film of (i) A380/TMA/$VOCl_3$, (ii) A380/TMA/$VOCl_3$/TMA. The difference spectra were generated by subtracting the spectrum of A380.

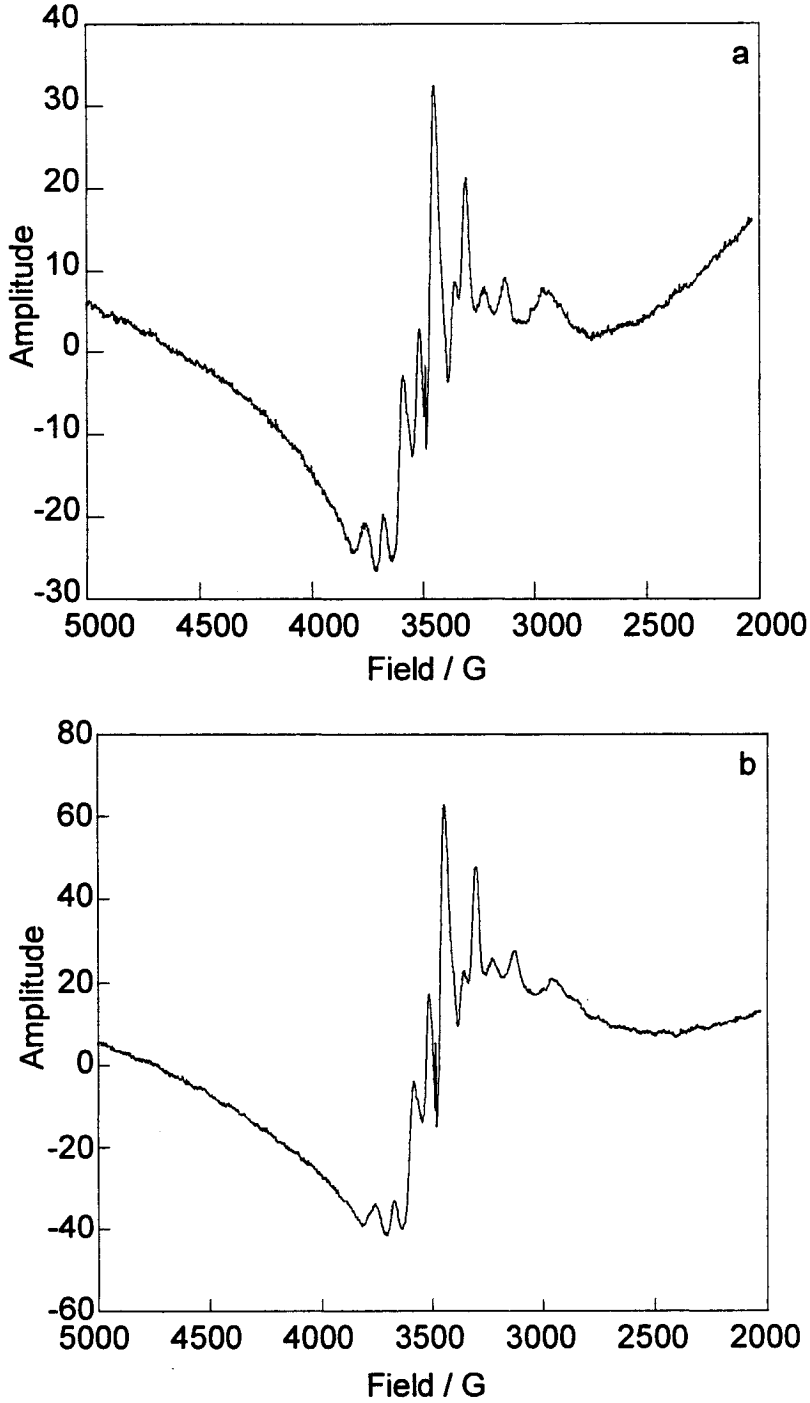

Figure 5.6 ESR spectra of (a) A380/TMA/$VOCl_3$, (b) A380/TMA/$VOCl_3$/TMA.

5.3.4 Proposed structure

As we will discuss later, disruption of the Si-O-Al bonds of A380/TMA by $VOCl_3$ and their replacement by Si-O-V anchoring sites is unlikely due to greater stability of Al-O bonds relative to V-O bonds.[13] Therefore, we suggest that the first step in the $VOCl_3$ grafting reaction is its binding to an empty coordination site at aluminum, forming the Lewis adduct **2a**. The adduct may then proceed to eliminate one equivalent of CH_3Cl, with formation of an oxo-bridged intermediate **2b**. In order to attain the observed reaction stoichiometry, another $VOCl_3$ must bind to the second Al center, as in **2d**, at an open coordination site created by migration of a mobile methyl ligand. This adduct may then eliminate a second equivalent of CH_3Cl, forming the final product **2**. These rearrangements are shown in Scheme 5.1.

We remind the reader that the "structures" shown in Scheme 5.1 merely represent the empirical composition of each intermediate, since we have no direct structural information about the organization of the ligands around each metal. Due to their paramagnetism, these materials do not give useful NMR spectra. Furthermore, these systems are not candidates for XAS structural analysis, since their complexity will result in a superposition of signals which is difficult to deconvolute. However, we may speculate about the structure of **2** by analogy to molecular complexes with similar compositions. For example, the oligomeric alkylalumoxanes $(RAlO)_n$ are known to have cage structures with three-coordinate oxygen vertices.[14]

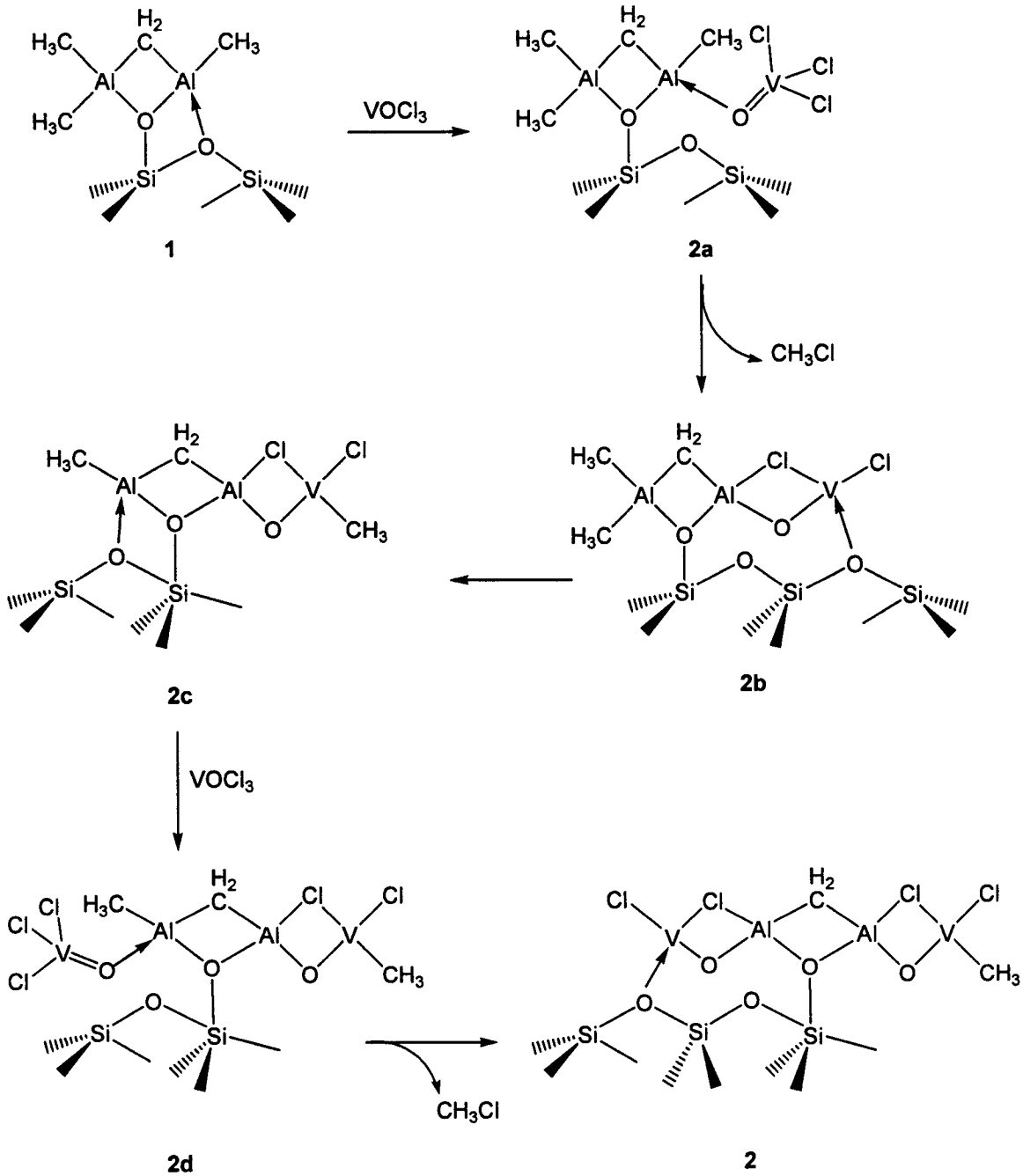

Scheme 5.1 Proposed mechanism for the reaction of $VOCl_3$ with TMA-modified silica.

5.4 Reaction of $AlMe_3$ with A380/TMA/$VOCl_3$

When **2** was exposed to TMA vapor at room temperature, its color changed from dark green to dark brown, suggesting further changes in the oxidation state of vanadium and/or the nature of its ligands. CH_4 was detected as the exclusive gas phase product by IR, GC and GC-MS. 0.72±0.11 mmol O_2 was consumed during reoxidation of 1.45 mmol vanadium to V(V) as described above indicates that the oxidation state of vanadium is (III).

5.4.1 Stoichiometry of the reaction

Elemental analysis of the product after prolonged desorption of volatiles under dynamic vacuum revealed the presence of (2.99 ± 0.16) mmol Al/g silica corresponding to (3.69 ± 0.18) equiv. Al per original OH, Table 5.3, and a doubling of the original Al content of A380/TMA. The vanadium content remained unchanged at (1.45 ± 0.05) mmol V/g silica. Therefore the ratio of Al:V is 2:1.

The methane yield was quantified by IR gas phase to be (1.64 ± 0.06) mmol/g silica, equivalent to (2.02 ± 0.07) per original silanol. Calcination of the material at 500°C in 400 Torr oxygen caused complete loss of surface hydrocarbyl groups with formation of H_2O and (5.0 ± 0.2) mmol CO_2/g silica, equivalent to 6.1 C per original silanol. Thus the total carbon recovered from the first grafting of TMA (1.74 as CH_4/OH), grafting of $VOCl_3$ (1.80 as CH_3Cl/OH), second grafting of TMA (2.02 as CH_4/OH) and subsequent calcinations

Table 5.3 Quantitative analysis of grafting of trimethylaluminum on A380/TMA/$VOCl_3$[a]

V mmol/g	V/OH	Al mmol/g	Al/OH	CH_4 mmol/g	CH_4/OH	Al:V:CH_4
1.42	1.75	3.20	3.95	1.69	2.09	2.25:1.00:1.19
1.43	1.77	2.82	3.48	1.54	1.90	1.97:1.00:1.08
1.51	1.86	3.14	3.87	1.65	2.03	2.01:1.00:1.09
1.48	1.83	2.95	3.64	1.67	2.06	1.99:1.00:1.12
1.38	1.71	2.84	3.50	-	-	2.05:1.00: -
1.44	1.78	2.96	3.65	-	-	2.05:1.00: -
-	-	1.87[b]	2.31[b]	1.70	2.09	-
-	-	-	-	1.70	2.09	-
-	-	-	-	1.59	1.96	-
1.45 ± 0.05	1.79 ± 0 .05	2.99 ± 0.16	3.69 ± 0.18	1.64 ± 0.06	2.02 ± 0.07	2.05:1.00:1.13

[a] Hydroxyl content of A380 is (0.81±0.03) mmol OH/g silica after 500°C treatment.

[b] Excluded from the average as it is obviously an outlier.

(6.10 as CO_2/OH) is (11.66 ± 0.6) per original OH site. The reaction stoichiometry can therefore be written as in eq. 5.4:

$$\equiv SiOAl_2(CH_2)(CH_3)(VOCl_2)_2 \quad + \quad Al_2Me_6 \longrightarrow$$

2

$$\equiv SiOAl_4(CH_2)_3(CH_3)_3(VOCl_2)_2 \quad + \quad 2\ CH_4 \qquad (5.4)$$

3

5.4.2 Infrared characterization

The IR spectrum of the product is similar to that observed after the reaction of the TMA with silica. No hydroxyl groups reappeared, Figure 5.1d. The IR spectrum of a self-supporting disk of the product shows vibrations in the ν(C-H) region, Figure 5.2d, similar to those bands observed after the reaction of TMA with silica (2831, 2900, 2946 and 2962 cm^{-1}) as well as a minor band at 2855 cm-^{1}. The latter has been assigned to the C-H vibration of methoxy groups in samples exposed to adventitious O_2.[1]

In the low frequency region, the band at 715 cm^{-1}, previously observed upon initial addition of $AlMe_3$ to silica, reappeared, while the band at 920 cm^{-1} almost completely disappeared, Figure 5.4d. These changes are seen more clearly by spectral subtraction in the region of the partial IR transparency of a thin film, Figure 5.5ii.

5.4.3 ESR Spectroscopy

The material **3** is ESR-active, with the spectrum shown in Figure 5.6ii. Hyperfine interaction characteristic of ^{51}V similar to that observed for material **2** is observed indicates that both have vanadium with same oxidation state.

5.4.4 Proposed Structure

TMA is a Lewis acid which also serves as a reducing and alkylating agent for transition metal complexes. Regardless of the detailed structure of **2**, the first step in its reaction with TMA is likely coordination at the bridging oxygen sites, forming a Lewis adduct such as **3a**.[16,17] The next step may be ligand exchange and transfer of methyl groups to vanadium, forming the intermediate **3b**. Alkyl transfer from aluminum to vanadium has been reported for the reactions of $Al(CH_2SiMe_3)_3$ with $V(O)(CH_2SiMe_3)_n(OSiPh_3)_{3-n}$ (n = 0-3)[8] and with a vanadium(V) silsesquioxane.[9] The formation of two equivalents of methane suggests that this step is followed by C-H activation to give the product **3** which must contain two additional bridging methylenes, Scheme 5.2. Facile C-H activation in early transition metal-TMA adducts has already been reported.[15]

The empirical composition of **3** is $\equiv SiOAl_4V_2O_2Cl_4(CH_2)_3(CH_3)_3$. The analogous alkylalumoxane has a drum structure. We therefore suggest the following as a possible structure for **3**:

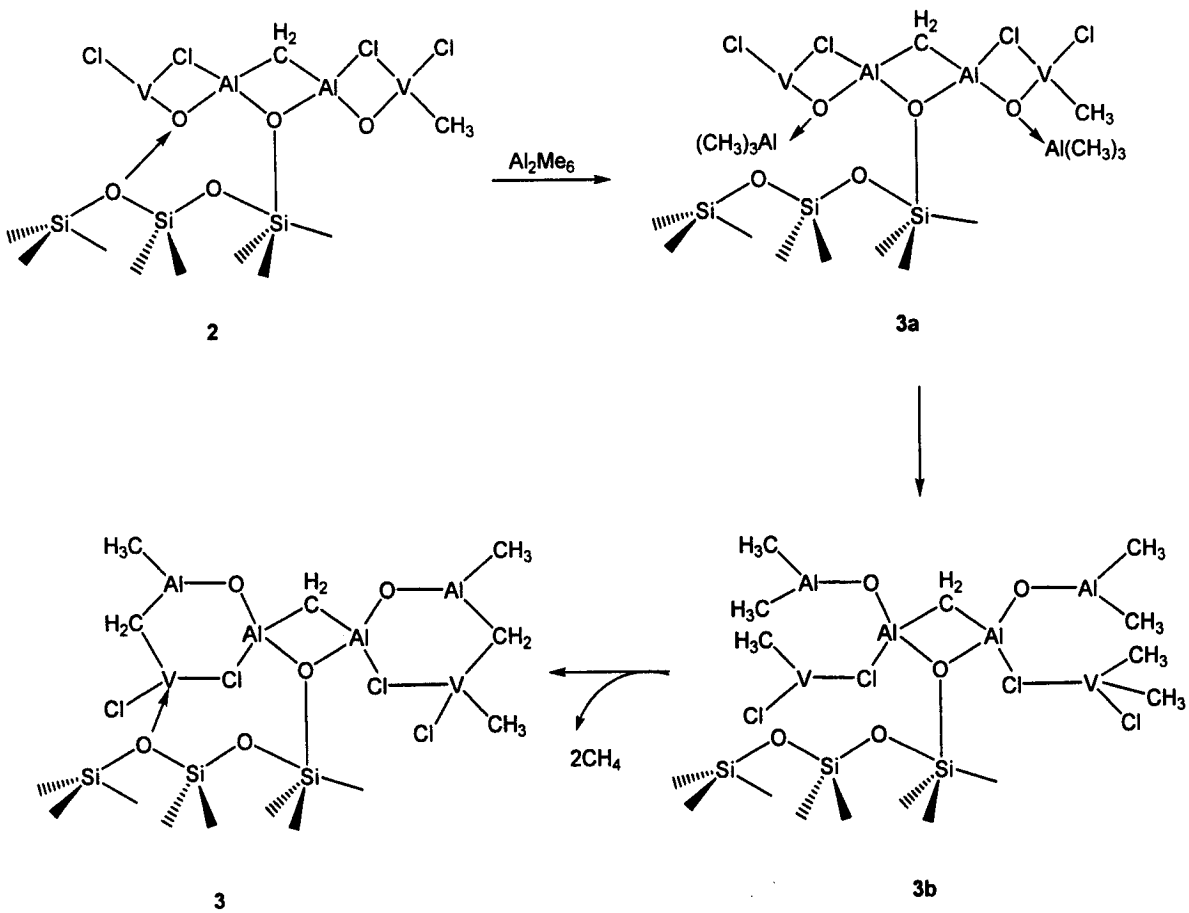

Scheme 5.2 Proposed mechanism for the reaction of TMA with **2.**

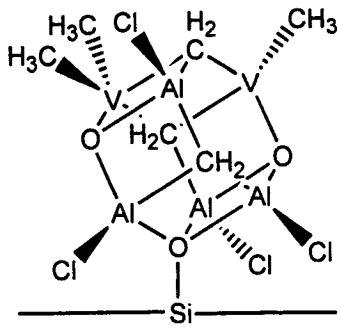

3

5.5 Reaction of $AlMe_3$ with vanadium-modified silica

When $\equiv SiOVOCl_2$ is exposed to an excess of TMA vapor at room temperature, a chemical reaction takes place resulting in the formation of **4**, with a concomitant color change from white to dark violet and liberation of CH_4, CH_3CH_3 and CH_3Cl as gaseous products detected by IR, GC and GC-MS. The change in color is assumed to result from the reduction of vanadium(V). The oxidation state of vanadium was determined by measuring the amount of oxygen consumed during its re-oxidation to vanadium(V), as described above. The average vanadium oxidation state was found to be (IV), where (0.17 ± 0.04) mmol O_2 was used during reoxidation of (0.67 ± 0.05) mmol V to V(V).

5.5.1 Stoichiometry of the reaction

As already mentioned, $VOCl_3$ chemisorption measurements indicate that A380-500 contains (0.81 ± 0.03) mmol of accessible OH/g silica. Elemental analysis of

the material after reaction with excess TMA and prolonged desorption of volatile products under dynamic vacuum revealed the presence of (0.65 ± 0.03) mmol V/g silica and (1.52 ± 0.08) mmol Al/g silica. The ratio of chemisorbed vanadium and aluminum to surface hydroxyl groups is therefore (0.81 ± 0.03) and (1.88 ± 0.10), respectively, Table 5.4.

We note that treatment of the vanadium-modified silica with TMA results in a significant decrease in its vanadium content from 0.81 to 0.65 mmol/g silica. Similar results were observed previously for the Ti content of a $TiCl_4/MgCl_2$ catalyst treated with $AlEt_3$ or $AlEt_2Cl$ at ambient temperature and a molar ratio Al/Ti of 1-2.[18,19]

When excess TMA was added to a sample of vanadium-modified silica, (1.41 ± 0.06) mmol CH_4/g silica was evolved, which corresponds to (1.74 ± 0.07) equiv. CH_4 per ≡SiOH, Table 5.4. The ethane yield was found to be (0.35 ± 0.04) mmol/g, which is equivalent to (0.44 ± 0.05) CH_3CH_3/OH. Finally (0.15 ± 0.03) mmol CH_3Cl/g silica was liberated, the yield determined by measuring the intensity of ν(C-Cl) band at 731 cm^{-1}, after destroying the excess TMA by addition of H_2O vapor. Quantitation of CH_3Cl by GC gave the same result.

Hydrolysis of A380/$VOCl_3$/TMA with excess water vapor at room temperature resulted in liberation of (2.4 ± 0.1) mmol CH_4/g silica, corresponding to (3.0 ± 0.1) CH_4 per original silanol. Thus the total CH_4 recovered from grafting TMA (1.74 as CH_4/OH, 0.43 as CH_3CH_3 and 0.19 as CH_3Cl) and subsequent hydrolysis (3.00 as CH_4/OH), is 5.79 per original OH site, indicating that the chemisorbed organometallic fragment is binuclear in aluminum. Furthermore,

Table 5.4: Quantitative analysis of grafting of TMA on vanadium-modified A380-500 [a, b]

V mmol	V/OH	Al mmol	Al/OH	Products of grafting			
				CH_4 mmol	CH_4/OH	C_2H_6 mmol	C_2H_6/OH
0.66	0.83	1.49	1.84	1.43	1.77	0.40	0.49
0.65	0.81	1.44	1.78	-	-	-	-
0.70	0.86	1.57	1.94	-	-	-	-
0.69	0.86	1.49	1.84	-	-	-	-
0.62	0.78	1.63	2.01	1.50	1.85	0.33	0.41
0.62	0.78	1.63	2.01	1.35	1.67	0.31	0.38
0.63	0.79	1.56	1.92	1.38	1.70	0.38	0.47
0.61	0.76	1.51	1.86	-	-	-	-
0.67	0.84	1.37	1.69	1.38	1.70	0.34	0.42
0.65 ± 0.03	0.81 ± 0.03	1.52 ± 0.08	1.88 ± 0.10	1.41 ± 0.06	1.74 ± 0.07	0.35 ± 0.04	0.43 ± 0.05

[a] Hydroxyl content is (0.81±0.03) mmol OH/g silica after 500°C treatment.

[b] All values are normalized per gram of silica.

hydrolysis led to the liberation of (1.32 ± 0.05) HCl/g silica, which is equivalent to 2.03 Cl/V. Calcination at 500°C in 400 Torr O_2 resulted in the liberation of (2.20 ± 0.15) CO_2/g silica. Thus the total carbon recovered in grafting and calcination is 4.46 mmol/g silica, which is equivalent to 3 C/Al.

Although the stoichiometry of this surface reaction is more complex than those considered previously, we identify the major surface fragment as a trinuclear complex Al_2V, or possibly a dimer of trinuclear complexes $[Al_2V]_2$. The formation of methane proceeds in a straightforward manner by C-H activation, as before, and results in the formation of two methylene bridges per Al_2V unit. Both CH_3CH_3 and CH_3Cl products can be considered to arise from reductive elimination, of two methyl ligands or one methyl and one chloride ligand, respectively. The *sum* of their yields is 0.62 mmol per original OH or per Al_2V unit, implying a reduction in V oxidation state. Therefore, reductive elimination is presumed to occur across two Al_2V units, with the overall stoichiometry shown in eq. 5.5:

$$2\ \equiv SiOVOCl_2 + 2\ Al_2Me_6 \rightarrow [\equiv SiOAl_2(CH_2)_2(CH_3)VOCl_2]_2 + CH_3CH_3 + 4\ CH_4 \quad (5.5)$$

4

5.5.2 Infrared characterization

The IR spectrum of a self-supporting disk of A380/$VOCl_3$/TMA showed no changes in the ν(O-H) region, confirming that residual unreacted hydroxyl groups are inaccessible to TMA, Figure 5.7. However, several changes were observed in the ν(C-H) and low frequency regions.

New vibrations in the ν(C-H) region are similar to those observed upon reaction of silica with TMA (2962 sh, 2941, 2898 and 2831 cm^{-1}), Figure 5.8, and two weak deformation bands are observed at 1432 and 1413 cm^{-1}, Figure 5.9i. Bands characteristic of =$SiOVOCl_2$, including the overtone 2ν(V=O) at 2070 cm^{-1}, Figure 5.9ii, ν(V=O) at 1043 and ν(V-Cl) at 505 cm^{-1}, Figure 5.10, completely disappear. In the low frequency region, new bands at 688 and 715 cm^{-1} are similar to those observed after addition of TMA to silica, Figure 5.11.

5.5.3 ESR Spectroscopy

The ESR spectrum recorded after A380/$VOCl_3$ is exposed to TMA is shown in Figure 5.12. Once again the appearance of a strong ESR signal with eight-line hyperfine splitting to the ^{51}V nucleus (I = 7/2) is evidence of reduction of vanadium, probably to V(IV) state. The similarity of the ESR signal in its shape with the signals reported in the previous literatures[20-22] with g value equal 1.937 indicated that the sample containing vanadium in oxidation state (IV).

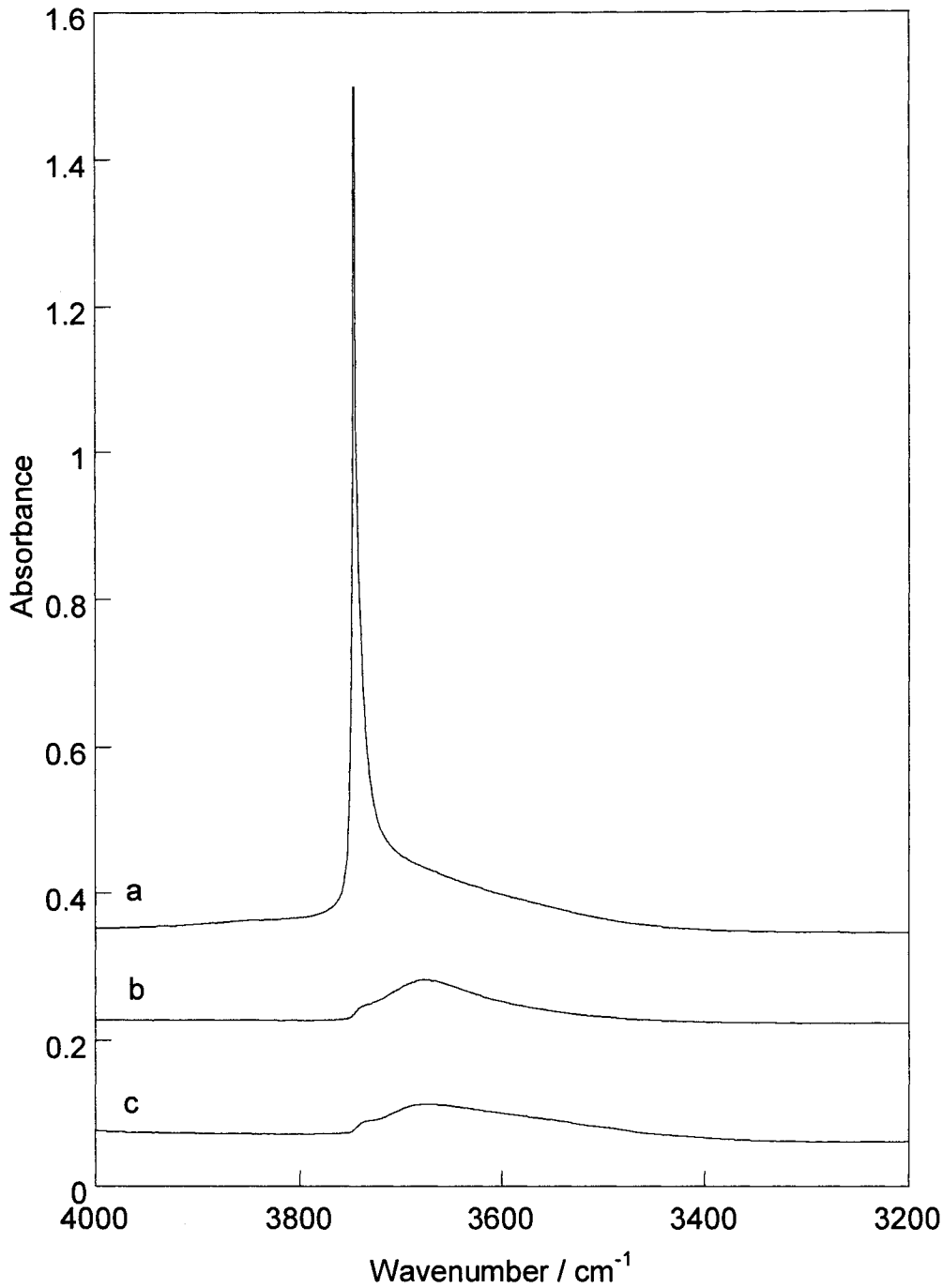

Figure 5.7 Infrared spectra of a self-supporting disk, in the ν(O-H) region, of (a) A380-500, (b) A380/$VOCl_3$, (c) A380/$VOCl_3$/TMA.

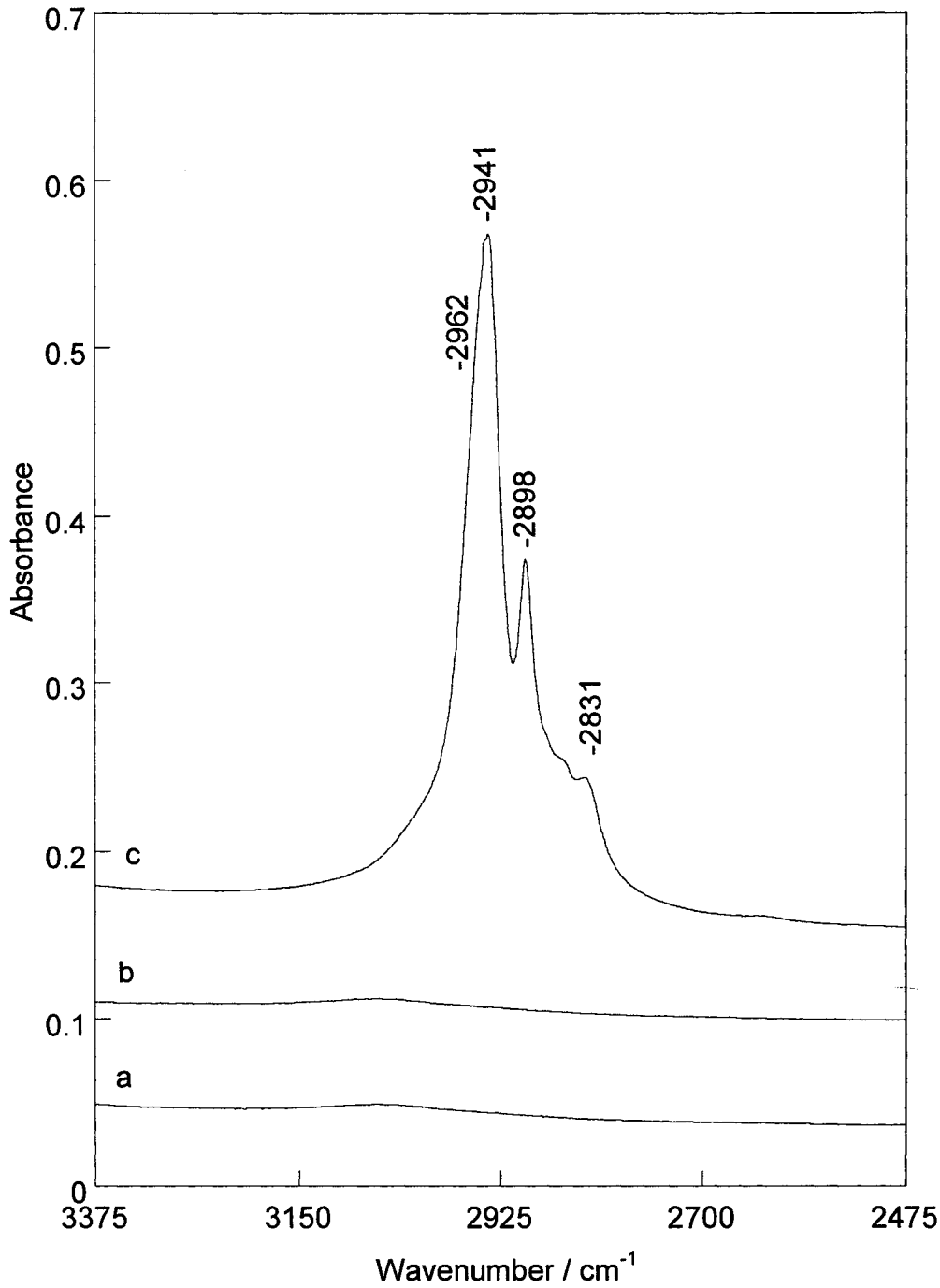

Figure 5.8 Infrared spectra in the ν(C-H) region of a self-supporting disk of (a) A380-500, (b) A380/$VOCl_3$, (c) A380/$VOCl_3$/TMA.

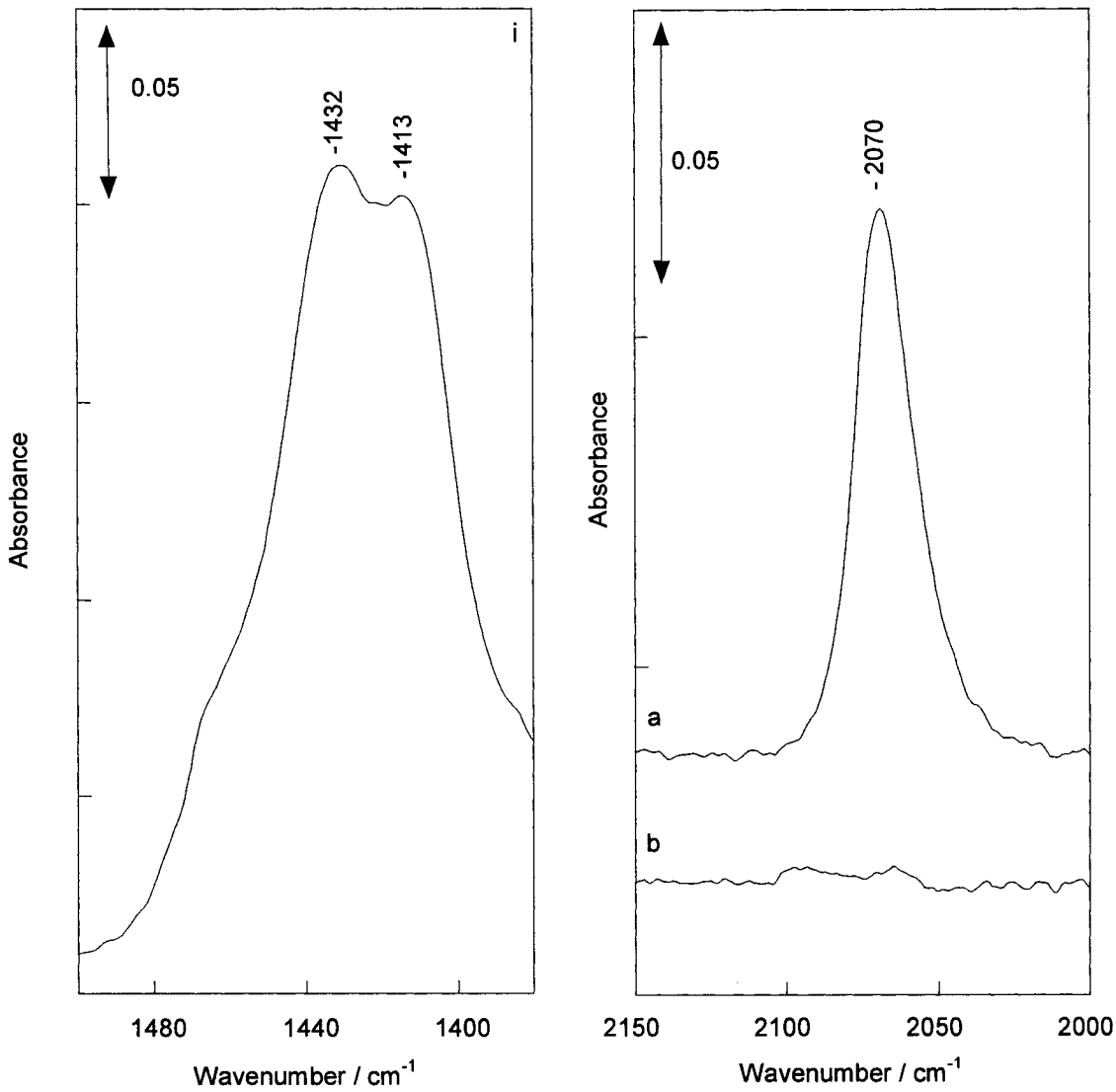

Figure 5.9 Difference infrared spectra of a self-supporting disk showing (i) the $\delta(CH_3)$ region for A380/$VOCl_3$/TMA; (ii) the $\nu(V=O)$ overtone region for (a) A380/$VOCl_3$, (b) A380/$VOCl_3$/TMA. The difference spectra were generated by subtracting the spectrum of A380.

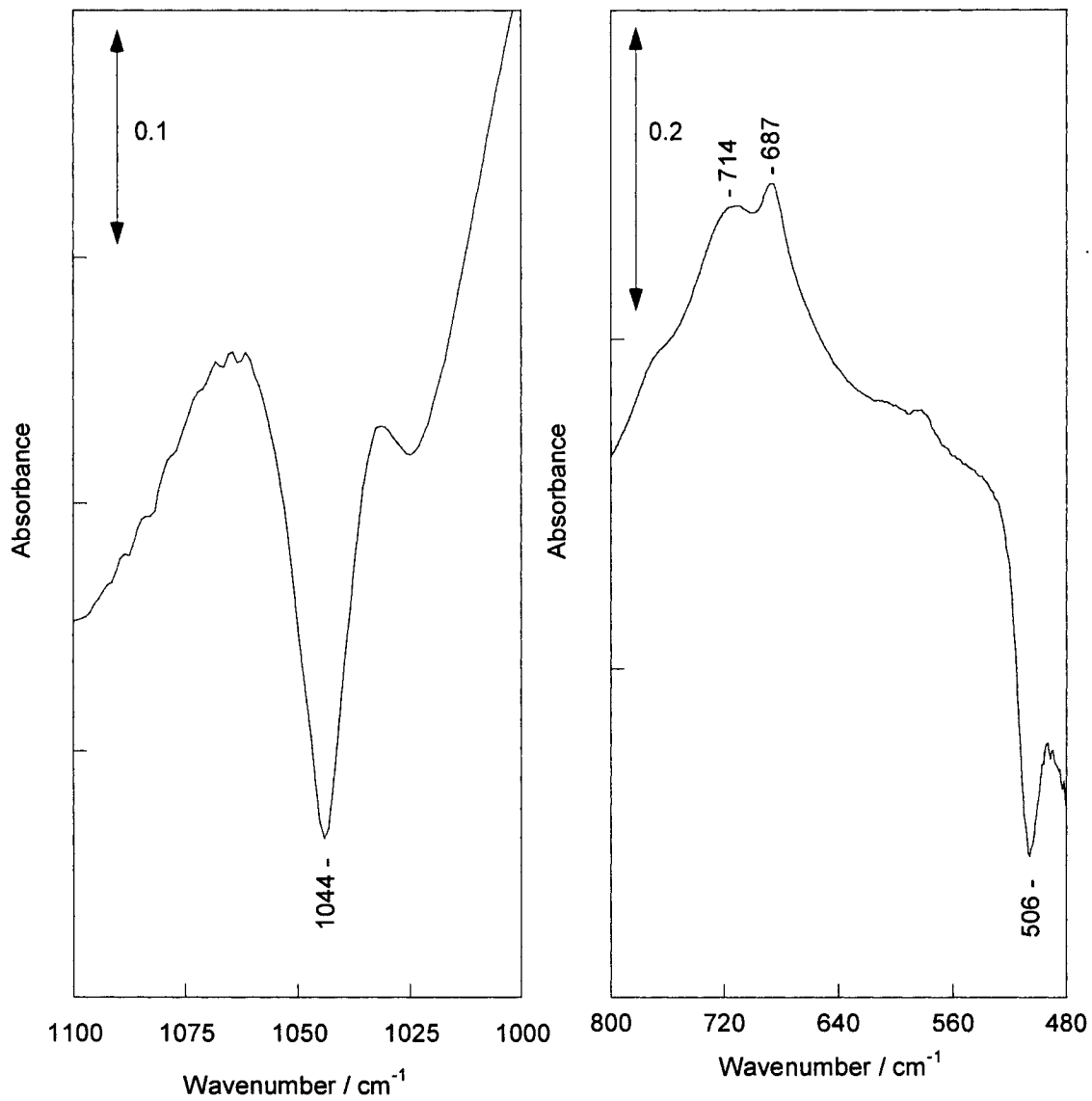

Figure 5.10 Difference infrared spectra in the low frequency region of a ZnSe-supported silica thin film of A380/$VOCl_3$/TMA. The difference spectra were generated by subtracting the spectrum of A380/$VOCl_3$.

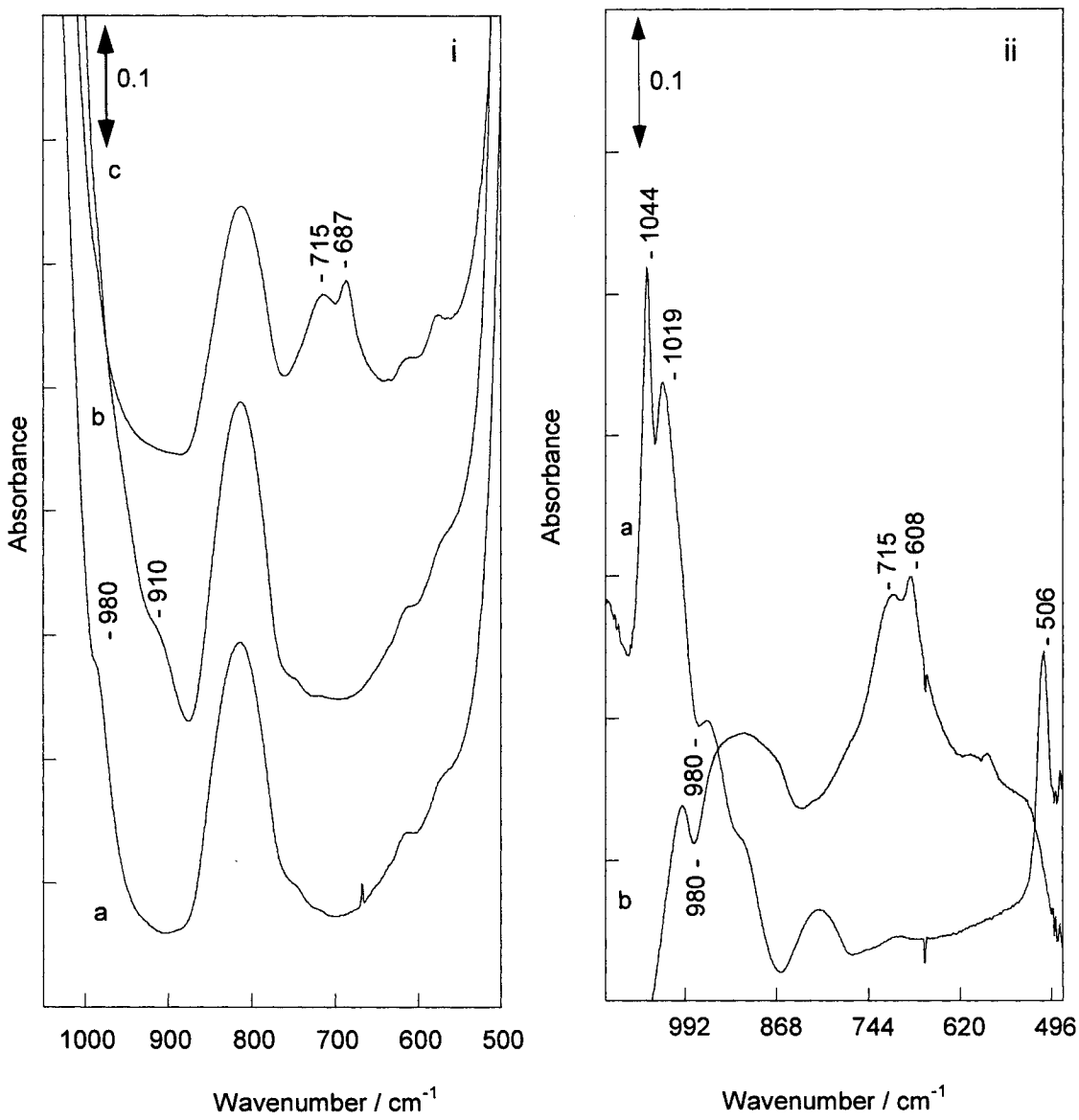

Figure 5.11 Infrared spectra in the low frequency region of a ZnSe-supported silica thin film. Frame (i): a) A380-450, b) A380/$VOCl_3$, c) A380/$VOCl_3$/TMA. Frame (ii): difference spectrum of A380/$VOCl_3$/TMA. The difference spectrum was generated by subtracting the spectrum of A380.

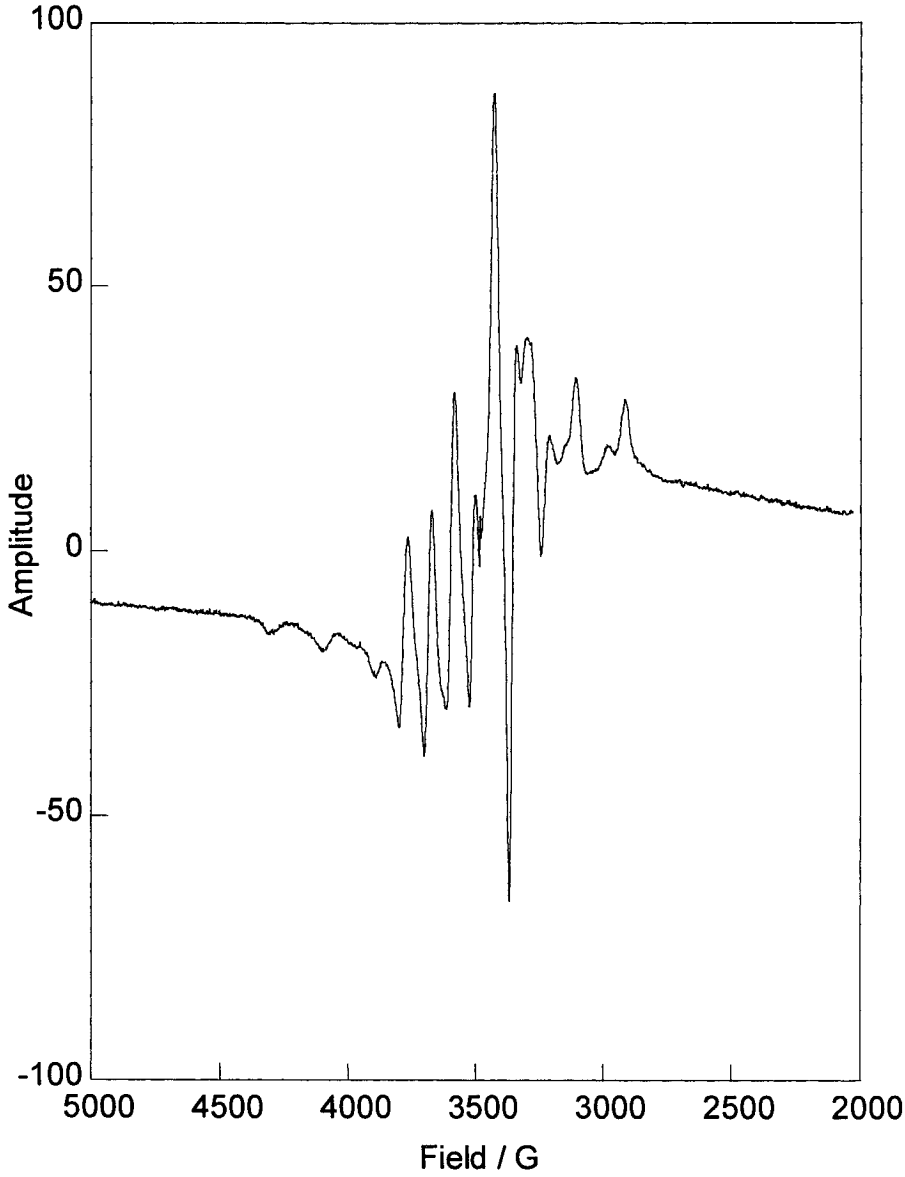

Figure 5.12 ESR spectrum of A380/$VOCl_3$/TMA.

5.5.4 Proposed structure

$VOCl_3$-modified silica has two potential binding sites for $AlMe_3$: the vanadyl oxygen V=O and the bridging oxygen (Si-O-V). Since the reaction stoichiometry indicates that two equivalents of $AlMe_3$ are involved and two equivalents of methane are released, we suggest that $AlMe_3$ coordinates at both sites, forming the Lewis adduct **4a**.

Participation of the V=O is confirmed by disappearance of the ν(V=O) fundamental at 1043 cm^{-1} and the 2ν(V=O) overtone at 2070 cm^{-1}. The same observation has been reported by other groups.[9] The coordination of a second equivalent of $AlMe_3$ to the oxygen atom of (Si-O-V) may be the cause of displacement of vanadium from the surface with formation of the more stable (μ-$SiOAl_2$) structure characteristic of silica/TMA. Similar behavior has been reported in the reaction of $AlMe_3$ with $\equiv SiOTiCl_3$.[22]

The next step is methyl migration from aluminum to vanadium, to give **4b**, followed by C-H activation releasing two moles of methane and forming methylene bridges between Al and V, **4c**. Chloride transfer from V to Al is suggested by the disappearance of the ν(V-Cl) mode upon addition of $AlMe_3$.

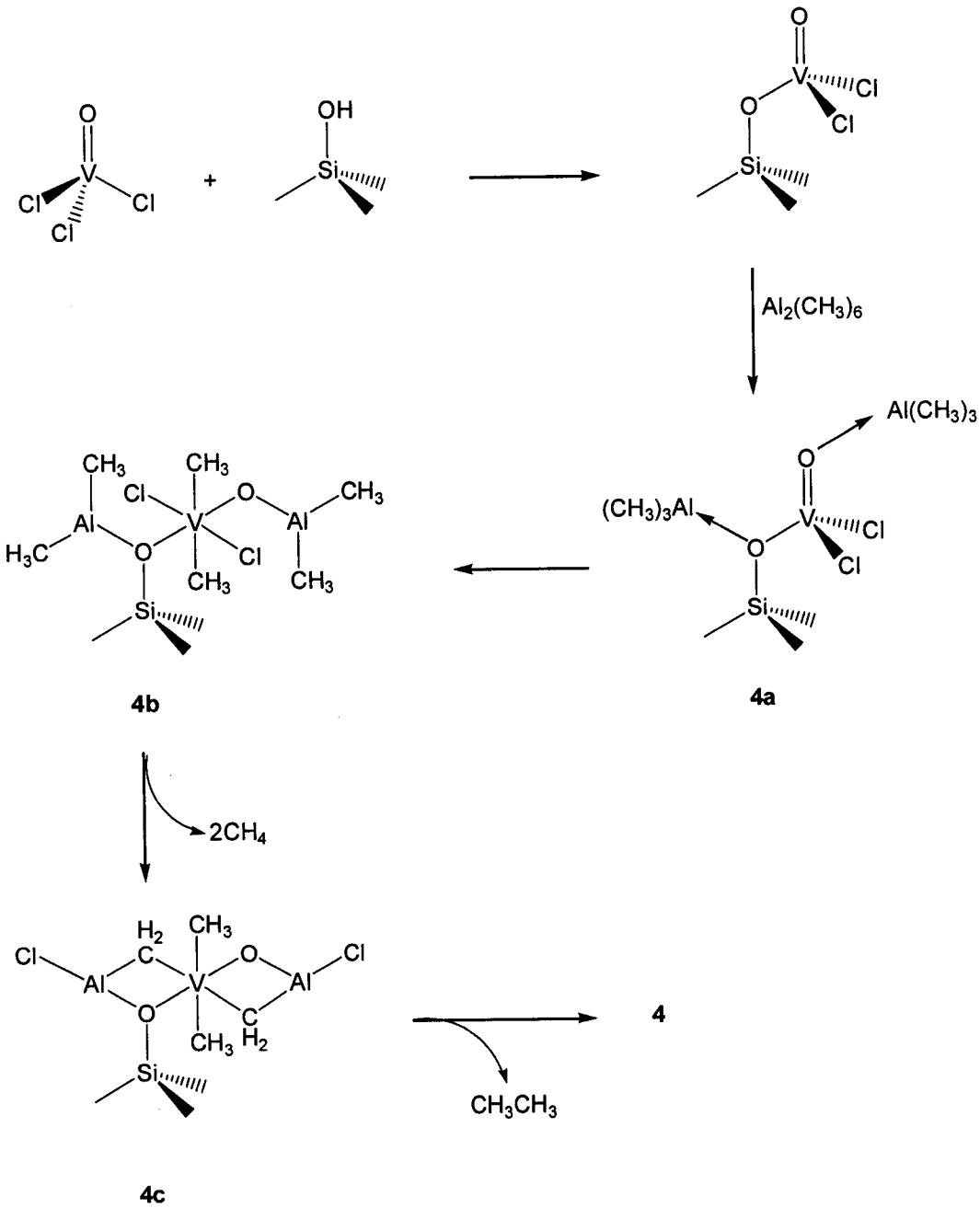

Scheme 5.3 Proposed mechanism for the reaction of $AlMe_3$ with vanadium-modified silica.

5.6 Conclusion

In this chapter, we have prepared $\equiv SiOAl_2(CH_2)(CH_3)(VOCl_2)_2$ (**2**) by reaction of $VOCl_3$ with TMA-modified silica, $\equiv SiOAl_2(CH_2)(CH_3)_3$ (**1**). Grafting of additional TMA on **2** led to the formation of $\equiv SiOAl(CH_2)_3(CH_3)(VOCl_2)_2$ (**3**). In contrast, TMA onto silica-supported vanadium gave $[\equiv SiOAl_2(CH_2)_2(CH_3)VOCl_2]_2$ (**4**). Each material was characterized by IR, EPR and elemental analysis. Stoichiometric ratios are remarkably close to integers, suggesting a fairly high degree of homogeneity of the supported materials. This will facilitate comparisons of their behavior as olefin polymerization catalysts, to be presented in the next chapter.

5.7 References

1) Church, T. L.; Fengfu, L.; Facey, G. A.; Mader, E. A.; Scott, S. L. submitted for publication.

2) Rice, G. L.; Scott, S. L. *Langmuir* **1997**, *13*, 1545-1551.

3) Minkova, L.; Velikova, M.; Damyanov, D. *Eur. Polym. J.* **1988**, *24*, 661-665.

4) Novokshonova, L. A.; Meshkova, I. N. *Polym. Sci.* **1994**, *36*, 1357-136.

5) Chien, J. C. W.; Hsieh, J. T. T. *Coord. Polym.* **1975**, 305-325.

6) Mcfaddin, D.; Reinking, M. J. *Polym. Sci. Part A: Polym. Chem.* **1995**, *33*, 563-570.

7) Feher, F. J.; Walzer, J. F.; Blanski, R. L. *J. Am. Chem. Soc.* **1991**, *113*, 3618-3619.

8) Feher, F. J.; Blanski, R. L. *Organomet.* **1993,** *12*, 958-963.

9) Feher, F. J.; Blanski, R. L. *J. Am. Chem. Soc.* **1992,** *114*, 5886-5887.

10) Morrow, B. A.; McFarlan, A. J. *Langmuir* **1991**, *7*, 1695-1699.

11) Yates, D. J. C.; Deinbinski, G. W.; Kroll, W. R.; Elliot, J. J. *J. Phys. Chem.* **1969**, *73*, 911-921.

12) Kinney, J. B.; Staley, R. H.; *J. Phys. Chem.* **1983**, *87*, 3735-3740.

13) Pasynkiewicz, S. *Polyhedron* **1990**, *9*, 429-453.

14) Barron, A. R. *"Alkylalumoxanes: Synthesis, Structure and Reactivity", In Metallocene-based Polyolefins,* J. Scheirs, W. Kaminsky, Eds, Wiley: New York, **2000**, p. 33-67.

15) Kickham, J. E.; Guérin, F.; Stephan, D. W. *J. Am. Chem. Soc.*, **2002**, *124*, 11468-11494.

16) Wrobel, O.; Schaper, F.; Wieser, U.; Gregorius, H.; Brintzinger, H. H. *Organometallics* **2003**, *22*, 1320-1325.

17) Mulhaupt, R.; Calabrese, J.; Itte, D. *Organometallics* **1991**, *10*, 3403-3406.

18) Potapov, A. G.; Terskikh, V. V.; Zakharv, V. A.; Bukatov, G. D. *J. Mol. Cat. A: Chem.* **1999**, *145*, 147-152.

19) Zakharov, V. A.; Makhatarulin, S. I.; Poluboyarov, V. A.; Anufrienko, V. F. *Makromol. Chem.* **1984**, *185*, 1781-1793.

20) Kucherov, A. V.; Slinkin, A. A. *J. Mol.Cata.* **1994**, *90*, 323-354.

21) Sass, C. E.; Chen, X.; Kevan, L. *J. Chem. Soc., Faraday Trans.* **1990**, *86*, 189-191.

22) Murray, J.; Sharp, J. M.; Hockey, A. J. *J. Catal.* ***1970***, *18*, 52-56.

Chapter Six

Kinetics of Olefin Polymerization by Silica-supported Vanadium Complexes

6.1 Introduction

The catalytic activity of vanadium-based polymerization catalysts is lower than that of Group IV-based Ziegler-Natta catalysts. However, the former have several advantages, including synthesis of high molecular weight polymers with narrow polydispersity, synthesis of ethylene/α-olefin copolymers with high α-olefin contents and synthesis of syndiotactic polypropylene, among others.[1,2] These unique polymer qualities make vanadium catalysts important in the manufacture of synthetic rubber and elastomers.[2] The low catalytic activity of vanadium-based catalysts is attributed to reduction of the catalytically active vanadium sites to less active or even inactive low-valent sites during polymerization.

In this chapter, we report a study of the kinetics of homopolymerization of ethylene, propylene, as well as copolymerization of ethylene-propylene mixtures, by the silica-supported vanadium catalysts described in Chapter 5. The activities of A380/TMA/$VOCl_3$ (**2**), A380/TMA/$VOCl_3$/TMA (**3**) and A380/$VOCl_3$/TMA (**4**) are compared.

6.2 Ethylene polymerization

When a 14.8 mg self–supporting disk of **4** was exposed to 20 Torr ethylene at room temperature, polymerization was detected visually, by the changes in the physical properties of the disk, as well as by in situ IR. The silica pellet underwent a color change from its original color (dark violet) to white, as a plastic film formed on its surface. The fragile silica pellet became a thick, rigid disk, eq 6.1.

$$n\ CH_2{=}CH_2 \xrightarrow{\mathbf{4}} \text{polyethylene} \qquad (6.1)$$

GC-MS analysis of the volatiles remaining after the ethylene had been consumed revealed the presence of the following oligomers: 2-butene, 1-butene, 2-methylpropene and 2,2-dimethylbutene.

The same physical observations were made when self-supporting disks of **2** or **3** were exposed to ethylene. However, in these reactions, GC-MS analysis of the volatiles revealed no oligomers.

6.2.1 Infrared characterization

The infrared difference spectrum of self-supporting disk of **4** exposed to ethylene is shown in Figure 6.1.

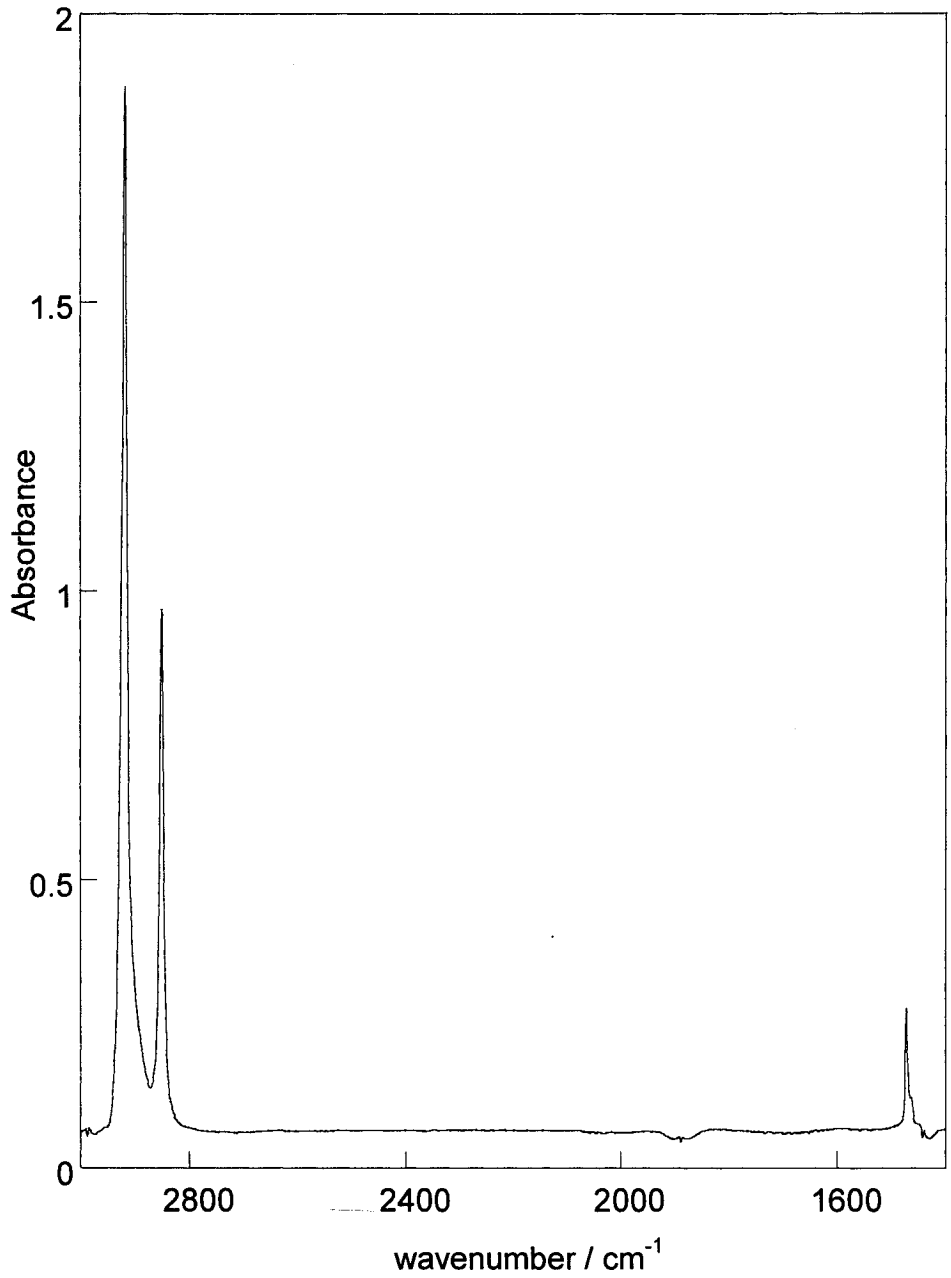

Figure 6.1. Transmission infrared difference spectrum obtained by subtraction the spectrum of **4** from its spectrum 1 hour after addition of 20 Torr ethylene at room temperature.

The spectrum shows an increase in intensity in the ν(C-H) region, with new bands at 2924 and 2850 cm^{-1} assigned to the asymmetric and symmetric CH_2 stretching modes of polyethylene.[3] The peak at 1471 cm^{-1} is attributed to methylene bending mode of polyethylene. The frequency of this band is characteristic of the crystalline phase of linear polyethylene.[3-6] In the low frequency region, the spectrum shows two new bands at 718 and 730 cm^{-1}, Figure 6.2, assigned to the methylene rocking mode.[6,7] A splitting of this mode is observed in the IR spectrum of crystalline polyethylene.[8]

6.2.2 Kinetics

The kinetics of polymerization of 100 Torr ethylene by a 107 mg sample of **4** (3.37 wt. % V) were examined at 22°C (water bath). Ethylene uptake was monitored by following the decrease in intensity of the absorbance in its gas phase IR spectrum between 1150 and 825 cm^{-1}, Figure 6.3a. The fit of the single exponential curve to the data shows that the reaction is pseudo-first-order, with k_{app} = (0.00530 ± 0.00007) min^{-1}. This experiment was repeated at 22°C with various amounts of catalyst, Figure 6.4. The pseudo-first-order rate constants are directly proportional to amount of the vanadium present, Table 6.1. The slope of the plot of k_{app} vs. number mmol vanadium present (n_v) yields the second-order rate constant k = (1.25 ± 0.01) $s^{-1}(mol\ V)^{-1}$, Figure 6.5.

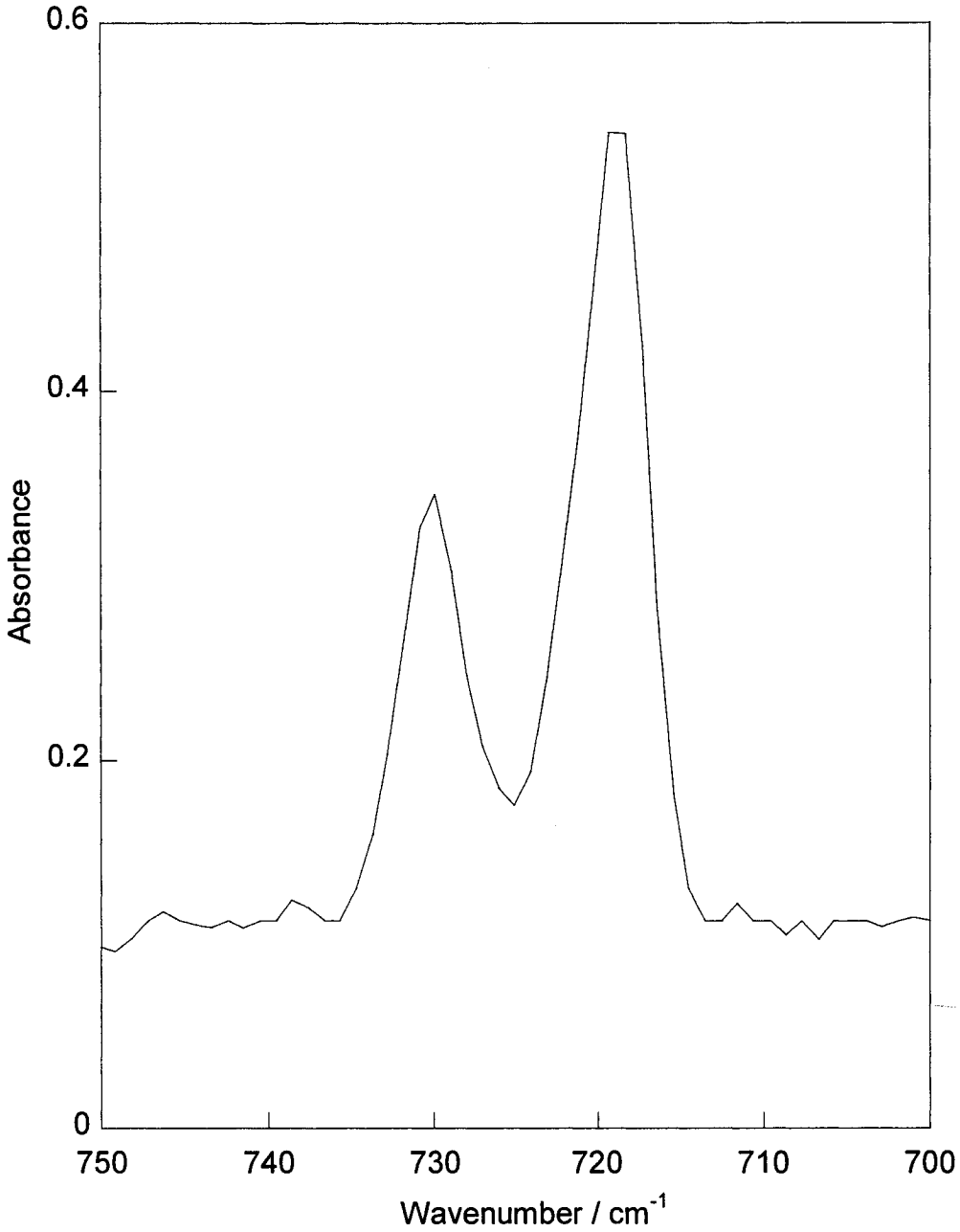

Figure 6.2. Transmission infrared difference spectrum of the same sample described in Figure 6.1, in the low frequency region.

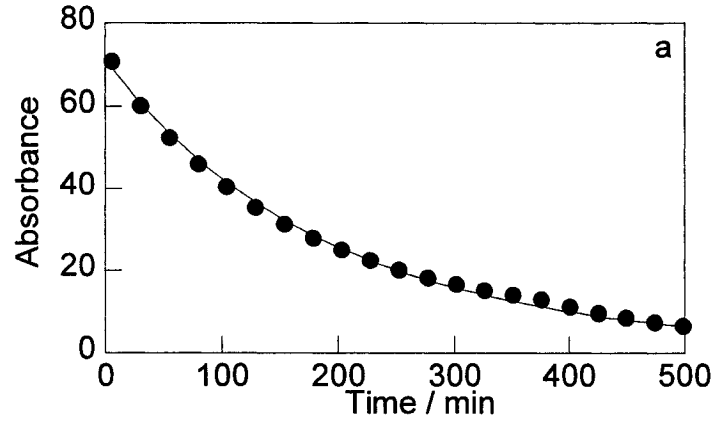

$A = A_\infty+(A_0-A_\infty)*\exp(-k_{app}t)$		
	Value	Error
A_∞	1.5	0.2
A_o	71.3	0.4
k_{app}	0.00530	0.00007
R^2	0.998	NA

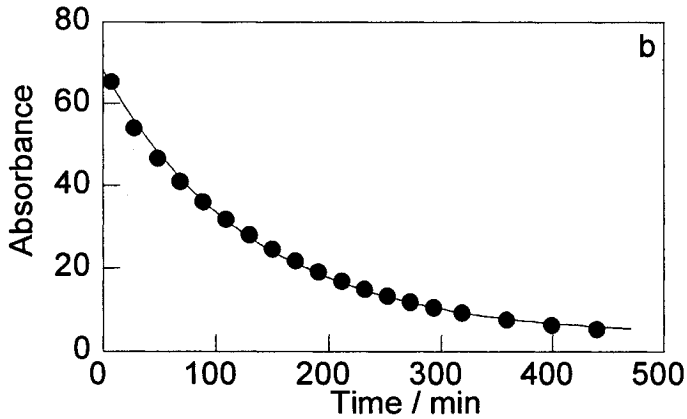

$A = A_\infty+(A_0-A_\infty)*\exp(-k_{app}t)$		
	Value	Error
A_∞	3.7	0.4
A_o	68.1	0.4
k_{app}	0.0077	0.0002
R^2	0.998	NA

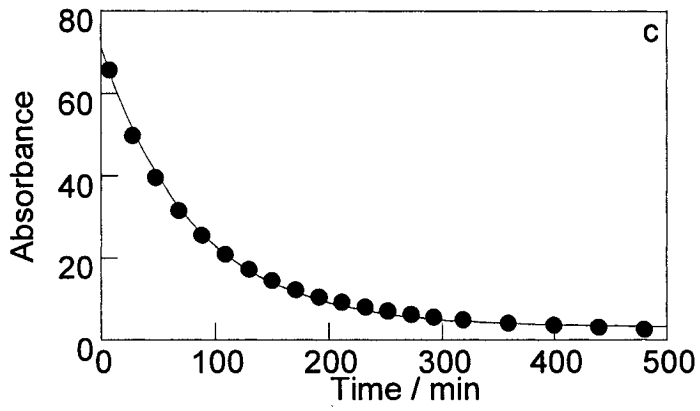

$A = A_\infty+(A_0-A_\infty)*\exp(-k_{app}t)$		
	Value	Error
A_∞	3.1	0.2
A_o	71.0	0.5
k_{app}	0.0123	0.0002
R^2	0.998	NA

Figure 6.3. Time-resolved polymerization of ethylene by **4**: (a) 107 mg, 0.0713 mmol V at 22°C; (b) 105 mg, 0.0671 mmol V at 39°C; (c) 97.1 mg, 0.0572 mmol at 67°C. Solid curves are three parameter single-exponential fits to the first-order integrated kinetic rate equation.

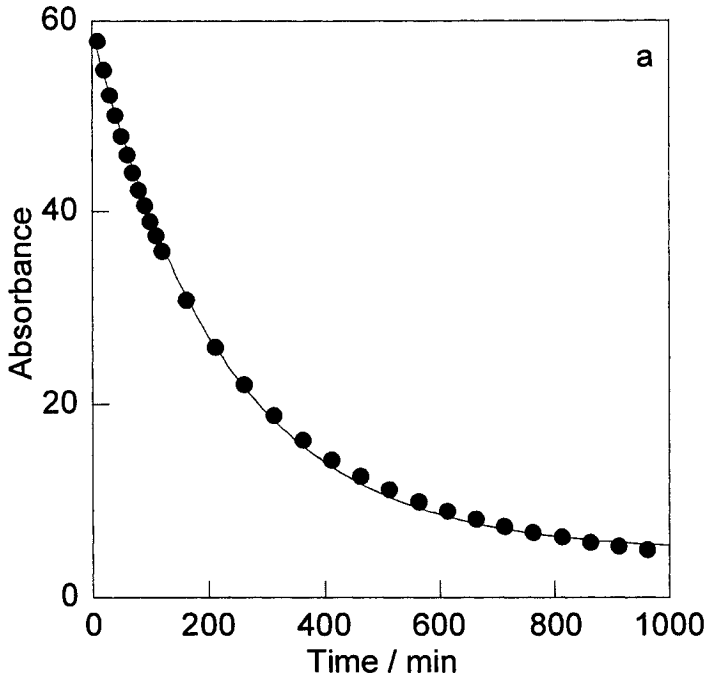

$A = A_\infty+(A_0-A_\infty)*\exp(-k_{app}t)$		
	Value	Error
A_∞	4.8	0.1
A_o	59.1	0.2
k_{app}	0.00443	0.00004
R^2	0.999	NA

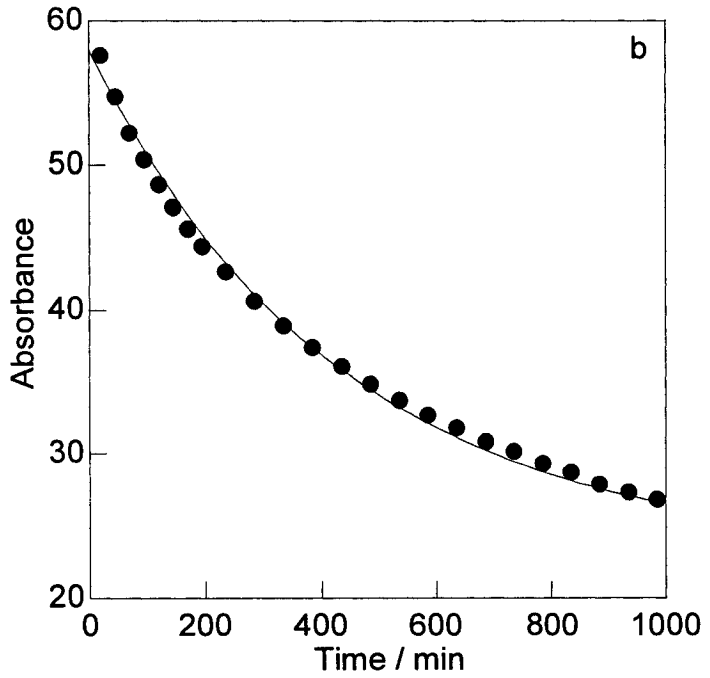

$A = A_\infty+(A_0-A_\infty)*\exp(-k_{app}t)$		
	Value	Error
A_∞	23.0	0.2
A_o	57.9	0.19
k_{app}	0.00230	0.00004
R^2	0.998	NA

Figure 6.4. Time-resolved ethylene polymerization 22°C, by (a) 100 mg **4**, 0.059 mmol V, (b) 70 mg **4**, 0.030 mmol V. Solid curves are three parameter single-exponential fits to the first-order integrated kinetic rate equation.

Table 6.1. Pseudo-first-order rate constants[a] for the polymerization of olefins by silica-supported vanadium catalysts

Catalyst	Temperature / °C	Olefin	n_v / mmol	10^{-3} k_{app} / min^{-1}
4	22	C_2H_4	0.071	5.30 ± 0.07
			0.059	4.43 ± 0.04
			0.030	2.30 ± 0.04
3	22	C_2H_4	0.188	36 ± 2
			0.125	24.4 ± 0.1
			0.073	14.2 ± 0.1
			0.054	9.9 ± 0.1
		C_2D_4	0.091	17.4 ± 0.4
			0.035	6.91 ± 0.07
			0.010	1.74 ± 0.03
		C_3H_6	0.075	1.157 ± 0.04
			0.060	0.93 ± 0.03
			0.047	0.73 ± 0.03
3	58	C_2H_4	0.155	133 ± 14
			0.057	48 ± 2
			0.087	79 ± 2

[a] Errors are from non-linear least squares fit to a single exponential function.

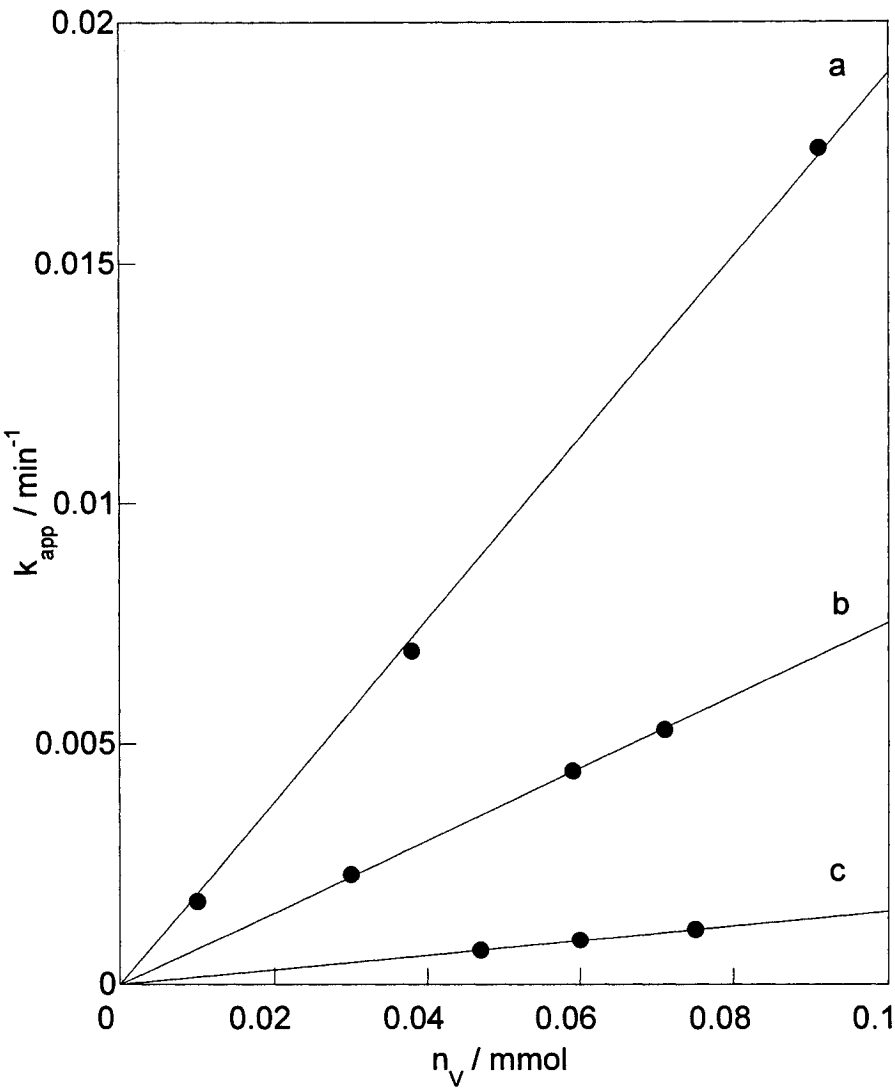

Figure 6.5. Dependence on the number of moles of V, n_v, of the pseudo-first-order rate constants for polymerization of (a) C_2D_4 by **3**; (b) C_2H_4 by **4**; (c) C_3H_6 by **3**, at 22°C.

The rate law for polymerization is therefore first-order with respect to pressure of ethylene and first-order in the number of vanadium active sites, eq. 6.2.

$$-dP(C_2H_4)/dt = k_{app}P(C_2H_4) = kn_VP(C_2H_4) \qquad (6.2)$$

Independent kinetics experiments with **4** were undertaken at 39 and 67°C. In both cases, pseudo-first-order behavior was observed, Figure 6.3b-c, with rate constants k_{app} = (0.0077 ± 0.0002) and k_{app} = (0.0123 ± 0.0002) min^{-1}, respectively, Table 6.2. The second-order rate constants k at 39 and 67°C were calculated using eq. 6.2 and are tabulated in Table 6.2. From the Eyring equation, eq. 6.3, the plot of $ln(k/T)$ vs. $1/T$ yields a curve with slope $-\Delta H^{\ddagger}/R$ and intercept $[ln(R/Nh) + (\Delta S^{\ddagger}/R)]$.

$$ln(k/T) = ln(R/Nh) + \Delta S^{\ddagger}/R - \Delta H^{\ddagger}/RT \qquad (6.3)$$

The Eyring plot, Figure 6.6a, yields $\Delta H^{\ddagger}$ = (16.9 ± 0.6) kJ/mol, and $\Delta S^{\ddagger}$ = (-186 ± 3) J/K·mol. The errors in the activation parameters were calculated from the error propagation formulae, eq. 6.4 - 6.5.[9]

$$(\sigma\Delta H^{\ddagger})^2 = \frac{R^2 T_{max}^2 T_{min}^2}{\Delta T^2}\left\{\left(\frac{\sigma T}{T}\right)^2\left[\left(1+T_{min}\frac{\Delta L}{\Delta T}\right)^2+\left(1+T_{max}\frac{\Delta L}{\Delta T}\right)^2\right]+2\left(\frac{\sigma k}{k}\right)^2\right\} \quad (6.4)$$

$$\sigma\Delta S^{\ddagger} = \frac{R^2}{\Delta T^2}\left\{\left(\frac{\sigma T}{T}\right)^2\left[T_{max}^2\left(1+T_{min}\frac{\Delta L}{\Delta T}\right)^2+T_{min}^2\left(1+T_{max}\frac{\Delta L}{\Delta T}\right)^2\right]+\left(\frac{\sigma k}{k}\right)^2\left(T_{max}^2-T_{min}^2\right)\right\} \quad (6.5)$$

where $\Delta T = (T_{max} - T_{min})$

$\Delta L = [ln(k_{max}/T_{max}) - ln(k_{min}/T_{min})]$

The kinetics of ethylene polymerization was also studied with catalysts **2** and **3** at three different temperatures, Figure 6.7 and 6.8. Pseudo-first-order behavior was observed in all cases. The dependence of k_{app} on n_V is reported for **3** at 22, Figure 6.8 and 6.9, and 58°C, Table 6.1. In these cases, second-order rate constants were obtained from the slopes of plots of k_{app} vs. n_V, Figure 6.3. In all other cases, k was calculated using eq 6.2. Values of k_{app} and k are summarized in Table 6.2. The activation parameters $\Delta H^{\ddagger}$ and $\Delta S^{\ddagger}$ were calculated from the Eyring plots shown in Figure 6.6. For polymerization of ethylene by **3**, $\Delta H^{\ddagger}$ = (32 ± 1) kJ/mol and $\Delta S^{\ddagger}$ = (-123 ± 14) J/mol K, while for **2**, $\Delta H^{\ddagger}$ = (35 ± 4) kJ/mol and $\Delta S^{\ddagger}$ = (-142 ± 8) J/mol K.

Table 6.2. Pseudo-first-order rate constants k_{app} and second-order rate constants k for ethylene polymerization catalyzed by silica-supported vanadium complexes

Catalyst	Temperature K	n_v mmol	10^{-3} k_{app} [a] min^{-1}	k s^{-1} (mol V)$^{-1}$
4	295	0.071	5.30 ± 0.07	1.25 ± 0.01 [b]
	312	0.067	7.7 ± 0. 2	1.92 ± 0.05
	340	0.057	12.3 ± 0. 2	3.59 ± 0.06
2	295	0.165	1.51 ± 0.02	0.153 ± 0.002
	316	0.160	4.39 ± 0.05	0.457 ± 0.005
	347	0.160	14.5 ± 0.1	1.51 ± 0.01
3	295	0.187	36 ± 2	3.20 ± 0.07 [b]
	315	0.180	100 ± 2	9.2 ± 0.2
	331	0.151	133 ± 1	15 ± 1 [b]

[a] Errors are from non-linear least squares fit to a single exponential function.

[b] Error is from the slope of the plot of k_{app} vs. n_v.

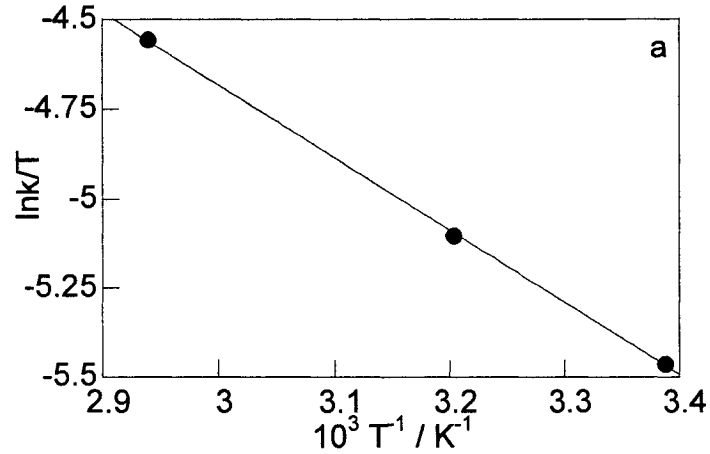

$\ln(k/T) = \ln(R/Nh) + \Delta S^{\ddagger}/R - \Delta H^{\ddagger}/R$		
	Value	Error
$\ln(R/Nh) + \Delta S^{\ddagger}/R$	1.401	0.089
$\Delta H^{\ddagger}/R$	-2.027	0.027
R^2	0.999	NA

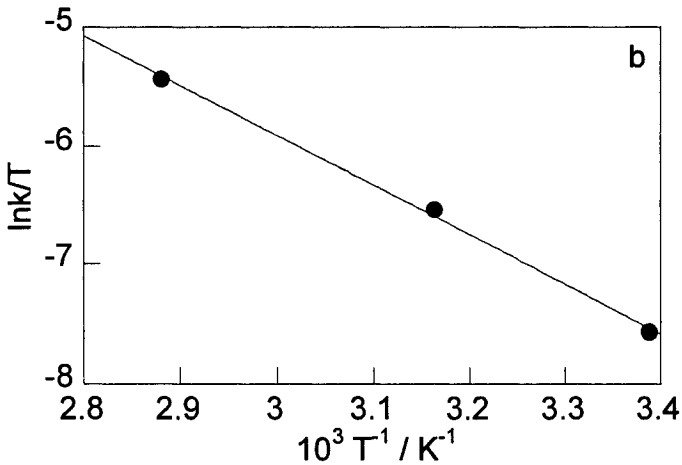

$\ln(k/T) = \ln(R/Nh) + \Delta S^{\ddagger}/R - \Delta H^{\ddagger}/R$		
	Value	Error
$\ln(R/Nh) + \Delta S^{\ddagger}/R$	6.663	0.605
$\Delta H^{\ddagger}/R$	-4.191	0.191
R^2	0.998	NA

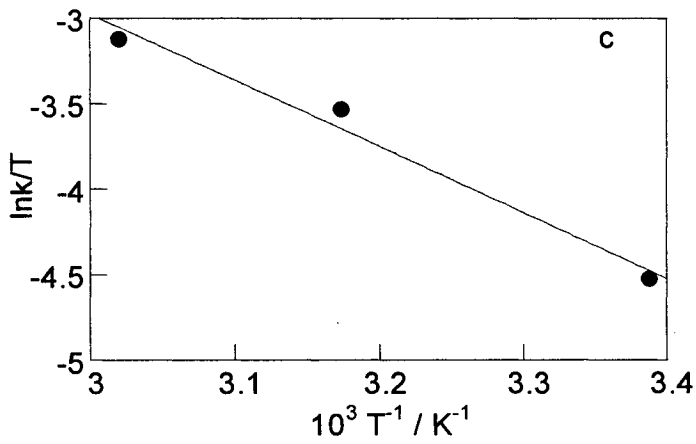

$\ln(k/T) = \ln(R/Nh) + \Delta S^{\ddagger}/R - \Delta H^{\ddagger}/R$		
	Value	Error
$\ln(R/Nh) + \Delta S^{\ddagger}/R$	8.657	1.723
$\Delta H^{\ddagger}/R$	-3.877	0.539
R^2	0.981	NA

Figure 6.6. Eyring plots for ethylene polymerization catalyzed by (a) **4**; (b) **2**; (c) **3**.

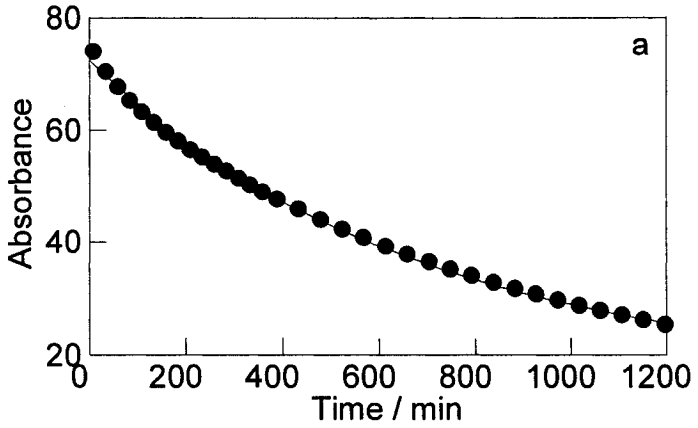

$A = A_\infty+(A_0-A_\infty)*\exp(-k_{app}t)$		
	Value	Error
A_∞	16.6	0.4
A_0	72.6	0.2
k_{app}	0.00151	0.00002
R^2	0.998	NA

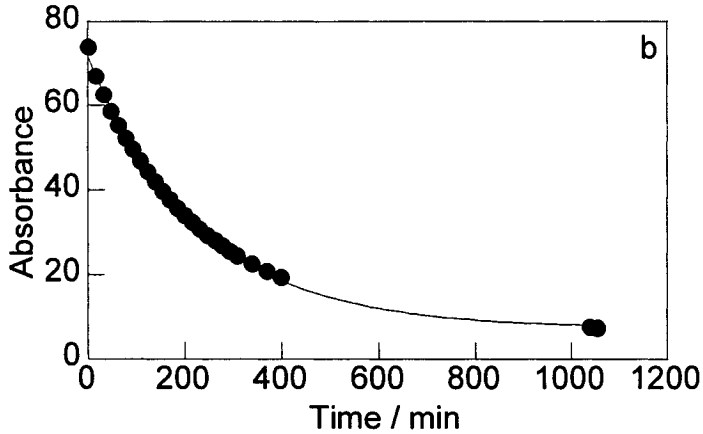

$A = A_\infty+(A_0-A_\infty)*\exp(-k_{app}t)$		
	Value	Error
A_∞	7.5	0.3
A_0	71.8	0.3
k_{app}	0.00439	0.00005
R^2	0.998	NA

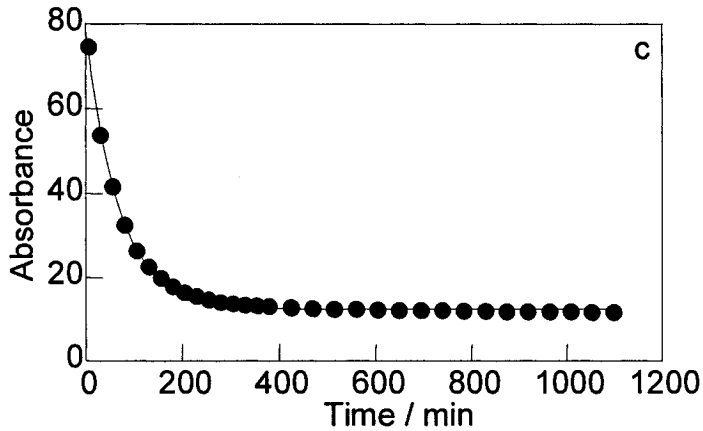

$A = A_\infty+(A_0-A_\infty)*\exp(-k_{app}t)$		
	Value	Error
A_∞	12.34	0.06
A_0	78.3	0.3
k_{app}	0.01453	0.0001
R^2	1.0	NA

Figure 6.7. Time-resolved ethylene polymerization catalyzed by **2**: (a) 103 mg, 0.165 mmol V at 22°C; (b) 100 mg, 0.160 mmol V at 43°C; (c) 100 mg, 0.160 mmol V at 74°C. Solid curves are three parameter single-exponential fits to the first-order integrated kinetic rate equation.

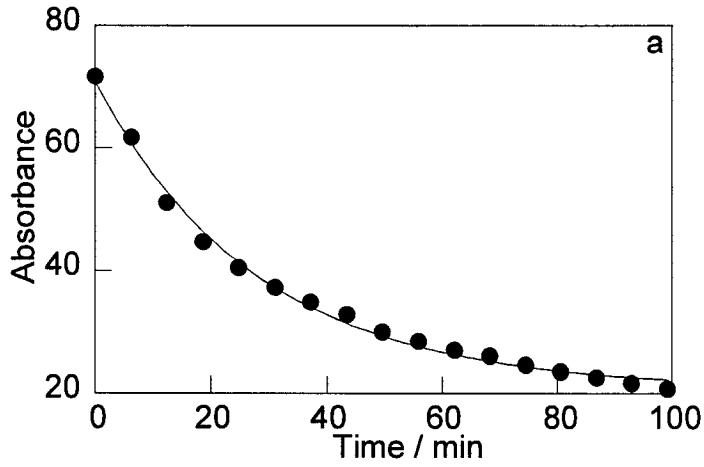

$A = A_\infty+(A_0-A_\infty)*\exp(-k_{app}t)$		
	Value	Error
A_∞	20.8	0.7
A_0	70.79	0.9
k_{app}	0.036	0.002
R^2	0.998	NA

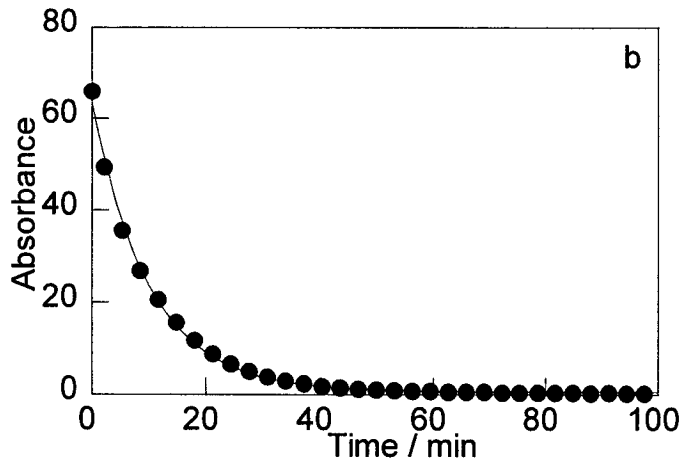

$A = A_\infty+(A_0-A_\infty)*\exp(-k_{app}t)$		
	Value	Error
A_∞	0.6	0.2
A_0	63.6	0.6
k_{app}	0.010	0.002
R^2	0.999	NA

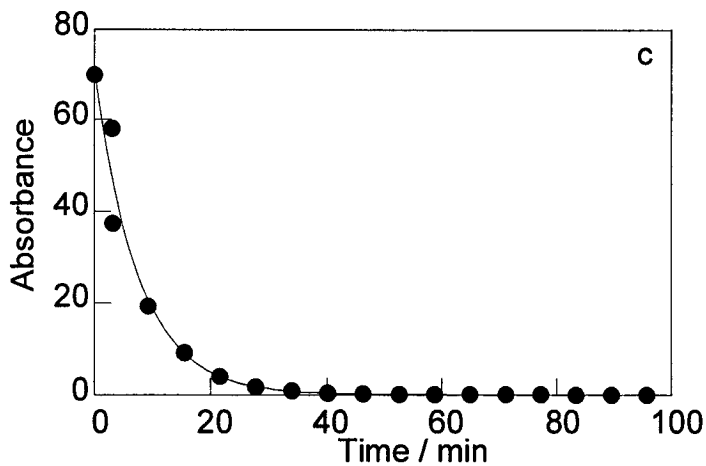

$A = A_\infty+(A_0-A_\infty)*\exp(-k_{app}t)$		
	Value	Error
A_∞	0.1	0.9
A_0	70	3
k_{app}	0.13	0.01
R^2	0.9880	NA

Figure 6.8. Time-resolved ethylene polymerization catalyzed by **3**: (a) 110 mg, 0.188 mmol V at 22°C; (b) 110.8 mg, 0.1830 mmol V at 42°C; (c) 97.0 mg, 0.155 mmol V at 58°C. Solid curves are three parameter single-exponential fits to the first-order integrated kinetic rate equation.

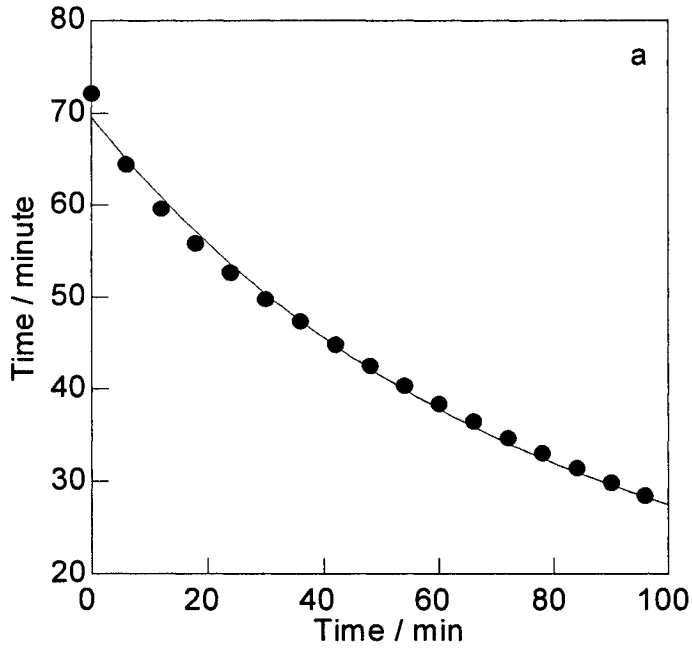

$A = A_\infty+(A_0-A_\infty)*\exp(-k_{app}t)$		
	Value	Error
A_∞	14	2
A_o	69.6	0.6
k_{app}	0.0142	0.0001
R^2	0.998	NA

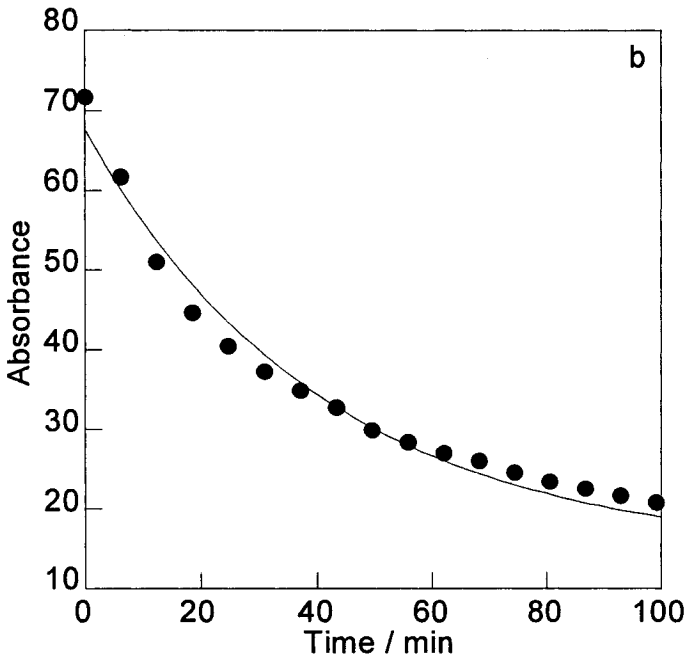

$A = A_\infty+(A_0-A_\infty)*\exp(-k_{app}t)$		
	Value	Error
A_∞	14.3	0.7
A_o	67.6	1
k_{app}	0.0243	0.0001
R^2	0.998	NA

Figure 6.9. Time-resolved ethylene polymerization at 22°C, catalyzed by **3**: (a) 103.7 mg, 0.0730 mmol V, (b) 95.2 mg, 0.125 mmol V. Solid curves are three parameter single-exponential fits to the first-order integrated kinetic rate equation.

6.2.3 Catalyst recycling

The "activities" of catalyst **4** was studied by recording the kinetics, as described previously, for three sequential additions of 100 Torr ethylene at 67°C. The kinetic curves are shown in Figure 6.10. All three absorbance-time profiles exhibited pseudo-first-order behavior, but with progressively lower rate constants, indicating deactivation of the catalyst during polymerization. The apparent rate constants are tabulated in Table 6.3.

Similar behavior was observed during sequential ethylene additions to catalyst **3**. A possible explanation is that the growing polymer chains block access to the active centers, thus preventing incoming ethylene monomer from reacting with some of the vanadium sites. Alternately, reduction of the catalytically active vanadium site to a less active or even inactive low valent state may occur during polymerization as a result of the instability of the V-C bond.

6.3 Kinetics of C_2D_4 polymerization

The polymerization of D-labeled ethylene by catalysts **3** and **4** was also studied at 22°C, following the method described above. Uptake of C_2D_4 was monitored as the decrease in absorbance from 825-650 cm^{-1} in the gas phase IR spectrum. The polymerization of C_2D_4 is pseudo-first-order, Figure 6.11. The rate constants k_H *and* k_D are tabulated in Table 6.4.

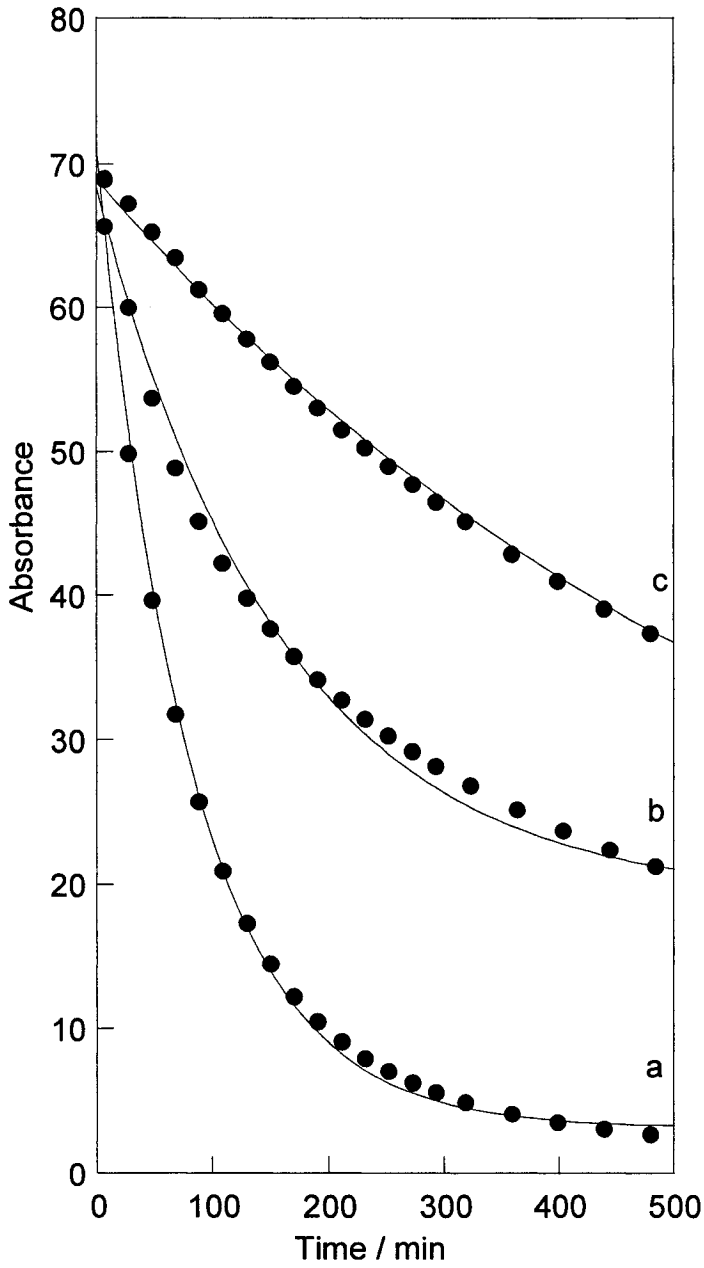

$A = A_\infty+(A_0-A_\infty)*\exp(-k_{app}t)$		
	Value	Error
A_∞	10.6	0.2
A_0	68.9	0.1
k_{app}	0.00161	0.00001
R^2	1.0	NA

$A = A_\infty+(A_0-A_\infty)*\exp(-k_{app}t)$		
	Value	Error
A_∞	18.9	0.4
A_0	68.4	0.6
k_{app}	0.0063	0.0002
R^2	0.994	NA

$A = A_\infty+(A_0-A_\infty)*\exp(-k_{app}t)$		
	Value	Error
A_∞	3.1	0.2
A_0	71.0	0.5
k_{app}	0.0123	0.0002
R^2	0.998	NA

Figure 6.10. Time-resolved polymerization in three sequential additions of 100 Torr ethylene to 97 mg **4** (0.057 mmol V) at 67°C: (a) first addition; (b) second addition; (c) third addition. Solid curves are three parameter single-exponential fits to the first-order integrated kinetic rate equation.

Table 6.3. Apparent pseudo-first-order rate constants[a] for ethylene polymerization catalyzed by **4** in successive additions of ethylene at 67°C

	$P(C_2H_4)$ / Torr	10^{-3} k_{app}/min^{-1}
first addition	100	12.3 ± 0.2
second addition	100	6.3 ± 0.2
third addition	100	1.61 ± 0.01

[a] Errors are from non-linear least squares fit to a single exponential function.

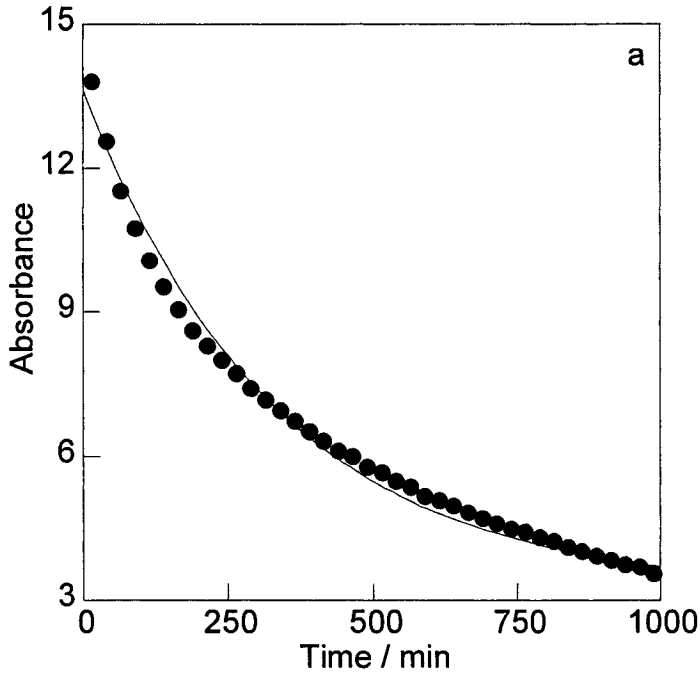

$A = A_\infty+(A_0-A_\infty)*\exp(-k_{app}t)$		
	Value	Error
A_∞	3.20	0.07
A_0	13.6	0.1
k_{app}	0.00305	0.00007
R^2	0.993	NA

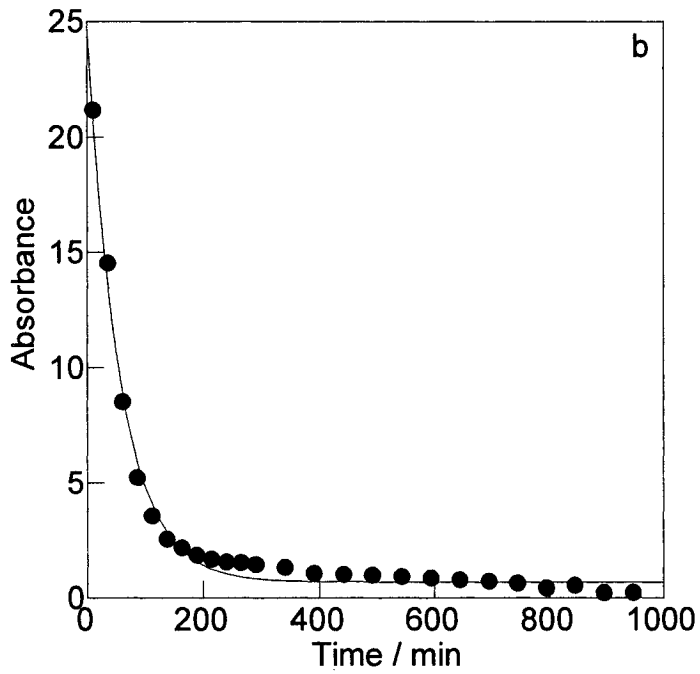

$A = A_\infty+(A_0-A_\infty)*\exp(-k_{app}t)$		
	Value	Error
A_∞	0.68	0.06
A_0	24.66	0.3
k_{app}	0.0174	0.0004
R^2	0.993	NA

Figure 6.11. Time-resolved polymerization of D-labeled ethylene catalyzed by (a) 55.7 mg **4** (0.0381 mmol V); (b) 54.2 mg **3** (0.0893 mmol V), at 22°C. Solid curves are three parameter single-exponential fits to the first-order integrated kinetic rate equation.

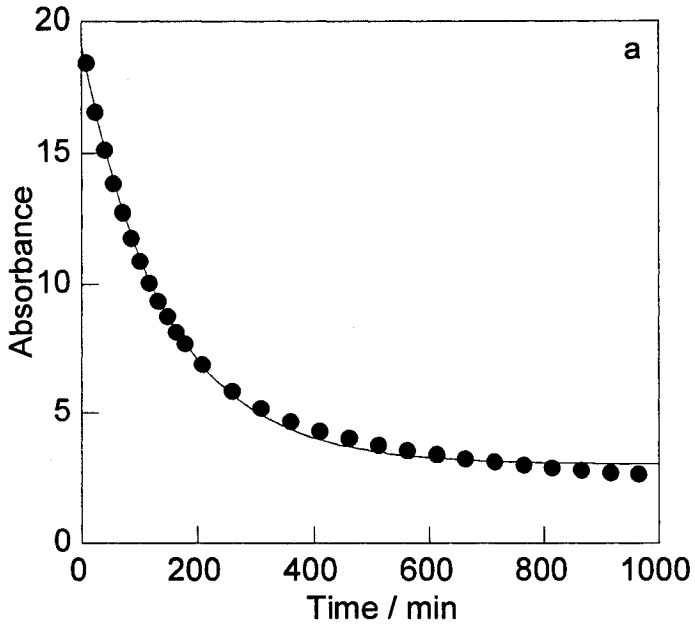

$A = A_\infty+(A_0-A_\infty)*\exp(-k_{app}t)$		
	Value	Error
A_∞	3.03	0.03
A_o	19.07	0.07
k_{app}	0.00691	0.00007
R^2	0.999	NA

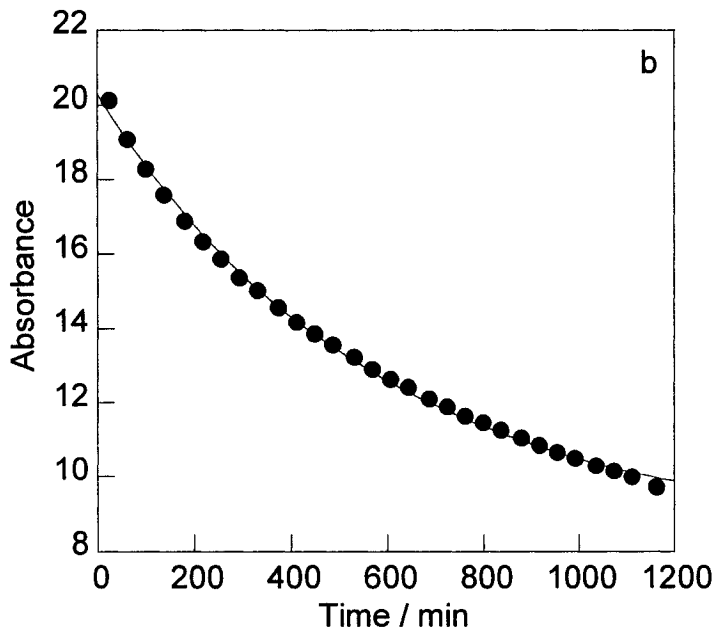

$A = A_\infty+(A_0-A_\infty)*\exp(-k_{app}t)$		
	Value	Error
A_∞	8.41	0.08
A_o	20.23	0.04
k_{app}	0.00174	0.00003
R^2	0.999	NA

Figure 6.12. Time-resolved polymerization of D-labeled ethylene at 22°C catalyzed by (a) 53 mg **3**, 0.038 mmol V; (b) 25 mg **3**, 0.010 mmol V. Solid curves are three parameter single-exponential fits to the first-order integrated kinetic rate equation.

Table 6.4. Second-order rate constants k for polymerization of C_2H_4 and C_2D_4 at 22°C

catalyst	monomer	k s^{-1} $(mol\ V)^{-1}$
4	C_2H_4	1.25 ± 0.01 [a]
	C_2D_4	1.32 ± 0.03 [b]
		k_H/k_D = 0.95 ± 0.01
3	C_2H_4	3.20 ± 0.07 [a]
	C_2D_4	3.24 ± 0.06 [a]
		k_H/k_D = 0.98 ± 0.03

[a] Calculated from the slope of the plot of n_V vs. k_{app}, Figure 6.5.

[b] Calculated from eq 6.2.

The kinetic isotope effects for ethylene polymerization by **3** and **4** are negligible (k_H/k_D = 0.98 and 0.95, respectively). Therefore the Cossee mechanism is favored for propagation, since it involves no α-H activation.[10,11]

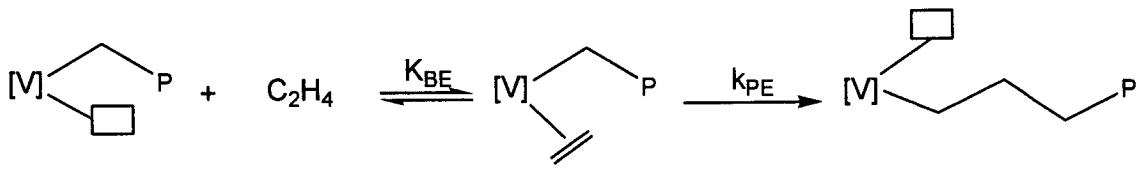

The rate law for ethylene polymerization is given by eq. 6.6:

$$-\frac{dP(C_2H_4)}{dt} = \frac{K_{BE}k_{PE}n_V P(C_2H_4)}{1+K_{BE}P(C_2H_4)} \qquad (6.6)$$

where K_{BE} is the binding constant of olefin E to the active site and k_{PE} is the propagation rate constant for the rate-determining incorporation of olefin X into the growing polymer chain. If the binding constant K_{BE} is small and the ethylene pressure is low, the rate law is consistent with eq. 6.2, where $k = K_B k_P$.

The temperature dependence of the composite rate constant $k = K_B k_p$ is given by eq. 6.8.[12]

$$k = K_B k_p = \left(\frac{RT}{Nh}\right) exp\left(\frac{\Delta S_p^{\ddagger}}{R}\right) exp\left(-\frac{\Delta H_p^{\ddagger}}{RT}\right) exp\left(\frac{\Delta S_B^{o}}{R}\right) exp\left(-\frac{\Delta H_B^{o}}{RT}\right) \qquad (6.7)$$

where R is the ideal gas constant, N is Avogadro's number, h is Plank's constant, $\Delta H^{\ddagger}_{p}$ and $\Delta S^{\ddagger}_{p}$ are the activation parameters for migratory insertion and ΔH^{o}_{B} and ΔS^{o}_{B} are the enthalpy and entropy of ethylene binding, respectively. After rearrangement, equation 6.7 can be written as

$$ln\frac{k}{T} = ln\frac{R}{Nh} + \left(\frac{\Delta S_p^{\ddagger} + \Delta S_B^{o}}{R}\right) - \left(\frac{\Delta H_p^{\ddagger} + \Delta H_B^{o}}{RT}\right) \qquad (6.8)$$

The Eyring plot, $ln(k/T)$ vs. T^{-1}, is therefore expected to be linear. Furthermore, since the binding enthalpy (ΔH^{o}_{B}) is negative, the observed activation enthalpy ($\Delta H^{\ddagger}_{obs}$) will be smaller than ($\Delta H^{\ddagger}_{p}$) by $|\Delta H^{o}_{B}|$.[13]

The enthalpy barriers for polymerization initiated by catalysts **2**, **3** and **4** are (35 ± 4), (32 ± 1) and (16.9 ± 0.6) kJ/mol, respectively. These values are in the range of others reported for Ziegler-Natta catalysts (20-70 kJ/mol).[14] The more negative value of ($\Delta S^{\ddagger}_{obs}$) in our system compared to that reported by Doherty et. al for olefin insertion into a Nb-H bond in solution might be due to the loss of entropy upon binding the gas phase ethylene or propylene to the catalyst, ($\Delta S^{\ddagger}_{p}$).[15]

6.4 Propylene polymerization

When a self-supporting disk of **4** was exposed to 40 Torr propylene at room temperature, several physical changes were observed. The color changed from

dark violet to white and the transparent disk became opaque. The initially fragile silica pellet became rigid, confirming the formation of a hard polymer disk. GC-MS analysis of the gas phase did not show the formation of propylene oligomers. Finally, formation of polypropylene, eq. 6.9, was confirmed by FTIR.

4

$$n\ CH_3CH{=}CH_2 \rightarrow \text{polypropylene} \qquad (6.9)$$

Similar changes were observed when samples of catalysts **2** or **3** were exposed to propylene.

6.4.1 Infrared characterization

The IR spectrum of a self-supporting disk of **4** exposed to 20 Torr propylene at room temperature shows an increase in the ν(C-H) region, Figure 6.13. New bands which appear from 3000-2800 cm^{-1} are assigned to the asymmetric and symmetric CH_3 and CH_2 stretching modes of the polypropylene.[16] The strong absorption at 1461 cm^{-1} and shoulder at 1449 cm^{-1} are assigned to the asymmetric methyl deformation mode, while the sharp peak at 1377 cm^{-1} is due to symmetric methyl deformation mode.[8,17] CH and CH_2 deformations also contribute to this mode due to mixing of vibrational energy levels.[18]

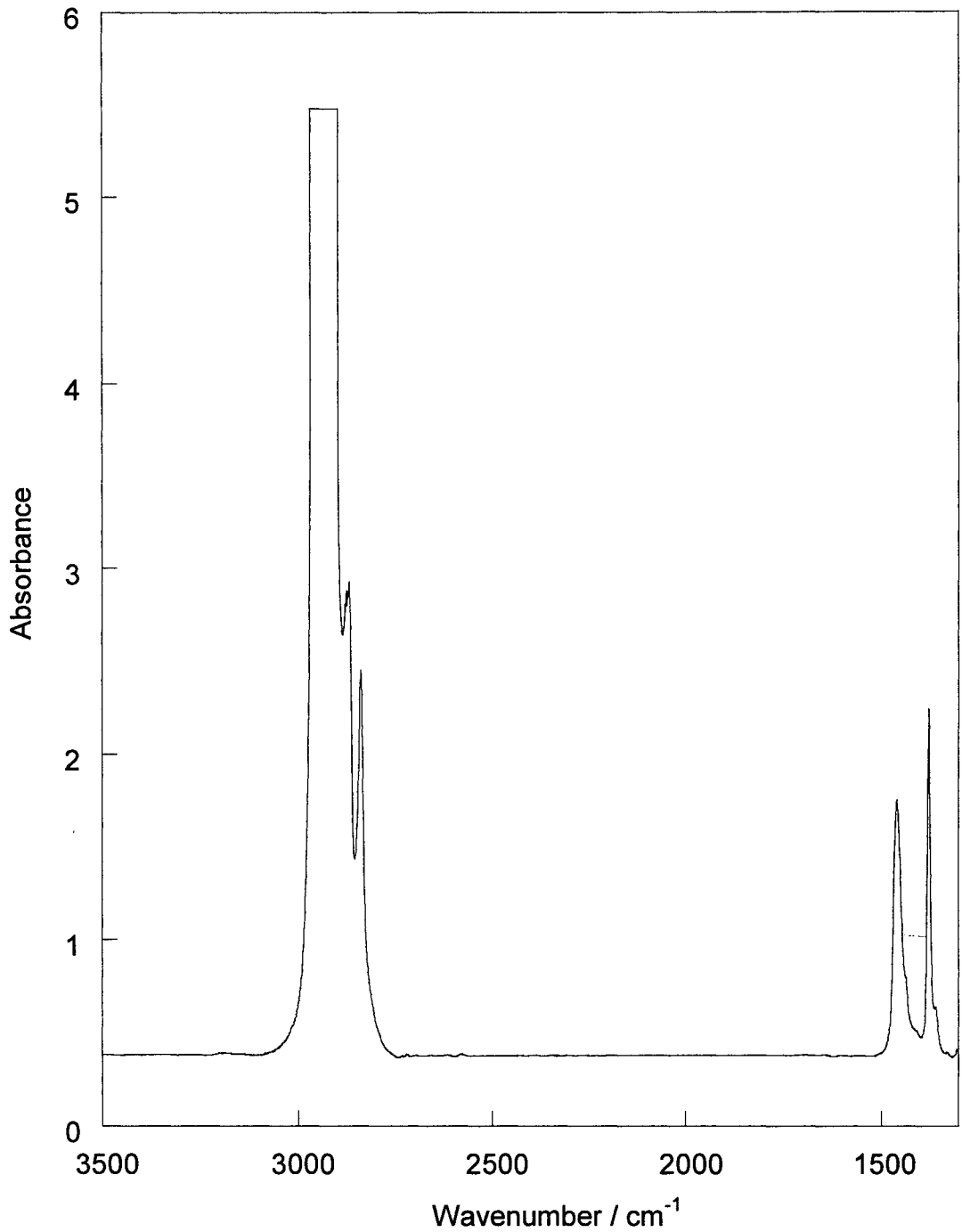

Figure 6.13 Transmission infrared difference spectrum obtained by subtraction the spectrum of **4** from its spectrum 72 hours after addition of 20 Torr propylene at room temperature, and evacuation of volatiles.

6.4.2 Kinetics

The kinetics of propylene polymerization catalyzed by **4** was studied using the procedure described for ethylene, by monitoring the integrated absorbance between 3200 and 2800 cm^{-1}. Propylene was introduced into the reactor containing 101 mg catalyst (0.0642 mmol V) and its reaction was followed at 22°C (water bath). The uptake of propylene is presumed to be pseudo-first-order, with rate constant k_{app}= (9.0 ± 0.7) x 10^{-4} min^{-1}, Figure 6.14a. Two independent experiments were carried out at 43 and 73°C, Figure 6.14b,c. The temperature-dependent second–order rate constants *k*, calculated using eq. 6.2, are tabulated in Table 6.5. They were used to construct the Eyring plot shown in Figure 6.15a. From the linear fit, $\Delta H^{\ddagger}$ = (8.2 ± 1.9) kJ/mol and $\Delta S^{\ddagger}$ = (-230 ± 37) J/K·mol.

The kinetics of propylene polymerization was also studied with samples of catalysts **2** and **3** at three different temperatures. Although some experiments show evidence of slight biphasic behavior, Figures 6.16 and 6.17, all were treated as pseudo-first-order. The second-order rate constant *k* at 22°C was calculated for **3** from the slope of the plot of n_V vs. k_{app}, Figure 6.5. Rate constants are tabulated in Table 6.5. Activation parameters obtained from the Eyring plots in Figure 6.15b,c are: $\Delta H^{\ddagger}$ = (6.8 ± 0.8) kJ/mol and $\Delta S^{\ddagger}$ = (-244 ± 7) J/K·mol for **2** and $\Delta H^{\ddagger}$ = (11 ± 1.0) kJ/mol and $\Delta S^{\ddagger}$ = (-220 ± 10) J/K·mol for **3**.

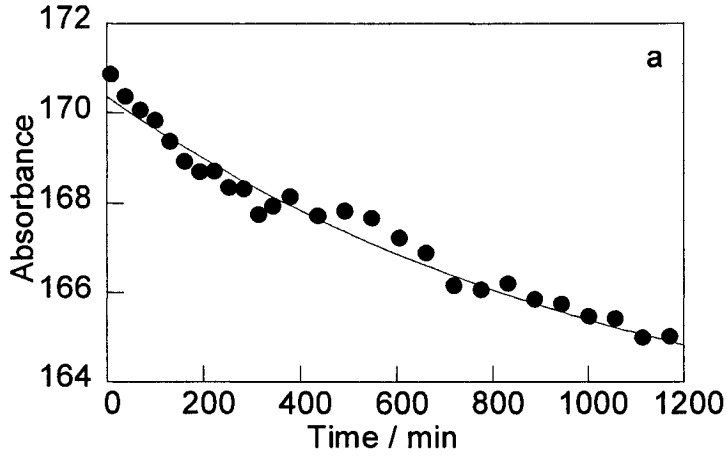

$A = A_\infty+(A_0-A_\infty)*\exp(-k_{app}t)$		
	Value	Error
A_∞	161.9	0. 4
A_0	170.37	0.06
k_{app}	0.00090	0.00008
R^2	0.988	NA

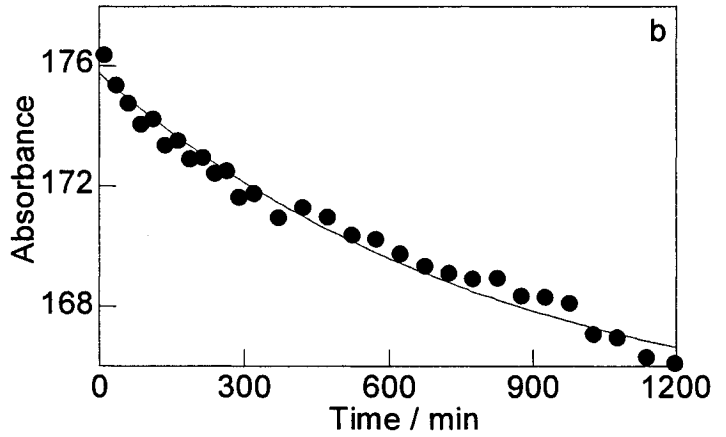

$A = A_\infty+(A_0-A_\infty)*\exp(-k_{app}t)$		
	Value	Error
A_∞	163.9	0.5
A_0	175.8	0.1
k_{app}	0.00121	0.00009
R^2	0.984	NA

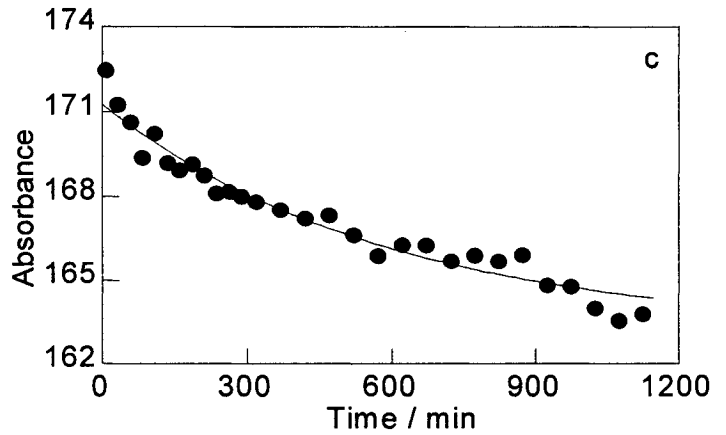

$A = A_\infty+(A_0-A_\infty)*\exp(-k_{app}t)$		
	Value	Error
A_∞	163.21	0.3
A_0	171.27	0.1
k_{app}	0.0017	0.0001
R^2	0.976	NA

Figure 6.14 Time-resolved propylene polymerization catalyzed by **4**: (a) 101 mg, 0.0642 mmol V at 22°C; (b) 98.1 mg, 0.0656 mmol V at 43°C; (c) 104 mg, 0.0651 mmol V at 73°C. Solid curves are three parameter single-exponential fits to the first-order integrated kinetic rate equation.

Table 6.5. Pseudo-first-order rate constants k_{app} and second-order rate constants k for propylene polymerization catalyzed by silica-supported vanadium complexes

Catalyst	Temperature K	n_v mmol	10^{-3} k_{app}[a] min^{-1}	k s^{-1} (mol V)$^{-1}$
4	295	0.064	0.90 ± 0.08	0.23 ± 0.02
	316	0.065	1.2 ± 0.1	0.31 ± 0.03
	346	0.065	1.7 ± 0.1	0.43 ± 0.03
2	295	0.160	0.66 ± 0.02	0.069 ± 0.002
	320	0.160	0.95 ± 0.03	0.099±0.003
	344	0.168	1.20 ± 0.02	0.119 ± 0.002
3	295	0.077	1.16 ± 0.04	0.25 ± 0.01[b]
	310	0.076	1.43 ± 0.04	0.31 ± 0.01
	335	0.075	2.15 ± 0.07	0.48 ± 0.02

[a] Errors are from non-linear least squares fit to a single exponential function.

[b] Error is calculated from the slope of the plot of n_v vs. k_{app}.

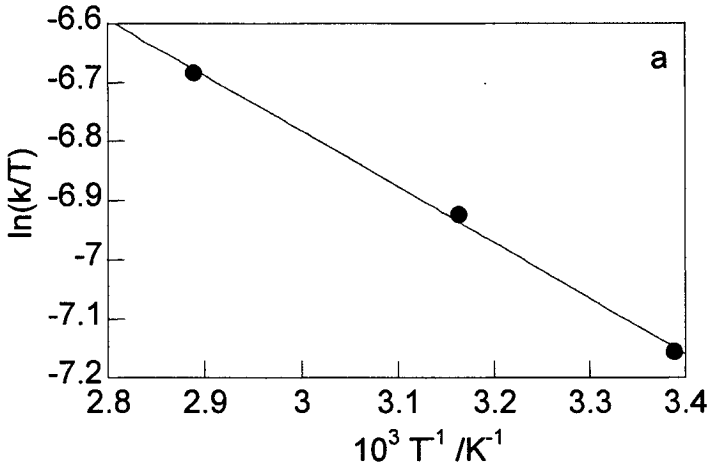

y = m_1 +m_2x		
	Value	Error
m_1	-3.949	0.142
m_2	-0.944	0.045
R^2	0.998	NA

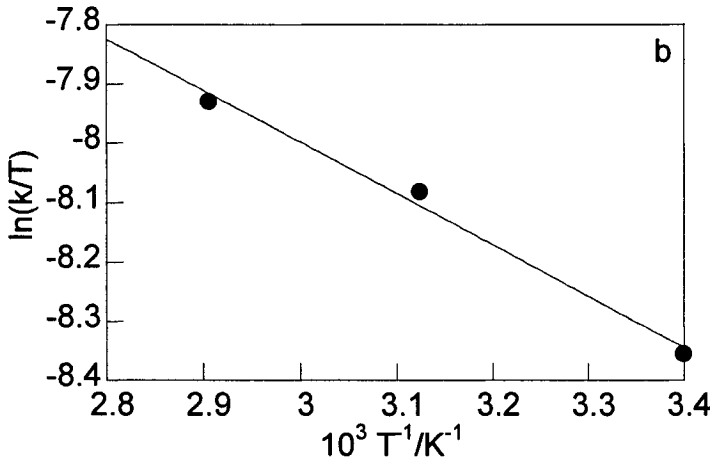

y = m_1 +m_2x		
	Value	Error
m_1	-5.396	0.268
m_2	-0.867	0.085
R^2	0.995	NA

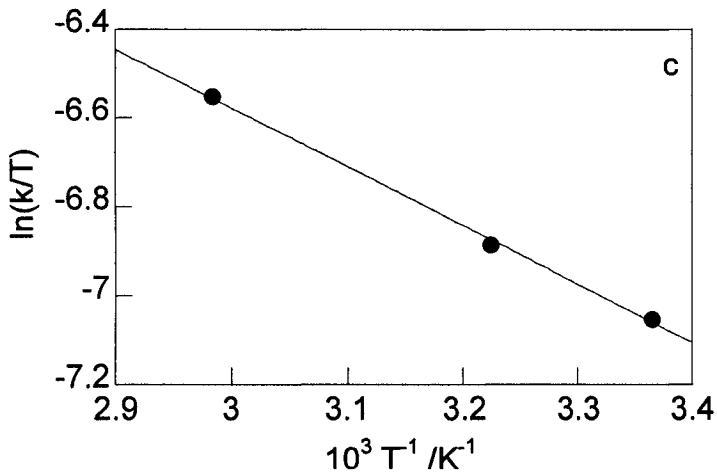

y = m_1 +m_2x		
	Value	Error
m_1	-2.615	0.167
m_2	-1.321	0.052
R^2	0.999	NA

Figure 6.15 Eyring plots for propylene polymerization catalyzed by a) **4**; b) **2**; c) **3**.

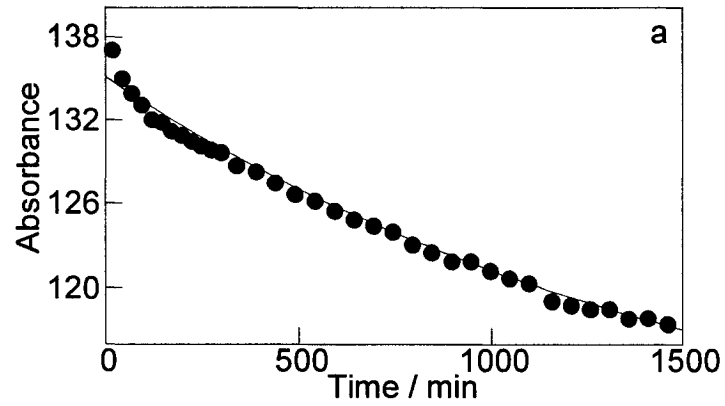

$A = A_\infty+(A_0-A_\infty)*\exp(-k_{app}t)$		
	Value	Error
A_∞	106.5	0.4
A_0	135.1	0.2
k_{app}	0.00066	0.00002
R^2	0.993	NA

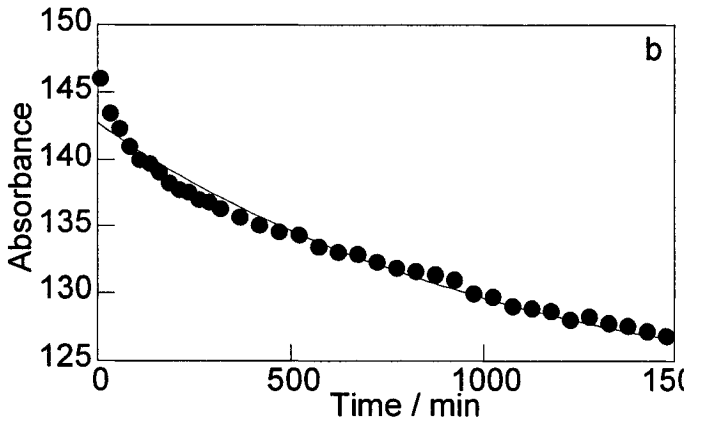

$A = A_\infty+(A_0-A_\infty)*\exp(-k_{app}t)$		
	Value	Error
A_∞	121.4	0.3
A_0	142.7	0.1
k_{app}	0.00095	0.00003
R^2	0.992	NA

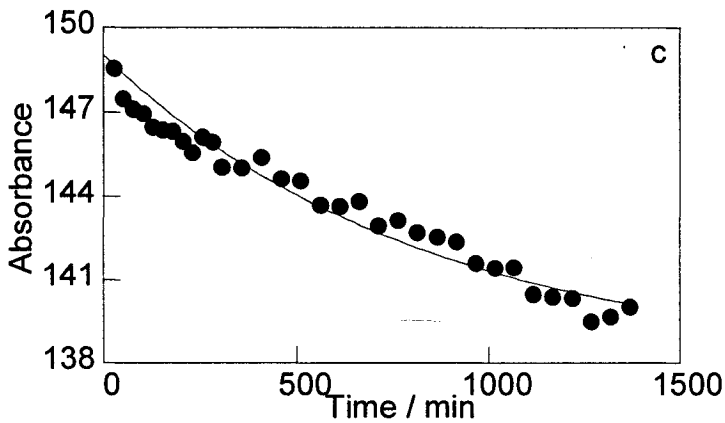

$A = A_\infty+(A_0-A_\infty)*\exp(-k_{app}t)$		
	Value	Error
A_∞	137.9	0.8
A_0	149.0	0.2
k_{app}	0.0012	0.0002
R^2	0.938	NA

Figure 6.16 Time-resolved propylene catalyzed by **2**: (a) 98.3 mg, 0.160 mmol V at 22°C; (b) 102.1 mg, 0.162 mmol V at 47°C; (c) 101.2 mg, 0.167 mmol V at 71°C. Solid curves are three parameter single-exponential fits to the first-order integrated kinetic rate equation.

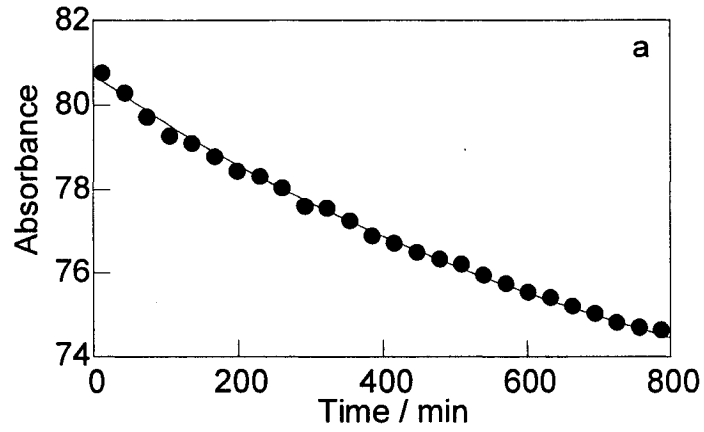

$A = A_\infty+(A_0-A_\infty)*\exp(-k_{app}t)$		
	Value	Error
A_∞	70.3	0.2
A_0	80.7	0.03
k_{app}	0.00116	0.00004
R^2	0.998	NA

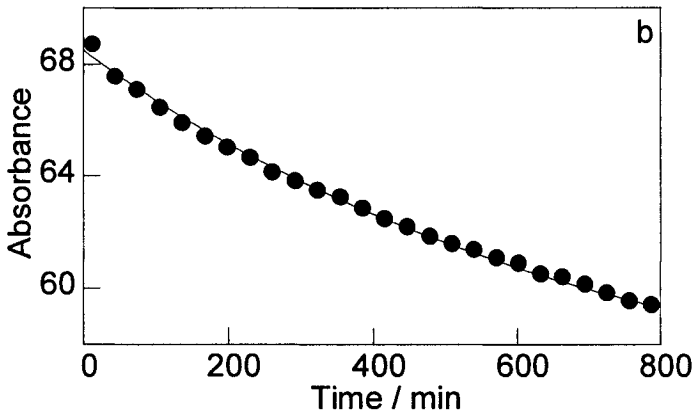

$A = A_\infty+(A_0-A_\infty)*\exp(-k_{app}t)$		
	Value	Error
A_∞	55.0	0.2
A_0	68.50	0.05
k_{app}	0.0014	0.00039
R^2	0.998	NA

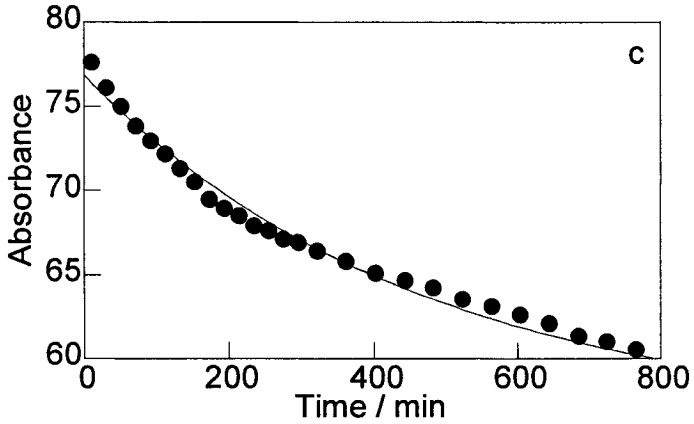

$A = A_\infty+(A_0-A_\infty)*\exp(-k_{app}t)$		
	Value	Error
A_∞	56.3	0.3
A_0	76.8	0.2
k_{app}	0.0015	0.0007
R^2	0.995	NA

Figure 6.17 Time-resolved propylene polymerization catalyzed by **3**: (a) 48.1 mg, 0.0770 mmol V at 22°C; (b) 47.3 mg, 0.0757mmol V at 37°C; (c) 46.9 mg, 0.0750 mmol V at 62°C. Solid curves are three parameter single-exponential fits to the first-order integrated kinetic rate equation.

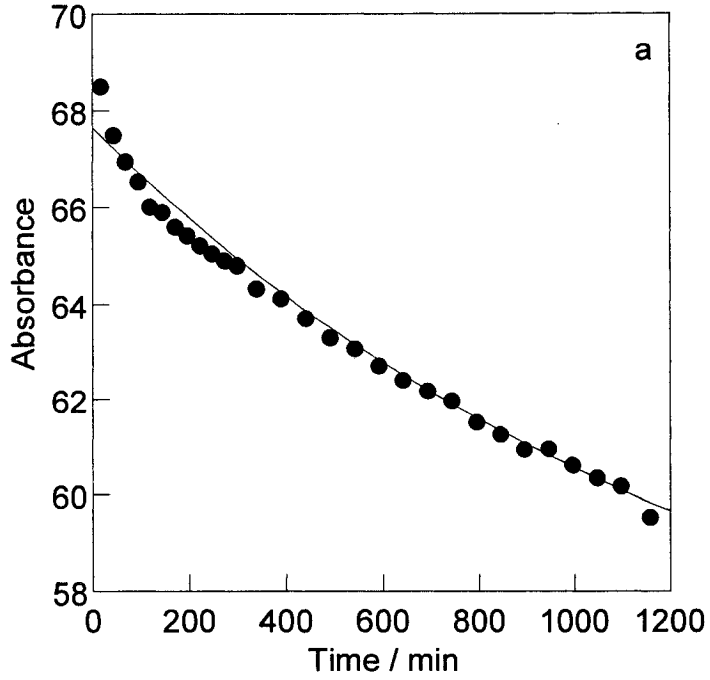

$A = A_\infty+(A_0-A_\infty)*\exp(-k_{app}t)$		
	Value	Error
A_∞	53.9	0.2
A_0	67.6	0.08
k_{app}	0.00073	0.00002
R^2	0.992	NA

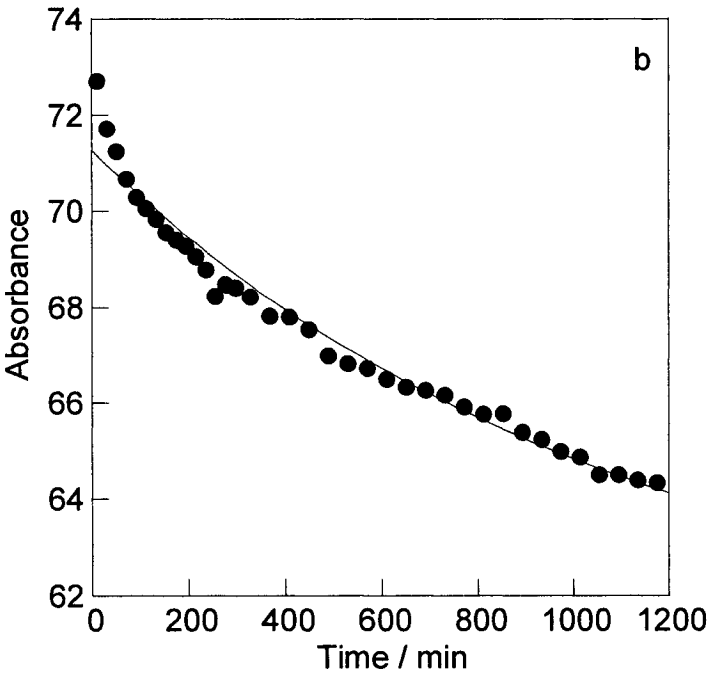

$A = A_\infty+(A_0-A_\infty)*\exp(-k_{app}t)$		
	Value	Error
A_∞	60.6	0.1
A_0	71.27	0.07
k_{app}	0.00093	0.00003
R^2	0.993	NA

Figure 6.18 Time-resolved propylene polymerization at 22°C catalyzed by **3**: (a) 49.2 mg, 0.0472 mmol V; (b) 51.3 mg, 0.0603 mmol V. Solid curves are three parameter single-exponential fits to the first-order integrated kinetic rate equation.

The rate constants for low pressure propylene polymerization, Table 6.5, are lower than the corresponding rate constants for ethylene polymerization, Table 6.2, by factors of 4, 2 and 12 times for catalysts **4**, **2** and **3**, respectively. Being more electron-rich, propylene binds more strongly to the active site than ethylene (i.e., $K_{BP} > K_{BE}$), however, its migratory insertion should be slower (i.e., $k_{PP} > k_{PE}$) due to steric effects.[15] A modest lowering of the rate of polymerization of propylene relative to ethylene is consistent with these opposing trends.

6.5 Kinetics of ethylene-propylene copolymerization

Copolymerization kinetics were investigated in order to determine selectivity for the insertion of propylene versus ethylene. The kinetics were monitored by combining C_2D_4 and propylene in a 3:1 ratio over catalyst **4** at 22°C. The uptake of C_2D_4 was monitored as the decrease in gas phase IR absorbance from 825-650 cm^{-1}, while the uptake of propylene was simultaneously analyzed by monitoring the loss of ν(C-H) intensity from 3200-2800 cm^{-1}. Both are pseudo-first-order, as shown by the exponential curves in Figure 6.19. Since k_{app} is similar for both monomers, the ratio $P(C_2D_4)/P(C_3H_6)$ remains constant for the duration of the experiment. The rate constants *k* are shown in Table 6.6. Since the kinetic isotope effect for polymerization of C_2D_4 by **4** is negligible, the value k_{11} reflects the rate of homopolymerization of C_2H_4.

To calculate selectivity ratios for co-polymerization when propylene is the comonomer, the following insertion reactions must be considered:

$$[V]CH_2CH_2P + C_2H_4 \rightarrow [V]CH_2CH_2CH_2CH_2P \quad k_{11}$$

$$[V]CH_2CH(CH_3)P + C_2H_4 \rightarrow [V]CH_2CH_2CH_2CH(CH_3)P \quad k_{21}$$

$$[V]CH_2CH(CH_3)P + C_3H_6 \rightarrow [V]CH_2CH(CH_3)CH_2CH(CH_3)P \quad k_{22}$$

$$[V]CH_2CH_2P + C_3H_6 \rightarrow [V]CH_2CH(CH_3)CH_2CH_2P \quad k_{12}$$

where [V] denotes the active site and P is a growing polymer chain. We assume that almost all insertions occur with 1,2 regiochemistry.[19]

The overall rates of the consumption of each monomer are proportional to their molar fraction, so the propagation sites $[V]CH_2CH_2P$ and $[V]CH_2CH(CH_3)P$ are present in a ratio corresponding to the relative abundance of each monomer. Thus, the measured rate constants k_E and k_{Pr} for a 75:25 etylene:propylene mixture are:

$$k_E = 0.75\, k_{11} + 0.25\, k_{21} \qquad (6.10)$$

$$k_{Pr} = 0.25\, k_{22} + 0.75\, k_{12} \qquad (6.11)$$

Using the measured values for k_{11} and k_{22}, Table 6.6, the values for k_{21} and k_{12} are (0.640 ± 0.012) and (1.26 ± 0.04) $s^{-1}(mol\ V)^{-1}$, respectively for catalyst **4**. The ethylene selectivity ratio r_1 is therefore k_{11}/k_{21} = 2.1 and the propylene selectivity ratio r_2 is k_{22}/k_{12} = 0.18.

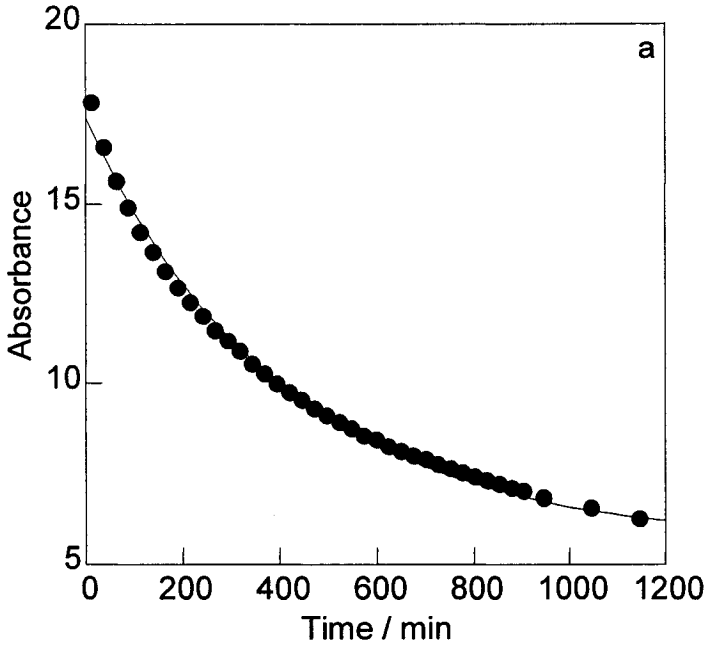

$A = A_\infty+(A_0-A_\infty)*\exp(-k_{app}t)$		
	Value	Error
A_∞	5.61	0.06
A_o	17.40	0.06
k_{app}	0.00248	0.00004
R^2	0.997	NA

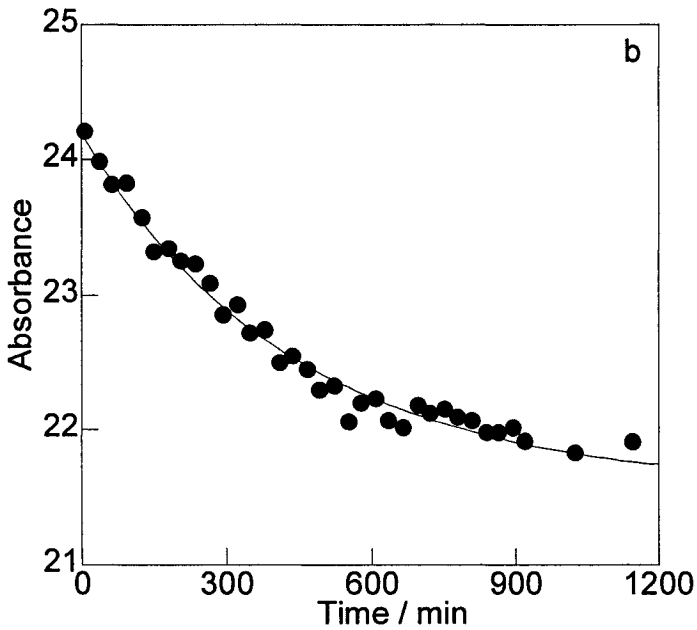

$A = A_\infty+(A_0-A_\infty)*\exp(-k_{app}t)$		
	Value	Error
A_∞	21.57	0.03
A_o	24.187	0.03
k_{app}	0.00228	0.00007
R^2	0.989	NA

Figure 6.19. Time-resolved copolymerization of 38 Torr C_2D_4 with 12 Torr propylene catalyzed by 50 mg **4** (0.036 mmol V) at 22°C, monitored as the simultaneous uptake of (a) C_2D_4; and (b) propylene. Solid curves are three-parameter single-exponential fits to the first-order integrated kinetic rate equation.

Table 6.6. Rate constants k for ethylene homopolymerization and copolymerization with propylene at 22°C catalyzed by **4**

Monomer composition			k [a] s^{-1} $(mol\ V)^{-1}$
C_2D_4	k_{11}		1.32 ± 0.03
C_3H_6	k_{22}		0.23 ± 0.02
0.75 C_2D_4 + 0.25 C_3H_6	C_2D_4	k_E	1.15 ± 0.02
		k_{21}	0.640 ± 0.010
	C_3H_6	k_{Pr}	1.05 ± 0.03
		k_{12}	1.26 ± 0.04

[a] Calculated from eq 6.2.

Thus ethylene uptake is 2 times slower in the presence of propylene while propylene uptake is 6 times faster in the presence of ethylene, relative to their respective homopolymerization by catalyst **4**. The ability of supported vanadium catalysts to readily incorporate comonomer is well-known, as described earlier.

Enhancement of the rate of ethylene polymerization in the presence of a substituted monomer (positive comonomer effect) and reduction of the rate of ethylene polymerization (negative comonomer effect) have been reported for ethylene/1-hexene copolymerization. The former was reported for $MgCl_2$-supported $TiCl_3$[20] and the latter for silica-supported Cr(IV) catalysts.[21] We observe a negative comonomer effect. A possible explanation is that the β-methyl group of recently inserted propylene sterically hinders the next insertion of ethylene. Similarly, propylene insertion following ethylene insertion is less sterically hindered, and therefore faster, than propylene homopolymerization.

6.6 Polymer Characterization

6.6.1 Gel Permeation Chromatography (GPC) analysis

The number-average molecular weights ($\overline{M}_n$), weight-average molecular weights ($\overline{M}_w$ (LS)) from light scattering and polydispersity indices ($\overline{M}_w/\overline{M}_n$) for polyethylene and polypropylene samples are presented in Table 6.7. The average value of $\overline{M}_w$ obtained for polyethylene made with catalyst **4** is (9.99±0.74) x 10^5 with $\overline{M}_w/\overline{M}_n$ = (7.6±1.3). For polypropylene made with catalyst **3**, $\overline{M}_w$ is (5.77±0.35) x 10^4 with $\overline{M}_w/\overline{M}_n$ = (2.9±0.5). The value of $\overline{M}_w/\overline{M}_n$ for polyethylene is close to literature values for samples made with vanadium-silica catalysts, ranging from 7 to 12, in contrast to those made with unsupported vanadium catalysts, which range from 3 to 4.[22]

Silica-supported vanadium catalysts usually produce polypropylene with slightly lower average molecular weights than for polyethylene and this consistent with our results.[23-25] The large difference in average molecular weights between polyethylene and polypropylene samples is due to the increased rate of chain termination and lower rate of insertion for propylene.

Table 6.7. $\overline{M}_w$(LS), calculated $\overline{M}_n$ and polydispersity index (PDI) values for polyethylene and polypropylene samples prepared with catalysts **4** and **3**, respectively

System	Run	$\overline{M}_w$ (LS)[a]	$\overline{M}_n$	PDI(PS)[b]
	1	980300	139406	7.032
Polyethylene	2	1018000	179225	5.680
using catalyst	3	1074000	122659	8.756
4	4	1042000	130331	7.995
	5	880800	100000	8.808
	Average	$(9.99\pm0.74)\times10^5$	$(1.34\pm0.29)\times10^5$	(7.6 ± 1.3)
	1	61960	24232	2.557
Polypropylene	2	56950	21955	2.594
using catalyst	3	60700	23054	2.633
3	4	54120	15017	3.604
	5	54650	17399	3.141
	Average	$(5.77\pm0.35)\times10^4$	$(2.03\pm0.39)\times10^4$	(2.9 ± 0.5)

[a] Values of M_w(LS) from light scattering measurements.

[b] Polydispersity index calibrated with polystyrene (PS).

6.6.2 NMR spectroscopy

The ^{1}H NMR spectrum of polyethylene shows a single intense resonance at 1.21 ppm due to the methylene protons of the polymer, while the ^{13}C NMR spectrum shows a signal at 29.58 ppm for the secondary carbons of the CH_2 backbone, as expected.[16]

The ^{13}C CP-MAS NMR spectrum of polypropylene shows three sharp signals at 21.7 ppm (s, CH_3), 26.3 ppm (s, CH) and 43.7 ppm (s, CH_2) (Figure 6.20). These chemical shifts similar to those reported by other authors.[26,27] The presence of a single sharp methyl signal is consistent with the formation of isotactic polypropylene.

The presence of three resonances at 0.85 ppm (s, 4H), 1.25 ppm (s, 1H) and 1.60 ppm (s, 1H) in the ^{1}H NMR spectrum of polypropylene (Figure 6.21) is also consistent with the formation of isotactic polypropylene.[28] The two protons of the -CH_2- group, located between the two tertiary C atoms in an isotactic arrangement, are magnetically inequivalent: one is syn and the other is anti to both CH_3 groups. As a result, in the ^{1}H NMR spectrum of isotactic polypropylene, the methylene resonance is split into two multiplets, at ca. 1.25 ppm (anti proton) and 0.9 ppm (syn proton). The latter largely overlaps with the resonance of the methyl protons at 0.85 ppm. The resonance at 1.60 ppm is assigned to the proton of the -CH- group.

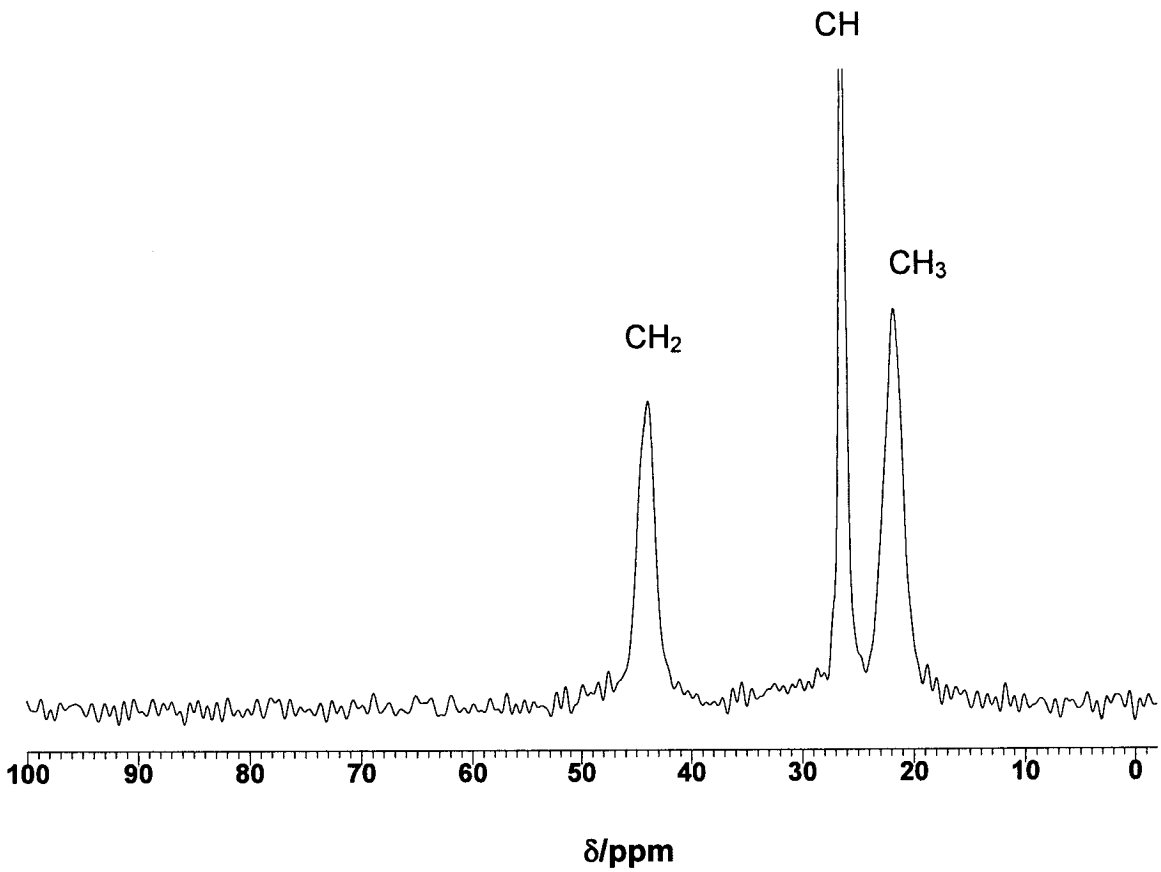

Figure 6.20. Solid-state ^{13}C CP-MAS NMR spectrum at room temperature of polypropylene prepared with catalyst **4** (spinning rate 5 kHz).

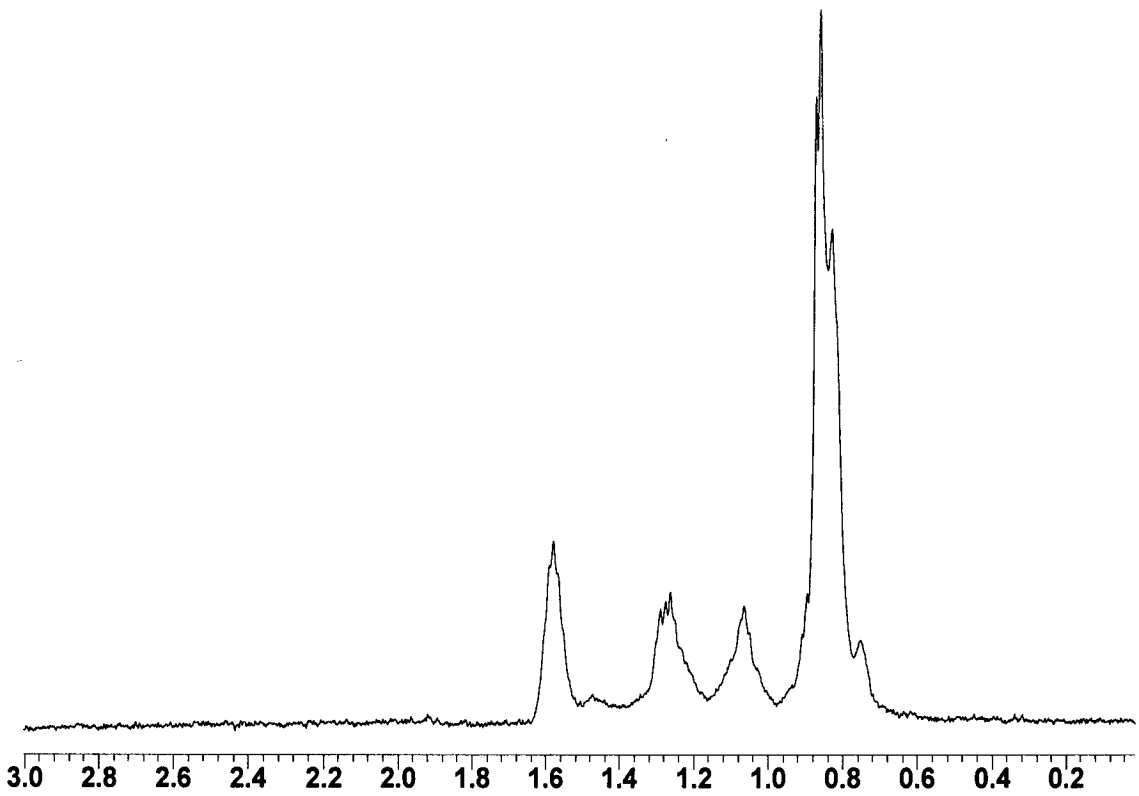

Figure 6.21. ^{1}H NMR spectrum of polypropylene prepared with catalyst **4** (recorded in 1,2,4-trichlorobenzene at 120 °C).

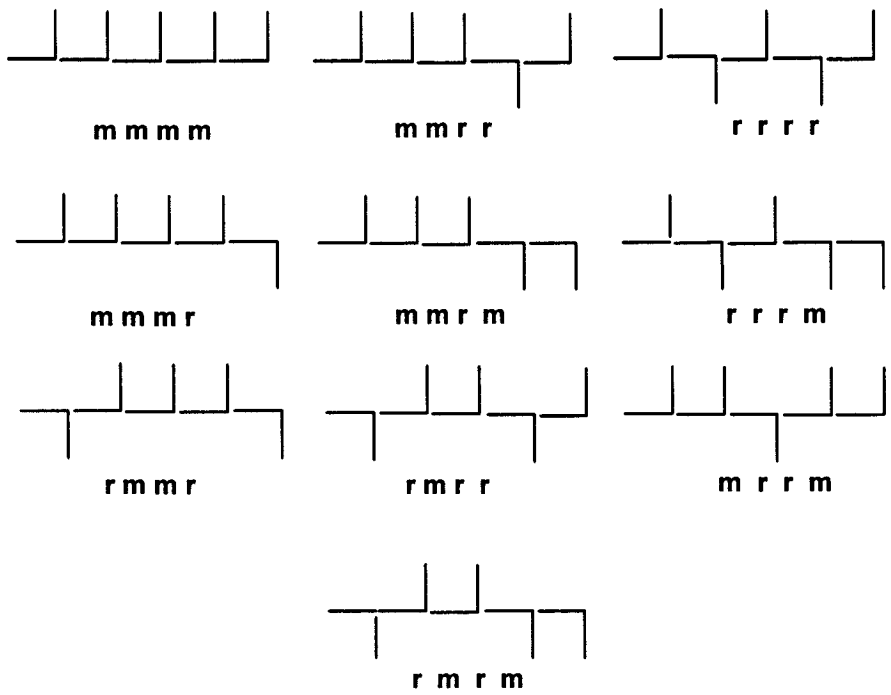

Scheme 6.1. The ten possible stereochemical pentads of polypropylene.

There are nine methyl resonances in the ^{13}C NMR spectrum, Figure 6.22, corresponding to the ten stereochemically inequivalent pentads in Scheme 6.1. The degree of isotacticity of polypropylene is defined by its content of meso pentads (%mmmm) and is determined from the methyl carbon signals in the ^{13}C NMR spectrum.[28] Using eq. 6.12, the content of mmmm-pentads calculated for polypropylene made with catalyst **4** at room temperature is ca. 40%.

$$\text{mmmm\%} = \frac{\text{area of mmmm (22 - 21.8 ppm)}}{\text{sum of the area of all methyl peaks (22 - 19) ppm}} \qquad (6.12)$$

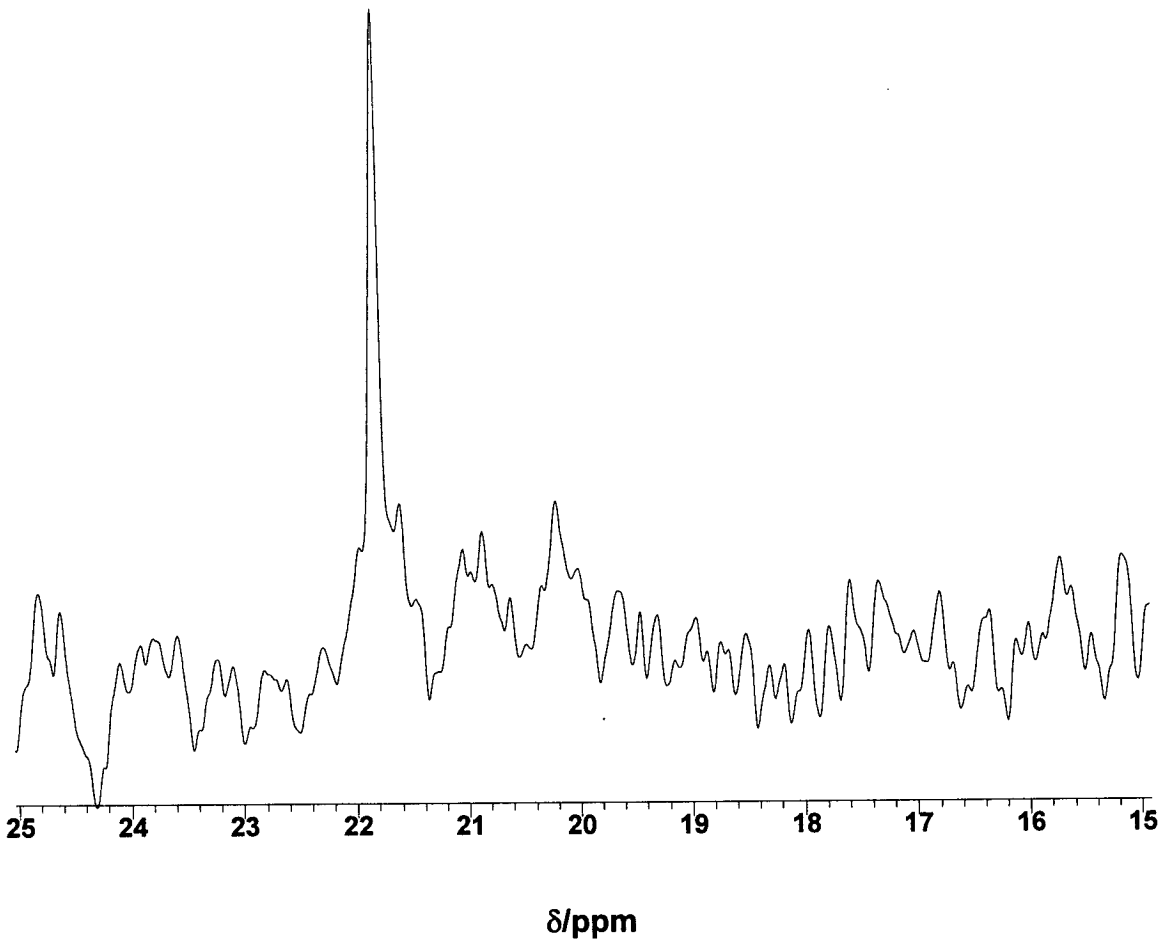

Figure 6.22. Methyl region of ^{13}C NMR spectrum of polypropylene prepared with catalyst 4 (recorded in 1,2,4-trichlorobenzene at 120 °C).

6.6.3 Thermal Analysis

Useful information about polymers can be obtained from thermal property measurements such as the glass transition temperature, T_g, the crystalline melting (conversion of microcrystalline polymer to liquid), the melting temperature, T_m, and the accompanying enthalpy and entropy changes. The data are displayed as the rate of change of heat flow ($d\Delta Q/dt$) versus temperature (ΔT).

Figure 6.23 shows thermograms for polyethylene samples. The melting curves appear similar, with melting temperatures (sharp troughs) at 406.15, 405.15 and 403.85 K for samples made with catalysts **2**, **3** and **4**, respectively. Our results are in good agreement with the melting range for High Density Polyethylene (HDPE) (398-408 K), but not with Low Density Polyethylene (LDPE) (378-393 K).[30] Thermograms for polypropylene samples (Figure 6.24) show melting points of 426.15, 432.15 and 432.15 K using catalysts **2**, **3** and **4**, respectively. The DSC curves also show glass transition temperatures, T_g, at 259.08 K for polyethylene (Figure 6.23) and 255.15 K for polypropylene (Figure 6.24) using catalyst **3.**

The enthalpy change is the amount of energy needed to overcome intermolecular forces in order to transform the polymer from a crystalline or partially crystalline state to a completely disordered amorphous state. The entropy change is a measure of the increase in the degree of disorder.

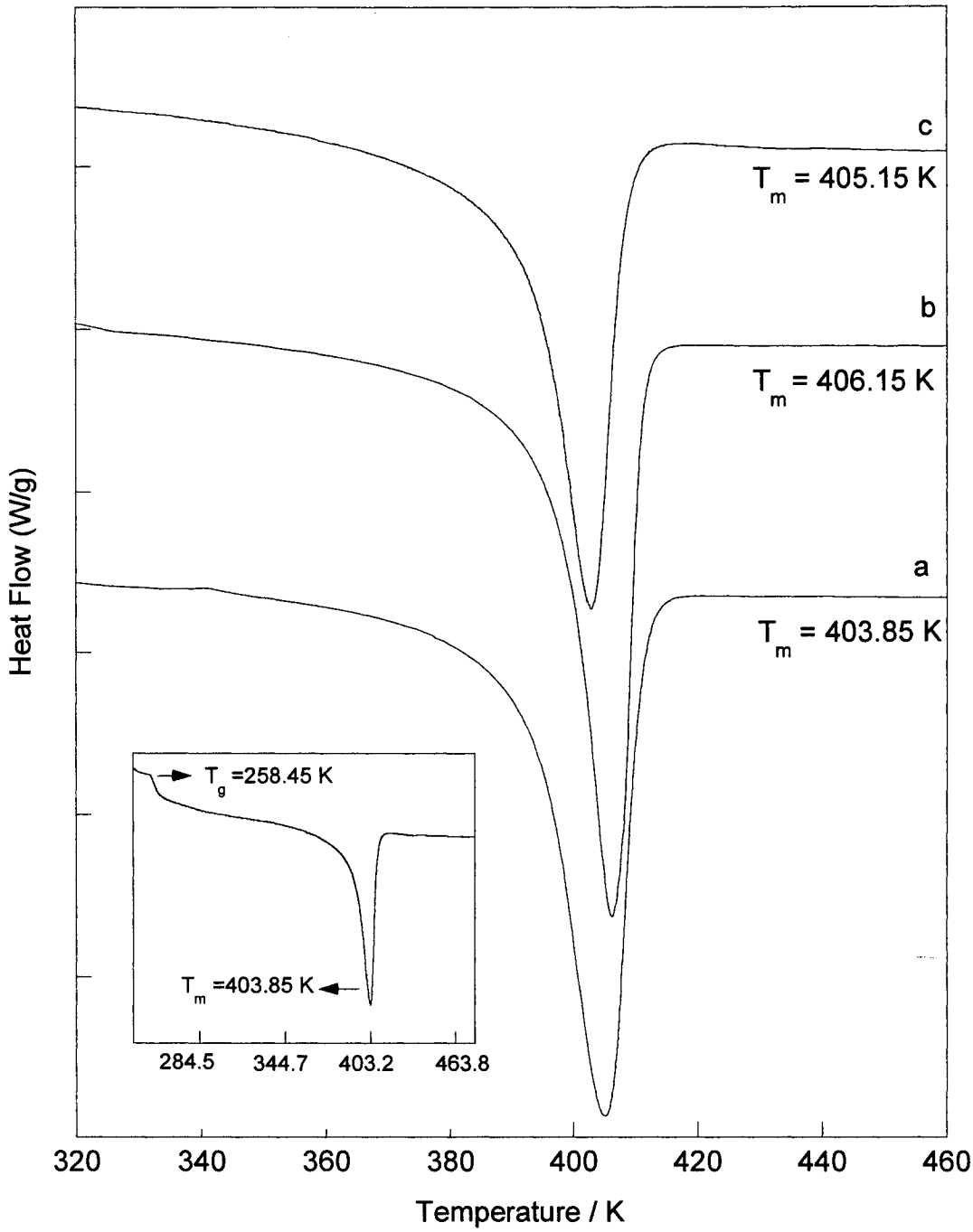

Figure 6.23. DSC curves (50-200 K) for polyethylene samples prepared with catalysts: (a) **4**; (b) **2**; and (c) **3**. The inset shows T_g for the polyethylene sample prepared with catalyst **3**.

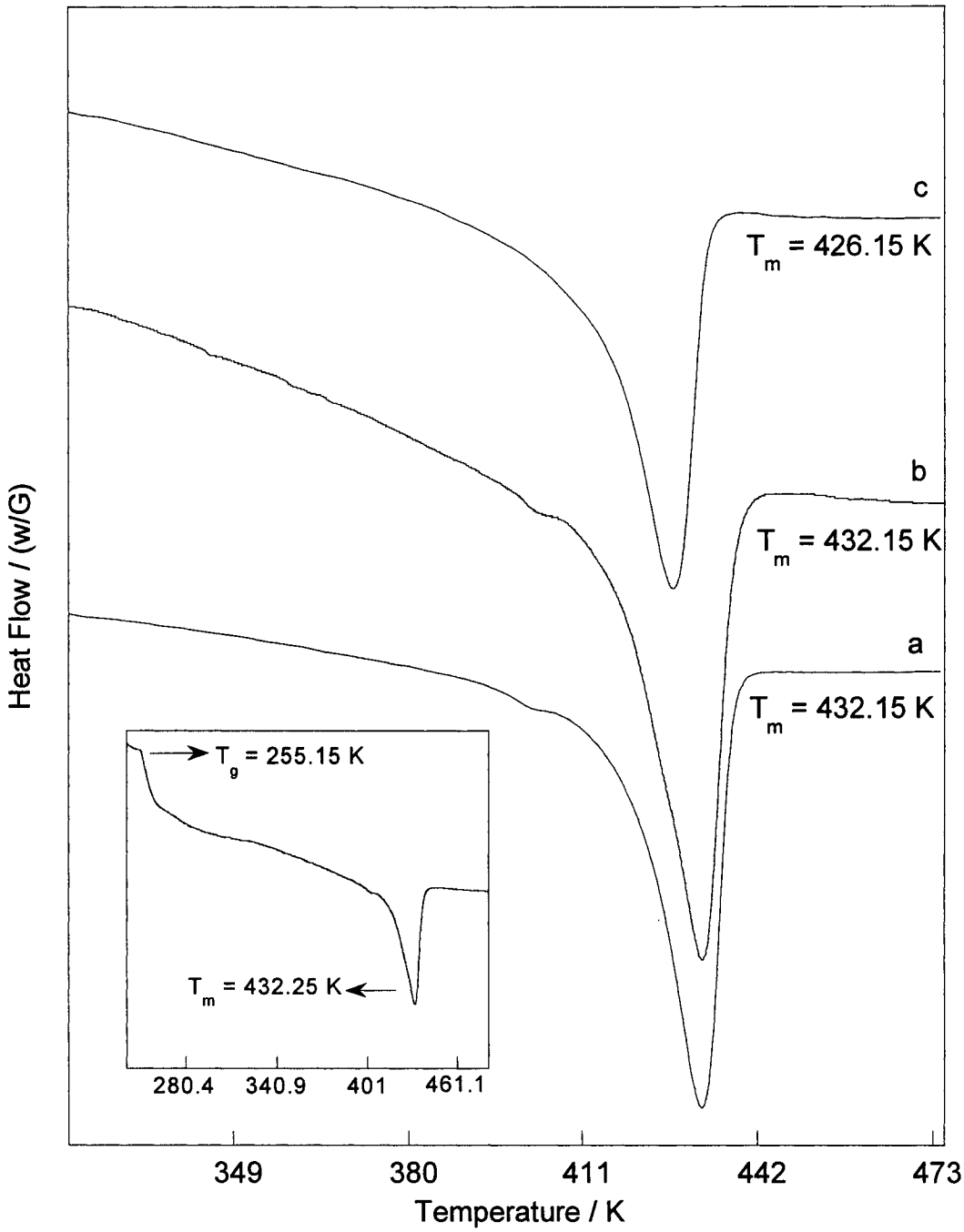

Figure 6.24. DSC curves (50-200 K) for polypropylene samples prepared with catalysts: (a) **4**; (b) **3**; and (c) **2.** The inset shows T_g for the polypropylene sample prepared with catalyst **3**.

Enthalpy changes obtained from the peak areas of the thermograms for melting are 51.32, 57.18 and 53.71 cal/g for polyethylene and 12.22, 14.80 and 13.61 cal/g for polypropylene samples made with catalysts **2**, **3** and **4**, respectively. From the enthalpy change (ΔH) and the melting point (T_m), entropy changes were calculated as $\Delta S = \Delta H / T_m$. ΔS values are 0.126, 0.141 and 0.133 cal/g.K for polyethylene and 0.029, 0.034 and 0.032 cal/g.K for polypropylene samples made using catalysts **2**, **3** and **4**, respectively.

The enthalpy and entropy changes are summarized in Table 6.8. Values for polyethylene are in reasonable agreement with those reported for HDPE.[6] The enthalpy and entropy changes for polypropylene are smaller than those of polyethylene due to the presence of methyl side groups on the polypropylene chains. In the solid state, polypropylene chains assume a helical structure so that adjacent methyl groups do not overlap, and in the molten state these methyl side groups hinder free rotation.[30, 31]

DSC can also be used to determine quantitatively the extent of branching in the polymer. The total number of side branches and end groups (A) per 1000 C atoms is obtained from the melting temperature of the polymer according to eq. 6.13.[6]

$$A = 13.1 - 0.097(T_m - 273.15) \qquad (6.13)$$

Values range from 2-4 per 1000 C atoms for polyethylene, meaning that the polymer chains are only slightly branched.

Table 6.8. DSC analysis of polyethylene and polypropylene samples

Polymer	Catalyst	T_m (K)	ΔH_m (cal/g)	ΔS_m (cal/g.K)	A	Crystallinity (%)
Polyethylene	[a]	414	68.35	0.165	0	97.6
	2	406.15	51.32	0.126	1.99	73.3
	3	405.15	57.18	0.141	2.96	81.6
	4	403.85	53.71	0.133	4.22	76.7
Polypropylene	**2**	426.15	12.22	0.029	-	-
	3	432.15	14.80	0.034	-	-
	4	432.15	13.61	0.032	-	-

[a] High density polyethylene literature reference.[6]

[b] Total side branches and end groups per 1000 C.

The degree of crystallinity for polyethylene samples was evaluated by comparing the measured melting enthalpy with the known melting enthalpy of highly crystalline polyethylene (293 J/g).[6] Resulting crystallinity values, listed in Table 6.8, agree with the values obtained with other supported Ziegler-Natta catalysts.

Thermal analysis data thus confirms that our polyethylene is high density, with significant crystallinity and chain stiffness due to structurally regular chains and very few, small branch points.

6.7 Conclusion

The catalytic activity of catalysts **4**, **2**, and **3** in ethylene polymerization was calculated using eq. 6.14:

$$\frac{dn(P_E)}{n(V)dt} = kn(C_2H_4) \qquad (6.14)$$

where $n(C_2H_4)$ is the number of moles of ethylene in 1 L, 0.041, at P = 1.0 atm, T= 295 K assuming ideal behavior. This calculation assumes that the fraction of active sites is invariant with pressure. Values are summarized in Table 6.9.[32] Activity for other olefin is also presented. Overall, catalyst **3** (A380/TMA/$VOCl_3$/TMA) with the highest Al/V ratio shows the highest activity and **2** (A380/TMA/$VOCl_3$) the lowest for ethylene and propylene. As well, catalyst **3** has more methyl group attached to vanadium compared to catalysts **2** and **4** which increase the rate of migratory insertion. **4** (A380/$VOCl_3$/TMA) is intermediate, although the differences are not great.

Table 6.9 Summary of second-order rate constants for olefin polymerization by silica-supported vanadium catalysts

Catalyst	Monomer	k s^{-1} (mol V)$^{-1}$	Catalytic activity kg PE(h.mol V.atm)
4	C_2H_4	1.25 ± 0.01	5.17
	C_3H_6	0.230 ± 0.02	1.43
2	C_2H_4	0.153 ± 0.002	0.630
	C_3H_6	0.069 ± 0.002	0.43
3	C_2H_4	3.20 ± 0.07	13.2
	C_3H_6	0.251 ± 0.009	1.59

6.8 References

1) Lehr, M. H.; Carmen, C. J. *Macromol.* **1969**, *2*, 217-219.

2) Doi, Y.; Tokuhiro, N.; Nunomura, M.; Miyake, H.; Suuki, S.; Soga, K. *Transition Metals and Organometallics as Catalysts for Olefin Polymerization*; Springer-Verlag: Berlin, **1988**.

3) Ghiotti, G.; Garrone, E.; Zecchina, A. *J. Mol. Catal.* **1988**, *46*, 61-77.

4) Bade, O. M.; Blom, R.; Dahl, I. M.; Karlsson, A. *J. Catal.* **1998**, *173*, 460-469.

5) Painter, P. C.; Coleman, M. M.; Koenig, J. L. *The Theory of Vibrational Spectroscopy and its Application to Polymeric Materials*; Wiley: New York, **1982**.

6) Groeneveld, C.; Wittgen, P. M.; Swimmen, H. P. M.; Wernsen, A.; Schuit, G. C. A. *J. Catal.* **1983**, *83*, 346-361.

7) Koenig, J. L. *Chemical Microstructure of Polymer Chains*; Wiley: New York, **1980**.

8) Koenig, J. L. *Spectroscopy of Polymers*; American Chemical Society: Washington, DC, **1992**.

9) Morse, P. M.; Spencer, M. D.; Wilson, S. R.; Girolami, G, S. *Organomet.* **1994**, *13*, 1646-1655.

10) Cossee, P. *Tetrahedron Lett.* **1960**, *17*, 12-16.

11) Cossee, P. *J. Catal.* ***1964***, *3*, 80.

12) Espenson, J. H. *Chemical Kinetics and Reaction Mechanisms*; McGraw-Hill: New York, **1981**.

13) Margl, P.; Deng, L.; Ziegler, T. *J. Am. Chem. Soc.* **1998**, *120*, 5517-5525.

14) Odian, G. *Principles of Polymerization*, 3rd ed.; Wiley: New York, **1991**.

15) Doherty, N. M.; Bercaw, J. E. *J. Am. Chem. Soc.* **1985**, *107*, 2670-2682.

16) Weiss, K.; Krauss, H. L. *J. Catal.* **1984**, *88*, 424-430.

17) Painter, P. C.; Watzek, M.; Koening, J. L. *Polymer* **1997**, *18*, 1169-1172.

18) Schachtschneider, J. H.; Snyder, R. G. *Spectrochim. Acta.* **1964**, *20,* 853

19) Karol, F. J.; Carrick, W. L. *J. Am. Chem. Soc.* **1961**, *83*, 2654-2658.

20) Chien, J. C. W.; Nozaki, T. *J. Polym. Sci; Part A: Polym. Chem.* **1993**, *31,* 227-237.

21) Amor Nait Ajjou, J.; Scott, S. L. *J. Am. Chem. Soc.* **2000**, *122*, 8968-8976.

22) Bullukat, T. J.; Hoff, R. E. *Catal. Rev.-sci. Eng.* **1999**, *41*, 389-428.

23) Sato, Y.; Nakayama, Y.; Yasuda, H.; *J. Appl. Polym. Sci*, **2003**, *89*, 1659-1662.

24) Scheuer, S.; Fischer, J.; Kress, I. *Organometallics* **1995**, *14*, 2627-2629.

25) Nomura, K.; Sagara, A.; Imanishi, Y. *Macromol* **2002**, *35*, 1583-1590.

26) Quijada-Garrido, I.; Wilhelm, M.; Spiess, H. W.; Barrales-Rienda, J. M. *Macromol. Chem. Phys.* **1998**, 985-995.

27) Locatelli, P.; Sacchi, M. C.; Tritto, I.; Zannomi, G.; Zambelli, A.; Piscitelli, V. *Macromolecules* **1985**, *18*, 627-630.

28) Busico, V.; Cipullo, R. *Prog. Polym. Sci.* **2001**, *26*, 443-553.

29) Charles, E.; Carraher, Jr. *Polymer Chemistry: an introduction*, 4th ed.; New York, **1996**.

30) Natta, G. *Angew. Chem.* **1949**, *17*, 223-229.

31) Ke, B. *J. Polym. Sci.* **1960**, *XLII*, 15-23.

32) Burwell, R. L., Jr. *Adv. Catal.* **1977**, *26*, 351-392.

Chapter Seven

General Conclusions

Siliceous materials are widely used as catalysts, and as supports for metal particles and metal complexes used in catalysis. The hydroxyl groups which terminate the surfaces of these silicas play an essential role in immobilizing the supported catalysts as well as in providing a source of Bronsted acidity. All amorphous silicas, regardless of origin, have been shown to have similar hydroxyl contents when fully hydrated. Silicas lose water through hydroxyl condensation during the thermal treatments (e.g., calcination) which form a part of many catalyst preparation protocols. The final hydroxyl content can have a dramatic effect on catalyst activity. We have developed a chemical method to measure the content of reactive hydroxyls on various silicas after thermal treatment. The reaction of excess $VOCl_3$ vapour with the surface OH groups of partially dehydroxylated silica is rapid and quantitative. Regardless of the degree of dehydroxylation, the stoichiometry of the reaction is invariable, as demonstrated by IR, XAS and solid state ^{51}V NMR spectroscopy. Using this technique, we have shown that silica has hydroxyl contents which decrease monotonically with increasing temperature of thermal treatment. We have found that there is no effect of surface area on the reactive hydroxyl contents. Porous silica gels have higher hydroxyl contents than the fumed silicas after the same thermal treatment. Furthermore, grafting of VOX_3 (X = Cl, ^{i}OPr) from solution results is incomplete reaction of the hydroxyls.

XAS has considerably expanded the information we possess regarding the vanadium site in silicas modified with vanadyl chloride. Both XANES and EXAFS are consistent with coordination to two oxygen and two chlorine atoms, giving pseudotetrahedral geometry at vanadium. This result is independent of the nature of the silica (pyrogenic or precipitated) or its pretreatment temperature.

We have prepared chemisorbed $\Xi SiOAl_2(CH_2)(CH_3)(VOCl_2)_2$ **2** by reaction of $VOCl_3$ with aluminium modified silica $\Xi SiOAl_2(CH_2)(CH_3)_3$ **1**. Also we have prepared $\Xi SiOAl(CH_2)_3(CH_3)(VOCl_2)_2$ **3** and $[\Xi SiOAl_2(CH_2)_2(CH_3)VOCl_2]_2$ dimmer **4** by reaction of TMA with **2** and $\Xi SiOVOCl_2$, respectively. These complexes were characterized by IR, ESR and elemental analysis which give information about the coordination sphere.

Finally, we have found that the catalysts **1**, **2** and **3** initiate the ethylene and propylene polymerization at room temperature. The catalytic polymerization is pseudo-first-order with rate constants which are linearly dependent on the amount of catalysts. The activation parameters ($\Delta H^{\ddagger}$, $\Delta S^{\ddagger}$) were measured for the propagation steps of ethylene and propylene polymerization are consisting of olefin binding followed by migratory insertion. No α-agostic interaction was found in the kinetic isotope effect for polymerization of D-labelled ethylene which is consistent with Cossee mechanism for the propagation step. The kinetic of ethylene-propylene copolymerization were undertaken in order to define the selectivity of the catalyst, which favour ethylene.